Development of high-performance catalysts for low temperature CO_2 hydrogenation to methanol

(低温における CO_2 水素化によるメタノール合成に有効な固体触媒の開発)

Shirun ZHAO

Graduate School of Chemical Sciences and Engineering
Hokkaido University

2026

Table of contents

Chapter 1

General introduction

1.1 The importance of methanol to human societies

As the global demand for energy continues to increase, the depletion of fossil fuels and the growing threat of climate change have become critical issues for modern societies.[1–4] Methanol (CH_3OH), a simple one-carbon alcohol, has emerged as one of the most promising renewable energy carriers and chemical feedstocks.[5–8] It serves not only as a platform molecule to produce numerous chemicals and fuels but also as a vital component of the "methanol economy" proposed to replace the current fossil-based system.[1,5,9–11]

Methanol is a versatile compound with wide-range of applications in daily life and industry (Figure 1.1). It is primarily used as a solvent, fuel, and raw material in the synthesis of formaldehyde, acetic acid, olefins, and other value-added chemicals.[5,6,8] In the transportation sector, methanol can be directly blended with gasoline or converted to dimethyl ether (DME), which can serve as a clean diesel substitute.[12–14] In addition, methanol is being explored as a potential hydrogen carrier due to its high hydrogen content (12.6 wt%) and liquid-state storage advantages.[15–19]

The global methanol market has maintained steady growth in recent years. In 2024, the market was valued at approximately USD 34.08 billion and is projected to reach around USD 47.91 billion by 2032, growing at a compound annual growth rate (CAGR) of about 4.4% from 2022 to 2032.[11] This growth is primarily driven by the rising demand for methanol as an essential feedstock in chemical manufacturing, as well as its increasing use in renewable energy systems such as methanol-to-olefins (MTO) processes and as a cleaner alternative fuel in marine and transportation sectors.[20–22]

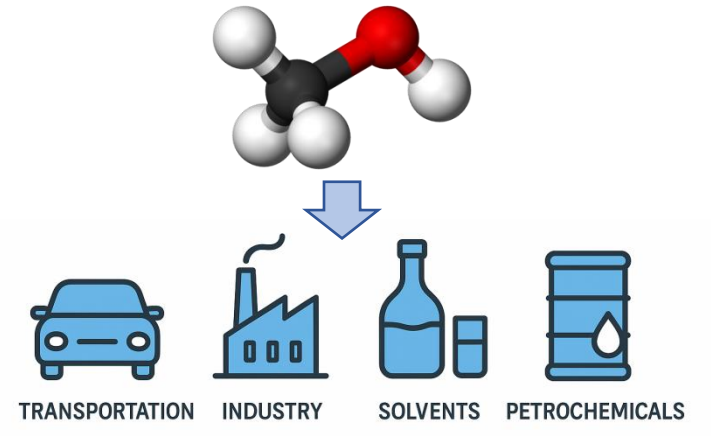

Figure 1.1 the application of methanol in different fields.

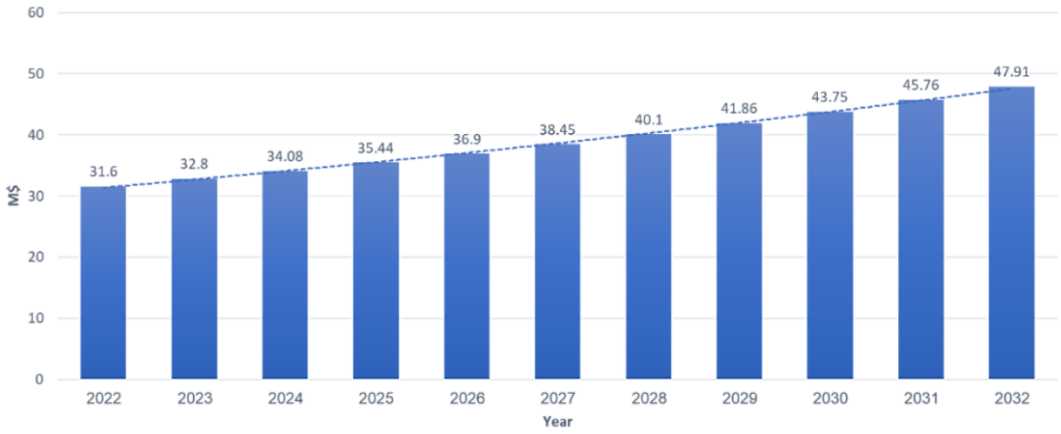

Figure 1.2 Global methanol market size forecasts[11]

1.2 The production of methanol

Currently, most of the industrial methanol is produced from fossil-based feedstocks such as natural gas and coal through syngas (CO + H_2) conversion.[8,23] The conventional industrial process involves three main steps: (1) steam reforming or partial oxidation of hydrocarbons to produce syngas, (2) catalytic conversion of syngas to methanol, and (3) methanol purification. Currently, Cu/ZnO/Al_2O_3-based systems are used industrially at high temperatures (>220 °C) and under high pressures (5-10 MPa).[8,24]

Moreover, the heavy reliance on fossil fuels in these processes inevitably results in significant CO_2 emissions. Consequently, to achieve carbon neutrality, considerable attention has turned to developing sustainable routes for methanol synthesis using renewable carbon sources such as CO_2 and biomass.[4,6,25]

Alternative technologies, including electrochemical CO_2 reduction and photocatalytic hydrogenation, are currently under active investigation.[26,27] Nevertheless, catalytic hydrogenation of CO_2 using H_2 derived from renewable sources (e.g., water electrolysis powered by wind or solar energy) remains the most feasible and scalable pathway toward carbon-neutral methanol production.[5,25,28]

1.3 CO_2 hydrogenation to methanol

The rapid rise in atmospheric CO_2 concentration has resulted in global warming, ocean acidification, and ecological degradation. Transforming CO_2 into methanol through catalytic hydrogenation not only mitigates carbon emissions but also offers a sustainable approach to producing fuels and chemicals. The overall reaction can be expressed as follows:

$$CO_2 + 3H_2 \rightarrow CH_3OH + H_2O$$

This reaction is exothermic ($\Delta H° = -49.5$ kJ mol^{-1}) in nature, and the equilibrium favors methanol formation at relatively low temperatures and high pressures. Therefore, we aimed to develop highly efficient catalysts under low-temperature conditions (Figure 1.3).[29]

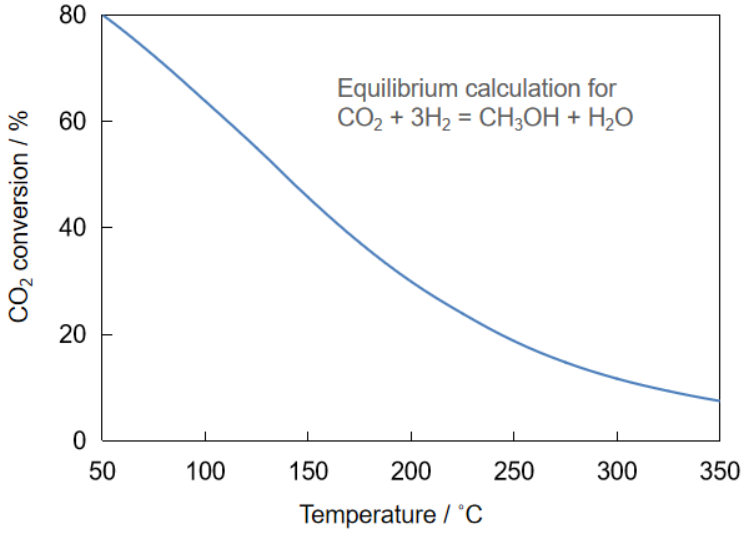

Figure 1.3 Thermodynamic equilibrium of CO_2 hydrogenation to methanol as a function of temperature and pressure.[29]

The main challenge in this process lies in the chemical inertness of CO_2 and the competition with the reverse water–gas shift (RWGS) reaction ($CO_2 + H_2 \rightleftharpoons CO + H_2O$), which reduces methanol selectivity.[30] Thus, the design of efficient catalysts capable of activating CO_2, facilitating hydrogenation, and suppressing CO formation is crucial.

(1) Cu-based catalysts

$Cu/ZnO/Al_2O_3$ catalysts remain the industrial benchmark for CO_2-to-methanol conversion.[24,31] Cu acts as the primary active site for hydrogenation, while ZnO and Al_2O_3 serve as promoters and stabilizers, enhancing CO_2 adsorption and preventing Cu sintering. The reaction mechanism generally involves the formation of formate (HCOO*) intermediates, followed by stepwise hydrogenation to methanol.[32,33] However, these catalysts typically require elevated temperatures (>250 °C) and suffer from deactivation due to water-induced sintering and Cu oxidation.[34]

(2) In-based catalysts

Recent studies have highlighted In_2O_3-based catalysts as promising alternatives with superior methanol selectivity and water tolerance.[35,36] The active oxygen vacancies on In_2O_3 facilitate CO_2 activation and promoted formate intermediate stabilization, while the introduction of metals such as Pd, Pt, or Ni enhances hydrogen dissociation and spillover.[35,37–39] For instance, Pd/In_2O_3 catalysts have shown high methanol selectivity of >60% at 300 °C.[37,39,40] Such systems demonstrate high potential for CO_2 hydrogenation, an essential step toward energy-efficient methanol synthesis.

(3) Other emerging catalysts

Beyond Cu and In systems, Ga-based and Zr-based materials have been reported to exhibit excellent activity and selectivity.[24,41–44] These catalysts often feature bifunctional interfaces that enable both CO_2 activation and C–O bond hydrogenation while suppressing CO formation.[8,24,35] Moreover, hybrid catalysts combining metal nanoparticles with oxide supports such as Cu/ZrO_2 and Pd/ZnO are being explored for enhanced performance and stability. [45–47]

(4) Challenges and future prospects

Although significant progress has been achieved, several challenges remain before CO_2 hydrogenation to methanol becomes industrially viable.[26,28] For example, currently used copper-based catalysts require high-temperature (>220 °C), high-pressure conditions for the reaction, while the hydrogenation of carbon dioxide to methanol is thermodynamically favored at lower temperatures. Advanced catalyst design strategies such as atomic-level structural tuning, defect engineering, and machine-learning-guided screening are being actively pursued to overcome these limitations.[48–52]

With continued research and technological innovation, CO_2 hydrogenation to methanol is expected to play a central role in realizing a carbon-neutral circular economy, linking renewable energy, chemical production, and carbon recycling in a sustainable loop.[8,9,12,20]

1.4 Thesis outline

The objective of this dissertation is to develop high-performance heterogeneous catalysts for low temperature CO_2 hydrogenation to methanol. This thesis will be divided into the following chapters:

Chapter 2: Development of highly active catalysts for low-temperature CO_2 hydrogenation to methanol using a machine learning approach

An extrapolated machine learning (ML) method was employed to develop highly efficient catalysts for methanol synthesis via CO_2 hydrogenation in batch reactor. Starting with an initial dataset of 80 catalysts, we conducted 43 iterations of a closed loop discovery system (ML predictions + experimental validation), testing a total of 580 catalysts. The multi-element Pt(5)/Mo(8)-Re(1)-W(0.7)/TiO_2_P25_550 catalyst, where the numbers in parentheses represent the content amount (wt%), was identified as the most effective catalyst (STY_{MeOH}: 1.42 mmol g_{cat}^{-1} h^{-1}) for methanol synthesis. Additionally, more than 30 catalysts with superior activity were discovered through this data-driven approach. And we also do operando spectroscopic studies on mechanism for the best catalyst.

Chapter 3: Nb-promoted Pt/MoO_x/TiO_2 catalysts for low‐temperature CO_2 hydrogenation to methanol

We developed an efficient catalyst for low temperature methanol synthesis under flow system, Pt(5)/Mo(10)-Nb(1) /TiO_2, which enhances the methanol space time yield (STY_{MeOH}) to 3.8 mmol g_{cat}^{-1} h^{-1}, under optimized conditions (150 °C, 4 MPa). Furthermore, we investigated the roles of each constituent element using *in situ/operando* spectroscopy, and these results demonstrate that all components are necessary for efficient methanol synthesis.

Chapter 4: Machine-learning-assisted catalysts discovery for low-temperature methanol synthesis from CO_2 and H_2 in flow system

Based on the existing machine learning model foundation, we optimized and expanded the existing model and applied it to flow reactors to explore high-performance catalysts. After 25 iterations, we developed the catalyst, Pt(5)/Mo(8)-Cr(0.7)-V(0.7)-La(0.7)-Re(1)/TiO_2 (P25)_550, which showed on of the highest methanol formation rate (6.2 mmol g_{cat}^{-1} h^{-1}) ever reported at low temperatures (<180 °C). Additionally, *in situ*/*operando* characterizations were carried out to understand the structure of the catalyst under reaction condition and the role of each component in promoting methanol synthesis.

1.5 Reference

(1) Jeffry, L.; Ong, M. Y.; Nomanbhay, S.; Mofijur, M.; Mubashir, M.; Show, P. L. Greenhouse Gases Utilization: A Review. *Fuel* **2021**, *301*, 121017.

(2) Hao, Y.; Mao, J.; Bachmann, C. M.; Hoffman, F. M.; Koren, G.; Chen, H.; Tian, H.; Liu, J.; Tao, J.; Tang, J.; Li, L.; Liu, L.; Apple, M.; Shi, M.; Jin, M.; Zhu, Q.; Kannenberg, S.; Shi, X.; Zhang, X.; Wang, Y.; Fang, Y.; Dai, Y. Soil Moisture Controls over Carbon Sequestration and Greenhouse Gas Emissions: A Review. *npj Clim. Atmos. Sci.* **2025**, *8* (1), 16.

(3) Parker, W. E.; Brown, M. K.; Linares, R. Greenhouse Gases Reduce the Satellite Carrying Capacity of Low Earth Orbit. *Nat. Sustain.* **2025**, *8* (4), 363–372.

(4) Zhang, Y.; Du, J.; Shan, Y.; Wang, F.; Liu, J.; Wang, M.; Liu, Z.; Yan, Y.; Xu, G.; He, G.; Shi, X.; Lian, Z.; Yu, Y.; Shan, W.; He, H. Toward Synergetic Reduction of Pollutant and Greenhouse Gas Emissions from Vehicles: A Catalysis Perspective. *Chem. Soc. Rev.* **2025**, *54* (3), 1151–1215.

(5) Al-Attas, T.; Khan, M. A.; Kibria, M. G. Electrification of Chemical Industry: A Case Study on Methanol Production. *ACS Sustain. Chem. Eng.* **2025**, *13* (21), 7915–7925.

(6) Marques da Cunha, M.; Petrollese, M.; Farinelli, E.; Morea, D.; Leonzio, G. Performance Analysis of Bio-Methanol Production through Bi and Tri-Reforming Processes Integrated into a Carnot Battery. *Energy* **2025**, *335*, 138104.

(7) Fasihi, M.; Breyer, C. Global Production Potential of Green Methanol Based on Variable Renewable Electricity. *Energy Environ. Sci.* **2024**, *17* (10), 3503–3522.

(8) Zang, G.; Sun, P.; Elgowainy, A.; Wang, M. Technoeconomic and Life Cycle Analysis of Synthetic Methanol Production from Hydrogen and Industrial Byproduct CO_2. *Environ. Sci. Technol.* **2021**, *55* (8), 5248–5257.

(9) Filosa, C.; Gong, X.; Bavykina, A.; Chowdhury, A. D.; Gallo, J. M. R.; Gascon, J. Enabling the Methanol Economy: Opportunities and Challenges for Heterogeneous Catalysis in the Production of Liquid Fuels via Methanol. *Acc. Chem. Res.* **2023**, *56* (23), 3492–3503.

(10) Sen, R.; Goeppert, A.; Surya Prakash, G. K. Homogeneous Hydrogenation of CO_2 and CO to Methanol: The Renaissance of Low-Temperature Catalysis in the Context of the Methanol Economy. *Angew. Chemie Int. Ed.* **2022**, *61* (42), e202207278.

(11) Hosseinpour, A.; shayesteh, K.; Es'haghi, P. A Review of the Importance, Production, Economics, and Future of Methanol in Iran and the World. *Chem. Res. Technol.* **2025**, *2* (1), 1–11.

(12) Merkouri, L.-P.; Ahmet, H.; Ramirez Reina, T.; Duyar, M. S. The Direct Synthesis of Dimethyl Ether (DME) from Landfill Gas: A Techno-Economic Investigation. *Fuel* **2022**, *319*, 123741.

(13) Vu, T. T. N.; Desgagnés, A.; Iliuta, M. C. Efficient Approaches to Overcome Challenges in Material Development for Conventional and Intensified CO_2 Catalytic Hydrogenation to CO, Methanol, and DME. *Appl. Catal. A Gen.* **2021**, *617*, 118119.

(14) van Kampen, J.; Boon, J.; van Sint Annaland, M. Separation Enhanced Methanol and Dimethyl Ether Synthesis. *J. Mater. Chem. A* **2021**, *9* (26), 14627–14629.

(15) Usman, M. R. Hydrogen Storage Methods: Review and Current Status. *Renew. Sustain. Energy Rev.* **2022**, *167*, 112743.

(16) Xu, X.; Dong, Y.; Hu, Q.; Si, N.; Zhang, C. Electrochemical Hydrogen Storage Materials: State-of-the-Art and Future Perspectives. *Energy & Fuels* **2024**, *38* (9), 7579–7613.

(17) Bai, M.; Liu, S.; Qi, M.; Kim, J.; Moon, I.; Feng, W.; Kim, J.; Liu, Y. Comprehensive Design of Hydrogen-Battery Hybrid Energy Storage System in Green Methanol Production from Economic, Safety, and Resilience Perspectives. *ACS Sustain. Chem. Eng.* **2025**, *13* (10), 3877–3894.

(18) Onishi, N.; Laurenczy, G.; Beller, M.; Himeda, Y. Recent Progress for Reversible Homogeneous Catalytic Hydrogen Storage in Formic Acid and in Methanol. *Coord. Chem. Rev.* **2018**, *373*, 317–332.

(19) Shao, Z.; Li, Y.; Liu, C.; Ai, W.; Luo, S.-P.; Liu, Q. Reversible Interconversion between Methanol-Diamine and Diamide for Hydrogen Storage Based on Manganese Catalyzed (de)Hydrogenation. *Nat. Commun.* **2020**, *11* (1), 591.

(20) Tian, P.; Wei, Y.; Ye, M.; Liu, Z. Methanol to Olefins (MTO): From Fundamentals to Commercialization. *ACS Catal.* **2015**, *5* (3), 1922–1938.

(21) Zhong, J.; Han, J.; Wei, Y.; Liu, Z. Catalysts and Shape Selective Catalysis in the Methanol-to-Olefin (MTO) Reaction. *J. Catal.* **2021**, *396*, 23–31.

(22) Zhou, J.; Gao, M.; Zhang, J.; Liu, W.; Zhang, T.; Li, H.; Xu, Z.; Ye, M.; Liu, Z. Directed Transforming of Coke to Active Intermediates in Methanol-to-Olefins Catalyst to Boost Light Olefins Selectivity. *Nat. Commun.* **2021**, *12* (1), 17.

(23) Qazi, I. A.; Abd, A. A.; Hasan, M. M.; Othman, M. R. Optimizing Hydrogen Purification Performance by Membrane from Industrial Waste of Methanol Production. *Chem. Eng. J. Adv.* **2023**, *14*, 100490.

(24) Meunier, N.; Chauvy, R.; Mouhoubi, S.; Thomas, D.; De Weireld, G. Alternative Production of Methanol from Industrial CO_2. *Renew. Energy* **2020**, *146*, 1192–1203.

(25) Harris, K.; Grim, R. G.; Huang, Z.; Tao, L. A Comparative Techno-Economic Analysis of Renewable Methanol Synthesis from Biomass and CO_2: Opportunities and Barriers to Commercialization. *Appl. Energy* **2021**, *303*, 117637.

(26) Battaglia, P.; Buffo, G.; Ferrero, D.; Santarelli, M.; Lanzini, A. Methanol Synthesis through CO_2 Capture and Hydrogenation: Thermal Integration, Energy Performance and Techno-Economic Assessment. *J. CO2 Util.* **2021**, *44*, 101407.

(27) Belkin, M.; Hsu, D.; Ma, S.; Mandal, S. Reconciling Modern Machine-Learning Practice and the Classical Bias–Variance Trade-Off. *Proc. Natl. Acad. Sci. U. S. A.* **2019**, *116* (32), 15849–15854.

(28) Huang, R.; Kang, L.; Liu, Y. Renewable Synthetic Methanol System Design Based on Modular Production Lines. *Renew. Sustain. Energy Rev.* **2022**, *161*, 112379.

(29) Toyao, T.; Kayamori, S.; Maeno, Z.; Siddiki, S. M. A. H.; Shimizu, K. I. Heterogeneous Pt and MoO_x Co-Loaded TiO_2 Catalysts for Lowerature CO_2 Hydrogenation to Form CH_3OH. *ACS Catal.* **2019**, *9* (9), 8187–8196.

(30) González-Castaño, M.; Dorneanu, B.; Arellano-García, H. The Reverse Water Gas Shift Reaction: A Process Systems Engineering Perspective. *React. Chem. Eng.* **2021**, *6* (6), 954–976.

(31) Kondratenko, E. V; Mul, G.; Baltrusaitis, J.; Larrazábal, G. O.; Pérez-Ramírez, J. Status and Perspectives of CO_2 Conversion into Fuels and Chemicals by Catalytic, Photocatalytic and Electrocatalytic Processes. *Energy Environ. Sci.* **2013**, *6* (11), 3112–3135.

(32) Behrens, M.; Studt, F.; Kasatkin, I.; Kühl, S.; Hävecker, M.; Abild-Pedersen, F.; Zander, S.; Girgsdies, F.; Kurr, P.; Kniep, B.-L.; Tovar, M.; Fischer, R. W.; Nørskov, J. K.; Schlögl, R. The Active Site of Methanol Synthesis over Cu/ZnO/Al_2O_3 Industrial Catalysts. *Science (80-.).* **2012**, *336* (6083), 893–897.

(33) Fichtl, M. B.; Schlereth, D.; Jacobsen, N.; Kasatkin, I.; Schumann, J.; Behrens, M.; Schlögl, R.; Hinrichsen, O. Kinetics of Deactivation on Cu/ZnO/Al2O3 Methanol Synthesis Catalysts. *Appl. Catal. A Gen.* **2015**, *502*, 262–270.

(34) Jiang, Z.; Li, D.; Gu, H.; Jin, S.; Zhu, M. Understanding the Environmental Sensitivity of Copper-Metal Oxides Interactions in Cu/ZnO and Cu/Al2O3 Catalysts. *ChemCatChem* **2024**, *16* (23), e202401323.

(35) Gao, B.; Wen, Z.; Wang, Y.; Chen, D.; Yang, B.; Ishihara, T.; Guo, L. Recent Advances in Alloy Catalysts for CO_2 Hydrogenation to Methanol. *ChemCatChem* **2024**, *16* (19), e202400814.

(36) Tsoukalou, A.; Bushkov, N. S.; Docherty, S. R.; Mance, D.; Serykh, A. I.; Abdala, P. M.; Copéret, C.; Fedorov, A.; Müller, C. R. Surface Intermediates in In-Based ZrO_2-Supported Catalysts for Hydrogenation of CO_2 to Methanol. *J. Phys. Chem. C* **2022**, *126* (4), 1793–1799.

(37) Rui, N.; Wang, Z.; Sun, K.; Ye, J.; Ge, Q.; Liu, C. CO_2 Hydrogenation to Methanol over Pd/In_2O_3: Effects of Pd and Oxygen Vacancy. *Appl. Catal. B Environ.* **2017**, *218*, 488–497.

(38) Sun, K.; Shen, C.; Zou, R.; Liu, C. Highly Active Pt/In_2O_3-ZrO_2 Catalyst for CO_2 Hydrogenation to Methanol with Enhanced CO Tolerance: The Effects of ZrO_2. *Appl. Catal. B Environ.* **2023**, *320*, 122018.

(39) Araújo, T. P.; Morales-Vidal, J.; Giannakakis, G.; Mondelli, C.; Eliasson, H.; Erni, R.; Stewart, J. A.; Mitchell, S.; López, N.; Pérez-Ramírez, J. Reaction-Induced Metal-Metal Oxide Interactions in Pd-In_2O_3/ZrO_2 Catalysts Drive Selective and Stable CO_2 Hydrogenation to Methanol. *Angew. Chemie Int. Ed.* **2023**, *62* (42), e202306563.

(40) Lorenz, H.; Turner, S.; Lebedev, O. I.; Van Tendeloo, G.; Klötzer, B.; Rameshan, C.; Pfaller, K.; Penner, S. Pd–In_2O_3 Interaction Due to Reduction in Hydrogen: Consequences for Methanol Steam Reforming. *Appl. Catal. A Gen.* **2010**, *374* (1), 180–188.

(41) Bagchi, D.; Raj, J.; Singh, A. K.; Cherevotan, A.; Roy, S.; Manoj, K. S.; Vinod, C. P.; Peter, S. C. Structure-Tailored Surface Oxide on Cu–Ga Intermetallics Enhances CO_2 Reduction Selectivity to Methanol at Ultralow Potential. *Adv. Mater.* **2022**, *34* (19), 2109426.

(42) Proaño, L.; Jones, C. W. CO_2 Hydrogenation to Methanol over Ceria-Zirconia NiGa Alloy Catalysts. *Appl. Catal. A Gen.* **2024**, *669*, 119485.

(43) Rameshan, C.; Stadlmayr, W.; Penner, S.; Lorenz, H.; Mayr, L.; Hävecker, M.; Blume, R.; Rocha, T.; Teschner, D.; Knop-Gericke, A.; Schlögl, R.; Zemlyanov, D.; Memmel, N.; Klötzer, B. In Situ XPS Study of Methanol Reforming on PdGa Near-Surface Intermetallic Phases. *J. Catal.* **2012**, *290*, 126–137.

(44) Bonura, G.; Cordaro, M.; Cannilla, C.; Arena, F.; Frusteri, F. The Changing Nature of the Active Site of Cu-Zn-Zr Catalysts for the CO_2 Hydrogenation Reaction to Methanol. *Appl. Catal. B Environ.* **2014**, *152–153*, 152–161.

(45) Ye, R.-P.; Li, Q.; Gong, W.; Wang, T.; Razink, J. J.; Lin, L.; Qin, Y.-Y.; Zhou, Z.; Adidharma, H.; Tang, J.; Russell, A. G.; Fan, M.; Yao, Y.-G. High-Performance of Nanostructured Ni/CeO_2 Catalyst on CO_2 Methanation. *Appl. Catal. B Environ. Energy* **2020**, *268*, 118474.

(46) Bahruji, H.; Bowker, M.; Hutchings, G.; Dimitratos, N.; Wells, P.; Gibson, E.; Jones, W.; Brookes, C.; Morgan, D.; Lalev, G. Pd/ZnO Catalysts for Direct CO_2 Hydrogenation to Methanol. *J. Catal.* **2016**, *343*, 133–146.

(47) Samson, K.; Śliwa, M.; Socha, R. P.; Góra-Marek, K.; Mucha, D.; Rutkowska-Zbik, D.; Paul, J.-F.; Ruggiero-Mikołajczyk, M.; Grabowski, R.; Słoczyński, J. Influence of ZrO_2 Structure and Copper Electronic State on Activity of Cu/ZrO_2 Catalysts in Methanol Synthesis from CO_2. *ACS Catal.* **2014**, *4* (10), 3730–3741.

(48) Shi, Y.-F.; Kang, P.-L.; Shang, C.; Liu, Z.-P. Methanol Synthesis from CO_2/CO Mixture on Cu–Zn Catalysts from Microkinetics-Guided Machine Learning Pathway Search. *J. Am. Chem. Soc.* **2022**, *144* (29), 13401–13414.

(49) Zhao, H.; Liu, X.; Zeng, C.; Liu, W.; Tan, L. Thermochemical CO_2 Reduction to Methanol over Metal-Based Single-Atom Catalysts (SACs): Outlook and Challenges for Developments. *J. Am. Chem. Soc.* **2024**, *146* (34), 23649–23662.

(50) Ren, X.; Zhao, J.; Li, X.; Shao, J.; Pan, B.; Salamé, A.; Boutin, E.; Groizard, T.; Wang, S.; Ding, J.; Zhang, X.; Huang, W.-Y.; Zeng, W.-J.; Liu, C.; Li, Y.; Hung, S.-F.; Huang, Y.; Robert, M.; Liu, B. In-Situ Spectroscopic Probe of the Intrinsic Structure Feature of Single-Atom Center in Electrochemical CO/CO_2 Reduction to Methanol. *Nat. Commun.* **2023**, *14* (1), 3401.

(51) Zhang, Z.; Liu, J.; Wang, J.; Wang, Q.; Wang, Y.; Wang, K.; Wang, Z.; Gu, M.; Tang, Z.; Lim, J.; Zhao, T.; Ciucci, F. Single-Atom Catalyst for High-Performance Methanol Oxidation. *Nat. Commun.* **2021**, *12* (1), 5235.

(52) Zhao, S.; Mine, S.; Wang, G.; Zhang, W.; El Fakir, A. A.; Yang, B.; Qin, Z.; Dostagir, N. H. M. D.; Matsushita, K.; Takigawa, I.; Shimizu, K.; Toyao, T. Development of Highly Active Catalysts for Low-Temperature CO_2 Hydrogenation to Methanol Using a Machine Learning Approach. *J. Am. Chem. Soc.* **2025**, *147* (34), 31121–31135.

Chapter 2

Development of highly active catalysts for low-temperature CO_2 hydrogenation to methanol using a machine learning approach

2.1 Introduction

Renewable carbon sources have recently gained significant attention for energy generation and chemical production, driven by growing concerns over the depletion of fossil fuel and climate change.[1,2] Despite being a major greenhouse gas, CO_2 is considered a promising precursor for manufacturing crucial industrial chemicals and fuels. Among various chemicals derived from CO_2, the synthesis of methanol through CO_2 hydrogenation has been of great interest in the industrial and scientific communities. This interest stems from methanol's versatility as a chemical precursor and its utility as a fuel and liquid energy carrier.[3]

The significance of CO_2 hydrogenation for methanol production is clear in the context of CO_2 utilization and the circular economy, with methanol serving as a chemical energy carrier.[4] Direct industrial production of methanol via CO_2 hydrogenation has been achieved using copper-based catalysts under harsh reaction conditions (5-10 MPa; >220 °C).[5] Despite this milestone, the method suffers from low equilibrium conversion of CO_2 to methanol, necessitating extensive recycling of the effluent stream after product separation. Industrial methanol production at lower temperatures offers advantages, potentially enabling higher or complete conversion of CO_2 to methanol and reducing operating costs. However, developing highly active catalysts for methanol synthesis at lower temperatures poses a challenge.[6–10] While methanol synthesis is exothermic in nature, the chemical inertness of CO_2 hinders hydrogenation at temperatures below 200 °C,[11–14] leading to poor methanol productivity.[15–20] Therefore, the development of highly active catalysts for low-temperature CO_2 hydrogenation to methanol is crucial.

Recent advances in molecular and materials informatics have brought about a significant change in molecular and materials science, providing fresh opportunities for the systematic design of functional molecules/materials.[21–30] While artificial intelligence (AI) has demonstrated proof-of-concept success in accelerating catalyst discovery, significantly reducing both time and cost, most studies have been restricted to benchmark problems, yielding no fundamentally new molecules, materials, or synthetic transformations.[31] A key challenge of machine learning (ML) models is their tendency to optimize known datasets rather than extrapolating beyond existing materials to discover exceptional candidates. This issue is particularly evident in catalysis informatics, where reactions involve dynamic and time-dependent phenomena.[24,32–36] In contrast to materials informatics, catalysis research is often empirical, lacking high-quality datasets due to the high computational costs of

accurately modeling heterogeneous catalysts.[37–42] Furthermore, high-throughput experimental techniques, which have successfully advanced other scientific fields, are still underdeveloped in catalysis.[43–45] Moreover, the scarcity of negative outcomes in catalysis research presents a significant challenge for data-driven approaches.[46] Therefore, developing ML models capable of efficiently identifying novel catalysts within diverse chemical space from experimental catalysis data is highly desirable.[47–49]

In this context, our group has proposed an ML approach that utilizes elemental features as input representations instead of directly inputting the catalyst compositions.[50,51] Specifically, every catalyst is described as a set of elemental descriptors, such as electronegativities and melting points, which are weighted according to the elemental content.[50,52,53] This approach allows for catalyst design and discovery in regions with little overlap in compositions and can even incorporate elements not originally present in the dataset, enabling extrapolative predictions beyond the training data. Other studies have also confirmed the relevance of such predictions using advanced feature engineering and selection techniques.[54] Beyond the theoretical support for identifying novel catalysts and high-performance materials through extrapolative prediction,[50,52,55] we recently developed multi-elemental reverse water-gas shift catalysts using this approach.[56] The optimal catalyst was Pt(3)/Rb(1)–Ba(1)–Mo(0.6)–Nb(0.2)/TiO_2; notably, Nb was absent from the original dataset, and the resulting catalyst composition was unexpected even for human experts. This success demonstrated the ability of ML-driven catalyst design to move beyond conventional human-intuition-based exploration. However, although this approach successfully identified novel high-performance catalysts, it was limited to a single catalytic system, focusing only on the effect of additive oxides while keeping Pt and TiO_2 fixed as the supported metal and support, respectively. More recently, therefore, we extended our extrapolative ML strategy to develop new multi-elemental catalysts for low-temperature NO reduction via selective catalytic reduction using H_2 (H_2-SCR).[57] Using an initial dataset of 45 catalysts, we performed 24 iterative cycles of ML-guided discovery (ML predictions + experiment), experimentally testing 425 catalysts and identifying several catalysts with superior activity compared to previously reported high-performance catalysts in the 50–150 °C range. The optimal catalyst was Pt(1.3)–Ir(0.2)/Ba(1.5)–Co(1)/H-ZSM-5 (Si/Al = 11), where Co was absent from the initial dataset. This study further highlights the potential of extrapolative ML for identifying unexpected and highly efficient catalytic systems. There is a strong demand to apply this ML approach to other valuable catalytic reaction processes.

In this study, we utilized our ML approach to develop new multi-elemental catalysts for methanol production via low-temperature CO_2 hydrogenation. Initially, we analyzed a dataset of 90 catalysts and conducted 43 cycles of a closed-loop discovery process involving ML predictions and experimental validations. This iterative approach led to the experimental evaluation of 580 catalysts, identifying catalysts with superior activity compared to the previously recognized high-performance catalyst, Pt(3)/Mo(20)/TiO_2.[58]

2.2 Materials and methods

2.2.1 Catalyst preparation

The catalysts were prepared using the sequential impregnation method and named $PGM_1(X_{P1})$-$PGM_2(X_{P2})$-$PGM_3(X_{P3})$/$Add_1(X_{A1})$-$Add_2(X_{A2})$-$Add_3(X_{A3})$-$Add_4(X_{A4})$/Support_CalcT. In this study, PGM refers to Pt, Pd, Ru, Rh, Ir, and Au. For the additive (Add) elements, a total of 57 elements with atomic numbers 3 (Li) to 83 (Bi), excluding Be, B, C, N, O, F, Cl, As, Br, Tc, Pm, Hg, Tl, and platinum group metals, were used, along with 17 different supports (X represents the loading amount of PGM and Add elements). Information regarding the purity and sources of the support can be found in **Table 2.1**. CalcT denotes the corresponding calcination temperature in degrees Celsius. In the first step of catalyst preparation, single or multiple additive components (Add) were impregnated onto the support. An appropriate amount of support and the corresponding Add elements were combined in a 500 mL glass vessel with 100 mL of deionized water, stirred for 15 min at room temperature, evaporated to dryness at 50 °C, dried at 110 °C for 12 h, and calcinated in static air for 3 h to yield $Add_1(X_{A1})$–$Add_2(X_{A2})$–$Add_3(X_{A3})$–$Add_4(X_{A4})$/Support_CalcT. Subsequently, the formed $Add_1(X_{A1})$–$Add_2(X_{A2})$–$Add_3(X_{A3})$–$Add_4(X_{A4})$/Support_CalcT was further impregnated with an aqueous solution containing the precursors of the PGM elements (with a maximum loading of 5%). The mixture was evaporated to dryness at 50°C, followed by drying in static air at 110°C for 12 h to obtain the $PGM_1(X_{P1})$–$PGM_2(X_{P2})$–$PGM_3(X_{P3})$/$Add_1(X_{A1})$–$Add_2(X_{A2})$–$Add_3(X_{A3})$–$Add_4(X_{A4})$/Support_CalcT (Unreduced sample). Prior to the hydrogenation reaction, the catalyst was reduced in a quartz tube under a flow of H_2 (20 mL min^{-1}) at 300 °C for 0.5 h.

Table 2.1. Sources and additional information of the supports used.

Support name	Company name	Code name	Comment
γ-Al_2O_3	Sasol	Puralox	Gamma phase
Al_2O_3_AKP-G07	Sumitomo Chemical	AKP-G07	Theta phase
TiO_2_P25	Evonik (formerly Degussa)	P25	Anatase + rutile
SiO_2	Fuji Silysia Chemical	CARiACT Q-10	
ZrO_2_JRC3_RC-100	Daiichi Kigenso Kagaku Kogyo	RC-100 (JRC-ZRO-3)	Tetragonal + monocliric
ZrO_2_JRC4_EP	Daiichi Kigenso Kagaku Kogyo	EP (JRC-ZRO-4)	Tetragonal + monocliric
CeO_2_JRC2	Daiichi Kigenso Kagaku Kogyo	Type A (JRC-CEO-2)	
Nb_2O_5	Companhia Brasileira de Metalurgia e Mineração	HY-340	Prepared by calcining (500 °C for 3 h) niobic acid ($Nb_2O_5 \cdot nH_2O$, HY-340)
Co_3O_4	US Research Nanomaterials		>99.5%, 30–50 nm
MgO	Ube Material Industries	500A (JRC-MGO-4 500A)	
CeO_2(50%)-ZrO_2	Daiichi Kigenso Kagaku Kogyo	Z-1119	CeO_2 = 50 wt.%
SiO_2-Al_2O_3_JRC-SAL-6	Nikki-Shokubai Kasei	JRC-SAL-6	Al_2O_3 = 13 wt.%
SiO_2-Al_2O_3_JRC-SAH-7	Nikki-Shokubai Kasei	JRC-SAH-7	Al_2O_3 = 28 wt.%
H-ZSM-5_11	Tosoh	JRC-Z-HM20	Si/Al ratio = 11
H-ZSM-5_45	Clariant	JRC-Z-HM90	Si/Al ratio = 45
H-Y_15	Tosoh	HSZ-372HUA	Si/Al ratio = 15
H-BEA_20	Tosoh	HSZ-940HOA	Si/Al ratio = 20
H-MOR_10	Tosoh	JRC-Z-HM20	Si/Al ratio = 10
H-CHA_11	Tosoh		Si/Al ratio = 11

2.2.2 Catalytic methanol synthesis reactions

Methanol synthesis reactions for the ML-assisted catalyst exploration were conducted in a batch reactor. Following the reduction of the catalyst with H_2 at 300 °C for 0.5 h, either 100 mg or 150 mg of the catalyst and 1,4-dioxane (1 mL) were loaded into a 10 mL autoclave. The reaction mixture was stirred magnetically at 150 °C under a pressure of 6 MPa. Upon completion of the reaction, the liquid phase was analyzed through GC-FID (Shimadzu GC-2014 equipped with a capillary column PoraBond Q; Agilent Technologies) using 1-propanol as an internal standard. The gas phase was analyzed through GC-FID (Shimadzu GC-2014 having a Porapak Q column) equipped with a Shimadzu MTN^{-1} methanizer. It is noteworthy that the optimization of the catalyst using ML was based solely on experimental reaction data

obtained under identical conditions in a batch reactor (150 °C, 60 bar, H_2 : CO_2 = 5 : 1). While flow reactors are more applicable for industrial purposes, batch reactors were chosen for catalyst optimization with ML due to their higher experimental efficiencies. This strategy is particularly advantageous considering the substantial amount of data necessary for ML-driven catalyst optimization.

The methanol formation rate (mmol g^{-1} h^{-1}) was calculated using Equation (1) as follows.

$$\mathrm{CH_3OH\ formation\ rate} = \frac{\frac{(\mathrm{n_{CH_3OH}})}{(\mathrm{n_{1-propanol}})} \times \mathrm{mmol_{1-propanol}}}{(\mathrm{g_{cat}} \times \mathrm{t})} \qquad \text{Equation (1)}$$

Here, n represents the amount of substance of the respective compounds in GC analysis (1-propanol was added as the internal standard), g_{cat} indicates the mass of the catalyst in g, and t stands for the reaction time (h).

CO_2 hydrogenation reactions were also conducted in a flow reaction system using the ML-identified best catalyst and a commercial Cu/ZnO/Al_2O catalyst (Alfa Aesar; 64.2 wt% CuO) in a fixed-bed continuous-flow reactor operating at a total pressure of 4 MPa. H_2/Ar (H_2 : Ar = 99:1) and CO_2 gas cylinders were utilized to provide the reaction gases, with Ar serving as the internal standard. The catalyst (300 mg) was positioned between quartz wool pieces inside a 1/4-inch fixed-bed reactor (inner diameter: 3.79 mm). Before the catalytic measurements, the catalyst was pretreated at 300 °C for 0.5 h under an H_2/Ar atmosphere (flow rate = 20 mL min^{-1} under ambient pressure). Subsequently, a gas mixture of H_2/CO_2/Ar (74.4/24.8/0.8) at a total flow rate of 40 mL min^{-1} was passed through the catalyst bed at 4 MPa. The weight hourly space velocity was 8000 mL g_{cat}^{-1} h^{-1}. An aging treatment was conducted at 210 °C for 12 h under the reaction gas mixture as an accelerated aging test before recording the catalytic results at 150 °C. The products were analyzed using an online gas chromatograph (Shimadzu GC-2014) equipped with TCD (Shincarbon-ST column) and FID (Porapak Q column) detectors.

The CO_2 conversion (X_{CO_2}) and selectivity (S_i) of individual products in the flow system were calculated using Equation (2) and (3) respectively as shown below.

$$X_{\mathrm{CO_2}} = \frac{\frac{c^{in}_{\mathrm{CO_2}}}{c^{in}_{\mathrm{Ar}}} - \frac{c^{out}_{\mathrm{CO_2}}}{c^{out}_{\mathrm{Ar}}}}{\frac{c^{in}_{\mathrm{CO_2}}}{c^{in}_{Ar}}} \times 100\%$$

Equation (2)

$$S_i = \frac{C_i \times N_i}{\sum(C_i \times n_i)} \times 100\%$$

Equation (3)

Here C_i is the molar fraction of product *i* (CO, hydrocarbons, or oxygenates), and n_i is the carbon number of product *i* in the reaction.

2.2.3 Catalyst representations for ML

As detailed in Section 2.1, each catalyst consisted of three components (PGM, Add, and Support) in addition to CalcT. The initial step in optimizing this data with ML involves developing a suitable input format for the ML model. For PGM, Add, and Support, each containing multiple elements with corresponding composition ratios, two types of representation schemes were used: The first method, which is a conventional method, is similar to one-hot encoding and constructs a feature vector by storing the composition ratios of each element in an n-dimensional vector, with unused elements represented by zeros. The second approach, referred to as "element descriptors" for PGM and Add, and "support descriptors" for Support, simplifies the representation by emphasizing specific chemical properties over individual element types. Assuming a catalyst comprises m elements, $E_1, E_2, \cdots, E_m$, with their respective composition ratios denoted by $X_1, X_2, \cdots, X_m$. Considering n candidate elements under consideration, the first representation becomes an n-dimensional vector. The second representation, which is defined as the weighted sum of elemental descriptors for each E_i scaled by its composition fraction X_i and can be expressed as

$$X_1\, vec(E_1) + X_2 vec(E_2) + \cdots + X_m vec(E_m)$$

where the elemental descriptor vector for element E_i is represented by $vec(E_i)$. Technically, this representation aggregates unordered information using weighted sum pooling, a permutation-invariant operation in which each element's contribution is weighted by its composition fraction. This is also referred to as the composition-based feature vector (CBFV).[47]

Based on these two schemes, three types of input representations were explored for each component of PGM, Add, and Support: (0) a direct representation that uses only elemental compositions or the support type (first scheme only); (1) an exploitative representation that uses both elemental compositions (or support type) and elemental/support properties (first and second schemes); and (2) an explorative representation that uses only elemental or support properties (second scheme only). With these representation options (0), (1), and (2), the input representation for a catalyst is denoted as a code ijk, where $i, j, k \in \{0,1,2\}$ with i, j, and k correspond to the chosen representation type for PGM, Add, and Support, respectively. For example, a catalyst representation coded as 012 indicates that the PGM is represented using (0), Add using (1), and Support using (2). A representative list of element descriptors for PGM, Add, and Support, along with the distribution of descriptor values and correlations between descriptors, is shown in **Table 2.2** and **Figures 2.1-2.3**. The actual input to the ML model is a feature vector formed by appending a single numerical value—the calcination temperature in °C (CalcT), which is explored in 50 °C intervals from 300 °C to 700 °C—to the catalyst representation vector. The choice of catalyst representation can be switched at each iteration. A detailed list of the descriptors used for each iteration is provided in a separate Excel file on the authors' institutional repository (https://aist.repo.nii.ac.jp/records/2003358).

Table 2.2. List of descriptors used in the ML-based catalyst exploration and statistical analysis in the present study[a].

Type	Descriptors
PGM	Electronegativity (EN_Mulliken)
	Group
	Melting point (m. p.)
	Electron affinity
	Adsorption energy of a CO_2 molecule on metallic surfaces (Eads_CO_2)
	Surface energy (E_surf)
	Atomic radius (Atom rad)
Add	Adsorption energy of a CO_2 molecule on metallic surfaces (Eads_CO_2)
	Thermal expansion
	E_form_Metal
	Solubility
	Surface energy (E_surf)
Support	BG_PBEsol
	Ionization potential
	Density
	Electronegativity (EN_bulk)

[a] Descriptors for PGM shown in this table were used for the initial exploration of the catalysts (prediction of catalysts tested at the iteration = 1), whereas those for Add and Support were used in the post-analysis of the final dataset consisting of 580 points.

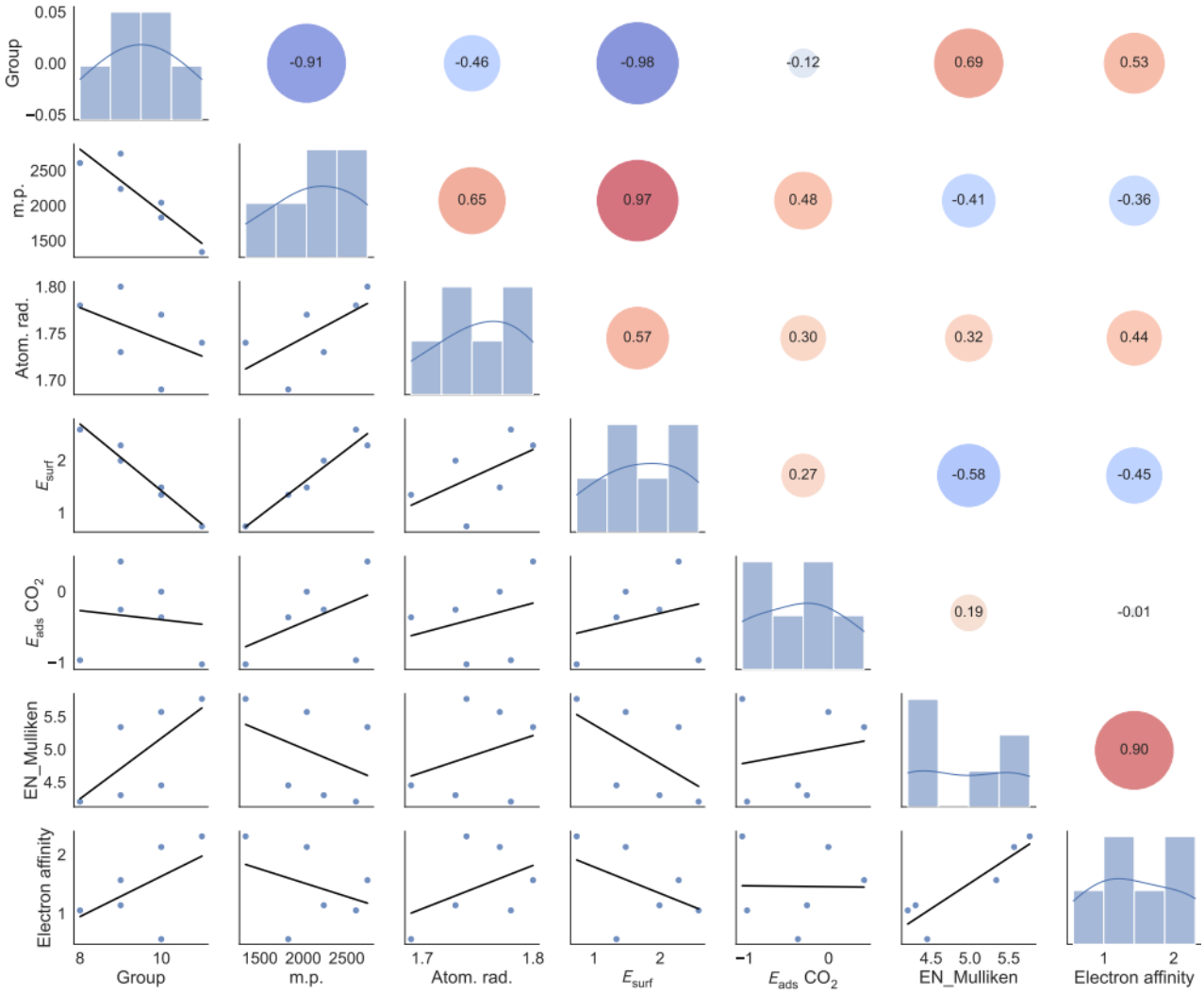

Figure 2.1. Correlation map for the seven selected descriptors for the PGM elements.

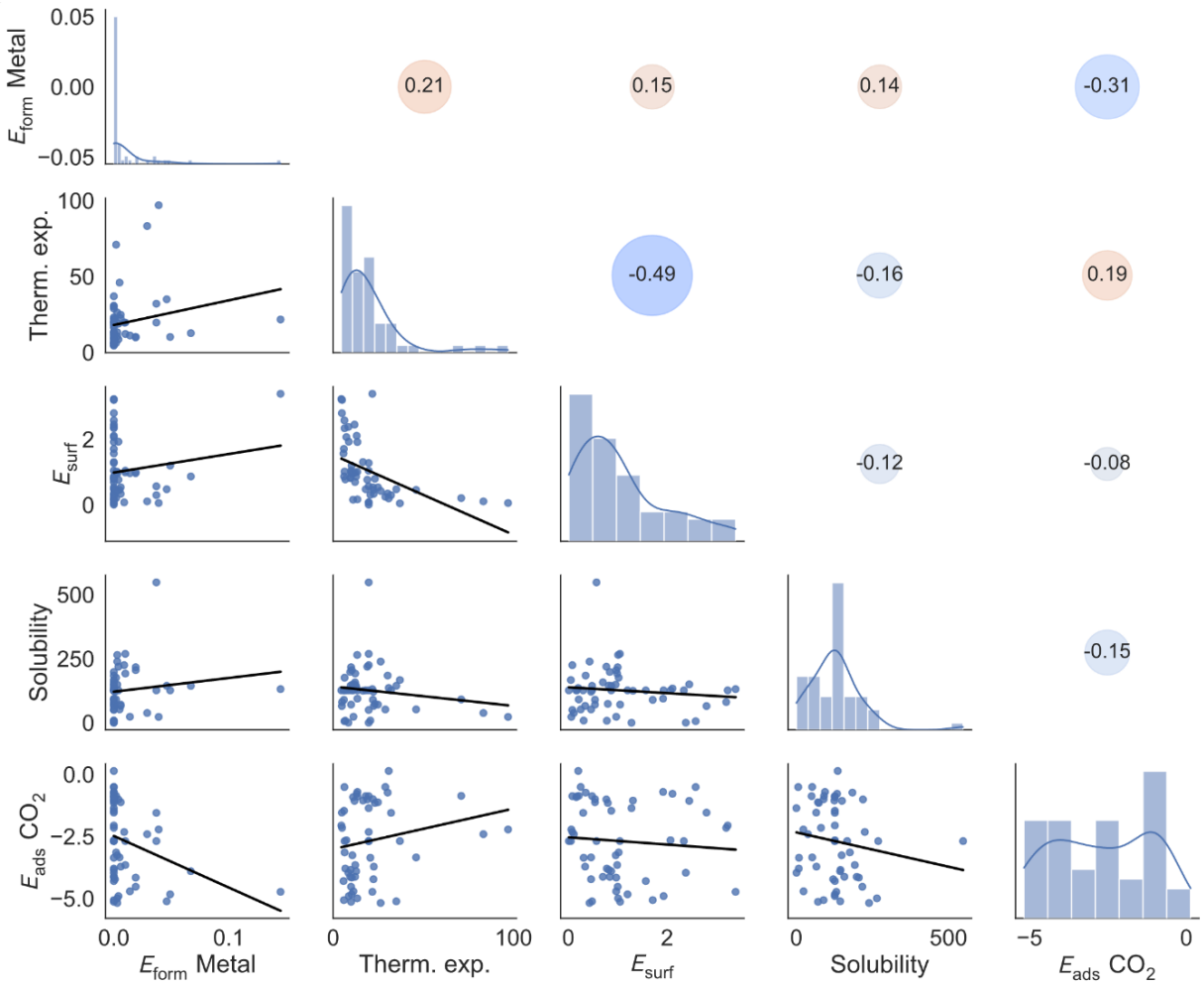

Figure 2.2. Correlation map for the five selected descriptors for the Additive elements.

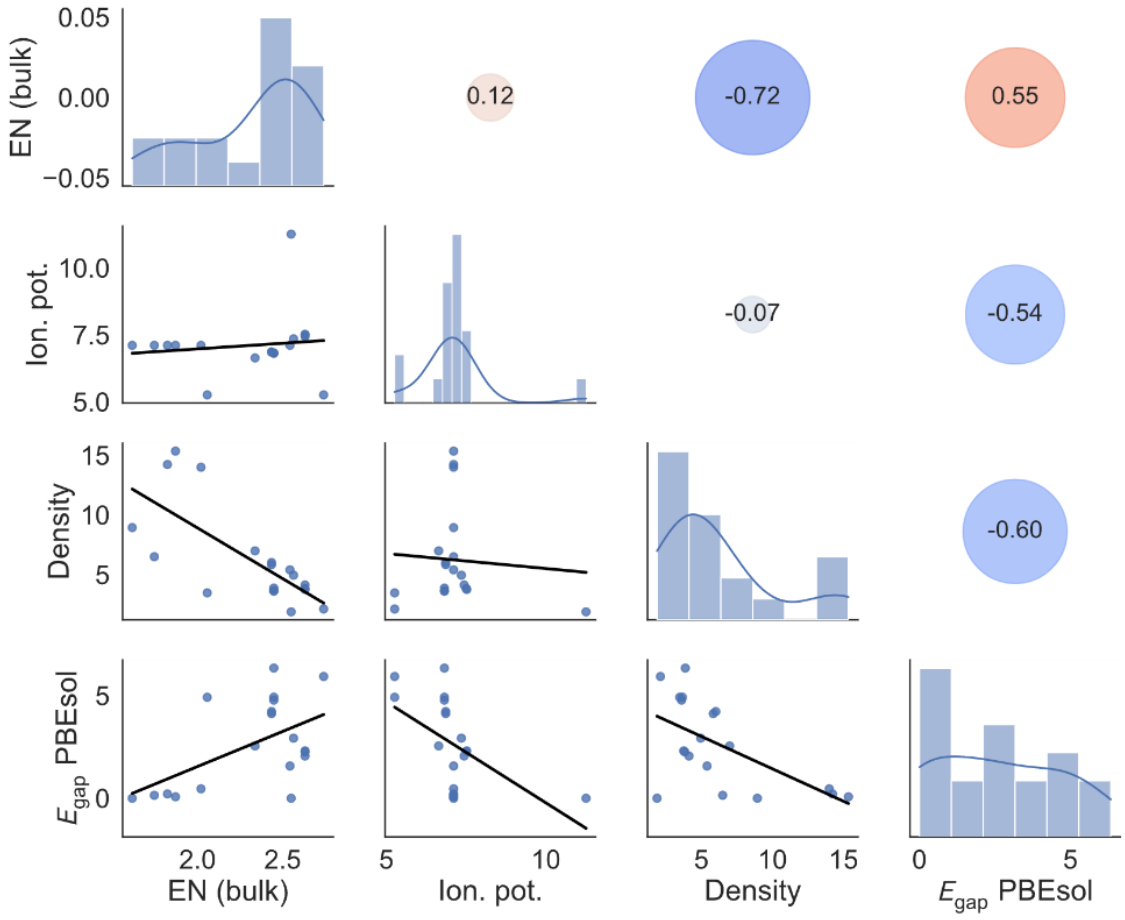

Figure 2.3. Correlation map for the four selected descriptors for the Supports.

As PGM elemental descriptors, we selected the following parameters for the initial exploration of catalysts (catalyst prediction at iteration = 1): electronegativity (EN_Mulliken), group, melting point (m.p.), electron affinity, surface energy (E_surf), atomic radius (Atom rad), and adsorption energy of a CO_2 molecule on metallic surfaces (Eads_CO_2) calculated using the Vienna ab initio simulation package (VASP, version 5.4.4).[59,60] The Perdew-Burke-Ernzerhof functional revised for solids (PBEsol)[61] was employed in combination with the projector augmented wave (PAW)[62] method for calculations using VASP. An energy cut-off of 400 eV was used for the plane-wave basis set. Gaussian smearing with a width of 0.2 eV was applied for the occupation of electronic levels. The Brillouin zone was sampled using 2×2×1 Monkhorst-Pack grids. Van der Waals interactions were described using the dispersion-corrected DFT-D3 (BJ) function.[63] The convergence of the force on each atom was set to 0.03 eV $Å^{-1}$. The most stable and common metallic bulk structures and facets for each element were used.[64] Note that these descriptors were presented as representatives and were not used in the post-analysis of the final dataset comprising 580 points. This is

because the elemental descriptors were unnecessary for describing the PGM in the final dataset, as the 011 descriptor representation was applied in the post-analysis.

For Add elemental descriptors, we used the following five parameters for post-analysis of the final dataset: thermal expansion, adsorption energy of a CO_2 molecule on metallic surfaces (Eads_CO_2), solubility, formation energy of the metal (E_form_M), and surface energy (E_surf).[65]

As support descriptors for the support materials, we used the following four parameters for the post-analysis of the final dataset: band gap energy calculated using VASP with the GGA/PBEsol functional (BG_PBEsol), ionization potential, density, and electronegativity of compounds according to Sanderson's definition (EN_bulk).[66,67]

Although other chemical properties were also used as descriptors for elements and supports during the catalyst exploration process, only a representative list of descriptors for each catalyst component is provided in the main text due to space constraints. However, a comprehensive list of descriptors can be accessed on the authors' institutional repository (https://aist.repo.nii.ac.jp/records/2003358).

The direct input representation (Code number = 0) generated feature vectors with dimensions of 6, 57, and 17 for PGM, Add, and Support, respectively, corresponding to the elements considered in this study (6 for PGM, 57 for Add, and 17 for Support). Specifically, the representation for Add frequently exhibits high sparsity and lacks statistical significance when the training dataset is small but encompasses a large variety of elements and supports. Moreover, it struggles to adequately address elements that are missing or statistically underrepresented in the training data.

In contrast, the explorative representation (Code number = 2) maintains a dimensionality equivalent to that of the user-specified elemental descriptor, typically resulting in more statistically stable outcomes for small-data problems. The feature vector dimensions for this representation were seven, five, and four for PGM, Add, and Support, respectively, when the element descriptors listed in **Table 3** were used. Unlike a direct representation, it is not explicitly restricted to the elements present in the training dataset.

Notably, the explorative representation (Code number = 2) characterizes catalysts based solely on their physicochemical properties using specific descriptors without directly attributing contributions to individual elements. This abstraction enables broader and more

exploratory analyses, allowing extrapolations beyond the elements in the training data while focusing solely on the defined physicochemical property space.[56] However, due to its irreversible nature, even if an optimal value is identified within this physicochemical property space, the exact catalyst composition cannot be directly inferred. In a previous study,[50] a method was developed to estimate the potential catalyst composition from elemental property representations. In the current study, we employed a more direct "grid search" approach, systematically testing all possible combinations of elemental loading values and calcination temperature values within a predefined discrete grid, ensuring explicit determination of the original catalyst composition and the calcination temperature.

2.2.4 ML-assisted CO_2 hydrogenation to methanol catalysts discovery

The overall pipeline of our ML-based catalyst exploration is dependent on the sequential model-based optimization we developed.[56,68,69] In this study, we used Extra-Trees regression (ETR)[50] in scikit-learn (version = 1.0.2)[70] as a base ML model and used the expected improvement (EI)[70] score as the guiding acquisition function.

We prepared and tested 90 different catalysts manually, without the assistance of ML, and constructed an initial dataset of 90 points, which was set as "Iteration" = 0. The ML method was trained using the ETR model with the initial dataset (90 points). The EI was calculated for all test points in the catalyst composition grid. Several notable catalyst candidates were chosen based on EI values and catalyst variety. The catalysts were synthesized using the sequential impregnation method. The CO_2 hydrogenation reaction was conducted to determine the "CH_3OH formation rate," which served as the ML prediction target. The dataset was updated by incorporating the obtained data to close the loop. Subsequently, the ML model was retrained with the updated dataset, and a new set of catalyst candidates was selected for the next experiment. This iterative cycle was repeated 43 times, testing a total of 580 catalysts. During the initial 20 iterations, we used ETR model (with n_estimators=100, keeping the other hyperparameters at scikit-learn's default values) using only the explorative representation (Code number = 2) for PGM, Add, and Support to allocate resources for exploring new candidates (222 representation). Starting from the 21st iteration, the results up to the tth iteration ($t \geq 21$) were considered for representation selection. The best representation up to that point was chosen from all 27 combinations of ijk, ranging from 000 to 222, based on prediction performance evaluated through 10-fold cross-validation. The optimal combination was then used to tune the ETR hyperparameter settings (n_estimators

[100, 500, 1000, 1500] and [True, False]) through grid-search cross-validation in scikit-learn, employing 10-fold cross-validation. The ETR model with the highest accuracy was utilized for the (t+1)-th exploration, along with 222 and 111 representations, and this cycle was repeated. It is important to note that the 222 representation was consistently used throughout the study, while the 111 representation was introduced from the 21st iteration onwards as an additional base model for actual catalyst exploration.

In our ML approach, we incorporated human-in-the-loop exploration by utilizing expert judgment to select multiple catalyst candidates (the batch) in each iteration.[71] It is generally important to consider various objectives and ambiguous criteria, such as novelty, cost, diversity, and the availability of catalyst compositions, when choosing catalysts for experiments. Hence, reducing these considerations to a single formulaic statistic is challenging. To address this issue, our ML system generates a list of the top 100 promising catalyst candidates for each representation, from which the experts select those to advance for catalytic experiments, primarily considering the diversity of constituent elements. Given that it is nearly impossible to test every suggested candidate in real tests, reducing the number of alternatives to this degree makes human selection feasible, because no candidates outside the ML-provided catalysts are considered. Therefore, even if some degree of bias is introduced during the selection process, the method would remain robust because candidates are primarily chosen based on high EI scores, each selected catalyst is still among the top recommendations from the ML model (catalyst candidates with high EI scores are essentially given preference). Following clustering with K = 100 for candidates with the highest EI values, a list of the top 100 candidates for each representation examined at each iteration was produced.

2.1 Results and Discussion

2.3.1 ML-based discovery of catalysts for methanol synthesis

To develop catalysts for low-temperature CO_2 hydrogenation to methanol, we explored PGM elements up to three types additive elements (Add) up to four types and one type of support for the $PGM_1(X_{P1})$–$PGM_2(X_{P2})$–$PGM_3(X_{P3})$/$Add_1(X_{A1})$–$Add_2(X_{A2})$–$Add_3(X_{A3})$–$Add_4(X_{A4})$/Support_CalcT catalysts (X represents the unique loading amount of PGM and Add elements). We used six PGM elements, 57 Add elements, and 17 different supports for this study. Therefore, the total number of catalyst candidates easily exceeded 10^{13} even if only three and four distinct values were considered as the loading amount of PGM and Add elements, respectively, along with nine distinct values for CalcT. An ML model trained on all collected data up to the previous iteration calculated EI values at each grid point in every iteration. The most promising points were recommended to experts for selecting candidates for actual tests in the subsequent iteration.

After experimentally testing 580 predicted new catalysts in total across 43 cycles of a closed-loop discovery system (ML prediction + experiment), we identified 33 catalysts that exhibited superior performance compared to the previously reported high-performance catalyst Pt(3)/Mo(20)/TiO_2 (P25)_600.[58] The composition of the best catalyst discovered through this approach was Pt(5)/Mo(8)–Re(1)–W(0.7)/TiO_2 (P25)_550, demonstrating the highest methanol production rate of 1.42 mmol g_{cat}^{-1} h^{-1} in a batch reactor system (**Figure 2.4** Compared to the previous best catalyst,[58] the performance of the best catalyst improved about 70% under the same reaction conditions using a batch reactor (150 °C, 60 bar, H_2 : CO_2 = 5 : 1). The industrial Cu/ZnO/Al_2O_3 catalyst also exhibited lower activity under the same conditions. The best catalyst showed a higher methanol formation rate than most of the reported catalysts at low temperatures (**Table 2.3**). We also investigated the effect of each additive element and confirmed that the best activity was achieved when all additive elements (Mo, Re, and W) coexisted (**Figure 2.5**). It is also worth noting that in the original dataset ("Iteration" = 0), we did not test the Re element (**Figure 2.6**). In other words, our ML model can not only develop catalysts using known high-performance components but also discover new elements that have not been used before. Our extrapolative ML predictions using explorative representations led to this discovery. The emergence of new elements and supports predominantly occurred during the initial iterations, particularly within the first 20 iterations utilizing only 222 representations. The appearance of new elements and supports

throughout the iterations was displayed in **Figure 2.7**. To facilitate interpolation across this abstracted representation, our approach incorporates continuous quantities for elemental descriptors defined by user-selected properties (e.g., density and electronegativity). Each element is represented as a distributed representation by several continuous elemental feature values, rather than as discrete, separate symbols.[50,52,72] This makes it possible to take into account similarities between elements based on chemical features, enabling the inclusion of components not present in the training data during the exploration process.

Table 2.3. Reports on low temperature (T ≤ 180 °C) CO_2 hydrogenation to methanol.

Catalyst	Additive	T (°C)	P (MPa)	H_2:CO_2	Space velocity (mL h^{-1} g_{cat}^{-1})	MeOH formation rate (mmol h^{-1} g_{cat}^{-1})	Reaction System	Selectivity (%)			Reference
								MeOH	CO	CH_4	
Homogeneous catalytic system:											
Ru complex & $Sc(OTf_3)$	MeOH	135	4.0	3:1	-	2.5[a]	Batch	Not shown			73
Ru/Triphos	$HNTf_2$	140	8.0	3:1	-	9.2[a]	Batch	Not shown			74
Ru/Triphos	$HNTf_2$	140	8.0	3:1	-	18.4[a]	Batch	Not shown			75
Ru-Macho-BH	PEHA	145	7.5	9:1	-	6.0[a]	Batch	Not shown			76
Co/Triphos	$HNTf_2$	100	9.0	4.5:1	-	2.1[a]	Batch	Not shown			77
Fe(II)/C-scorpionate	PEHA	80	7.5	3:1	-	95[a]	Batch	Not shown			78
Mn(I)-PNP pincer	K_3PO_4	150	8.0	1:1	-	1.0[a]	Batch	Not shown			79
Ru complex	$^{i}Pr_2NH$, NaOEt	100	4.0	3:1	-	4.5[b]	Batch	Not shown			80
Ru-MACHO-BH	PEHA	145	7.0[c]	-	-	2.9[a]	Batch	Not shown			81
Co/modified triphos	$HNTf_2$	100	9.0	3.5:1	-	5.2[a]	Batch	Not shown			82
Heterogeneous catalytic system:											
Cu/ZnO-Al_2O_3	DEEA	100	7.0	6:1	–	0.54	Batch	Not shown			83
Cu-Cr_2CuO_4 & Cu/Mo_2C	EtOH	135	4.0	3:1	–	0.023	Batch	77	Not shown		84
Cu/Mo_2C	–	135	4.0	3:1	–	0.0034	Batch	93	4.1	2.6	16
Pd/Mo_2C	–	135	4.0	3:1	–	0.0046	Batch	95	3.6	1.6	16
Co/Mo_2C	–	135	4.0	3:1	–	0.003	Batch	84	5.7	9.4	16
Pt/Co_3O_4	–	140	8.0	3:1	–	0.05	Batch	Not shown			18
Pt_3Co octapods	–	150	3.2	3:1	–	0.18	Batch	Not shown			17
$Rh_{75}W_{25}$ nanosheets	–	150	3.2	3:1	–	0.004	Batch	Not shown			85
Pt_4Co nanowires/Carbon	–	150	3.2	3:1	–	0.19	Batch	Not shown			86
Pt/MoS_2	–	150	3.2	3:1	–	0.05	Batch	81	Not shown		87
RhCo porous nanosphere	–	150	3.2	3:1	–	0.1	Batch	Not shown			88
Cu/ZnO/Al_2O_3	NEt_3, EtOH	120	6.0	2:1	–	0.874	Batch	Not shown			89
MoS_2 nanosheets	–	120	5.0	3:1	1500	0.28	Flow	>96	-	-	8
MoS_2 nanosheets	–	180	5.0	3:1	15000	4.06	Flow	96	-	-	8
PdCuZnZrBa/Al_2O_3	–	150	3.0	4:1	12000	1.17	Flow	100	0	0	9
B/Cu/ZnO	–	170	7.0	-	1800	1.56	Flow	100	0	0	90
h-PdMo/Mo_2N	–	160	0.1	3:1	30000	0.05	Flow	5.16	93.9	0.94	20
$Cu_{10}Ga_{10}$/SBA-15	–	180	0.5	3:1	15000	0.07	Flow	100	0	0	19
MoS_2-NS	–	140	5.0	3:1	36000	7.81	Flow	＞98	＜1	＜1	3
Cu/MoS_2@SiO_2	–	180	5.0	4:1	8000	2.0	Flow	95	-	5	91
5% Cu-MoS_2	–	180	5.0	4:1	12000	1.82	Flow	87	5	8	92
Mo_3S_4@NaZSM-5	–	150	4.0	3:1	1200	0.26	Flow	>99	-	-	15
h-MoS_2/ZnS	–	160	5.0	4:1	6000	0.53	Flow	>99	-	-	93
$Er_{0.2}$CuZnO	–	170	5.0	3:1	1800	1.53	Flow	90	10	-	94
Pt(5)/Mo(8)-Re(1)-W(0.7)/ TiO_2 (P25)_550	–	150	6.0	5:1	-	1.46	Batch	71	18	11	This study
Pt(5)/Mo(8)-Re(1)-W(0.7)/ TiO_2 (P25)_550 [c]	–	150	4.0	3:1	8000	1.8	Flow	44	56	<1	This study
Pt(5)/Mo(8)-Re(1)-W(0.7)/ TiO_2 (P25)_550 [c]	–	150	4.0	3:1	20000	2.8	Flow	32	67	1	This study

[a] Calculated based on amount of MeOH/total amount of active metal. [b] Calculated based on MeOH production rate/number of active sites per unit square area at t = 2 h. [c] Calculated based on CO_2 conversion rate/number of active sites per unit square area at t = 2 h.

Triphos = 1,1,1-tris(diphenylphosphinomethyl)ethane; HNTf2 = Triflimide; PEHA = pentaethylenehexamine; $^{i}Pr_2NH$ = di-iso-propylamine; DEEA = *N,N*-diethylethanolamine. [c] Catalytic results were obtained after accelerated aging at 210 °C for 12 h.

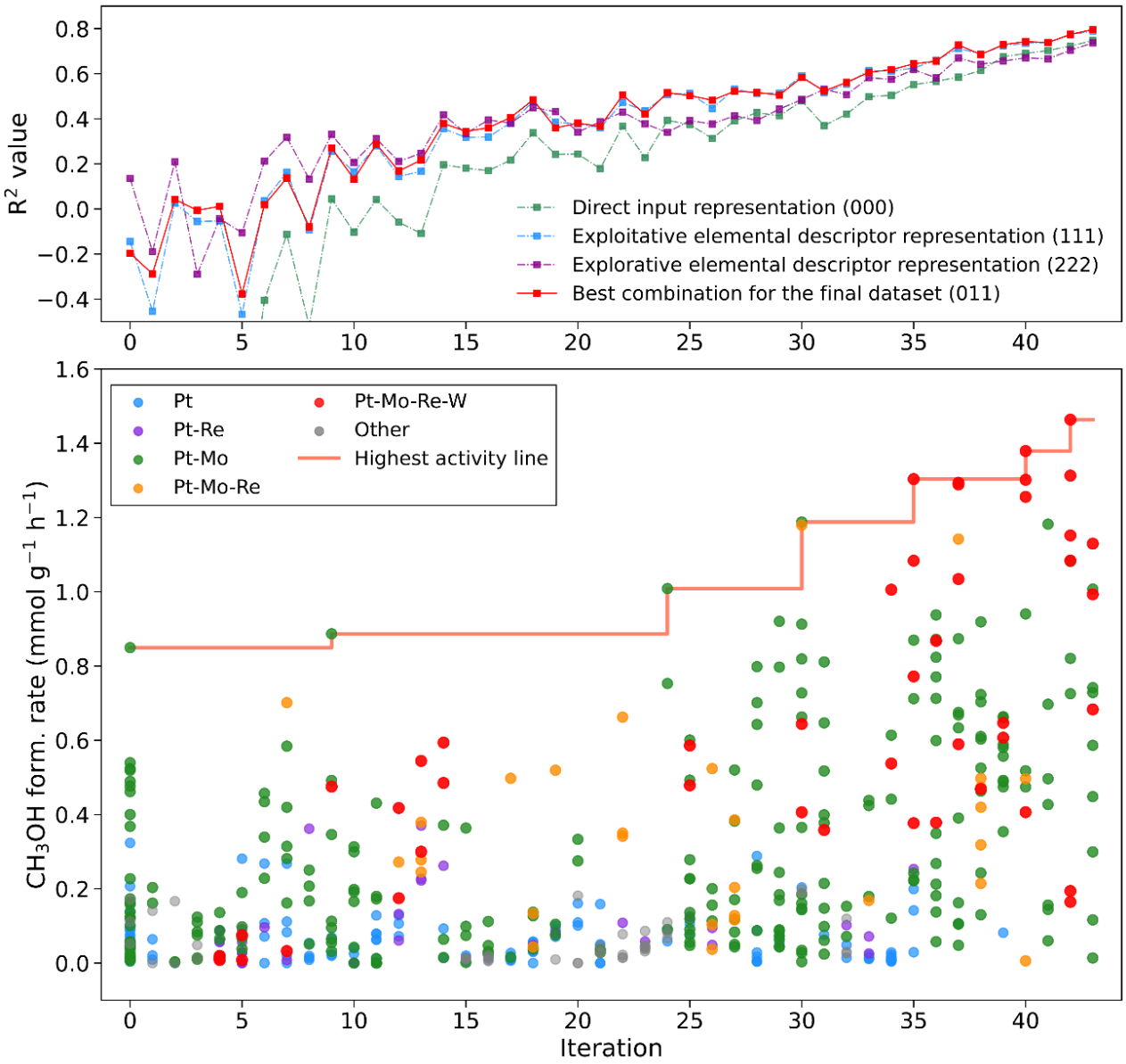

Figure 2.4. ML-assisted catalyst exploration for low-temperature CO_2 hydrogenation to methanol. Catalysts containing elements not included in the original dataset are indicated by diamond-shaped symbols, while those with elements from the original dataset are shown as circle-shaped symbols. The solid orange line represents the highest methanol synthesis activity (methanol formation rate at 150 °C) observed in each iteration. R^2 values were calculated using the 10-fold cross-validation as described in the ML methods section, based on the dataset at each iteration before experimental validation. From left to right, each representation name includes three numbers corresponding to descriptor types for the PGM, Additive, and Support, respectively. A value of 0 represents a direct input representation, which uses only elemental compositions or support name; 1 represents an exploitative representation, which uses both elemental compositions/support name and elemental/support properties; and 2 represents an explorative representation, which uses only elemental/support properties.

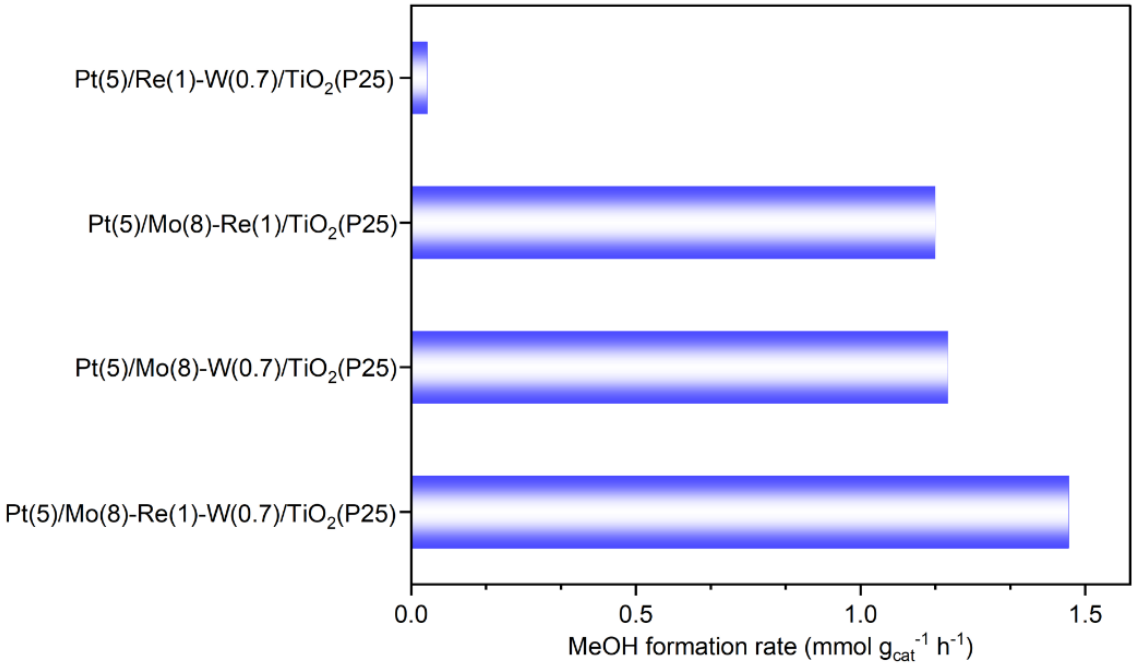

Figure 2.5. Effect of additive elements on the MeOH formation rate. Reaction conditions: 1, 4-Dioxane (1 mL), 150 °C, H_2 (5 MPa), CO_2 (1 MPa), 6 h.

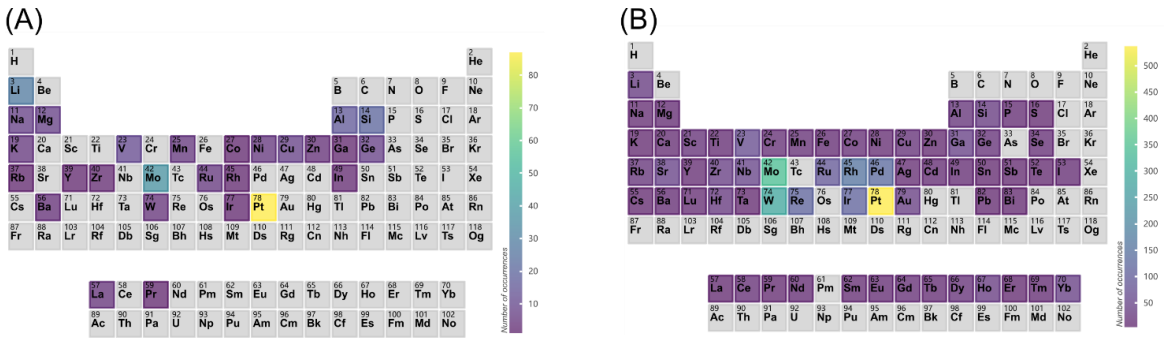

Figure 2.6. The elements in the (A) original and (B) final datasets are shown in the periodic tables.

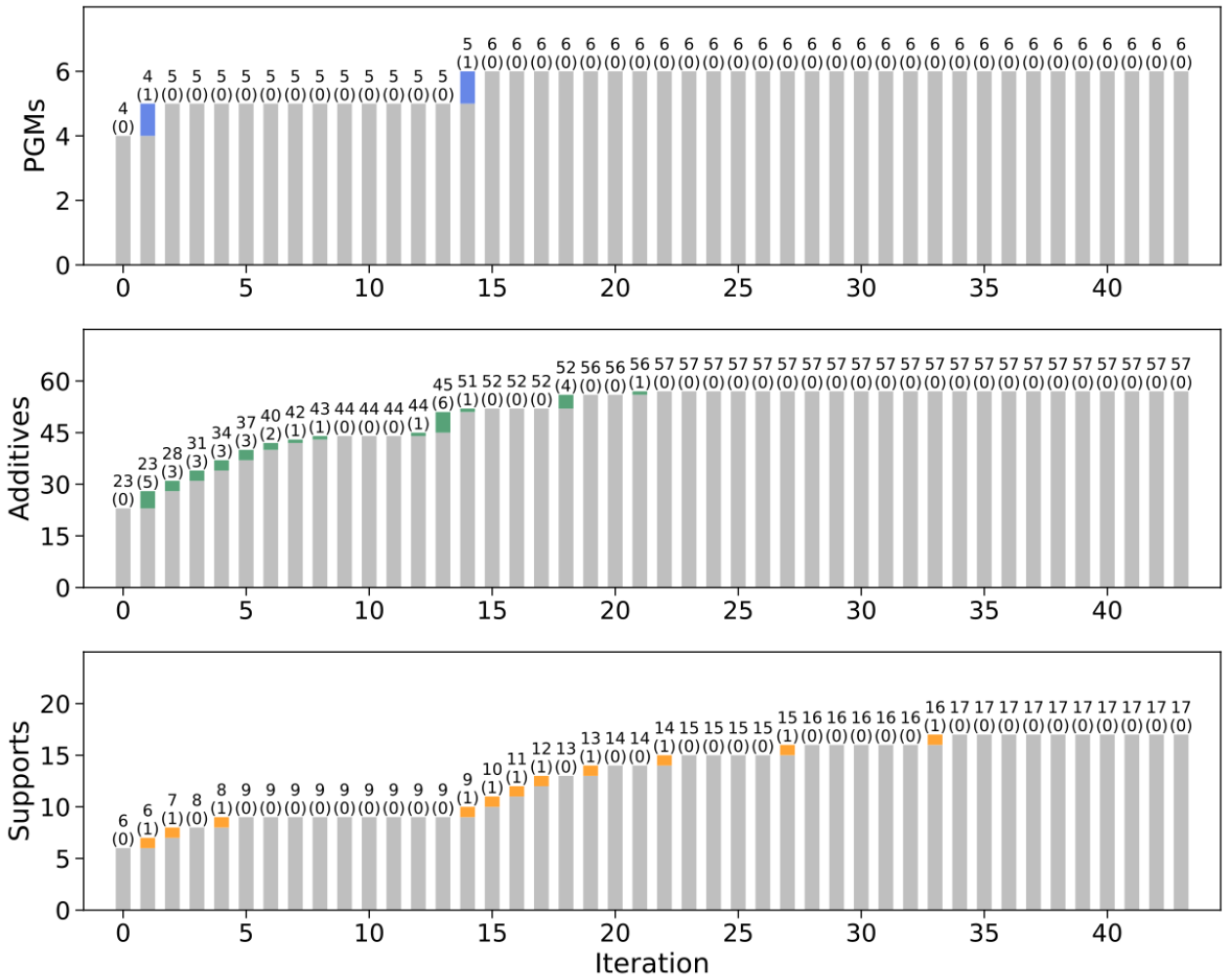

Figure 2.7. Visualization of the number PGMs, additives, and supports appeared for the first time in each iteration. Elements/supports appearing for the first time are shown in color, while those already present are shown in gray. The numbers above indicate the total count of elements/supports present at each iteration, while the numbers in parentheses below represent the count of elements/supports appeared for the first time in that iteration.

Figure 2.1 and **2.8** display the variations in prediction accuracies of the ML models with different choices of representation (000, 111, 222, and 011) for each iteration. A 10-fold cross-validation, based on the data collected up to that iteration, was used to calculate the prediction accuracy (R^2, MAE, RMSE, and MSE) of each iteration. We used only the 222 representation method for the first 20 iterations of the exploration process. Subsequently, we incorporated 111, 222, and the best model at each iteration according to the evaluated prediction accuracy. Identifying effective catalysts posed an initial challenge due to the low prediction accuracy of the ML model in the early stages, stemming from the difficulty in predicting catalytic results from a small and diverse set of examples. However, we were able to identify good catalysts as the volume of data grew and the prediction accuracy increased.

In the realm of ML, this phenomenon is commonly referred to as the exploration-exploitation trade-off, emphasizing the requirement of balance between "exploration" to gather additional data on unknown parts and "exploitation" to utilize the existing data. Our strategy of using 222 during the initial phase and subsequently transitioning to the best model based on prediction accuracy after the initial 20 iterations exemplified this trade-off.

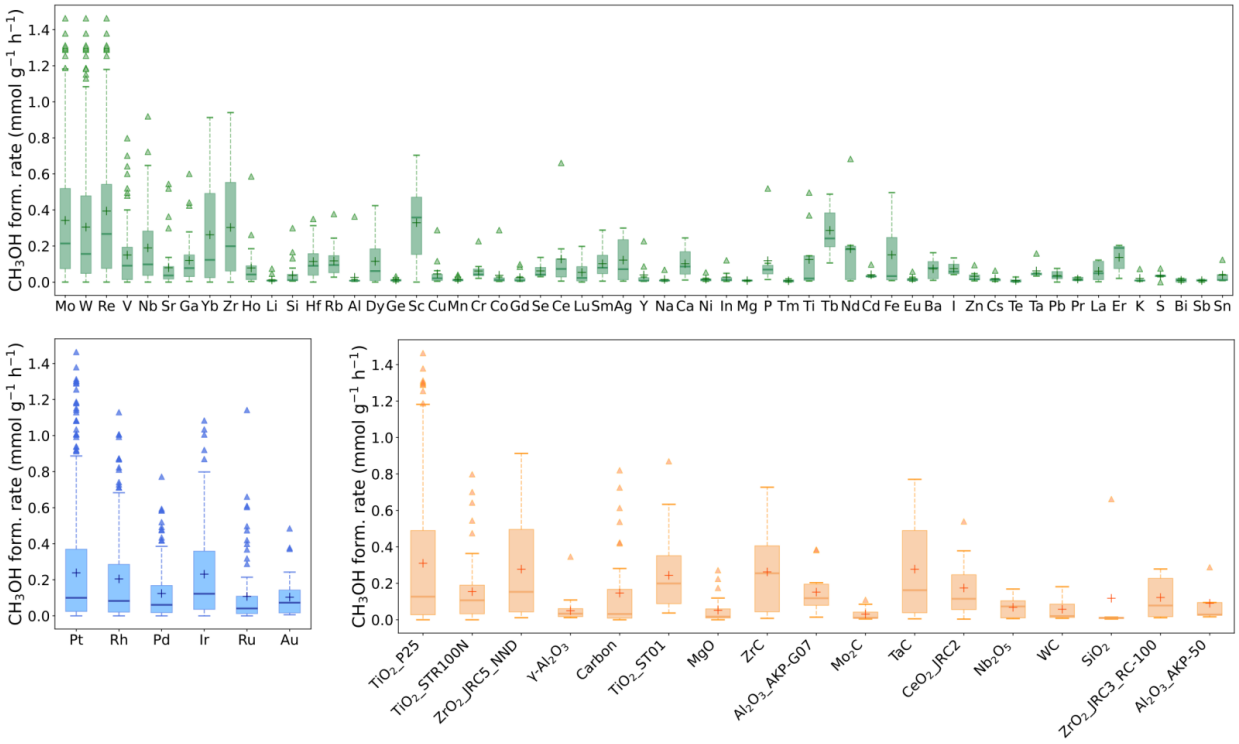

Figure 2.8. Visualization of methanol formation catalyst datasets. Boxplot for each additive oxide component. The boxes represent the interquartile range, spanning from the first quartile to the third quartile, with a horizontal line indicating the median. Whiskers extend up to 1.5 times the interquartile range, encompassing the largest and smallest observed data points falling within this range. Individual data points are displayed as dots.

The goal of this study was to employ an iterative and sequential experimental design, even if our dataset is small (580 data points) and the best prediction accuracy achieved after 43 cycles (R^2 = 0.79) is not significantly high. As a result, more attention is paid to optimizing the utilization of the available data (even though they are relatively small in size from a statistical perspective) to plan future experiments for identifying superior catalysts.[95] Thus, we believe that the prediction accuracy achieved through a standard approach (up to R^2 = 0.79) would suffice for statistically guiding the direction of forthcoming research.

Figure 2.9 displays histograms for each (A) Additive, (B) PGM, and (C) Support component, along with (D) the catalyst calcination temperature, categorized by their methanol

synthesis activity (CH_3OH formation rate (mmol g^{-1} h^{-1}) at 150 °C). Pt appeared most frequently among the PGM, while Mo, W, and Re appeared frequently among the additive elements. For support, TiO_2 (P25) (a mixture of anatase and rutile)[96] was the most frequent. These elements and supports are frequently associated with a higher proportion of highly active catalysts. These trends are also depicted in the boxplots for visualization of CO_2 hydrogenation to methanol catalyst (**Figure 2.8**). To gain further insights into the catalytic system, the impacts of the loading amounts of PGM and Add elements, as well as the descriptor values of the Add elements, on the CH_3OH formation rate are summarized in **Figure 2.10** and **2.11**. Catalysts with relatively low loading of additive oxides (below 2%, except for Mo; optimal loading of Mo is over 5 wt%) tend to exhibit a high CH_3OH formation rate. **Figure 2.9D** indicates that catalysts calcined at 500–600 °C constituted a significant portion of highly active catalysts. It should be noted that by incorporating CalcT as an input variable in our ML model, a broader design space of both catalyst composition and preparation parameters was taken into account as compared to the design space when only catalyst composition was considered.

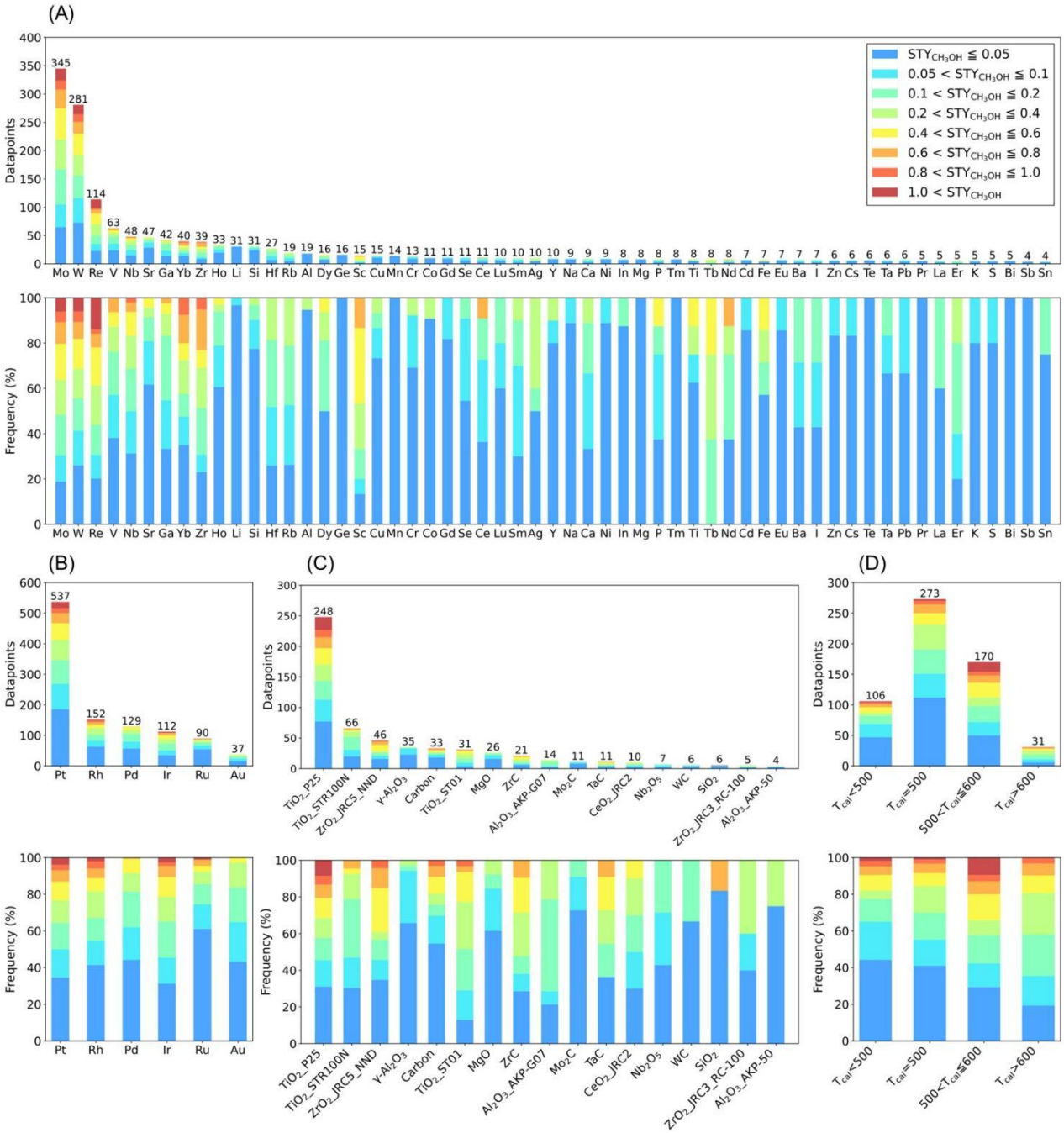

Figure 2.9. Histograms for each (A) Add, (B) PGM, and (C) Support components, along with (D) calcination temperature, categorized by methanol synthesis activity (methanol formation rate at 150 °C). The upper panels show the absolute number of data points for each category, while the lower panels indicate the percentage distribution across methanol synthesis activity levels. The maximum Y-axis values in the top figures reflect the sum of the number of data points, while those in the bottom figures represent percentage of catalysts within each methanol formation rate category.

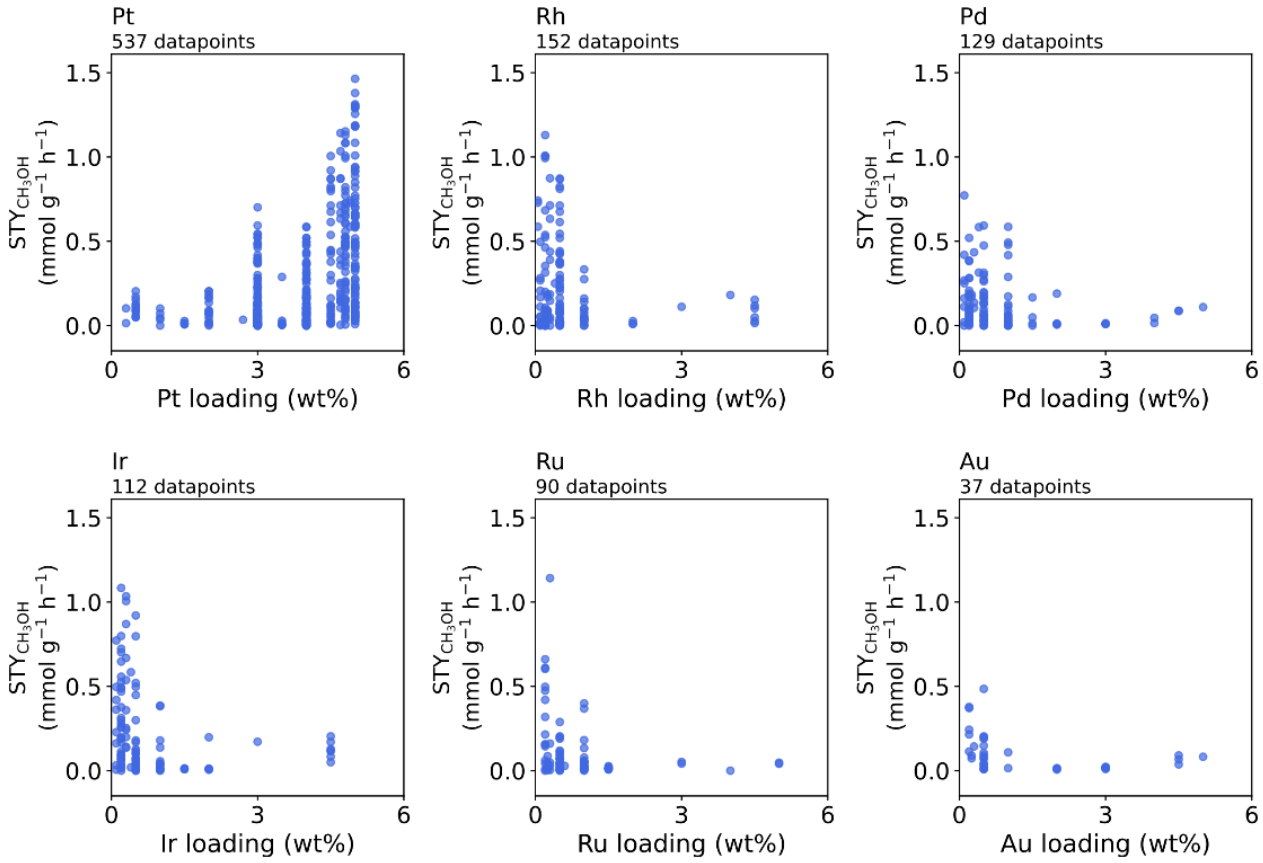

Figure 2.10. Effects of the loading amount of PGM elements on the CH_3OH formation rate.

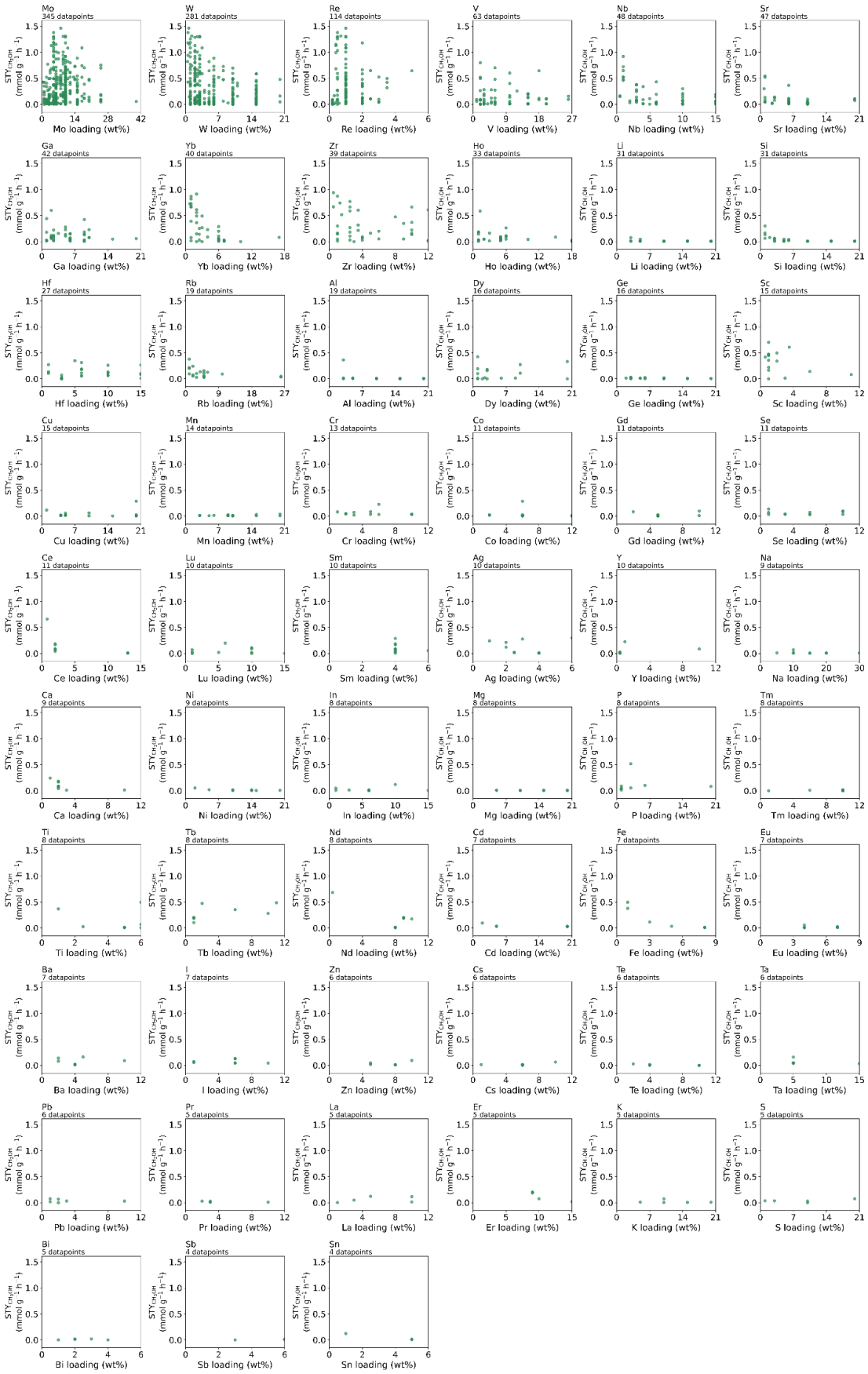

Figure 2.11. Effects of the loading amount of Additive elements on the CH_3OH formation rate.

After determining the best catalyst composition (Pt(5)/Mo–(8)–Re(1)–W(0.7)/TiO_2 (P25)_550), we compared the catalytic activity of the best catalyst with that of a conventional Cu-based industrial catalyst (Cu/ZnO/Al_2O_3) in a flow reactor system, which is more appropriate for industrial applications than liquid-phase batch reactions. An accelerated aging test was conducted by subjecting both catalysts to an aging treatment at 210 °C for 12 h under a reaction gas mixture. The results are presented in **Figure 2.12**, where Pt(5)/Mo–(8)–Re(1)–W(0.7)/TiO_2 (P25)_550 demonstrated higher performance compared to the industrial Cu/ZnO/Al_2O_3 catalyst exhibiting methanol yield almost twice as compared to that over the industrial catalyst.

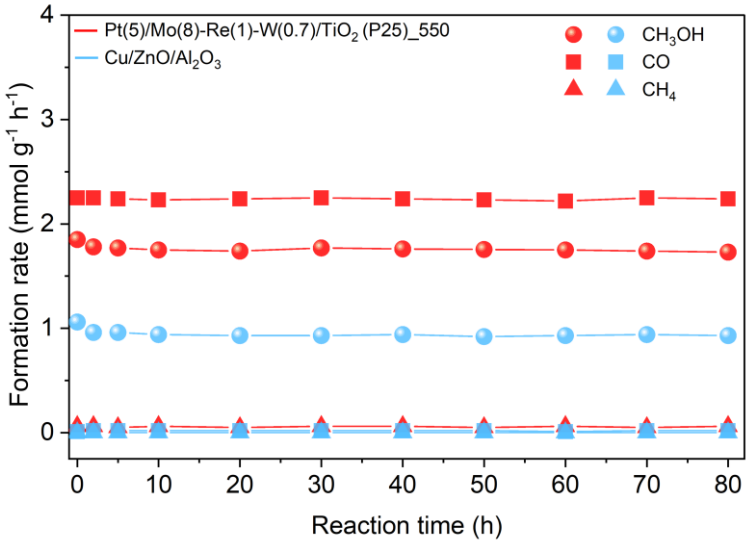

Figure 2.12. Comparison of catalytic activity between Pt(5)/Mo(8)–Re(1)–W(0.7)/TiO_2 (P25)_550 and Cu/ZnO/Al_2O_3 for CO_2 hydrogenation in a flow reactor for 80 h onstream. Pretreatment: H_2 (20 mL min^{-1}), 300 °C, 0.5 h. Catalytic reaction conditions: catalyst (300 mg), 150 °C, 40 bar, 8000 mL h^{-1} g_{cat}^{-1}, H_2 : CO_2 = 3 : 1.

2.3.2 ML-based statistical analysis (post hoc analysis)

Although ML is often utilized as a black box, supervised ML models can reveal significant chemical insights that impact predictions, even without detailed knowledge of the underlying mechanisms.[97–99] Besides identifying effective catalyst compositions, our extrapolative ML approach can offer essential elemental features and electronic properties crucial for designing optimal catalysts accurately. To assess the importance of each descriptor in ML predictions, we conducted a post hoc analysis using SHapley Additive exPlanations (SHAP)

on all 580 data points, as shown in **Figure 2.13**.[100–103] Elements such Pt, Mo and Re and TiO_2 support (P25) emerged as the most important descriptors of catalyst composition. The thermal expansion of additive elements (thermal expansion [Additives]) and the atomic radii of PGM elements (Atom rad [PGMs]) were identified as important features for predicting the CH_3OH formation rate (**Figure 2.13A**). SHAP analysis was used to understand the dependence of model output (e.g., CH_3OH formation rate) on the value of each descriptor.[50] For example, relatively high feature values (highlighted in red in **Figure 2.13A**) for "Pt" and "Mo" correlated with a high methanol formation rate (SHAP value), indicating a positive impact of these elements on achieving high activity.

Figure 2.13B illustrates the SHAP values analyzed using waterfall plots for two representative catalysts: the previous best catalyst composition - Pt(3)/Mo(20)/TiO_2 (P25)_600 and the current best catalyst - Pt(5)/Mo(8)-Re(1)-W(0.7)/TiO_2 (P25)_550. This analysis reveals the descriptors responsible for deviations from the average dataset value (0.25) relative to the predicted value for each catalyst. For the best catalyst, the presence of Pt, Re, and TiO_2 (P25), along with the thermal expansion of additives, strongly contributes to the high CH_3OH formation rate. In contrast, the low Pt loading and absence of Re and W have a negative impact on the CH_3OH formation rate over Pt(3)/Mo(20)/TiO_2 (P25)_600. Furthermore, the lower Pt loading compared to the best catalyst also has a negative effect. Therefore, the results of this ML-driven statistical analysis show that valuable insights into methanol synthesis catalysts can be obtained from our dataset developed in this study, even without prior domain knowledge.

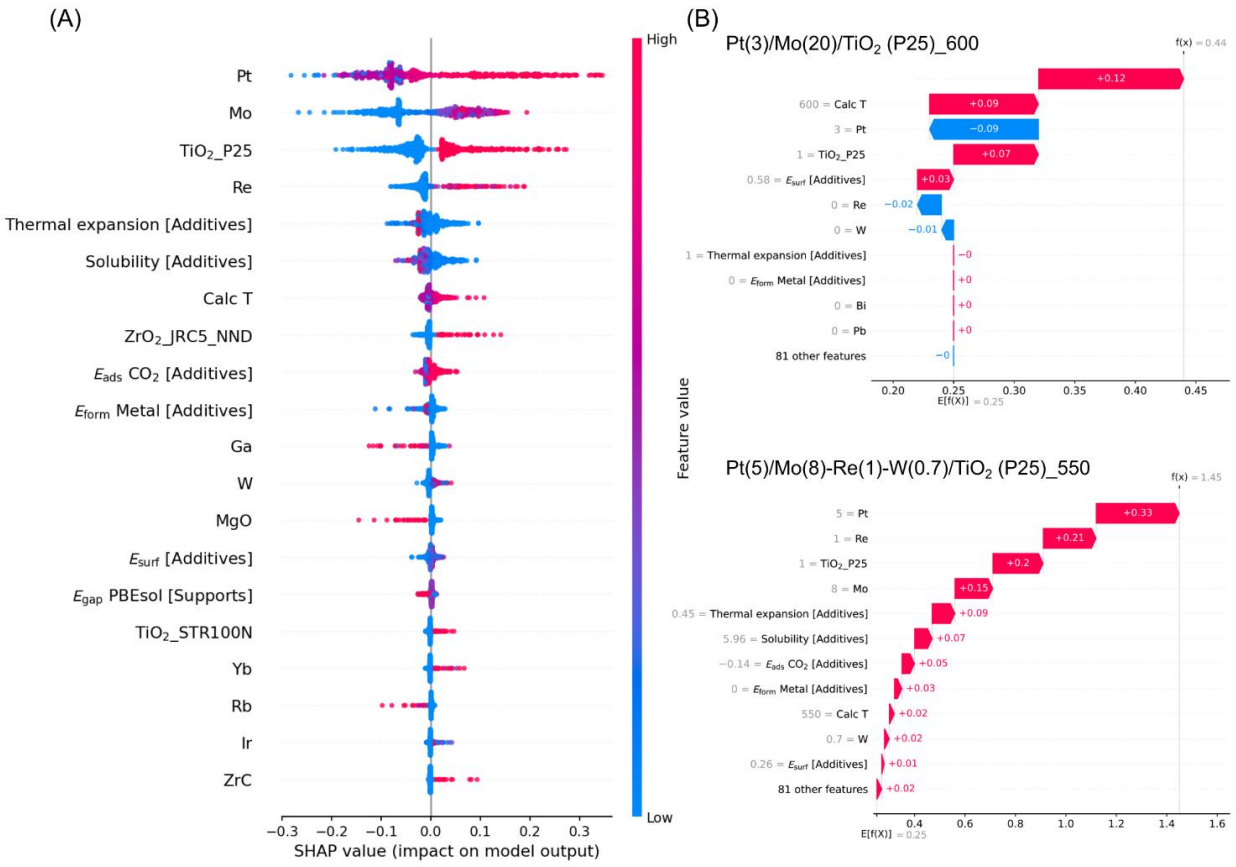

Figure 2.13. (A) SHAP values of the descriptors (summary plot) used to predict CH_3OH formation rates of all the 580 catalysts in our final dataset as a post hoc analysis (red and blue for SHAP analysis correspond to high and low features, respectively). Features are in descending order based on the sum of their absolute SHAP values. The vertical dispersion of dots indicates the density of data points at a given SHAP value. (B) Comparison between the current best catalysts, Pt(5)/Mo(8)–Re(1)–W(0.7)/TiO_2 (P25)_550 and Pt(3)/Mo(20)/TiO_2 (P25)_600, to identify feature values responsible for performance deviations from the base. The positive and negative contributions of each feature are shown in red and blue, respectively. The explorative elemental descriptor representation was used in the analysis.

2.3.3 Catalyst characterization

After confirming the high activity of the Pt(5)/Mo(8)–Re(1)–W(0.7)/TiO_2 (P25)_550 catalyst, various characterization techniques were utilized to investigate the structural details of the catalyst in operation. In the X-ray diffraction (XRD) pattern (**Figure 2.14**), both anatase and rutile phases were observed for the pristine TiO_2 (P25). Upon loading the Mo, Re, and W species onto TiO_2 (P25), Mo(8)–Re(1)–W(0.7)/TiO_2 (P25)_550 showed the presence of MoO_3. Peaks corresponding to the Re and W species were not observed. Similar observations were made for the unreduced Pt(5)/Mo(8)–Re(1)–W(0.7)/TiO_2 (P25)_550, suggesting that in the unreduced state, the Mo species exists as crystalline MoO_3. Simultaneously, the absence of structural features for Pt, Re and W indicates that these species were highly dispersed on the TiO_2 (P25) surface. Following reduction at 300 °C, the

MoO_3 peaks disappeared, and only the peaks for TiO_2 (P25) were observed, indicating the loss of crystallinity of the Mo oxides under the reduction conditions. It is important to note that even in the reduced sample, Pt, Re, and W species remained highly dispersed.

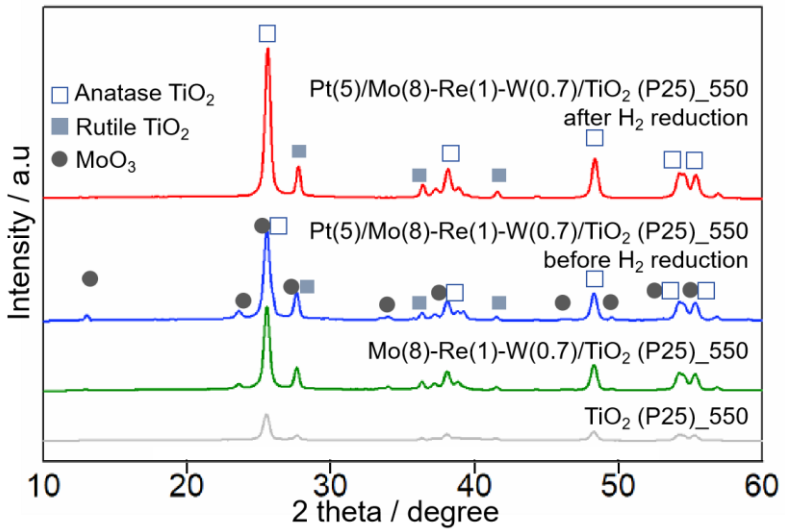

Figure 2.14. XRD patterns of pristine Pt(5)/Mo(8)–Re(1)-W(0.7)/TiO_2 (P25)_550 (after H_2 reduction), Pt(5)/Mo(8)–Re(1)–W(0.7)/TiO_2 (P25)_550 (before H_2 reduction), Mo(8)–Re(1)–W(0.7)/TiO_2 (P25)_550, and TiO_2 (P25)_ 550. 550 is the calcination temperature (°C).

High-angle annular dark-field scanning transmission electron microscopy (HAADF-STEM) was employed to further clarify the structure of the reduced Pt(5)/Mo(8)–Re(1)–W(0.7)/TiO_2 (P25)_550 catalyst (**Figure 2.15**). Highly dispersed Pt nanoparticles were observed with an average size of 2.3 nm. Notably, large individual oxide particles of Mo, W, and Re were not observed (**Figure 2.15**). According to the energy-dispersive X-ray spectroscopy (EDX) mapping analysis of Pt, bright nanoparticles in the HAADF-STEM image were Pt nanoparticles highly dispersed over the TiO_2 surface. It is worth mentioning that TiO_x overlayer formation over the Pt nanoparticle indicative of strong metal-support interaction (SMSI)[104] was not observed. Furthermore, CO adsorption band clearly observed over Pt nanoparticles (vide infra) during *in situ/operando* DRIFTS analyses also suggests that Pt surface was not covered by TiO_x species and remained accessible to reactant molecules. In addition, EDX mapping of Mo, Re, and W species suggested their high dispersion on the TiO_2 surface, consistent with XRD analysis of the reduced catalyst.

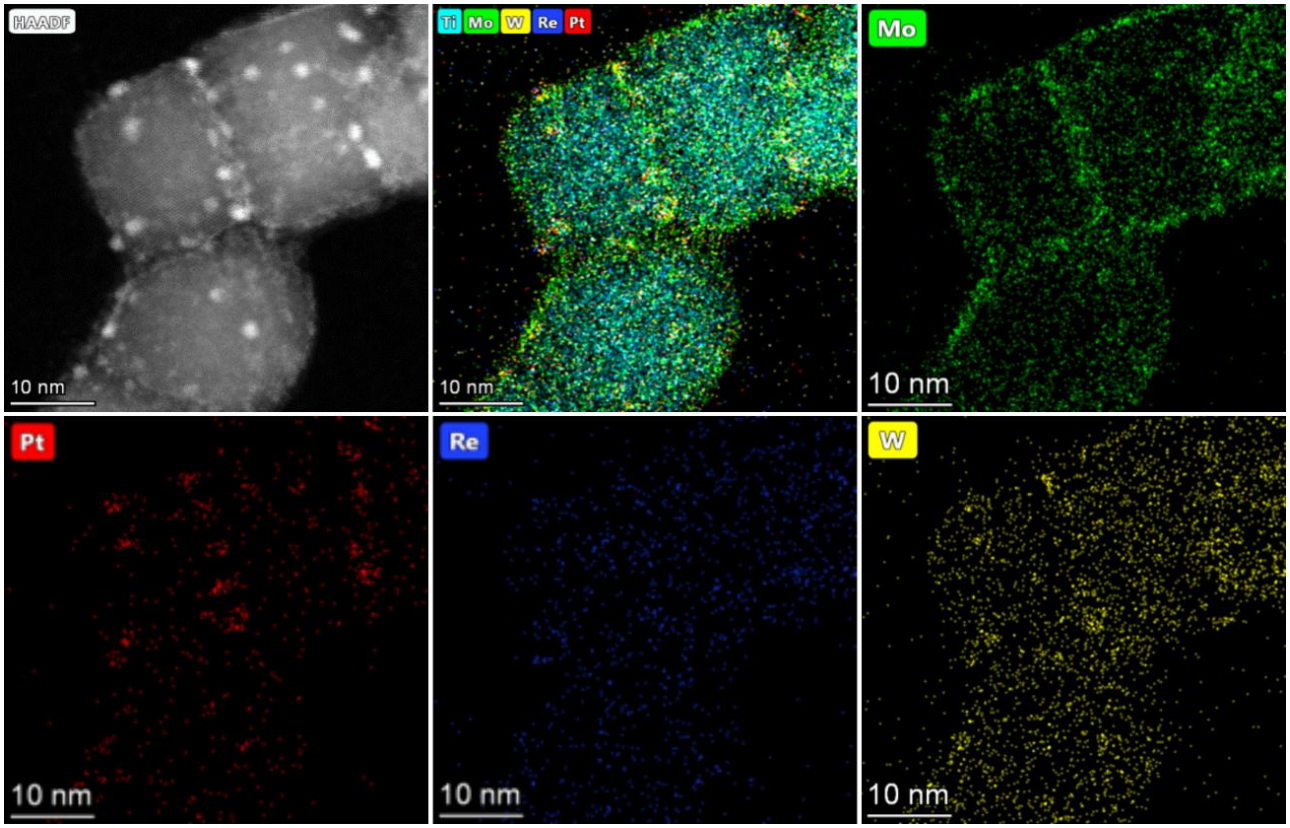

Figure 2.15. HAADF-STEM image and EDX mapping images of Pt(5)/Mo(8)–Re(1)–W(0.7)/TiO_2 (P25)_550 after reduction at 300 °C. The Pt, Mo, Re, W, and Ti signals are related to the catalyst composition.

To understand the chemical environments of Pt, Mo, Re, and W in the Pt(5)/Mo(8)–Re(1)–W(0.7)/TiO_2 (P25)_550 catalyst, X-ray absorption spectroscopy (XAS) analysis was carried out. It should be noted that because the best catalyst developed in this study contains multiple elements, we selected and measured absorption edges that could be analyzed without overlapping other absorption edges for each element. **Figure 2.16A** shows the Pt L_2-edge X-ray absorption near-edge structure (XANES) of the catalyst before reduction, after reduction at 300 °C under H_2, and after aging under reaction conditions (150 °C, 60 bar, H_2 : CO_2 = 5 : 1) for 24 h. Prior to reduction, the edge position of Pt in the unreduced catalyst resembled that of PtO_2, indicating the presence of PtO_2 particles. After reduction, the edge position of Pt became similar to that of Pt foil, suggesting the reduction of PtO_2 species to metallic Pt after H_2 treatment. The XANES spectrum remained almost unchanged after aging the catalyst under the reaction conditions for 24 h, suggesting the presence of metallic Pt nanoparticles under reaction condition.

The XANES spectrum for the Mo K-edge is shown in **Figure 2.16B**. Prior to catalyst reduction, the edge position and shape of the Mo K-edge XANES spectrum resembled those of MoO_3, serving as a reference material. This similarity suggests the presence of MoO_3 in the unreduced sample, consistent with XRD analysis. Following reduction and aging under reaction conditions, the Mo edge position fell between that of Mo foil and MoO_2. This observation implies that the Mo species persisted as a highly defective reduced Mo-oxide structure during the reaction conditions.[105]

The W L_3-edge XANES spectra display similar features to those of the Mo K-edge XANES spectra (**Figure 2.16C**). The W L_3-edge position for the unreduced sample closely resembles that of the WO_3 reference material. In contrast, the reduced sample shows a shift towards a lower position, suggesting the conversion of WO_3 to reduced W oxides after reduction. This position remains stable after aging under the reaction conditions, indicating the persistence of the W species as reduced W oxides.

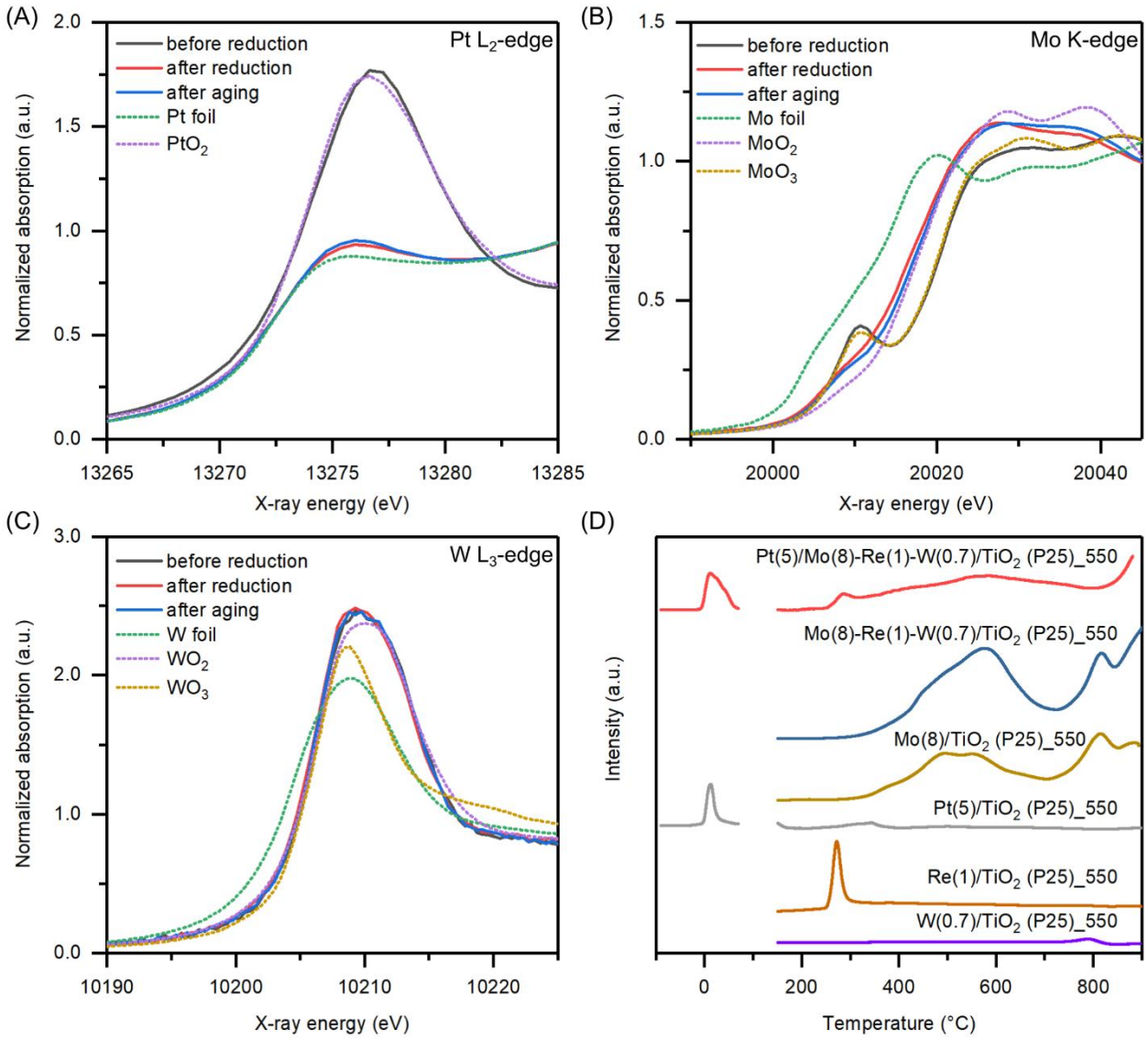

Figure 2.16. (A) Pt L_2-edge, (B) Mo K-edge, and (C) W L_3-edge XANES spectra of Pt(5)/Mo(8)–Re(1)–W(0.7) /TiO_2 (P25)_550 before reduction (black line), after reduction (red line), and after aging under reaction condition (blue line). The spectra were recorded at room temperature. After reduction treatment, the samples were not exposed to air and were contained in sealed vessels under N_2. (D) H_2-TPR profiles of Pt(5)/Mo(8)–Re(1)–W(0.7)/TiO_2 (P25)_550, Mo(8)–Re(1)–W(0.7)/TiO_2 (P25)_550, Mo(8)/TiO_2 (P25)_550, Pt(5)/TiO_2 (P25)_550, Re(1)/TiO_2 (P25)_550, and W(0.7)/TiO_2 (P25)_550.

We could not analyze Re using XAS. We speculated that the content of Re was too low to be measured in XAS. Therefore, we performed inductively coupled plasma mass spectrometry (ICP-MS) to measure the Re content in the catalyst. The actual Re loading in the catalyst was 0.02 wt%, lower than the expected 1%. This is due to the sublimation of oxidic Re species at high calcination temperatures.[106] Although the Re chemical environment could not be directly investigated, literature suggests that Re exists in a highly dispersed and partially reduced oxidic state.[10,107–109] It is noteworthy that even a small amount of Re is crucial

for achieving the highest activity. This suggests that even a small amount of Re contributes to the reaction and/or that, while Re may be lost through sublimation, its presence positively influences the structure of other catalyst components. The current best catalyst was calcined at 550 °C, leading to Re species sublimation. To prevent the sublimation of Re species, we performed catalytic reactions using catalysts calcined at 300 °C or left uncalcined. As a result (**Figure 2.17**), the methanol production rates were 1.18 mmol g_{cat}^{-1} h^{-1} and 0.35 mmol g_{cat}^{-1} h^{-1}, respectively, confirming the higher activity of the catalyst calcined at 550 °C. Catalyst experts typically avoid calcination at 550 °C owing to the known sublimation of oxidized Re species at high temperatures. However, in this ML-driven study, such an unconventional treatment was proposed by the ML model, leading to the discovery of a novel catalyst. This highlights the advantage of employing ML in catalyst development, as it can suggest strategies that human intuition might overlook. In summary, in the unreduced catalyst, all elements were in oxide forms, while under reaction conditions, Mo and W existed as highly dispersed partially reduced oxides, and Pt was present as metallic Pt nanoparticles on the TiO_2 surface.

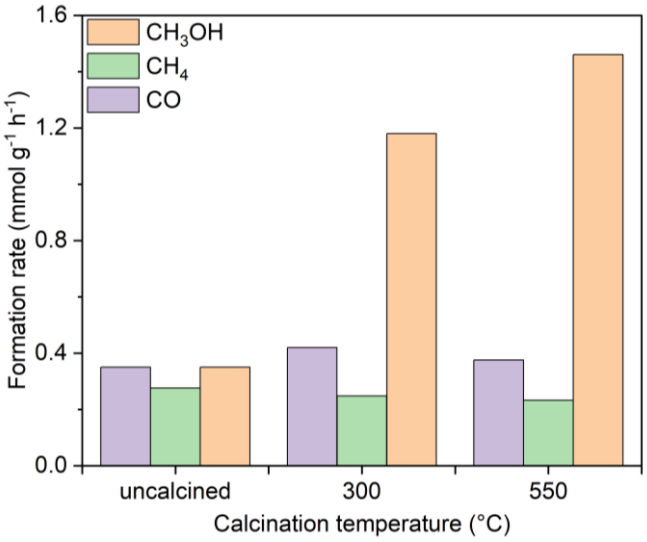

Figure 2.17. Catalytic activity result for CO_2 hydrogenation over Pt(5)/Mo(8)-Re(1)-W(0.7)/TiO_2 (P25) calcined at different temperatures. Before calcination, all the catalysts were dried at 110 °C for 12 h. Reaction condition: 150 °C, 6 MPa, H_2 : CO_2 = 5 : 1, 6 h. Prior to catalytic reaction, all the catalysts were reduced under H_2 at 300 °C for 0.5 h.

Furthermore, we compared the H_2-temperature programmed reduction (H_2-TPR) profile of the best catalyst with that of the control catalyst (**Figure 2.16D**). Without Pt, the Mo(8)–Re(1)–W(0.7)/TiO_2 (P25)_550 catalyst exhibited reduction peaks at higher temperatures compared to the Pt containing best catalyst. Pt underwent reduction at a significantly lower temperature and facilitated the reduction of other species during pretreatment at 300 °C. This observation aligns with the XANES results.

2.3.4 Mechanistic study

CO_2 hydrogenation to methanol can occur through two distinct mechanisms: (i) through the formate intermediate, and (ii) through the RWGS reaction combined with the CO hydrogenation pathway.[110–112] Our previous research demonstrated that a Pt/MoO_x/TiO_2 catalyst primarily generated methanol mainly using the formate intermediate.[58] The rate of methanol production via CO hydrogenation was lower compared to direct CO_2 hydrogenation. In this study, *operando* diffuse reflectance infrared Fourier-transform spectroscopy (DRIFTS) was employed to investigate the surface adsorbates involved in the catalytic processes of methanol synthesis over Pt(5)/Mo(8)–Re(1)–W(0.7)/TiO_2 (P25)_550 (**Figure 2.18A**). Upon the introduction of CO_2, spectral bands corresponding to surface adsorbates such as carbonate and formate immediately appeared in the 1800–1200 cm^{-1} range, concomitant

with the appearance of adsorbed CO, as suggested by bands observed at 2100–1950 cm^{-1}. Bands around 1550, 1388, and 1369 cm^{-1}, along with bands in the 2800–2980 cm^{-1} region, were assigned to v(CH), indicating the formate formation.[113] Notably, formate formation in the absence of H_2 should be attributed to the presence of dissociated hydrogen species on the surface during H_2 pretreatment. Formate was found to be a prevalent species on the surface. Following H_2 introduction, the intensity of the 1550 cm^{-1} formate band initially increased and then decreased. The emergence of the 1110 cm^{-1} peak indicated methoxy species formation. The evolution of methanol yield (determined by GC at the outlet) corresponded to the intensity of the formate peak in the DRIFTS spectrum, illustrating a direct correlation between surface formate species and methanol production (**Figure 2.18B**). Moreover, the adsorbed CO species decreased as the CO yield gradually increased, as detected by GC at the outlet. These findings suggest that methanol was predominantly produced via the formate pathway over the best catalyst, and CO did not serve as an intermediate in methanol production.

To clarify the role of each element in the reaction mechanism of methanol formation over the best catalyst, *Operando* XAS was conducted at 150 °C under ambient pressure. Measurements were taken after pretreatment in H_2 atmosphere, under CO_2, H_2, and CO_2 + H_2 mixture (H_2: CO_2 = 3:1) as reaction gases (**Figure 2.18C**). The *Operando* Mo K-edge XANES of Pt(5)/Mo(8)-Re(1)-W(0.7)/TiO_2 (P25)_550, as shown in **Figure 2.18C**, revealed that the edge position of the Mo K-edge curve shifted to a higher energy after the introduction of CO_2 (**Figure 2.18C,** red line), while CO was simultaneously detected by GC (**Figure 2.18D**). It should be noted that owing to instrumental constraints, this experiment was conducted at ambient pressure, resulting in CO as the only product instead of methanol. This suggests that CO_2 acts as an oxidant to oxidize the Mo species. The oxidized Mo species were reduced back when H_2 was introduced (**Figure 2.18C,** blue line), indicating the redox property of Mo.[113] This redox property of Mo would help MoO_x species to maintain a partially reduced state under the CO_2 + H_2 atmosphere, as observed in the *operando* XAS experiment under the CO_2 + H_2 atmosphere at ambient pressure (**Figure 2.18C,** green line). Notably, the higher CO production during methanol synthesis than under redox condition indicates that CO_2 hydrogenation mainly followed an associative mechanism, consistent with the *operando* DRIFTS study. The undercoordinated Mo sites would generate and stabilize the oxygenates, promoting CO_2 hydrogenation to methanol.[114] The W L_3-edge XANES spectra were also obtained using a protocol similar to that described above (**Figure 2.19**), but the edge position

did not change when flowing CO_2, indicating no redox reaction of W species during methanol synthesis.

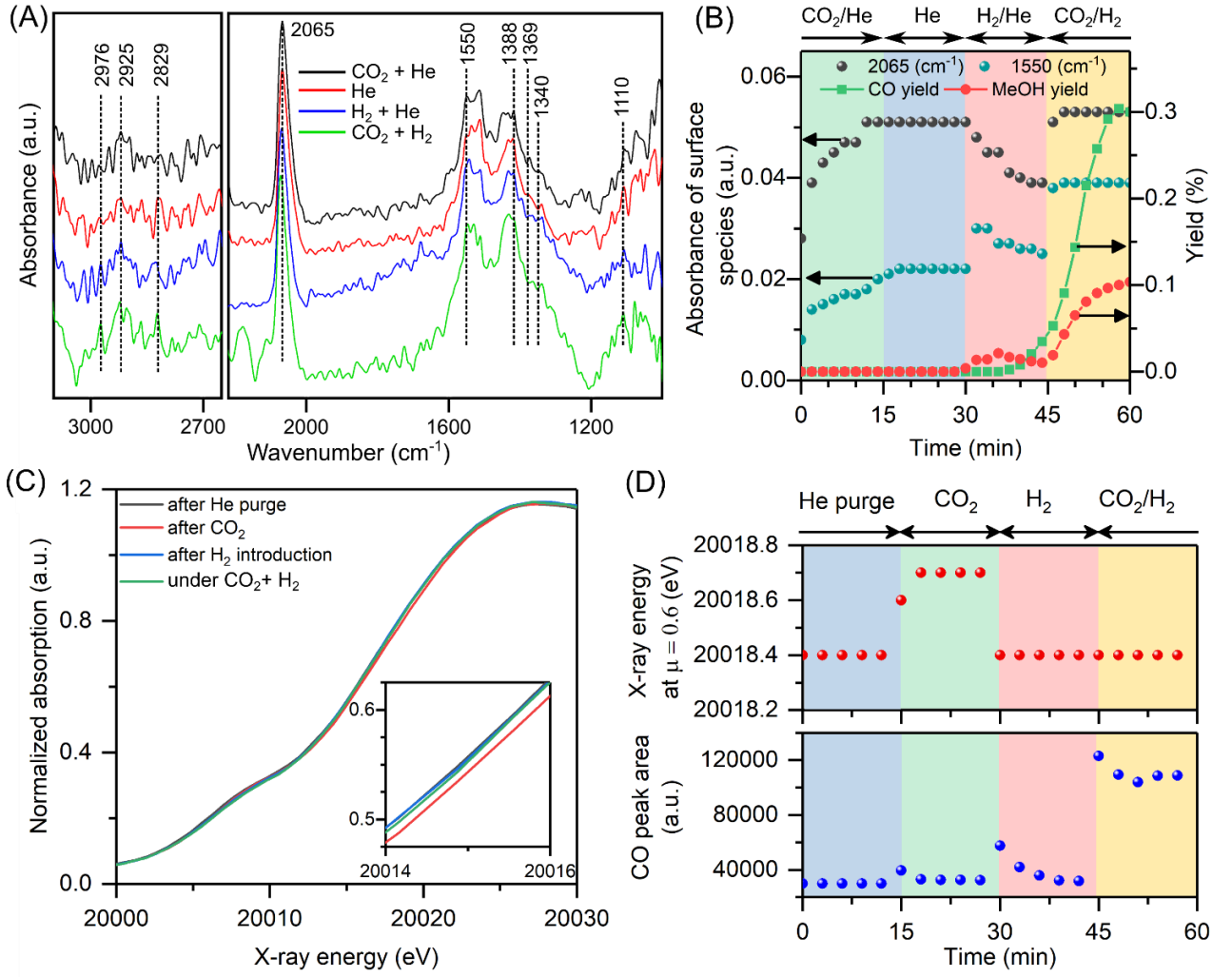

Figure 2.18. (A) *Operando* DRIFTS analyses of the Pt(5)/Mo(8)-Re(1)-W(0.7)/TiO_2 (P25)_550 catalyst conducted under a sequential flow of CO_2/He, He, H_2/He, and 25% CO_2 + 75% H_2 at 150 °C. (B) Temporal changes in the intensities of the DRIFTS peaks associated with surface-adsorbed species and the CO concentration in the effluent following CO_2 introduction. (C) *Operando* Mo K-edge XANES profile of Pt(5)/Mo(8)–Re(1)–W(0.7) /TiO_2 (P25)_550 measured under a sequential flow of 100% H_2, 100% He, 25% CO_2/He, 75% H_2/He, and 25% CO_2 + 75% H_2 at 150 °C. Prior to the experiment, the catalyst was pretreated under H_2 at 300 °C for 0.5 h. (D) Changes in the X-ray energy (at μ = 0.6 eV) of Mo K-edge XANES (top) and CO concentration in the gas phase (bottom).

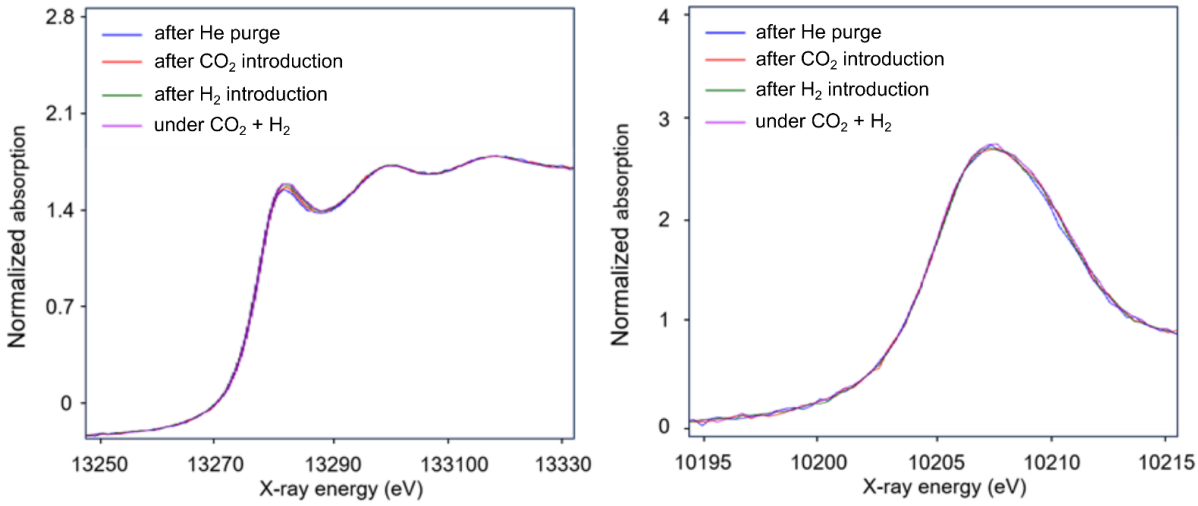

Figure 2.19. *In situ* XANES measurements of Pt L_2-dege(left) and W L_3-edge(right) for the Pt(5)/Mo(8)-Re(1)-W(0.7)/TiO_2 (P25)_550 catalyst conducted under a sequential flow of CO_2/He, He, H_2, and 25% CO_2 + 75% H_2 at 150 °C.

To gain further insights into role of different elements in the methanol formation reaction, *in situ* DRIFTS analysis was conducted under the reaction conditions using various control catalysts and compared with the outcomes obtained with the best catalyst (**Figure 2.20**). The Mo(8)–Re(1)–W(0.7)/TiO_2 (P25)_550 catalyst, without Pt, displayed minimal formate (1550 cm^{-1}), methoxy (1110 cm^{-1}), or adsorbed CO intermediates (2065 cm^{-1}) (**Figure 2.20**), highlighting Pt as the primary hydrogen-dissociating component. In the absence of Mo, the Pt(5)/Re(1)–W(0.7)/TiO_2 (P25)_550 catalyst showed weak formate and methoxy formation but a substantial presence of adsorbed CO. This suggests that the partially reduced MoO_x species predominantly facilitated oxygenate formation for methanol production, supporting the *operando* DRIFTS and XAS findings in **Figure 2.18**. Conversely, in the absence of Re, the Pt(5)/Mo(8)–W(0.7)/TiO_2 (P25)_550 catalyst exhibited high formate intensity and reduced methoxy intensity. Moreover, higher formate intensity and lower methanol yield was observed during *operando* DRIFTS analysis over Pt(5)/Mo(8)–W(0.7)/TiO_2 (P25)_550 catalyst than that over the best catalyst (**Figure 2.21**). These results indicate that the introduction of Re promoted the formate hydrogenation step to produce methoxy species. Regarding the role of W, it was not clear from the *in situ* DRIFTS study because the spectrum over the Pt(5)/Mo(8)-Re(1)/TiO_2 (P25)_550 catalyst without W resembled that over the best catalyst.

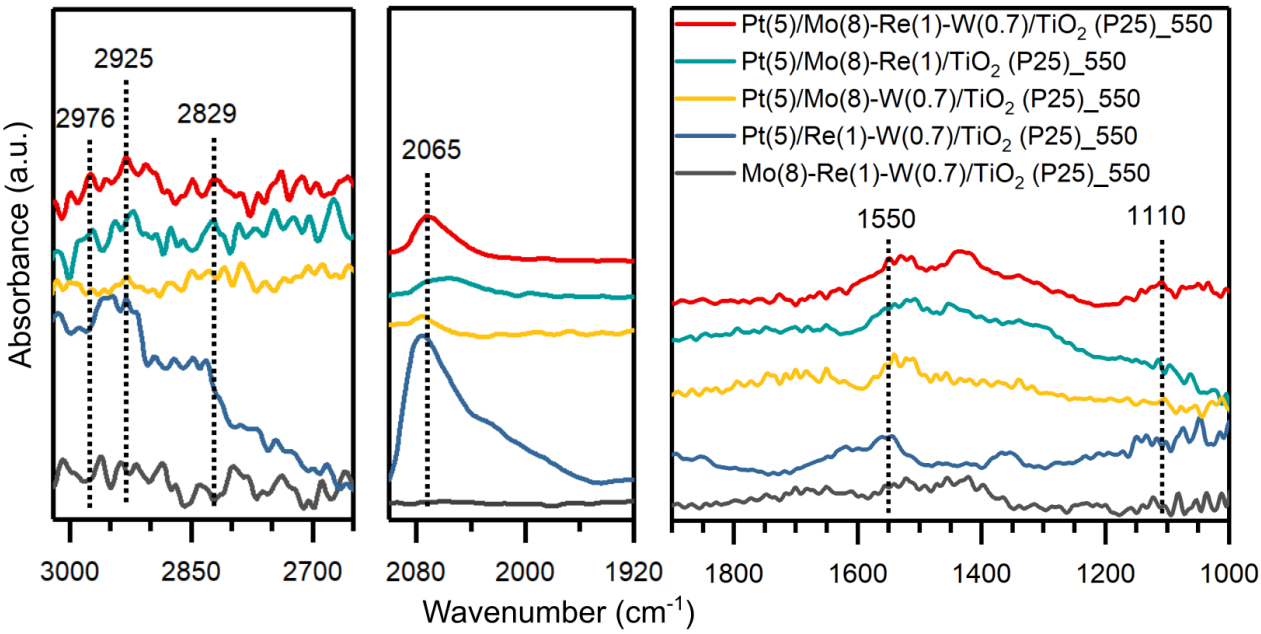

Figure 2.20. *In situ* DRIFTS analyses of Pt(5)/Mo(8)–Re(1)–W(0.7)/TiO_2 (P25)_550, Pt(5)/Mo(8)–Re(1) /TiO_2 (P25)_550, Pt(5)/Mo(8)–W(0.7)/TiO_2 (P25) _550, Mo(8)–Re(1)–W(0.7)/TiO_2 (P25)_550, and Pt(5)/Re(1)–W(0.7) /TiO_2 (P25)_550 conducted under a gas flow containing CO_2 (5 mL min^{-1}) and H_2 (15 mL min^{-1}) at 150 °C and under a pressure of 0.5 MPa.

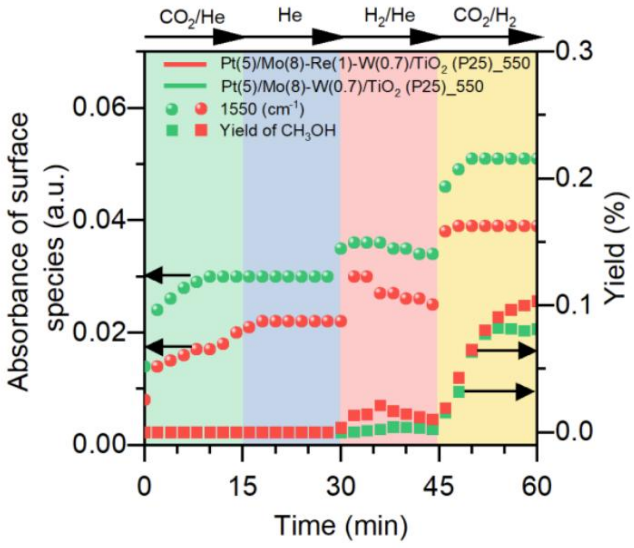

Figure 2.21. *Operando* DRIFTS analyses of the Pt(5)/Mo(8)-Re(1)-W(0.7)/TiO_2 (P25)_550 and Pt(5)/Mo(8)- W(0.7)/TiO_2 (P25)_550 catalyst conducted under a sequential flow of CO_2/He, He, H_2/He, and 25% CO_2 + 75% H_2 at 150 °C.

To further understand the role of W, we hypothesized that the acidic nature of W might help in the facile desorption of methanol from the catalyst surface. Previous studies have indicated that methanol decomposition reactions can take place on Pt/MoO_x/TiO_2 catalysts.[58]

Consequently, the easy removal of methanol from the catalyst surface would inhibit methanol decomposition and enhance methanol production. To investigate this, we studied methanol decomposition over the best catalyst and the Pt(5)/Mo(8)–Re(1)/TiO_2 (P25)_550 catalyst without W under a N_2 atmosphere (0.5 MPa). As illustrated in **Scheme 2.1**, the methanol decomposition rate over the best catalyst was lower than that observed for the Pt(5)/Mo(8)–Re(1)/TiO_2 (P25)_550 catalyst without W. This finding underscores the advantageous role of W species as acids in the facile desorption of methanol from the catalyst surface to facilitate methanol synthesis. Based on these findings, it can be inferred that CO_2 initially adsorbs on the oxygen-deficient sites of the undercoordinated MoO_x species. The primary H_2 dissociation agent, Pt nanoparticles, dissociate H_2, leading to the formation of formate over the MoO_x species. In addition to Pt, the Re species would help in converting formate to methanol, while W assists in the desorption of methanol molecules from the surface suppressing methanol decomposition and enhancing methanol production. Consequently, the co-existence of different elements with specific roles in different stages of methanol formation results in a highly active, selective, and stable catalyst for the direct CO_2 hydrogenation to methanol at low temperatures. It should be noted that although there is some ambiguity present in spectroscopic and microscopic analyses, our interpretation about the structure of Pt, Mo, Re and W species is supported by the evidences gathered from multiple characterization techniques. While mechanistic interpretations are based on observed correlations and trends, we treat them as hypotheses supported by multiple evidences rather than definitive conclusions.

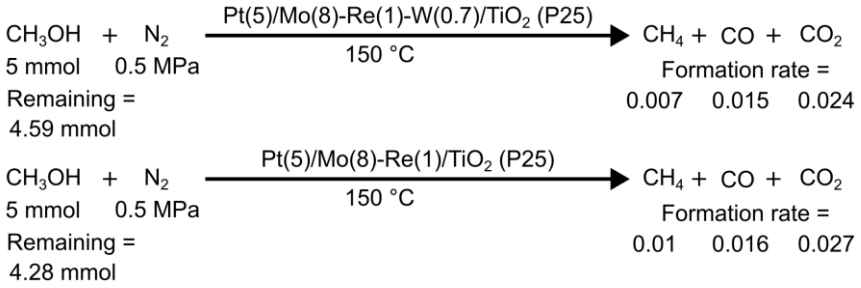

Scheme 2.1. Methanol decomposition over Pt(5)/Mo(8)–Re(1)–W(0.7)/TiO_2 (P25)_550 and Pt(5)/Mo(8)–Re(1)/TiO_2 (P25)_550. Pretreatment: H_2(20 mL min^{-1}), 300 ℃, 0.5 h. Catalytic reaction conditions: catalyst (100 mg), 150 °C. The formation rate was calculated in mmol h^{-1} unit.

2.4 Conclusion

In summary, we developed highly active catalysts for low-temperature CO_2 hydrogenation to methanol using an extrapolative ML method. Among the 33 newly discovered catalysts that showed higher methanol formation rates than a previously reported highly active catalyst (Pt(3)/Mo(20)/TiO_2 (P25)_600), the best catalyst was Pt(5)/Mo(8)–Re(1)–W(0.7)/TiO_2 (P25)_550. Remarkably, Re was absent in the original dataset signifying the efficacy of our extrapolative ML model. We also identified the physical and chemical properties governing catalytic activity. Therefore, in addition to the optimal catalyst compositions, our ML model unveiled the elemental features and electronic properties crucial for high catalytic activity. The Pt(5)/Mo(8)–Re(1)–W(0.7)/TiO_2 (P25)_550 catalyst exhibited significantly higher methanol yield compared to the industrial Cu/ZnO/Al_2O_3 catalyst. Moreover, experimental *in situ*/*operando* techniques were used to elucidate the reaction mechanism and role of each component of the best catalyst. Our findings revealed that Pt played a primary role in H_2 dissociation, partially reduced Mo oxides facilitated the activation of CO_2 to oxygenated species, Re promoted formate conversion to methoxy species, and W accelerated methanol desorption from the catalyst surface. We anticipate that our study will expedite the development of novel catalysts through machine learning approaches.

2.5 References

(1) Roosmalen, R. van; Rothenberg, G. Carbon Capture, Storage And Utilization: A Critical Overview. In *Handbook of Energy, Environment, and the Circular Economy*; Gitis, V., Rothenberg, G., Eds.;World Scientific Publishing Co, **2024**; pp 297–353.

(2) Fu, J.; Lym, J.; Zheng, W.; Alexopoulos, K.; Mironenko, A. V; Li, N.; Boscoboinik, J. A.; Su, D.; Weber, R. T.; Vlachos, D. G. C–O Bond Activation Using Ultralow Loading of Noble Metal Catalysts on Moderately Reducible Oxides. *Nat. Catal*. **2020**, *3* (5), 446–453.

(3) Zhang, Z.; Zuo, J.; Luo, L.; Yang, X.; Ma, Z.; Jin, H.; Yuan, Y.; Qian, Q.; Chen, Q.; Luo, Y. Sodium-Assisted MoS_2 for Boosting CO_2 Hydrogenation to Methanol: The Crucial Role of Sodium in Defect Evolution and Modification. *J. Catal.* **2024**, *436*, 115621.

(4) Olah, G. A. Towards Oil Independence Through Renewable Methanol Chemistry. *Angew. Chemie Int. Ed*. **2013**, *52* (1), 104–107.

(5) Segler, M. H. S.; Preuss, M.; Waller, M. P. Planning Chemical Syntheses with Deep Neural Networks and Symbolic AI. *Nature* **2018**, *555* (7698), 604–610.

(6) Gutterød, E. S.; Lazzarini, A.; Fjermestad, T.; Kaur, G.; Manzoli, M.; Bordiga, S.; Svelle, S.; Lillerud, K. P.; Skúlason, E.; Øien-ØDegaard, S.; Nova, A.; Olsbye, U. Hydrogenation of CO_2 to Methanol by Pt Nanoparticles Encapsulated in UiO-67: Deciphering the Role of the Metal-Organic Framework. *J. Am. Chem. Soc.* **2020**, *142* (2), 999–1009.

(7) Butler, K. T.; Davies, D. W.; Cartwright, H.; Isayev, O.; Walsh, A. Machine Learning for Molecular and Materials Science. *Nature.* **2018**, *559*(7715), 547–555.

(8) Hu, J.; Yu, L.; Deng, J.; Wang, Y.; Cheng, K.; Ma, C.; Zhang, Q.; Wen, W.; Yu, S.; Pan, Y.; Yang, J.; Ma, H.; Qi, F.; Wang, Y.; Zheng, Y.; Chen, M.; Huang, R.; Zhang, S.; Zhao, Z.; Mao, J.; Meng, X.; Ji, Q.; Hou, G.; Han, X.; Bao, X.; Wang, Y.; Deng, D. Sulfur Vacancy-Rich MoS_2 as a Catalyst for the Hydrogenation of CO_2 to Methanol. *Nat. Catal.* **2021**, *4* (3), 242–250.

(9) Gau, A.; Hack, J.; Maeda, N.; Meier, D. M. Operando Spectroscopic Monitoring of Active Species in CO_2 Hydrogenation at Elevated Pressure and Temperature: Steady-State versus Transient Analysis. *Energy and Fuels.* **2021**, *35* (18), 15243–15246.

(10) Ting, K. W.; Toyao, T.; Siddiki, S. M. A. H.; Shimizu, K. I. Low-Temperature Hydrogenation of CO_2 to Methanol over Heterogeneous TiO_2-Supported Re Catalysts. *ACS Catal.* **2019**, *9* (4), 3685–3693.

(11) Gaikwad, R.; Bansode, A.; Urakawa, A. High-Pressure Advantages in Stoichiometric Hydrogenation of Carbon Dioxide to Methanol. *J. Catal.* **2016**, *343*, 127–132.

(12) Porosoff, M. D.; Yan, B.; Chen, J. G. Catalytic Reduction of CO_2 by H_2 for Synthesis of CO, Methanol and Hydrocarbons: Challenges and Opportunities. *Energy and Environ. Sci.* **2016**, 9(1), 62–73.

(13) Álvarez, A.; Bansode, A.; Urakawa, A.; Bavykina, A. V; Wezendonk, T. A.; Makkee, M.; Gascon, J.; Kapteijn, F. Challenges in the Greener Production of Formates/Formic Acid, Methanol, and DME by Heterogeneously Catalyzed CO_2 Hydrogenation Processes. *Chem. Rev.* **2017**, *117*(14), 9804-9838.

(14) Olah, G. A.; Goeppert, A.; Prakash, G. K. S. Chemical Recycling of Carbon Dioxide to Methanol and Dimethyl Ether: From Greenhouse Gas to Renewable, Environmentally Carbon Neutral Fuels and Synthetic Hydrocarbons. Journal of Organic Chemistry. *J. Org. Chem.* **2009**, *74* (2), 487–498.

(15) Liu, G.; Liu, P.; Meng, D.; Zhao, T.; Qian, X.; He, Q.; Guo, X.; Qi, J.; Peng, L.; Xue, N.; Zhu, Y.; Ma, J.; Wang, Q.; Liu, X.; Chen, L.; Ding, W. CO_x Hydrogenation to Methanol and Other Hydrocarbons under Mild Conditions with Mo_3S_4@ZSM-5. *Nat. Commun.* **2023**, 14 (1), 513.

(16) Chen, Y.; Choi, S.; Thompson, L. T. Low Temperature CO_2 Hydrogenation to Alcohols and Hydrocarbons over Mo_2C Supported Metal Catalysts. *J. Catal.* **2016**, *343*, 147–156.

(17) Khan, M. U.; Wang, L.; Liu, Z.; Gao, Z.; Wang, S.; Li, H.; Zhang, W.; Wang, M.; Wang, Z.; Ma, C.; Zeng, J. Pt_3Co Octapods as Superior Catalysts of CO_2 Hydrogenation. *Angew. Chemie Int. Ed.* **2016**, *55* (33), 9548–9552.

(18) He, Z.; Qian, Q.; Ma, J.; Meng, Q.; Zhou, H.; Song, J.; Liu, Z.; Han, B. Water-Enhanced Synthesis of Higher Alcohols from CO_2 Hydrogenation over a Pt/Co_3O_4 Catalyst under Milder Conditions. *Angew. Chemie Int. Ed.* **2016**, *55* (2), 737–741.

(19) Hong, S.; Reddy, K. P.; Song, Y.; Park, D.; Park, J. Y. Enhanced Methanol Formation in CO_2 Hydrogenation through Synergistic Copper and Gallium Interaction. *J. Catal.* **2024**, *437*, 115643.

(20) Sugiyama, H.; Miyazaki, M.; Sasase, M.; Kitano, M.; Hosono, H. Room-Temperature CO_2 Hydrogenation to Methanol over Air-Stable Hcp-PdMo Intermetallic Catalyst. *J. Am. Chem. Soc.* **2023**, *145* (17), 9410–9416.

(21) Sanchez-Lengeling, B.; Aspuru-Guzik, A. Inverse Molecular Design Using Machine Learning: Generative Models for Matter Engineering. *Science* **2018**, *361* (6400), 360–365.

(22) Aykol, M.; Hegde, V. I.; Hung, L.; Suram, S.; Herring, P.; Wolverton, C.; Hummelshøj, J. S. Network Analysis of Synthesizable Materials Discovery. *Nat. Commun.* **2019**, *10* (1), 2018.

(23) Coley, C. W.; Thomas, D. A.; Lummiss, J. A. M.; Jaworski, J. N.; Breen, C. P.; Schultz, V.; Hart, T.; Fishman, J. S.; Rogers, L.; Gao, H.; Hicklin, R. W.; Plehiers, P. P.; Byington, J.; Piotti, J. S.; Green, W. H.; John Hart, A.; Jamison, T. F.; Jensen, K. F. A Robotic Platform for Flow Synthesis of Organic Compounds Informed by AI Planning. *Science* **2019**, *365* (6453), eaax1566.

(24) Ras, E. J.; Rothenberg, G. Heterogeneous Catalyst Discovery Using 21st Century Tools: A Tutorial. *RSC Adv.* **2014**, *4* (12), 5963–5974.

(25) Erdem Günay, M.; Yıldırım, R. Recent Advances in Knowledge Discovery for Heterogeneous Catalysis Using Machine Learning. *Catal. Rev.* **2021**, *63* (1), 120–164.

(26) Ooka, H.; Wintzer, M. E.; Nakamura, R. Non-Zero Binding Enhances Kinetics of Catalysis: Machine Learning Analysis on the Experimental Hydrogen Binding Energy of Platinum. *ACS Catal*. **2021**, *11* (10), 6298–6303.

(27) Miyazaki, R.; Belthle, K. S.; Tüysüz, H.; Foppa, L.; Scheffler, M. Materials Genes of CO_2 Hydrogenation on Supported Cobalt Catalysts: An Artificial Intelligence Approach Integrating Theoretical and Experimental Data. *J. Am. Chem. Soc.* **2024**, *146* (8), 5433–5444.

(28) Peng, J.; Schwalbe-Koda, D.; Akkiraju, K.; Xie, T.; Giordano, L.; Yu, Y.; Eom, C. J.; Lunger, J. R.; Zheng, D. J.; Rao, R. R.; Muy, S.; Grossman, J. C.; Reuter, K.; Gómez-Bombarelli, R.; Shao-Horn, Y. Human- and Machine-Centred Designs of Molecules and Materials for Sustainability and Decarbonization. *Nat. Rev. Mater.* **2022**, *7* (12), 991–1009.

(29) Jayarathna, R.; Onsree, T.; Drummond, S.; Naglic, J.; Lauterbach, J. Experimental Discovery of Novel Ammonia Synthesis Catalysts via Active Learning. *J. Mater. Chem. A* **2024**, *12* (5), 3046–3060.

(30) Mazheika, A.; Wang, Y.-G.; Valero, R.; Viñes, F.; Illas, F.; Ghiringhelli, L. M.; Levchenko, S. V; Scheffler, M. Artificial-Intelligence-Driven Discovery of Catalyst Genes with Application to CO_2 Activation on Semiconductor Oxides. *Nat. Commun.* **2022**, *13* (1), 419.

(31) Raccuglia, P.; Elbert, K. C.; Adler, P. D. F.; Falk, C.; Wenny, M. B.; Mollo, A.; Zeller, M.; Friedler, S. A.; Schrier, J.; Norquist, A. J. Machine-Learning-Assisted Materials Discovery Using Failed Experiments. *Nature* **2016**, *533* (7601), 73–76.

(32) Medford, A. J.; Kunz, M. R.; Ewing, S. M.; Borders, T.; Fushimi, R. Extracting Knowledge from Data through Catalysis Informatics. *ACS Catal.* **2018**, *8* (8), 7403–7429.

(33) Takahashi, K.; Takahashi, L.; Miyazato, I.; Fujima, J.; Tanaka, Y.; Uno, T.; Satoh, H.; Ohno, K.; Nishida, M.; Hirai, K.; Ohyama, J.; Nguyen, T. N.; Nishimura, S.; Taniike, T. The Rise of Catalyst Informatics: Towards Catalyst Genomics. *ChemCatChem.* **2019**, *11* (4), 1146–1152.

(34) Masood, H.; Toe, C. Y.; Teoh, W. Y.; Sethu, V.; Amal, R. Machine Learning for Accelerated Discovery of Solar Photocatalysts. *ACS Catal.* **2019**, *11* (6), 11774–11787.

(35) Toyao, T.; Maeno, Z.; Takakusagi, S.; Kamachi, T.; Takigawa, I.; Shimizu, K. I. Machine Learning for Catalysis Informatics: Recent Applications and Prospects. *ACS Catal.* **2019**, *10*(3), 2260-2297..

(36) Maldonado, A. G.; Rothenberg, G. Predictive Modeling in Homogeneous Catalysis: A Tutorial. *Chem. Soc. Rev.* **2010**, *39* (6), 1891–1902.

(37) Calle-Vallejo, F.; Loffreda, D.; Koper, M. T. M.; Sautet, P. Introducing Structural Sensitivity into Adsorption-Energy Scaling Relations by Means of Coordination Numbers. *Nat. Chem.* **2015**, *7* (5), 403–410.

(38) Ulissi, Z. W.; Medford, A. J.; Bligaard, T.; Nørskov, J. K. To Address Surface Reaction Network Complexity Using Scaling Relations Machine Learning and DFT Calculations. *Nat. Commun*. **2017**, *8* (1), 14621.

(39) Li, Z.; Wang, S.; Xin, H. Toward Artificial Intelligence in Catalysis. *Nat. Catal.* **2018**, *1* (9), 641–642.

(40) Bruix, A.; Margraf, J. T.; Andersen, M.; Reuter, K. First-Principles-Based Multiscale Modelling of Heterogeneous Catalysis. *Nat. Catal.* 2019, 2 (8), 659–670. (41) Shi, Y.-F.; Kang, P.-L.; Shang, C.; Liu, Z.-P. Methanol Synthesis from CO_2/CO Mixture on Cu–Zn Catalysts from Microkinetics-Guided Machine Learning Pathway Search. *J. Am. Chem. Soc.* **2022**, *144* (29), 13401–13414.

(42) Iwama, R.; Takizawa, K.; Shinmei, K.; Baba, E.; Yagihashi, N.; Kaneko, H. Design and Analysis of Metal Oxides for CO_2 Reduction Using Machine Learning, Transfer Learning, and Bayesian Optimization. *ACS Omega* **2022**, *7* (12), 10709–10717.

(43) Mosquera-Lois, I.; Kavanagh, S. R.; Ganose, A. M.; Walsh, A. Machine-Learning Structural Reconstructions for Accelerated Point Defect Calculations. *npj Comput. Mater.* **2024**, *10* (1), 121.

(44) Kalikadien, A. V; Valsecchi, C.; van Putten, R.; Maes, T.; Muuronen, M.; Dyubankova, N.; Lefort, L.; Pidko, E. A. Probing Machine Learning Models Based on High Throughput Experimentation Data for the Discovery of Asymmetric Hydrogenation Catalysts. *Chem. Sci.* **2024**, *15* (34), 13618–13630.

(45) Mou, T.; Pillai, H. S.; Wang, S.; Wan, M.; Han, X.; Schweitzer, N. M.; Che, F.; Xin, H. Bridging the Complexity Gap in Computational Heterogeneous Catalysis with Machine Learning. *Nat. Catal*. **2023**, *6* (2), 122–136.

(46) Taniike, T.; Takahashi, K. The Value of Negative Results in Data-Driven Catalysis Research. *Nat. Catal*. **2023**, *6* (2), 108–111.

(47) Schmack, R.; Friedrich, A.; Kondratenko, E. V; Polte, J.; Werwatz, A.; Kraehnert, R. A Meta-Analysis of Catalytic Literature Data Reveals Property-Performance Correlations for the OCM Reaction. *Nat. Commun*. **2019**, *10* (1), 441.

(48) Ting, K. W.; Kamakura, H.; Poly, S. S.; Takao, M.; Siddiki, S. M. A. H.; Maeno, Z.; Matsushita, K.; Shimizu, K. I.; Toyao, T. Catalytic Methylation of M-xylene, Toluene, and Benzene Using CO_2 and H_2 over TiO_2-supported Re and Zeolite Catalysts: Machine-Learning-Assisted Catalyst Optimization. *ACS Catal*. **2021**, *11* (9), 5829–5838.

(49) Mok, D. H.; Li, H.; Zhang, G.; Lee, C.; Jiang, K.; Back, S. Data-Driven Discovery of Electrocatalysts for CO_2 Reduction Using Active Motifs-Based Machine Learning. *Nat. Commun.* **2023**, *14* (1), 7303.

(50) Mine, S.; Takao, M.; Yamaguchi, T.; Toyao, T.; Maeno, Z.; Hakim Siddiki, S. M. A.; Takakusagi, S.; Shimizu, K. ichi; Takigawa, I. Analysis of Updated Literature Data up to 2019 on the Oxidative Coupling of Methane Using an Extrapolative Machine-Learning Method to Identify Novel Catalysts. *ChemCatChem* **2021**, *13* (16), 3636–3655.

(51) Suzuki, K.; Toyao, T.; Maeno, Z.; Takakusagi, S.; Shimizu, K. ichi; Takigawa, I. Statistical Analysis and Discovery of Heterogeneous Catalysts Based on Machine Learning from Diverse Published Data. *ChemCatChem* **2019**, *11* (18), 4537–4547.

(52) Mine, S.; Jing, Y.; Mukaiyama, T.; Takao, M.; Maeno, Z.; Shimizu, K. I.; Takigawa, I.; Toyao, T. Machine Learning Analysis of Literature Data on the Water Gas Shift Reaction toward Extrapolative Prediction of Novel Catalysts. *Chem. Lett*. **2022**, *51* (3), 269–273.

(53) Suvarna, M.; Preikschas, P.; Pérez-Ramírez, J. Identifying Descriptors for Promoted Rhodium-Based Catalysts for Higher Alcohol Synthesis via Machine Learning. *ACS Catal*. **2022**, *12* (24), 15373–15385.

(54) Wang, A. Y.-T.; Kauwe, S. K.; Murdock, R. J.; Sparks, T. D. Compositionally Restricted Attention-Based Network for Materials Property Predictions. *npj Comput. Mater*. **2021**, *7* (1), 77.

(55) Falkowski, A. R.; Kauwe, S. K.; Sparks, T. D. Optimizing Fractional Compositions to Achieve Extraordinary Properties. *Integr. Mater. Manuf. Innov.* **2021**, *10* (4), 689–695.

(56) Wang, G.; Mine, S.; Chen, D.; Jing, Y.; Ting, K. W.; Yamaguchi, T.; Takao, M.; Maeno, Z.; Takigawa, I.; Matsushita, K.; Shimizu, K.; Toyao, T. Accelerated Discovery of Multi-Elemental Reverse Water-Gas Shift Catalysts Using Extrapolative Machine Learning Approach. *Nat. Commun*. **2023**, *14* (1), 5861.

(57) Yuan Jing, Chenyang Zhang, M. S. et al. Extrapolative-Machine-Learning-Guided Discovery of Multi-Elemental Heterogeneous Catalysts for Low-Temperature NO Reduction by H_2. *Res.Sq.* **2025**, March 31, Doi: 10.21203/rs.3.rs-6336733/v1.

(58) Toyao, T.; Kayamori, S.; Maeno, Z.; Siddiki, S. M. A. H.; Shimizu, K. I. Heterogeneous Pt and MoO_x Co-Loaded TiO_2 Catalysts for Lowerature CO_2 Hydrogenation to Form CH_3OH. *ACS Catal.* **2019**, *9* (9), 8187–8196.

(59) Kresse, G.; Furthmüller, J. Efficient Iterative Schemes for Ab Initio Total-Energy Calculations Using a Plane-Wave Basis Set. *Phys. Rev. B* **1996**, *54* (16), 11169–11186.

(60) Kresse, G.; Furthmüller, J. Efficiency of Ab-Initio Total Energy Calculations for Metals and Semiconductors Using a Plane-Wave Basis Set. *Comput. Mater. Sci.* **1996**, *6* (1), 15–50.

(61) Perdew, J. P.; Ruzsinszky, A.; Csonka, G. I.; Vydrov, O. A.; Scuseria, G. E.; Constantin, L. A.; Zhou, X.; Burke, K. Restoring the Density-Gradient Expansion for Exchange in Solids and Surfaces. *Phys. Rev. Lett.* **2008**, *100* (13), 136406.

(62) Blöchl, P. E. Projector Augmented-Wave Method. *Phys. Rev. B* **1994**, *50* (24), 17953–17979.

(63) Grimme, S.; Ehrlich, S.; Goerigk, L. Effect of the Damping Function in Dispersion Corrected Density Functional Theory. *J. Comput. Chem.* **2011**, *32* (7), 1456–1465.

(64) Zheng, H.; Li, X.-G.; Tran, R.; Chen, C.; Horton, M.; Winston, D.; Persson, K. A.; Ong, S. P. Grain Boundary Properties of Elemental Metals. *Acta Mater*. **2020**, *186*, 40–49.

(65) Tran, R.; Xu, Z.; Radhakrishnan, B.; Winston, D.; Sun, W.; Persson, K. A.; Ong, S. P. Surface Energies of Elemental Crystals. *Sci. Data* **2016**, *3* (1), 160080.

(66) Hinuma, Y.; Toyao, T.; Kamachi, T.; Maeno, Z.; Takakusagi, S.; Furukawa, S.; Takigawa, I.; Shimizu, K. Density Functional Theory Calculations of Oxygen Vacancy Formation and Subsequent Molecular Adsorption on Oxide Surfaces. *J. Phys. Chem. C* **2018**, *122* (51), 29435–29444.

(67) Sanderson, R. T. Principles of Electronegativity Part II. Applications. *J. Chem. Educ.* **1988**, *65* (3), 227.

(68) Oviedo, F.; Ferres, J. L.; Buonassisi, T.; Butler, K. T. Interpretable and Explainable Machine Learning for Materials Science and Chemistry. *Accounts Mater. Res.* **2022**, *3* (6), 597–607.

(69) Choudhary, K.; DeCost, B.; Chen, C.; Jain, A.; Tavazza, F.; Cohn, R.; Park, C. W.; Choudhary, A.; Agrawal, A.; Billinge, S. J. L.; Holm, E.; Ong, S. P.; Wolverton, C. Recent Advances and Applications of Deep Learning Methods in Materials Science. *npj Comput. Mater.* **2022**, *8* (1), 59.

(70) Pedregosa, F.; Varoquaux, G.; Gramfort, A.; Michel, V.; Thirion, B.; Grisel, O.; Blondel, M.; Prettenhofer, P.; Weiss, R.; Dubourg, V.; Vanderplas, J.; Passos, A.; Cournapeau, D.; Brucher, M.; Perrot, M.; Duchesnay, É. Scikit-Learn: Machine Learning in Python. *J. Mach. Learn. Res.* **2011**, *12*, 2825–2830.

(71) Scheurer, C.; Reuter, K. Role of the Human-in-the-Loop in Emerging Self-Driving Laboratories for Heterogeneous Catalysis. *Nat. Catal.* **2025**, *8* (1), 13–19.

(72) Belkin, M.; Hsu, D.; Mitra, P. P. Overfitting or Perfect Fitting? Risk Bounds for Classification and Regression Rules That Interpolate. *Adv. Neural Inform. Process. Syst*. **2018**, *31*.

(73) Huff, C. A.; Sanford, M. S. Cascade Catalysis for the Homogeneous Hydrogenation of CO_2 to Methanol. *J. Am. Chem. Soc*. **2011**, *133* (45), 18122–18125.

(74) Wesselbaum, S.; vom Stein, T.; Klankermayer, J.; Leitner, W. Hydrogenation of Carbon Dioxide to Methanol by Using a Homogeneous Ruthenium–Phosphine Catalyst. *Angew. Chemie Int. Ed.* **2012**, 51 (30), 7499–7502.

(75) Wesselbaum, S.; Moha, V.; Meuresch, M.; Brosinski, S.; Thenert, K. M.; Kothe, J.; Stein, T. vom; Englert, U.; Hölscher, M.; Klankermayer, J.; Leitner, W. Hydrogenation of Carbon Dioxide to Methanol Using a Homogeneous Ruthenium–Triphos Catalyst: From Mechanistic Investigations to Multiphase Catalysis. *Chem. Sci.* **2015**, *6* (1), 693–704.

(76) Kothandaraman, J.; Goeppert, A.; Czaun, M.; Olah, G. A.; Prakash, G. K. S. Conversion of CO_2 from Air into Methanol Using a Polyamine and a Homogeneous Ruthenium Catalyst. *J. Am. Chem. Soc.* **2016**, *138* (3), 778–781.

(77) Schneidewind, J.; Adam, R.; Baumann, W.; Jackstell, R.; Beller, M. Low-Temperature Hydrogenation of Carbon Dioxide to Methanol with a Homogeneous Cobalt Catalyst. *Angew. Chemie Int. Ed.* **2017**, *56* (7), 1890–1893.

(78) Ribeiro, A. P. C.; Martins, L. M. D. R. S.; Pombeiro, A. J. L. Carbon Dioxide-to-Methanol Single-Pot Conversion Using a C-Scorpionate Iron(Ii) Catalyst. *Green Chem.* **2017**, *19* (20), 4811–4815.

(79) Kar, S.; Goeppert, A.; Kothandaraman, J.; Prakash, G. K. S. Manganese-Catalyzed Sequential Hydrogenation of CO_2 to Methanol via Formamide. *ACS Catal.* **2017**, *7* (9), 6347–6351.

(80) Everett, M.; Wass, D. F. Highly Productive CO_2 Hydrogenation to Methanol – a Tandem Catalytic Approach via Amide Intermediates. *Chem. Commun.* **2017**, *53* (68), 9502–9504.

(81) Kar, S.; Sen, R.; Goeppert, A.; Prakash, G. K. S. Integrative CO_2 Capture and Hydrogenation to Methanol with Reusable Catalyst and Amine: Toward a Carbon Neutral Methanol Economy. *J. Am. Chem. Soc.* **2018**, *140* (5), 1580–1583.

(82) Scharnagl, F. K.; Hertrich, M. F.; Neitzel, G.; Jackstell, R.; Beller, M. Homogeneous Catalytic Hydrogenation of CO_2 to Methanol – Improvements with Tailored Ligands. Adv. Synth. Catal. **2019**, *361* (2), 374–379.

(83) Reller, C.; Pöge, M.; Lißner, A.; Mertens, F. O. R. L. Methanol from CO_2 by Organo-Cocatalysis: CO_2 Capture and Hydrogenation in One Process Step. *Environ. Sci. Technol.* **2014**, *48* (24), 14799–14804.

(84) Chen, Y.; Choi, S.; Thompson, L. T. Low-Temperature CO_2 Hydrogenation to Liquid Products via a Heterogeneous Cascade Catalytic System. *ACS Catal.* **2015**, *5* (3), 1717–1725.

(85) Zhang, W.; Wang, L.; Liu, H.; Hao, Y.; Li, H.; Khan, M. U.; Zeng, J. Integration of Quantum Confinement and Alloy Effect to Modulate Electronic Properties of RhW Nanocrystals for Improved Catalytic Performance toward CO_2 Hydrogenation. *Nano Lett.* **2017**, *17* (2), 788–793.

(86) Bai, S.; Shao, Q.; Feng, Y.; Bu, L.; Huang, X. Highly Efficient Carbon Dioxide Hydrogenation to Methanol Catalyzed by Zigzag Platinum–Cobalt Nanowires. *Small* **2017**, *13* (22), 1604311.

(87) Li, H.; Wang, L.; Dai, Y.; Pu, Z.; Lao, Z.; Chen, Y.; Wang, M.; Zheng, X.; Zhu, J.; Zhang, W.; Si, R.; Ma, C.; Zeng, J. Synergetic Interaction between Neighbouring Platinum Monomers in CO_2 Hydrogenation. *Nat. Nanotechnol*. **2018**, *13* (5), 411–417.

(88) Zheng, X.; Lin, Y.; Pan, H.; Wu, L.; Zhang, W.; Cao, L.; Zhang, J.; Zheng, L.; Yao, T. Grain Boundaries Modulating Active Sites in RhCo Porous Nanospheres for Efficient CO_2 Hydrogenation. *Nano Res.* **2018**, *11* (5), 2357–2365.

(89) Kothandaraman, J.; Dagle, R. A.; Dagle, V. L.; Davidson, S. D.; Walter, E. D.; Burton, S. D.; Hoyt, D. W.; Heldebrant, D. J. Condensed-Phase Low Temperature Heterogeneous Hydrogenation of CO_2 to Methanol. *Catal. Sci.* Technol. **2018**, *8* (19), 5098–5103.

(90) Chen, F.; Liang, J.; Wang, F.; Guo, X.; Gao, W.; Kugue, Y.; He, Y.; Yang, G.; Reubroycharoen, P.; Vitidsant, T.; Tsubaki, N. Improved Catalytic Activity and Stability of Cu/ZnO Catalyst by Boron Oxide Modification for Low-Temperature Methanol Synthesis. *Chem. Eng. J.* **2023**, *458*, 141401.

(91) Zhou, S.; Ma, W.; Anjum, U.; Kosari, M.; Xi, S.; Kozlov, S. M.; Zeng, H. C. Strained Few-Layer MoS_2 with Atomic Copper and Selectively Exposed in-Plane Sulfur Vacancies for CO_2 Hydrogenation to Methanol. *Nat. Commun.* **2023**, *14* (1), 5872.

(92) Zhou, Y.; Liu, F.; Geng, S.; Yao, M.; Ma, J.; Cao, J. Tuning the Content of S Vacancies in MoS_2 by Cu Doping for Enhancing Catalytic Hydrogenation of CO_2 to Methanol. Mol. Catal. **2023**, *547*, 113288.

(93) Zhou, S.; Zeng, H. C. Boxlike Assemblages of Few-Layer MoS2 Nanosheets with Edge Blockage for High-Efficiency Hydrogenation of CO_2 to Methanol. *ACS Catal.* **2022**, *12* (16), 9872–9886.

(94) Huang, C.; Zhang, S.; Wang, W.; Zhou, H.; Shao, Z.; Xia, L.; Wang, H.; Sun, Y. Modulation of Electronic Metal-Support Interaction between Cu and ZnO by Er for Effective Low-Temperature CO_2 Hydrogenation to Methanol. *ACS Catal.* **2024**, *14* (3), 1324–1335.

(95) Kunkel, C.; Rüther, F.; Felsen, F.; Pare, C. W. P.; Terzi, A.; Baumgarten, R.; Gioria, E.; Naumann d'Alnoncourt, R.; Scheurer, C.; Rosowski, F.; Reuter, K. Systematic Exploration of a Multi-Promoter Catalyst Composition Space with Limited Experiments: Non-Oxidative Propane Dehydrogenation to Propylene. *ACS Catal*. **2024**, *14* (11), 9008–9017.

(96) Amano, F.; Nakata, M.; Yamamoto, A.; Tanaka, T. Rutile Titanium Dioxide Prepared by Hydrogen Reduction of Degussa P25 for Highly Efficient Photocatalytic Hydrogen Evolution. *Catal. Sci. Technol.* **2016**, *6* (14), 5693–5699.

(97) Esterhuizen, J. A.; Goldsmith, B. R.; Linic, S. Interpretable Machine Learning for Knowledge Generation in Heterogeneous Catalysis. *Nat. Catal.*. **2022**, *5*(3), 175-184.

(98) Yang, Q.; Skrypnik, A.; Matvienko, A.; Lund, H.; Holena, M.; Kondratenko, E. V. Revealing Property-Performance Relationships for Efficient CO_2 Hydrogenation to Higher Hydrocarbons over Fe-Based Catalysts: Statistical Analysis of Literature Data and Its Experimental Validation. *Appl. Catal. B Environ.* **2021**, *282*, 119554.

(99) Yang, W.; Abdelfatah, K. E.; Kundu, S. K.; Rajbanshi, B.; Terejanu, G. A.; Heyden, A. Machine Learning Accelerated First-Principles Study of the Hydrodeoxygenation of Propanoic Acid. *ACS Catal*. **2024**, *14* (13), 10148–10163.

(100) Lundberg, S. M.; Lee, S. I. A Unified Approach to Interpreting Model Predictions. In Advances in Neural Information Processing Systems. *Adv. Neural Inform. Process. Syst.* **2019**, 32.

(101) Lundberg, S. M.; Nair, B.; Vavilala, M. S.; Horibe, M.; Eisses, M. J.; Adams, T.; Liston, D. E.; Low, D. K.-W.; Newman, S.-F.; Kim, J.; Lee, S.-I. Explainable Machine-Learning Predictions for the Prevention of Hypoxaemia during Surgery. *Nat. Biomed. Eng.* **2018**, *2* (10), 749–760.

(102) Lundberg, S. M.; Erion, G.; Chen, H.; DeGrave, A.; Prutkin, J. M.; Nair, B.; Katz, R.; Himmelfarb, J.; Bansal, N.; Lee, S. I. From Local Explanations to Global Understanding with Explainable AI for Trees. *Nat. Mach. Intell.* **2020**, *2* (1), 56–67.

(103) Praveen, C. S.; Comas-Vives, A. Design of an Accurate Machine Learning Algorithm to Predict the Binding Energies of Several Adsorbates on Multiple Sites of Metal Surfaces. *ChemCatChem* **2020**, *12* (18), 4611–4617.

(104) van Deelen, T. W.; Hernández Mejía, C.; de Jong, K. P. Control of Metal-Support Interactions in Heterogeneous Catalysts to Enhance Activity and Selectivity. *Nat. Catal.* **2019**, *2* (11), 955–970.

(105) Ge, H.; Kuwahara, Y.; Yamashita, H. Development of Defective Molybdenum Oxides for Photocatalysis, Thermal Catalysis, and Photothermal Catalysis. *Chem. Commun.* **2022**, *58* (61), 8466–8479.

(106) Bouchmella, K.; Stoyanova, M.; Rodemerck, U.; Debecker, D. P.; Hubert Mutin, P. Avoiding Rhenium Loss in Non-Hydrolytic Synthesis of Highly Active Re–Si–Al Olefin Metathesis *Catalysts. Catal. Commun.* **2015**, *58*, 183–186.

(107) Toyao, T.; Ting, K. W.; Siddiki, S. M. A. H.; Touchy, A. S.; Onodera, W.; Maeno, Z.; Ariga-Miwa, H.; Kanda, Y.; Asakura, K.; Shimizu, K. ichi. Mechanistic Study of the Selective Hydrogenation of Carboxylic Acid Derivatives over Supported Rhenium Catalysts. *Catal. Sci. Technol*. **2019**, *9* (19), 5413–5424.

(108) Sreenithya, A.; Kolganov, A. A.; Yeu, I. W.; Risansyauqi, M. H.; Pidko, E. A. Oxidation State of Single-Atom Re/TiO_2 Hydrogenation Catalysts: A Computational Study. *ACS Catal.* **2024**, *14* (24), 18488–18498.

(109) Lwin, S.; Wachs, I. E. Reaction Mechanism and Kinetics of Olefin Metathesis by Supported ReO_x/Al_2O_3 Catalysts. *ACS Catal.* **2016**, *6* (1), 272–278.

(110) Li, G.; Meeprasert, J.; Wang, J.; Li, C.; Pidko, E. A. CO_2 Hydrogenation to Methanol over Cd_4/TiO_2 Catalyst: Insight into Multifunctional Interface. *ChemCatChem* **2022**, *14* (5), e202101646.

(111) Zhong, J.; Yang, X.; Wu, Z.; Liang, B.; Huang, Y.; Zhang, T. State of the Art and Perspectives in Heterogeneous Catalysis of CO_2 Hydrogenation to Methanol. *Chem. Soc. Rev.* **2020**, *49* (5), 1385–1413.

(112) Ra, E. C.; Kim, K. Y.; Kim, E. H.; Lee, H.; An, K.; Lee, J. S. Recycling Carbon Dioxide through Catalytic Hydrogenation: Recent Key Developments and Perspectives. *ACS Catal*. **2020**, *10* (19), 11318–11345.

(113) Kattel, S.; Yan, B.; Yang, Y.; Chen, J. G.; Liu, P. Optimizing Binding Energies of Key Intermediates for CO_2 Hydrogenation to Methanol over Oxide-Supported Copper. *J. Am. Chem. Soc.* **2016**, *138* (38), 12440–12450.

(114) Murugappan, K.; Anderson, E. M.; Teschner, D.; Jones, T. E.; Skorupska, K.; Román-Leshkov, Y. Operando NAP-XPS Unveils Differences in MoO_3 and Mo_2C during Hydrodeoxygenation. *Nat. Catal.* **2018**, *1* (12), 960–967.

Chapter 3

Nb-promoted $Pt/MoO_x/TiO_2$ catalysts for low-temperature CO_2 hydrogenation to methanol

3.1 Introduction

The increasing global focus on sustainable energy and chemical production has intensified research efforts toward utilizing renewable carbon sources, driven by the rapid depletion of fossil fuel reserves and escalating environmental consequences of greenhouse gas emissions.[1,2] Among various carbonaceous feedstocks, carbon dioxide (CO_2) is recognized as a viable C_1 platform molecule for the synthesis of value-added chemicals and alternative fuels despite its status as a major greenhouse gas.[3–5] In particular, methanol has emerged as a key target product because of its dual role as a fundamental chemical precursor and potential energy carrier.[6–9]

The catalytic hydrogenation of CO_2 to methanol holds strategic significance for carbon utilization and contributes to the development of a methanol-centered circular economy.[10] Industrial implementation of this reaction is typically achieved using copper-based catalysts under relatively harsh operating conditions (5–10 MPa, >220 °C).[11,12] Although this process is technologically mature, it suffers from limited equilibrium conversion, necessitating extensive recycling of unreacted reactants after product separation. From a process optimization standpoint, synthesizing methanol at lower temperatures is highly attractive, offering theoretical advantages, such as increased equilibrium yield and decreased energy consumption. Nevertheless, efficient methanol production at temperatures below 200 °C remains a formidable challenge, primarily because of the intrinsic inertness of CO_2.[13–15] Although methanol synthesis is thermodynamically favorable and exothermic, the activation energy required for it to proceed under mild conditions is high, rendering the activity of available catalysts insufficient.[13–25] Consequently, the development of highly active catalytic systems capable of promoting CO_2 hydrogenation to methanol under low-temperature conditions is crucial.

To date, the majority of research on CO_2 hydrogenation to methanol has been conducted within the temperature range of 220–300 °C employing well-established catalysts including those based on Cu,[12,26–36] Pd,[37–42] and metal oxides such as In_2O_3 and ZrO_2-based solid solutions.[43–56] While these systems exhibit excellent performances at elevated temperatures, their activity diminishes markedly under milder reaction conditions ($T < 200$ °C).[20,22,57] Recent studies have explored nanostructured catalyst systems with enhanced low-temperature performances.[13–25] Several catalyst design strategies have been proposed for improving activity in this

regime. For example, charge-transfer-induced electron accumulation on Pt in Pt_3Co octapods has been shown to enhance methanol formation at 150 °C.[58] Similarly, the negatively charged Rh species in $Rh_{75}W_{25}$ nanosheets has been shown to facilitate CO_2 adsorption and activation.[59] Enhanced metal-support interactions in the Er-doped CuZnO catalysts arising from reduced ZnO particle significantly improved methanol production.[19] Additionally, the introduction of sulfur vacancies in MoS_2-based systems was found to be critical for enhancing catalytic performance.[18,19,21,23–25] Although these findings represent significant progress, the realization of highly active methanol synthesis catalysts that are efficient at low temperatures remains elusive as it is often hindered by complex synthetic procedures and poor catalytic activity. This underscores the urgent need for the rational design of heterogeneous catalysts that can be readily synthesized and are capable of efficiently converting CO_2 to methanol under mild conditions, preferably below 200 °C.

In our previous study, we demonstrated that a Pt(3)/MoO_x(30)/TiO_2 catalyst exhibited notable activity and selectivity for low-temperature CO_2 hydrogenation to methanol in batch reactions.[60] Furthermore, we employed a machine learning (ML) approach and developed a highly active multi-elemental Pt(5)/Mo(8)-Re(1)-W(0.7)/TiO_2 catalyst for low-temperature methanol production in batch reactions.[61] The study, combining ML and experimental approaches, revealed the importance of additional additive oxides in order to promote methanol formation through the experimental testing of 580 catalysts. In particular, the addition of elements such as Nb, Yb, V, and Zr was found to be effective. However, the development of efficient catalyst systems for high methanol productivity in flow systems, as well as a systematic investigation of the promotional effects of these additives, is essential for practical application.

In this study, we investigated a series of additive oxides for enhancing the performance of the Pt/MoO_x/TiO_2 system, whereby a series of Pt(5)/Mo(10)-M(X)/TiO_2 catalysts (M = Nb, V, La, Sm, Zr, and Yb; X = loading of M in wt%) were tested. These additive elements were selected based on their appearance in highly active catalysts as shown in the violin-plot for each additive oxide component tested in our previous study using the ML approach (**Figure 3.1**).[61] Moreover, the oxides of these selected elements show a range of acid-base and redox properties, which can influence the key steps in methanol production from CO_2 hydrogenation. Among the

catalysts tested, the Nb-promoted Pt(5)/Mo(10)-Nb(1)/TiO_2 catalysts exhibited the best performance in facilitating methanol synthesis under mild reaction conditions. The catalyst showed much higher methanol productivity and better stability than the commercial Cu-ZnO/Al_2O_3 catalyst. *In situ* and *operando* spectroscopic analyses revealed that Pt predominantly facilitated H_2 dissociation, while partially reduced MoO_x species contributed to oxygenate formation. Notably, the incorporation of highly dispersed Nb species enhanced the desorption of methanol and suppressed its decomposition. Moreover, Nb helped in the mitigation of CO poisoning of Pt by making it more electron deficient via the electronic charge transfer process.

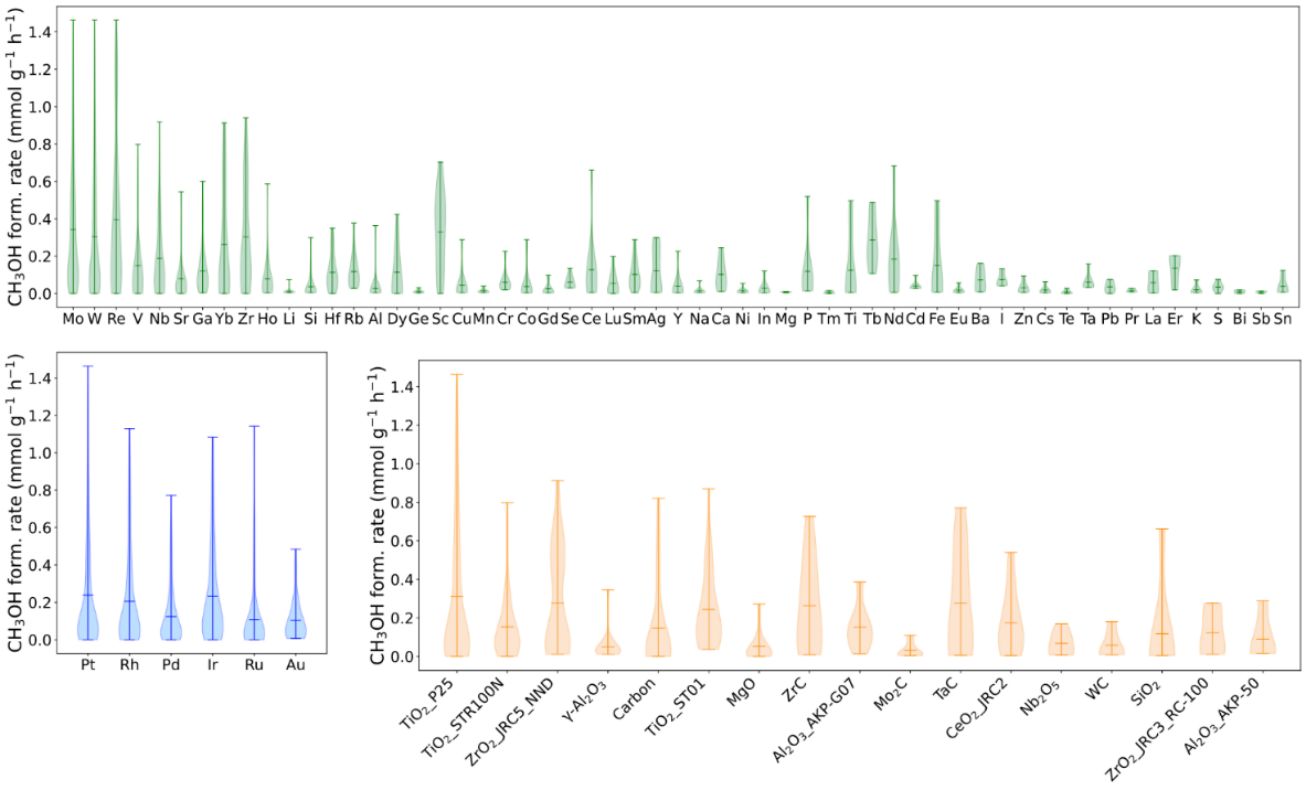

Figure 3.1. Visualization of methanol formation catalyst datasets. Violin-plot for each additive oxide component. The violin represents the interquartile range, spanning from the first quartile to the third quartile, with a horizontal line indicating the median. Whiskers extend up to 1.5 times the interquartile range, encompassing the largest and smallest observed data points falling within this range. Individual data points are displayed as dots.

3.2 Materials and methods

3.2.1 Materials and catalyst preparation

All chemicals and materials were obtained from commercial suppliers and used as received, without further purification (**Tables 3.1** and **3.2**). Pt(5)/Mo(10)-M(X)/TiO_2 catalysts (values in parentheses indicate wt% of the corresponding element) were synthesized via a successive wet impregnation method. In the first step, appropriate amounts of ammonium heptamolybdate ($(NH_4)_6Mo_7O_{24}\cdot 4H_2O$) and precursor of the additive oxide were dissolved in 30 mL of deionized water in a 100 mL glass vessel. The required amount of TiO_2 was added to the solution, and the resulting suspension was stirred at room temperature for 30 min. The mixture was subsequently evaporated to dryness at 50 °C under reduced pressure, dried at 110 °C for 12 h, and calcined in static air at 500 °C for 3 h. Mo loading was kept at 10 wt%.

In the second step, the Mo(10)-M(X)/TiO_2 material was impregnated with an aqueous solution of the Pt precursor to achieve a nominal Pt loading of 5 wt%. The slurry was evaporated to dryness at 50 °C under reduced pressure and dried at 110 °C for 12 h in static air to yield the unreduced Pt(5)/Mo(10)-M(X)/TiO_2 catalyst.

Table 3.1. The purity and source of the chemicals used in this research.

Chemical name	Purity	Source (Company name)
Ammonium metavanadate	>99%	Wako Chemical
Zirconyl Nitrate Dihydrate	>99%	Mitsuwa Chemical
Niobium pentaethoxide	N/A	Mitsuwa Chemical
Ammonium Molybdate Tetrahydrate	>99%	Wako Chemical
Samarium Nitrate Hexahydrate	99.5%	Mitsuwa Chemical
Ytterbium(III) Nitrate n-Hydrate	99.9%	Wako Chemical
Diamminedinitritoplatinum(II)	Pt content=4.6wt%(50g/L)	Furuya Metal

Table 3.2. Sources of the supports used.

Support name	Source (Company name)
γ-Al_2O_3	Sasol
TiO_2	Evonik (formerly Degussa)
SiO_2	Fuji Silysia Chemical
ZrO_2	Daiichi Kigenso Kagaku Kogyo
CeO_2	Daiichi Kigenso Kagaku Kogyo
MgO	Ube Material Industries

3.2.2 Catalyst characterization

X-ray diffraction (XRD) analysis was conducted using a Rigaku Miniflex diffractometer equipped with Cu Kα radiation. High-angle annular dark-field scanning transmission electron microscopy (HAADF-STEM) and energy-dispersive X-ray spectroscopy (EDX) were performed using an FEI Titan G2 microscope. The samples were prepared by drop-casting an ethanolic suspension of the catalyst onto carbon-coated copper grids.

X-ray absorption spectroscopy (XAS) measurements for the Pt L_3-edge, Mo K-edge, and Nb K-edge were performed in transmission mode at beamline BL01B1 of SPring-8, Japan Synchrotron Radiation Research Institute (JASRI) (Proposal No. 2024B1749), using a Si(311) double-crystal monochromator. For measurements involving less than 20 mg of catalyst, the sample was diluted with boron nitride (BN) for pellet preparation. The reference spectra of the standard compounds were collected at room temperature in air. The acquired XAS data were analyzed using the Athena and Artemis software (version 0.9.26) within the Demeter package.

For *in situ* XAS analysis, pelletized samples (φ: 7 mm) were placed in an *in situ* cell fitted with Kapton film windows. Sample pretreatment involved reduction under flowing H_2 (300 mL/min) at 300 °C for 30 minutes. The reaction gases were then sequentially introduced into the cell: 25% CO_2/He (400 mL/min), 75% H_2/He (400 mL/min), and repetitively interspersed with He purges between each gas exposure.

Hydrogen temperature-programmed reduction (H_2-TPR) measurements were performed using a BELCat II instrument equipped with a thermal conductivity detector (TCD). Approximately 100 mg of catalyst was loaded into a quartz tube, pretreated in flowing Ar at

200 °C for 2 hours to eliminate physisorbed water and surface carbonates, and cooled to 50 °C. TPR analysis was conducted by heating the sample to 800 °C at a rate of 10 °C/min under a gas mixture of 10 vol% H_2 in Ar.

Ambient pressure X-ray photoelectron spectroscopy (AP-XPS) was performed at beamline 13B of the Photon Factory (PF), High Energy Accelerator Research Organization (KEK). The powdered catalysts were coated onto an Au substrate. The incident X-ray energy was 632 eV. The sample temperature was monitored using a thermocouple in direct contact with the sample holder within the analysis chamber. H_2 and CO_2 were introduced into the chamber using variable leak valves. The catalyst was alternately exposed to H_2 and CO_2 at 0.1 Torr and 150 °C for 30 minutes per cycle. Subsequent alternating gas pulses were also applied. Binding energy calibration was referenced to Ti $2p_{3/2}$ in TiO_2 at 458.5 eV. The Mo 3d and Nb 3d spectra were deconvoluted using a combination of Gaussian and Lorentzian functions with a Shirley-type background. The signal intensities were normalized against the Ti $2p_{3/2}$ peak to correct the attenuation effects due to gas-phase interactions.

In situ/*operando* diffuse reflectance infrared Fourier transform spectroscopy (DRIFTS) measurements were conducted using a JASCO FT/IR-4600 instrument equipped with a mercury-cadmium-telluride detector. The catalyst powder was pressed into a DRIFTS cell (DR-650 Ci) using a CaF_2 window. Spectra were collected by averaging 20 scans at a resolution of 8 cm^{-1} under 0.5 MPa and 150 °C. The background spectrum recorded under He flow (20 scans) at the measurement temperature was subtracted from each DRIFTS spectrum. The effluent gas stream was analyzed using a high-sampling-rate TCD micro gas chromatograph (490 Micro GC, Agilent Technologies Inc.) connected to the reactor outlet. For NH_3-DRIFTS experiment, spectra were recorded at 50 °C after flowing 10% NH_3/He (20 mL min^{-1}) for 5 minutes followed by He (20 mL min^{-1}) for 10 min. Prior to the experiments, catalysts were pretreated at 300 °C under H_2 (20 mL min^{-1}) for 30 minutes followed by He (20 mL min^{-1}) for 30 minutes.

3.2.3 Catalytic reactions

Catalytic CO_2 hydrogenation reactions were carried out in a fixed-bed continuous-flow reactor system at a total pressure of 4 MPa. The feed gases were supplied from H_2/Ar (99:1) and CO_2 cylinders, with Ar serving as the internal standard. In a typical procedure, 300 mg of the catalyst was loaded between quartz wool plugs within a 1/4-inch stainless steel tubular reactor (inner diameter: 3.79 mm). Prior to reaction, the catalyst was pretreated under H_2/Ar

flow (20 mL min^{-1}) at 300 °C for 30 minutes at ambient pressure. Following pretreatment, a reaction gas mixture consisting of H_2/CO_2/Ar in a molar ratio of 74.4:24.8:0.8 was introduced at a total flow rate of 40 mL min^{-1} under 4 MPa. This corresponds to a gas hourly space velocity (GHSV) of 8000 mL g_{cat}^{-1} h^{-1}. Before catalytic evaluation at 150 °C, an accelerated aging treatment was conducted by maintaining the catalyst under reaction conditions at 210 °C for 12 h. The product analysis was performed using an online gas chromatograph (Shimadzu GC-2014) equipped with both a Shincarbon-ST column coupled with a TCD, and a Porapak Q column combined with a flame ionization detector (FID). A commercial $Cu/ZnO/Al_2O_3$ catalyst (Alfa Aesar; 64.2 wt% CuO) was used for comparison.

The CO_2 conversion (X_{CO_2}) and selectivity (S_i) of individual products were calculated using equations (1) and (2), respectively:

$$X_{CO_2} = \frac{\frac{C_{CO_2}^{in}}{C_{Ar}^{in}} - \frac{C_{CO_2}^{out}}{C_{Ar}^{out}}}{\frac{C_{CO_2}^{in}}{C_{Ar}^{in}}} \times 100\% \quad (1)$$

$$S_i = \frac{C_i \times n_i}{\sum(C_i \times n_i)} \times 100\% \quad (2)$$

where C_i is the molar fraction of product *i* (CO, hydrocarbons, or oxygenates), and n_i is the carbon number of product *i* in the reaction.

3.2.4 Methanol decomposition

Methanol decomposition experiments were performed in a batch reactor using the reduced catalyst. A 100 mg sample of catalyst was loaded into a quartz tube and pre-reduced in hydrogen at 300 °C for 30 minutes. After reduction, methanol (5 mmol) was added to the quartz tube, which was then sealed inside the batch reactor. Decomposition experiments were performed at 150 °C under a nitrogen atmosphere (0.5 MPa) for 1 h. The products were analyzed using GC comprising a Shincarbon-ST column coupled to a TCD, and a PoraBond Q column coupled with an FID.

3.3 Results and discussion

3.3.1 Catalytic performance

Catalytic CO_2 hydrogenation reactions were carried out at 150 °C, 4 MPa, 8000 mL h^{-1} g_{cat}^{-1}, and H_2 : CO_2 = 3 : 1. **Figures 3.2a and 3.3** show a comparative analysis of the catalytic performance between Pt(5)/Mo(10)/TiO_2 and Pt(5)/Mo(10)-M(X)/TiO_2 catalysts (M = Nb, V, La, Sm, Zr, and Yb). The unpromoted Pt(5)/Mo(10)/TiO_2 catalyst exhibited a methanol formation rate of 0.94 mmol g_{cat}^{-1} h^{-1}. Among the additives, Yb and Zr addition resulted in a lower methanol formation rate compared to that of the unpromoted catalyst. The Yb- and Zr-promoted catalysts mainly produced CO with high selectivity (>80%). The V, Sm, and La-promoted catalysts displayed a slightly improved methanol formation rate and selectivity. Among the catalysts, the Nb-promoted catalysts (Pt(5)/Mo(10)-Nb(X)/TiO_2) demonstrated the best performance for methanol production (**Figures 3.2a and 3.3**). In terms of the Nb loading, lower Nb loadings (X = 0.2 – 1.5 wt%) were found to be more effective in promoting methanol synthesis (**Figure 3.3a**). The catalyst with 1.0 wt% Nb, Pt(5)/Mo(10)-Nb(1.0)/TiO_2, displayed the highest activity, achieving a methanol formation rate of 2.1 mmol g_{cat}^{-1} h^{-1}. To elucidate the effect of each component in the optimized Pt(5)/Mo(10)-Nb(1.0)/TiO_2 catalyst, individual elements were systematically omitted, and the resulting catalytic activities were evaluated (**Figure 3.2b**). The removal of any single-component element led to a significant decrease in the methanol formation rate, highlighting the synergistic effect and essential coexistence of Pt, Mo, and Nb for achieving high catalytic performance. Furthermore, the influence of the catalyst support was investigated (**Figure 3.4**). Various supports, including SiO_2, γ-Al_2O_3, CeO_2, ZrO_2, and MgO, were tested in place of TiO_2. Among these, TiO_2 was identified as the most effective support for methanol synthesis, whereas catalysts comprising the other supports predominantly yielded CO as the main product.

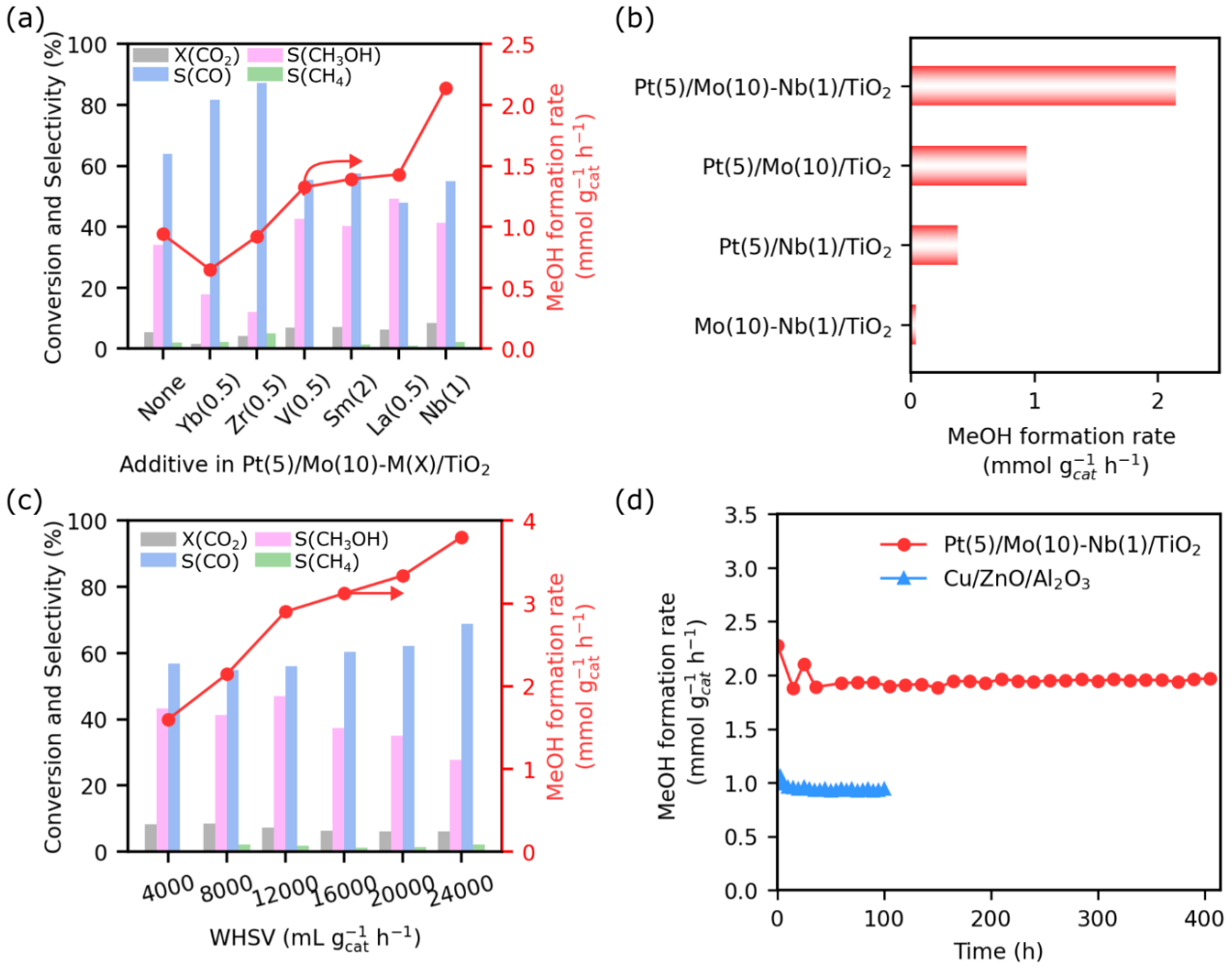

Figure 3.2. (a) Catalytic CO_2 hydrogenation activity of Pt(5)/Mo(10)/TiO_2 and Pt(5)/Mo(10)-M(X)/TiO_2 (M = Yb, Zr, V, Sm, La, and Nb) catalysts (X represents the wt% of the additives). (b) Comparison of methanol formation rate over Pt(5)/Mo(10)-Nb(1)/TiO_2 and the control catalysts prepared by omitting one element at one time. (c) Effect of GHSV on catalytic activity of Pt(5)/Mo(10)-Nb(1)/TiO_2 catalyst. (d) Stability test of Pt(5)/Mo(10)-Nb(1)/TiO_2 and Cu/ZnO/Al_2O_3 catalysts in the CO_2 hydrogenation reaction. Pretreatment: 300 °C under H_2 flow (20 mL min^{-1}) for 0.5 h. Reaction conditions: 300 mg of catalyst,150 °C, 4 MPa, 8,000 mL g_{cat}^{-1} h^{-1}, H_2 : CO_2 = 3 : 1, unless otherwise mentioned.

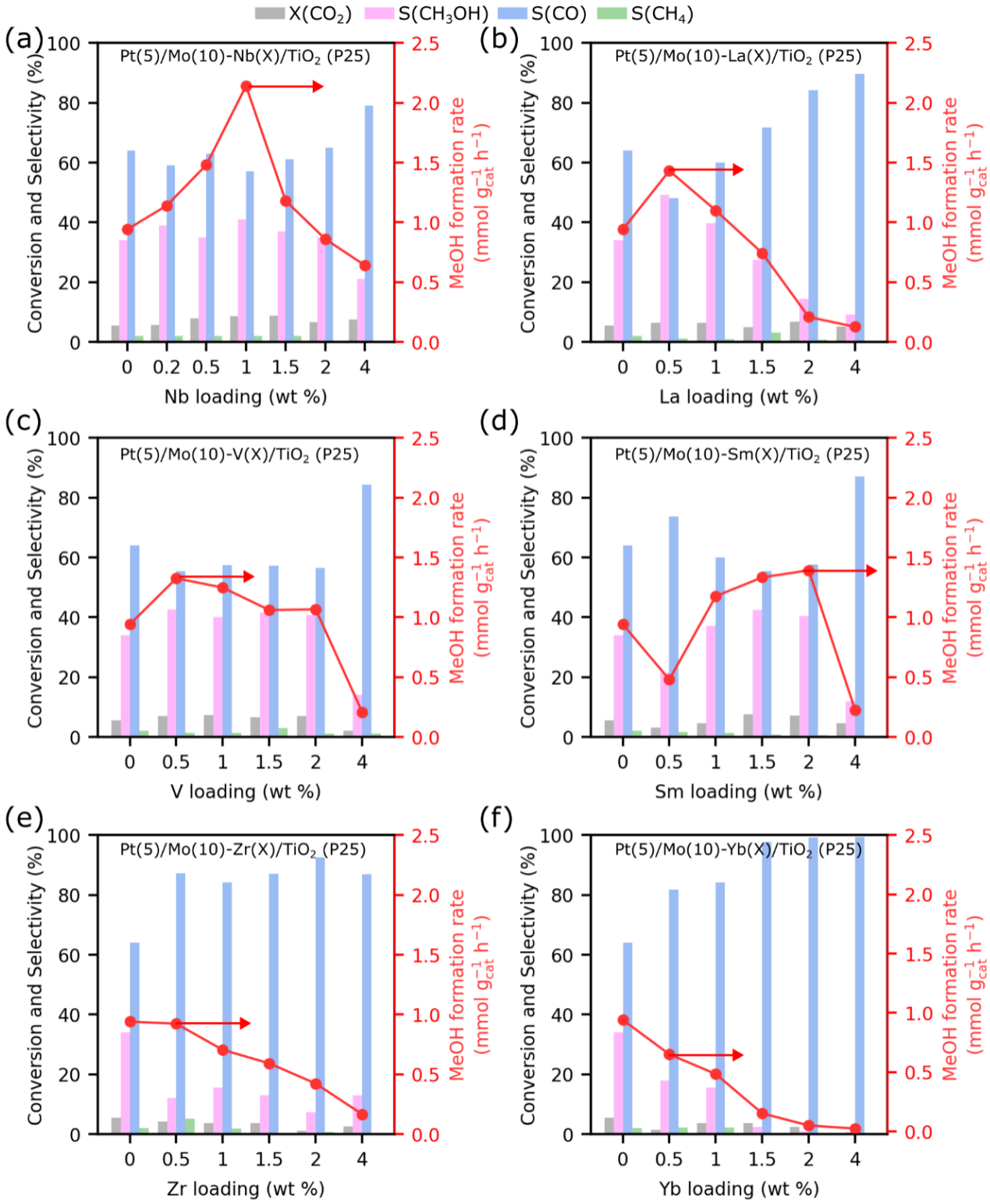

Figure 3.3. Catalytic activity of (a) Pt(5)/Mo(10)-Nb(X)/TiO_2,(b) Pt(5)/Mo(10)-La(X)/TiO_2, (c) Pt(5)/Mo(10)-V(X)/TiO_2, (d) Pt(5)/Mo(10)-Sm(X)/TiO_2, (e) Pt(5)/Mo(10)-Zr(X)/TiO_2, and (f) Pt(5)/Mo(10)-Yb(X)/TiO_2. Pretreatment: at 300 °C under H_2 flow (20 mL min^{-1}) for 0.5 h. Reaction conditions: 300 mg of catalyst,150 °C, 4 MPa, 8,000 mL g_{cat}^{-1} h^{-1}, H_2 : CO_2 = 3 : 1.

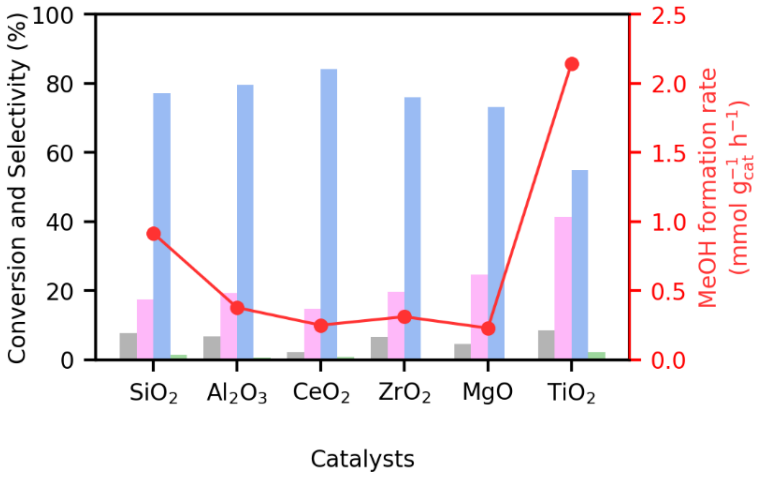

Figure 3.4. Effect of different supports on the hydrogenation of CO_2 catalyzed by P(5)/Mo(10)-Nb(1)/Supp. (Supp. = SiO_2, γ-Al_2O_3, CeO_2, ZrO_2, MgO and TiO_2). Pretreatment: H_2 (20 mL min^{-1}), 300 °C, 0.5 h.

With the optimal catalyst composition in hand (Pt(5)/Mo(10)-Nb(1.0)/TiO_2), the reaction conditions were optimized to further enhance the catalytic performance. A higher reaction temperature led to a higher methanol formation rate, while methanol selectivity remained largely unaffected (**Figure 3.5**). Nevertheless, to evaluate catalyst performance under low-temperature conditions, the standard reaction temperature was set to 150 °C. Additionally, increasing the GHSV from 8000 to 24,000 mL g_{cat}^{-1} h^{-1} increased the methanol formation rate from 2.1 to 3.8 mmol g_{cat}^{-1} h^{-1} (**Figure 3.2c**). A comparison of the performance with those of previously reported catalysts (**Table 3.3**) revealed that the methanol formation rate of the Pt(5)/Mo(10)-Nb(1.0)/TiO_2 system at low temperatures (T ≤ 180 °C) is among the highest. To benchmark our catalyst against a commercial standard, a long-term performance test was conducted to compare Pt(5)/Mo(10)-Nb(1.0)/TiO_2 and a commercial Cu/ZnO/Al_2O_3 catalyst (**Figure 3.2d**). Our catalyst demonstrated superior methanol productivity and maintained stable performance over 400 h of continuous operation.

Table 3.3. Reports on low temperature (T ≤ 180 °C) CO_2 hydrogenation to methanol.

Catalyst	Additive	T (˚C)	P (MPa)	H_2 :CO_2	Space velocity ($mL\ h^{-1}\ g_{cat}^{-1}$)	MeOH formation rate (mmol h^{-1} g_{cat}^{-1})	Reaction System	Selectivity (%)			Reference
								MeOH	CO	CH_4	
Homogeneous catalytic system:											
Ru complex & $Sc(OTf_3)$	MeOH	135	4.0	3:1	-	2.5	Batch	Not shown			S[62]
Ru/Triphos	$HNTf_2$	140	8.0	3:1	-	9.2	Batch	Not shown			S[63]
Ru/Triphos	$HNTf_2$	140	8.0	3:1	-	18.4	Batch	Not shown			S[64]
Ru-Macho-BH	PEHA	145	7.5	9:1	-	6.0	Batch	Not shown			S[65]
Co/Triphos	$HNTf_2$	100	9.0	4.5:1	-	2.1	Batch	Not shown			S[66]
Fe(II)/C-scorpionate	PEHA	80	7.5	3:1	-	95	Batch	Not shown			S[67]
Mn(I)-PNP pincer	K_3PO_4	150	8.0	1:1	-	1.0	Batch	Not shown			S[68]
Ru complex	$^iPr_2NH$, NaOEt	100	4.0	3:1	-	4.5	Batch	Not shown			S[69]
Ru-MACHO-BH	PEHA	145	7.0	-	-	2.9	Batch	Not shown			S[70]
Co/modified triphos	$HNTf_2$	100	9.0	3.5:1	-	5.2	Batch	Not shown			S[71]
Heterogeneous catalytic system:											
$Cu/ZnO-Al_2O_3$	DEEA	100	7.0	6:1	–	0.54	Batch	Not shown			S[72]
$Cu-Cr_2CuO_4$ & Cu/Mo_2C	EtOH	135	4.0	3:1	–	0.023	Batch	77	Not shown		S[73]
Pd/Mo_2C	–	135	4.0	3:1	–	0.0046	Batch	95	3.6	1.6	S[15]
Pt/Co_3O_4	–	140	8.0	3:1	–	0.05	Batch	Not shown			S[74]
Pt_3Co octapods	–	150	3.2	3:1	–	0.18	Batch	Not shown			S[58]
$Rh_{75}W_{25}$ nanosheets	–	150	3.2	3:1	–	0.004	Batch	Not shown			S[59]
Pt_4Co nanowires/Carbon	–	150	3.2	3:1	–	0.19	Batch	Not shown			S[75]
Pt/MoS_2	–	150	3.2	3:1	–	0.05	Batch	81	Not shown		S[76]
RhCo porous nanosphere	–	150	3.2	3:1	–	0.1	Batch	Not shown			S[77]
$Cu/ZnO/Al_2O_3$	NEt_3, EtOH	120	6.0	2:1	–	0.874	Batch	Not shown			S[78]
MoS_2 nanosheets	–	120	5.0	3:1	1500	0.28	Flow	>96	-	-	S[18]
MoS_2 nanosheets	–	180	5.0	3:1	15000	4.06	Flow	96	-	-	S[18]
$PdCuZnZrBa/Al_2O_3$	–	150	3.0	4:1	12000	1.17	Flow	100	0	0	S[79]
B/Cu/ZnO	–	170	7.0	-	1800	1.56	Flow	100	0	0	S[22]
h-PdMo/Mo_2N	–	160	0.1	3:1	30000	0.05	Flow	5.16	93.9	0.94	S[14]
$Cu_{10}Ga_{10}$/SBA-15	–	180	0.5	3:1	15000	0.07	Flow	100	0	0	S[17]
MoS_2-NS	–	140	5.0	3:1	36000	7.81	Flow	＞98	＜1	＜1	S[16]
$Cu/MoS_2@SiO_2$	–	180	5.0	4:1	8000	2.0	Flow	95	-	5	S[23]
5% Cu-MoS_2	–	180	5.0	4:1	12000	1.82	Flow	87	5	8	S[25]
Mo_3S_4@NaZSM-5	–	150	4.0	3:1	1200	0.26	Flow	>99	-	-	S[21]
h-MoS_2/ZnS	–	160	5.0	4:1	6000	0.53	Flow	>99	-	-	S[24]
$Er_{0.2}CuZnO$	–	170	5.0	3:1	1800	1.53	Flow	90	10	-	S[19]
Pt(5)/Mo(10)-Re(1)-W(0.7)/TiO_2	–	150	4.0	3:1	8000	1.8	Flow	44	56	＜1	S[61]
Pt(5)/Mo(10)-Nb(1)/TiO_2		150	4.0	3:1	8000	2.1	Flow	41.3	54.9	2.2	This study

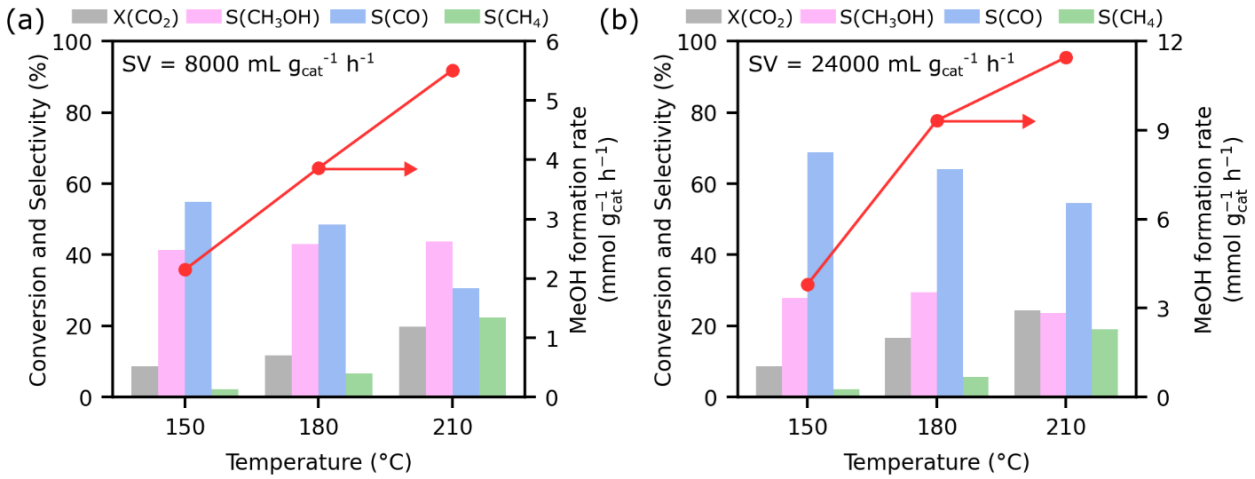

Figure 3.5. Effect of temperature on catalytic activity over Pt(5)/Mo(10)-Nb(1)/TiO_2 at (a) 8000 mL g_{cat}^{-1} h^{-1} and (b) 24000 mL g_{cat}^{-1} h^{-1}. Reaction conditions: catalyst (300 mg), 4 MPa, 8000 (and 24000) mL g_{cat}^{-1} h^{-1}, H_2 : CO_2 = 3 : 1.

3.3.2 Structural characterization

Following the confirmation of the high catalytic performance of the Pt(5)/Mo(10)-Nb(1)/TiO_2 catalyst, a series of characterization techniques were employed to investigate its structural evolution. XRD analysis (**Figure 3.6**) revealed that pristine TiO_2 exhibited diffraction patterns characteristic of both the anatase and rutile phases (corresponding to TiO_2 P25).[65] Upon the incorporation of Mo and Nb species, the Mo(10)-Nb(1.0)/TiO_2 catalyst displayed diffraction peaks corresponding to crystalline MoO_3, while no distinct peaks attributable to the Nb species were detected. Similar XRD features were observed in unreduced Pt(5)/Mo(10)-Nb(1.0)/TiO_2, suggesting that Mo remained in the form of crystalline MoO_3, while the Pt and Nb species were present in a highly dispersed state on the TiO_2 surface. After reduction at 300 °C, the diffraction peaks associated with MoO_3 disappeared, and only those corresponding to TiO_2 remained, indicating the loss of long-range crystallinity of the Mo oxides under reducing conditions. Importantly, even after reduction, no diffraction peaks associated with Pt and Nb species were observed, implying that the Pt and Nb species remained highly dispersed. Similar features were observed for the spent catalyst, as well as across various Nb loadings and supports (**Figure 3.7**), indicating consistent structural behavior.

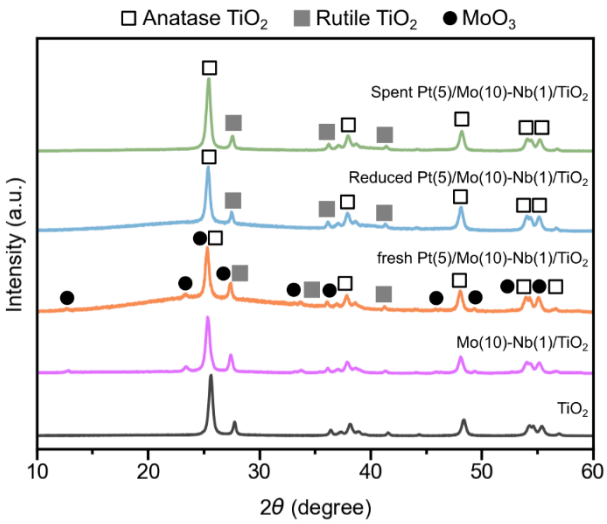

Figure 3.6. XRD patterns of TiO_2 (P25), Mo(10)-Nb(1)/TiO_2, and Pt(5)/Mo(10)-Nb(1)/TiO_2 (fresh, reduced at 300 °C, and spent).

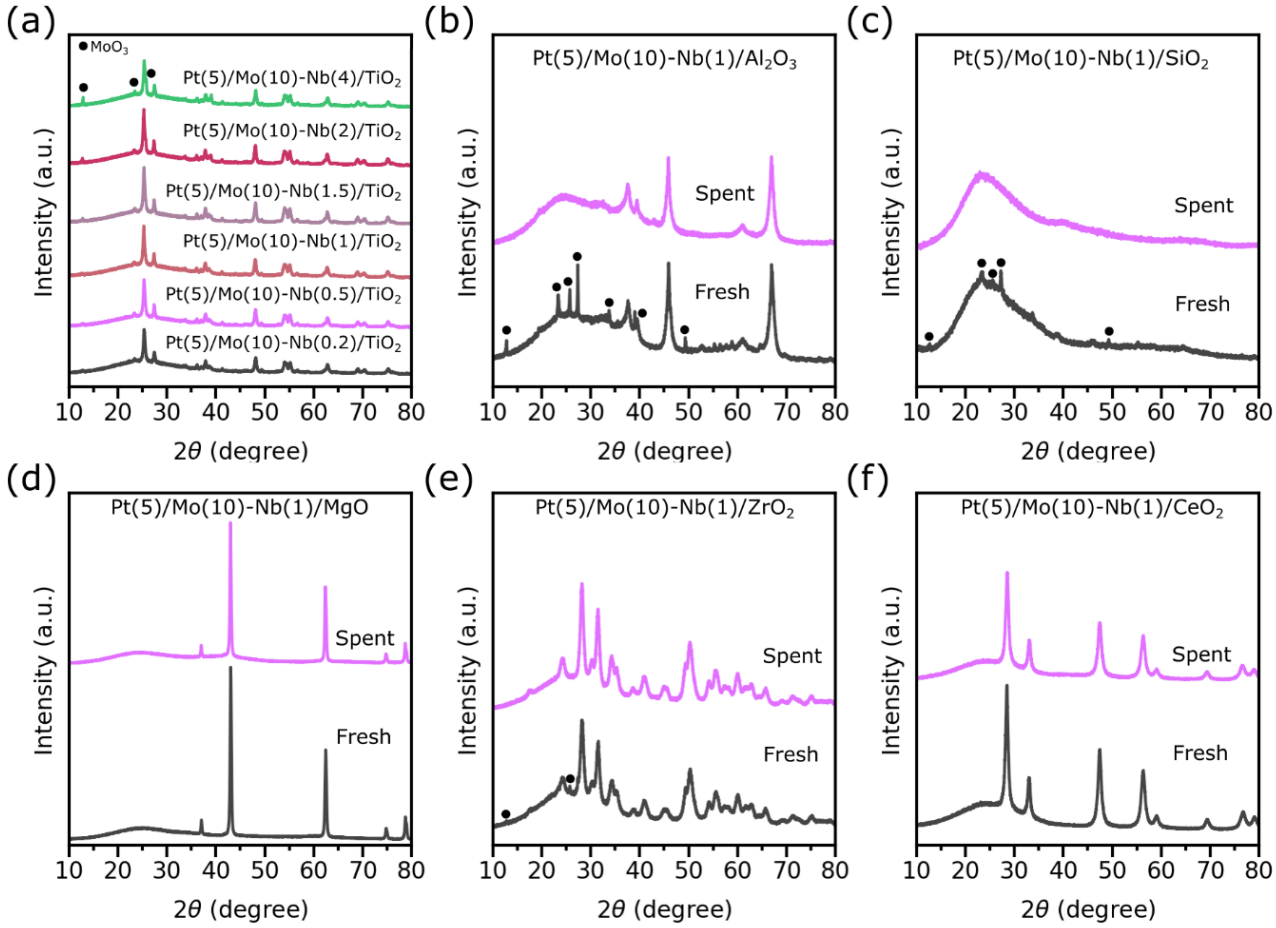

Figure 3.7. XRD patterns of (a) different loading of Nb on Pt(5)/Mo(10)-Nb(X)/TiO_2 (X =0.2, 0.5, 1, 1.5, 2, 4); (b-f) Spent and fresh Pt(5)/Mo(10)-Nb(1)/Support (Support = γ-Al_2O_3, SiO_2, MgO, ZrO_2, CeO_2).

HAADF-STEM was employed to further analyze the structure of the reduced Pt(5)/Mo(10)-Nb(1)/TiO_2 catalyst (**Figure 3.8**). The analysis revealed uniformly dispersed Pt nanoparticles with an average size of 2.0 nm. Notably, no large individual segregated oxide particles of Mo or Nb were detected. EDX mapping confirmed that the bright nanoparticles observed in the HAADF-STEM images corresponded to Pt dispersed over the TiO_2 surface. Furthermore, EDX elemental mapping of Mo and Nb indicated that these species were homogeneously distributed over the TiO_2 support, corroborating the XRD findings for the reduced catalyst.

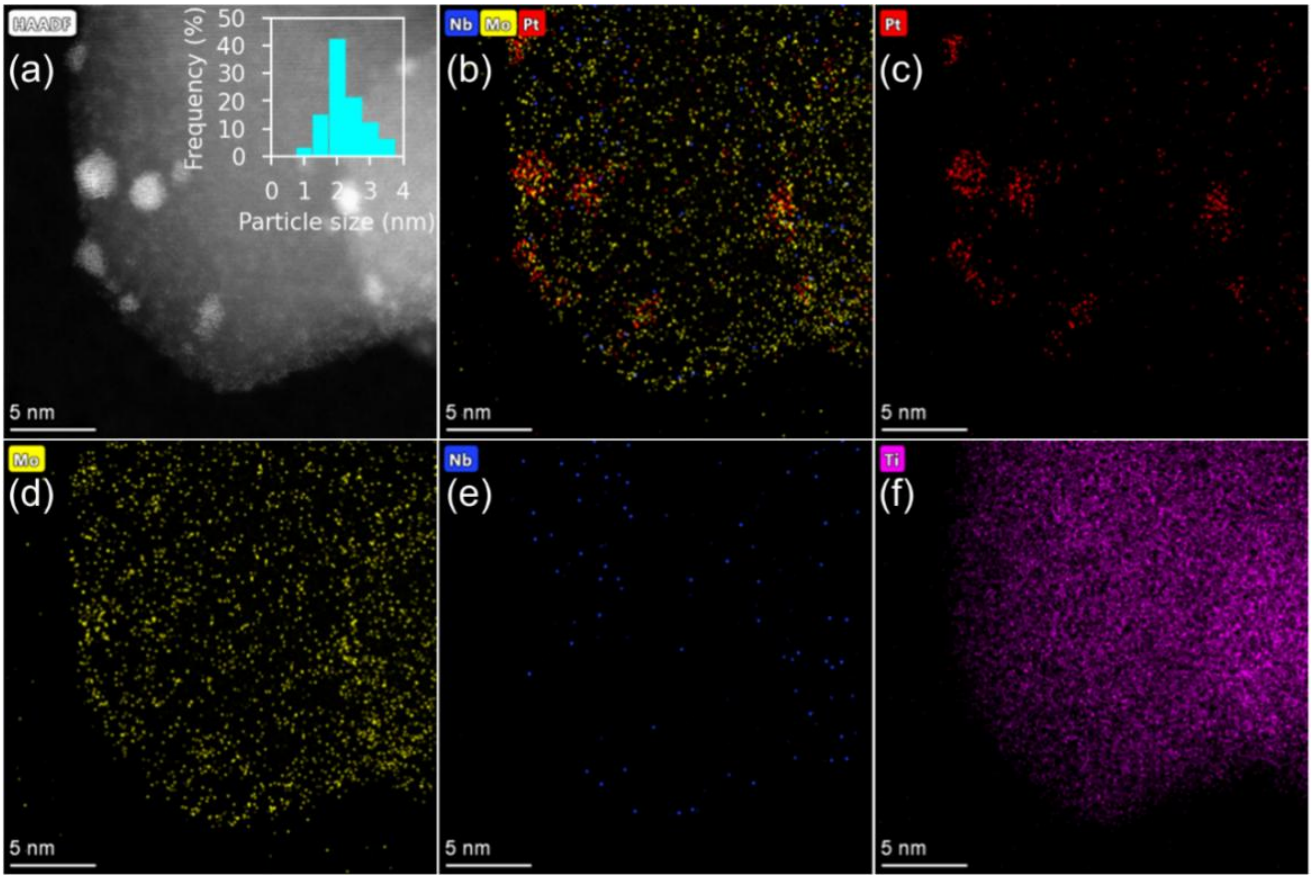

Figure 3.8. HAADF-STEM image and EDX mapping of Pt(5)/Mo(10)-Nb(1)/TiO_2 after reduction at 300 °C. The inset in the HAADF-STEM image shows the particle size distribution of Pt.

XAS analysis was performed to elucidate the chemical states of Pt, Mo, and Nb in the Pt(5)/Mo(10)-Nb(1)/TiO_2 catalyst. **Figure 3.9a** shows the Pt L_3-edge X-ray absorption near-edge structure (XANES) spectra of the catalyst before and after H_2 reduction at 300 °C. The edge position of Pt in the unreduced sample corresponded to that of PtO_2, indicating the presence of PtO_2 species. Upon reduction, the edge position resembled that of metallic Pt foil, confirming the reduction of PtO_2 to metallic Pt.

Figure 3.9b shows the Mo K-edge XANES spectra. Prior to reduction, the spectrum exhibited features characteristic of MoO_3, suggesting that Mo existed predominantly as the MoO_3 species in the unreduced catalyst, which is consistent with the XRD results. Following reduction, the Mo K-edge shifted to an intermediate position between those of MoO_3 and metallic Mo, indicating that the Mo species were partially reduced and existed as highly defective MoO_x species under the reaction conditions.[80–82]

The Nb K-edge XANES spectra (**Figure 3.9c**) revealed that both the unreduced and reduced samples exhibited edge positions similar to that of Nb_2O_5. This suggests that Nb remained in an oxidic state throughout, predominantly as Nb_2O_5. High pre-edge intensity (s → d-p hybridized transition)[83] was observed for the catalyst as compared to that of Nb_2O_5 reference, indicating that Nb is present as a highly distorted structure as compared to Nb_2O_5 mainly because of high dispersion of Nb species on the surface.[84,85] This is corroborated with the XRD and HAADF-STEM analysis. In summary, XAS analysis revealed that, in the unreduced state, Pt, Mo, and Nb were present in fully oxidized forms; following reduction, Pt was converted to its metallic state, while Mo was present as partially reduced MoO_x species, and Nb remained as the Nb_2O_5 species. All Pt, Mo, and Nb species were found to be highly dispersed on the TiO_2 support.

Furthermore, to understand the reduction behavior of the constituent elements, we compared the H_2-TPR profile of the best catalyst with those of control catalysts (**Figure 3.9d**). Among the Pt, Mo, and Nb species, the Pt species were reduced at a much lower temperature (below 100 °C). In the absence of Pt, the reduction features for the Mo and Nb species appeared above 450 and 700 °C, respectively, which are much higher than the reduction temperature during the pretreatment prior to the actual catalytic reaction (300 °C). For the Pt(5)/Nb(1)/TiO_2 control catalyst, the Nb reduction feature appeared at approximately 575 °C, which is likewise considerably higher than the pretreatment temperature, indicating the presence of oxidic Nb species in the reduced Pt(5)/Mo(10)-Nb(1)/TiO_2 catalyst. In contrast, the reduction feature for the Pt(5)/Mo(10)/TiO_2 control catalyst appeared below the pretreatment temperature. The same reduction feature also appeared for the Pt(5)/Mo(10)-Nb(1)/TiO_2 catalyst. Therefore, in the Pt(5)/Mo(10)-Nb(1)/TiO_2 catalyst, Pt facilitated the partial reduction of the Mo species. This is in agreement with the above-mentioned results of the XANES study.

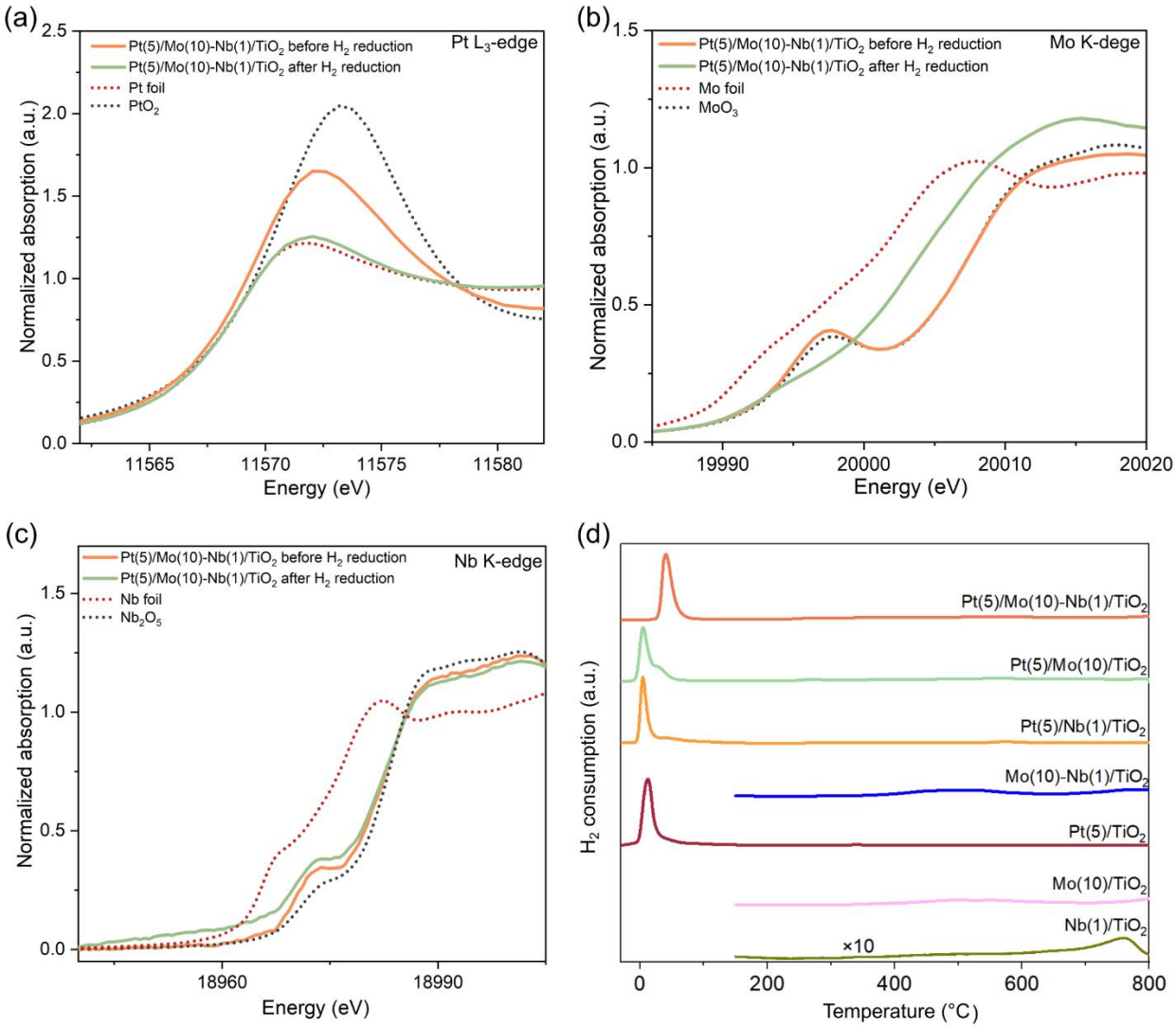

Figure 3.9. (a) Pt L_3-edge (b) Mo K-edge and (c) Nb K-edge XANES spectra of Pt(5)/Mo(10)-Nb(1)/TiO_2 before and after H_2 reduction recorded at room temperature. After reduction treatment at 300 °C, the samples were not exposed to air and were contained in sealed vessels under N_2. (d) H_2-TPR profiles of Pt(5)/Mo(10)-Nb(1)/TiO_2 and other control catalysts.

3.3.3 Investigation of reaction mechanism

Methanol synthesis via CO_2 hydrogenation can proceed via two primary pathways: (i) the formate-mediated pathway, and (ii) the reverse water-gas shift reaction followed by CO hydrogenation.[1,31,86–88] In our previous study, we demonstrated that the Pt/MoO_x/TiO_2 catalyst predominantly followed the formate route for methanol production.[31] Furthermore, the rate of CO hydrogenation to methanol was found to be significantly lower than that of direct CO_2 hydrogenation. In this study, *operando* DRIFTS analysis was employed to identify the surface intermediates involved in the catalytic process over the Pt(5)/Mo(10)-Nb(1)/TiO_2 catalyst

(**Figure 3.10a**). Upon the introduction of CO_2, characteristic IR bands in the 1800–1200 cm^{-1} region corresponding to surface carbonate and formate species appeared immediately, accompanied by bands in the 2100–1950 cm^{-1} range attributed to adsorbed CO. The presence of bands at 1540, 1380, and 1354 cm^{-1}, along with those in the 2800–2980 cm^{-1} region, which were assigned to C-H stretching vibrations (v(CH)), suggest the formation of surface formate species.[87,89–93] Notably, formate was observed even before the addition of H_2, which can be attributed to the presence of surface hydrogen species generated during the H_2 pretreatment step. Formate was identified as the dominant surface intermediate. Upon the subsequent introduction of H_2, the intensity of the formate band at 1540 cm^{-1} initially increased and then decreased, while the emergence of a band at 1110 cm^{-1} indicated the formation of the methoxy species (**Figures 3.10a and 3.10b**).[87,91,92] The evolution of the methoxy peak intensity and amount of methanol as quantified in the reactor effluent by GC closely tracked the formate band intensity, confirming that the formate species are the main intermediate for methanol production (**Figure 3.10b**). To further evaluate the possibility of methanol formation via the CO hydrogenation pathway, *operando* DRIFTS analysis was conducted under CO hydrogenation conditions and the results were compared with those obtained under the CO_2 hydrogenation conditions (**Figure 3.11**). Under the CO hydrogenation conditions, neither formate nor methoxy species were detected, and the methanol yield in the reactor effluent (measured by GC) was negligible relative to that observed for CO_2 hydrogenation. These results indicate that methanol production over the Pt(5)/Mo(10)-Nb(1)/TiO_2 catalyst proceeds predominantly via the formate pathway.

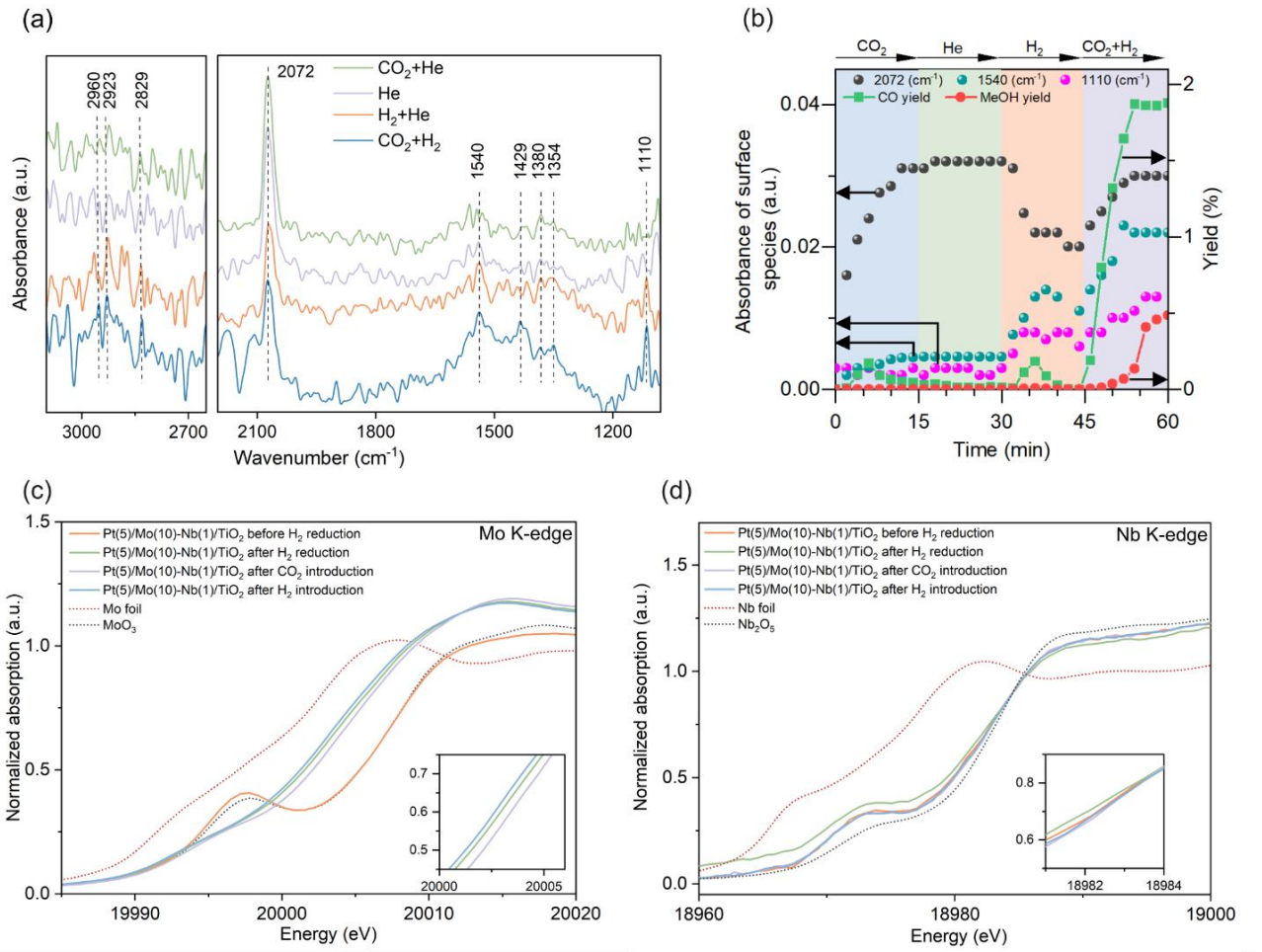

Figure 3.10. (a) *Operando* DRIFTS measurements for the Pt(5)/Mo(10)-Nb(1)/TiO_2 catalyst conducted under a sequential flow of CO_2 + He, He, H_2 + He, and 25% CO_2 + 75% H_2 at 150 °C. (b) Variations in the intensities of the peaks related to the surface-adsorbed species and concentration of CO in the effluent gas upon the introduction of CO_2. *In situ* analysis of (c) Mo K-edge XANES and (d) Nb k-edge XANES spectra of Pt(5)/Mo(10)-Nb(1)/TiO_2 obtained under a sequential flow of 100% He, 75% H_2/He, 25% CO_2/He, and 75% H_2/He at 150 °C.

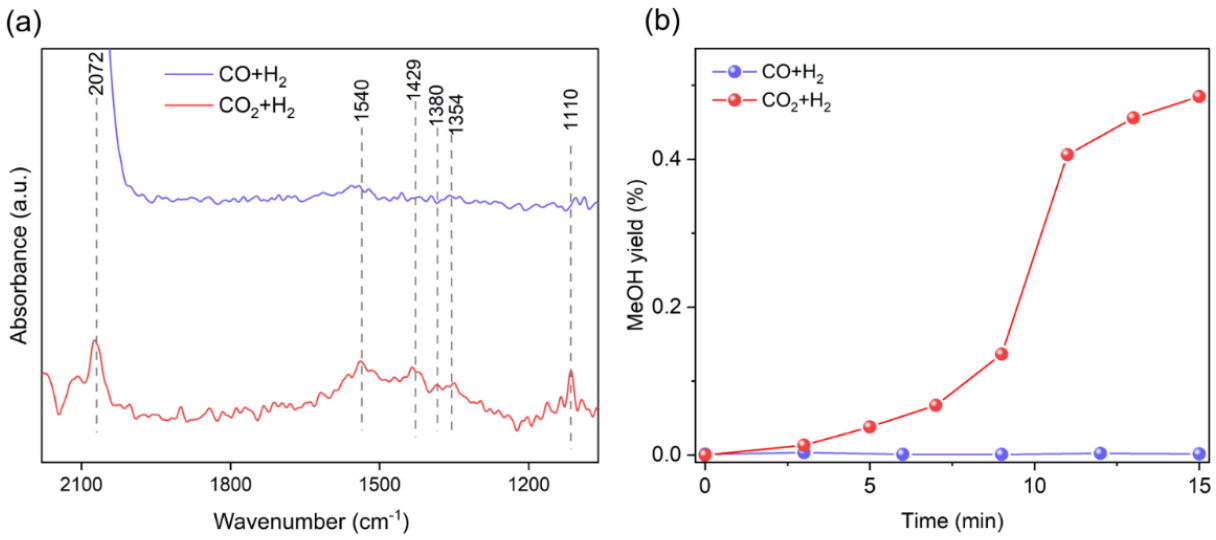

Figure 3.11. *Operando* DRIFTS spectra analysis over Pt(5)/Mo(10)-Nb(1)/TiO_2 under CO + H_2 and CO_2 + H_2 environment showing (a) comparison of DRIFTS spectra and (b) corresponding methanol yield calculated by GC at the outlet. Reaction condition: 150 °C, 0.5 MPa, H_2 : CO_2 (or CO) = 3 : 1. Prior to analysis, the catalyst was reduced at 300 °C for 0.5 h under H_2.

To elucidate the mechanistic role of each element in methanol formation over the optimized Pt(5)/Mo(10)-Nb(1)/TiO_2 catalyst, *in situ* XAS was performed under sequential exposure to CO_2 and H_2 at 150 °C and ambient pressure, following H_2 pretreatment (**Figure 3.10c**). The Mo K-edge XANES spectra revealed that the absorption edge shifted to lower energy after H_2 pretreatment, indicative of Mo reduction. Upon subsequent CO_2 introduction, the edge shifted to a higher energy, suggesting the oxidation of the Mo species by CO_2. The reintroduction of H_2 led to a reversal of this energy shift, confirming the reversible redox behavior of Mo. This redox cycle suggests that the MoO_x species maintained a partially reduced state under the reaction conditions, which is essential for catalytic activity.[94,95] The presence of undercoordinated, redox-active Mo sites is proposed to facilitate the generation and stabilization of oxygenated intermediates, thereby promoting CO_2 hydrogenation to methanol.[81] XANES analysis at the Nb K-edge (**Figure 3.10d**) was conducted under identical conditions. In contrast to Mo, the edge position of Nb remained unchanged upon CO_2 and H_2 exposure, indicating that Nb does not undergo redox transitions during the reaction. This suggests that Nb plays a non-redox role in the catalytic process.

To further investigate the redox behavior, AP-XPS was performed under H_2, CO_2, and a H_2 + CO_2 mixture (3 : 1 ratio) at 150 °C (**Figure 3.12a**). The Mo 3d XPS profiles are shown in **Figure 3.12b**. The peaks at 229.5, 231.3, and 234.1 eV are assigned to Mo^{2+} $3d_{5/2}$, Mo^{4+}

$3d_{5/2}$, and Mo^{6+} $3d_{5/2}$, respectively.[80,96–99] The corresponding distribution of the Mo oxidation states shown in **Figure 3.12e** revealed that, following H_2 treatment, the Mo species predominantly existed as Mo^{4+} (78%), followed by Mo^{2+} (16%) and Mo^{6+} (4%) (**Table 3.4**). Upon exposure to CO_2, partial oxidation of Mo^{2+} to Mo^{4+} was observed. Upon the reintroduction of H_2, Mo^{4+} was reduced back to Mo^{2+}, restoring the Mo^{2+} fraction. Under the H_2 + CO_2 conditions, Mo remained in a partially reduced state, further confirming its redox-active nature under the reaction conditions. It should be noted here that the binding energy assignments for Mo species in XPS vary across the literature, [80,96–99] and thus, the deconvolution results presented here should not be interpreted as quantitatively definitive. Nevertheless, the systematic changes in peak shape and spectral features observed under different reaction environments indicate that the surface Mo species undergo reversible redox transformations in response to H_2 and CO_2. In contrast, the Nb 3d XPS spectra (**Figure 3.12c**) indicated that Nb was primarily present as Nb^{5+} (206.7 eV), with a negligible contribution from Nb^{4+} (206.1 eV) (**Table 3.5**).[100,101] The relative fraction of the Nb oxidation states remained unchanged upon switching between the H_2 and CO_2 environments (**Figure 3.12f**), indicating that Nb does not participate in redox processes and remains in the Nb^{5+} state during methanol synthesis. These observations are consistent with the *in situ* XAS results. Analysis of the Ti $2p_{3/2}$ region (**Figure 3.12d, g**) indicated the generation of Ti^{3+} species (457.5 eV) under the reduction environment (**Table 3.6**).[102–104] This partial reduction of TiO_2 facilitates the activation of CO_2,[105] which may explain the high activity of the TiO_2 supported catalyst compared with that of the catalysts supported on other M_xO_y (M_xO_y = SiO_2, γ-Al_2O_3, CeO_2, ZrO_2, and MgO), as shown in **Figure 3.4**.

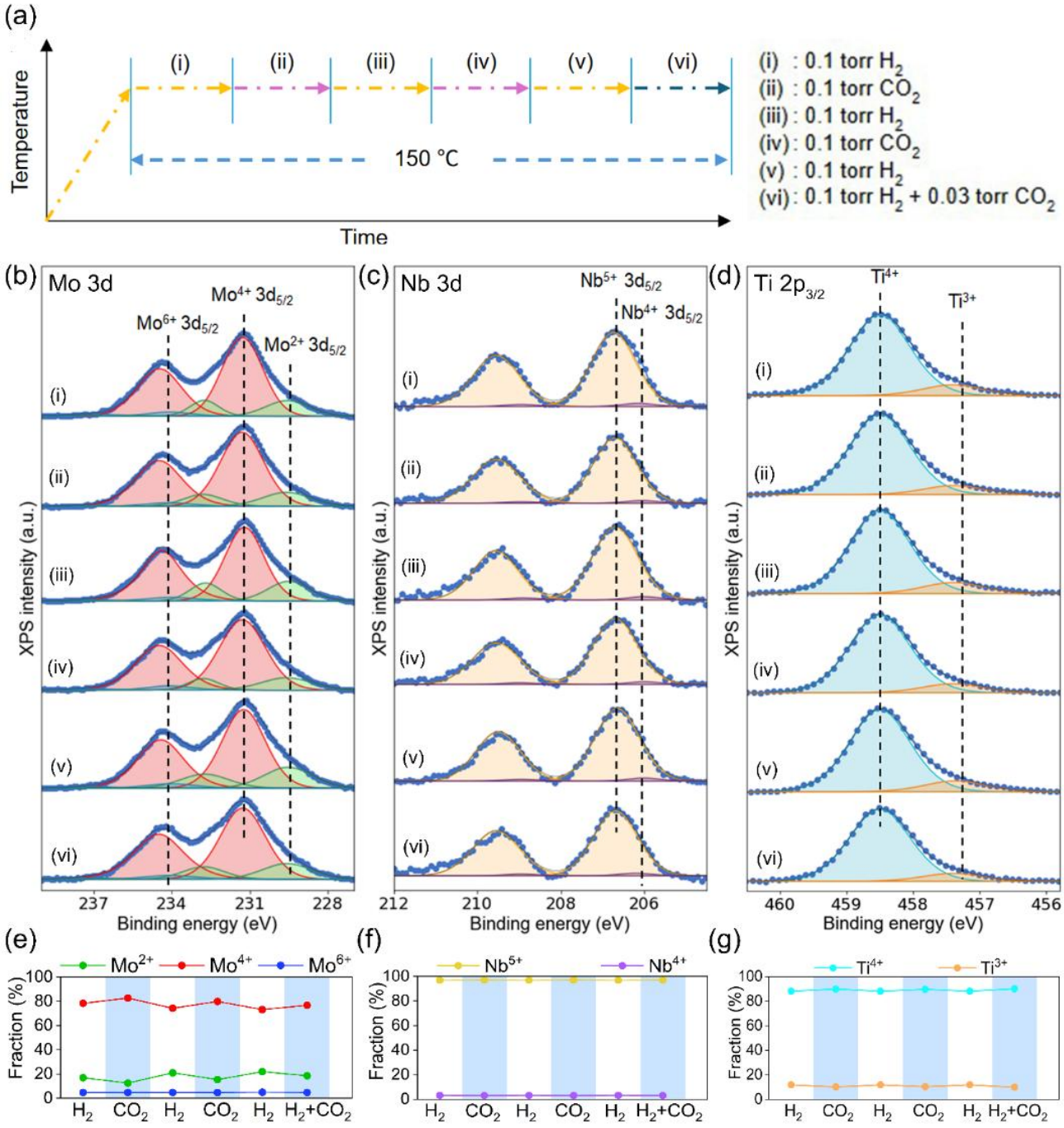

Figure 3.12. (a) AP-XPS analysis conditions and analysis results of (b) Mo 3d, (c) Nb 3d, and (d) Ti $2p_{3/2}$ of Pt(5)/Mo(10)-Nb(1)/TiO_2 under alternating exposure to 0.1 torr H_2 and 0.1 torr CO_2. (e, f, g) The relative percentage of the Mo, Nb, and Ti species in various oxidation states under distinct environments. For Mo 3d (panel b and e), light green, red, and blue represent Mo^{2+}, Mo^{4+} and Mo^{6+}, respectively. For Nb 3d (panel c and e), pale yellow and purple represent Nb^{5+} and Nb $^{4+}$, respectively. For Ti $2p_{3/2}$ (panel d and g), light cyan and orange represent Ti^{4+} and Ti^{3+}, respectively.

Table 3.4. Relative distribution of different Mo^{n+} species over Pt(5)/Mo(10)-Nb(1)/TiO_2 catalyst under different atmosphere.

Gas environment	Relative distribution (%)		
	Mo^{2+}	Mo^{4+}	Mo^{6+}
H_2	17	78	5
CO_2	12	83	5
H_2	21	74	5
CO_2	15	80	5
H_2	22	73	5
H_2 + CO_2	18	77	5

Table 3.5. Relative distribution of different Nb^{n+} species over Pt(5)/Mo(10)-Nb(1)/TiO_2 catalyst under different atmosphere.

Gas environment	Relative distribution (%)	
	Nb^{5+}	Nb^{4+}
H_2	97	3
CO_2	97	3
H_2	97	3
CO_2	97	3
H_2	97	3
H_2 + CO_2	97	3

Table 3.6. Relative distribution of different Ti^{n+} species over Pt(5)/Mo(10)-Nb(1)/TiO_2 catalyst under different atmosphere.

Gas environment	Relative distribution (%)	
	Ti^{4+}	Ti^{3+}
H_2	88	12
CO_2	90	10
H_2	88	12
CO_2	90	10
H_2	88	12
H_2 + CO_2	90	10

To gain further insight into the individual roles of Pt, Mo, and Nb in the methanol synthesis pathway, *in situ* DRIFTS analyses were conducted under the reaction conditions for various control catalysts and compared with the performance of the Pt(5)/Mo(10)-Nb(1)/TiO_2 catalyst (**Figure 3.13**). The Mo(10)-Nb(1)/TiO_2 catalyst, without Pt, showed no peaks corresponding to formate, methoxy, or adsorbed CO species, indicating that Pt is essential for H_2 dissociation. In contrast, when Mo was omitted, the Pt(5)/Nb(1)/TiO_2 catalyst exhibited only weak features of formate and methoxy species, suggesting that partially reduced MoO_x species are primarily responsible for stabilizing oxygenate intermediates necessary for methanol production. These results support the findings from the *operando* DRIFTS and XAS analyses (**Figure 3.10**).

The specific role of Nb was less evident from *in situ* DRIFTS analysis, as the spectra for the Pt(5)/Mo(10)/TiO_2 catalyst (without Nb) closely resembled that of the Nb-promoted

catalyst (**Figure 3.13**). However, the peak for CO adsorption over Pt nanoparticles appeared at higher wavenumbers for the Nb-containing catalysts, such as Pt(5)/Mo(10)-Nb(1)/TiO_2 (2071 cm^{-1}) and Pt(5)/Nb(1)/TiO_2 (2072 cm^{-1}), compared to that in Pt(5)/Mo(10)/TiO_2 (2066 cm^{-1}). This indicates that the introduction of Nb favors the formation of electron-deficient metallic Pt species.[106] This formation of electron-deficient metallic Pt species is important for mitigating CO poisoning during the CO_2 hydrogenation reaction.

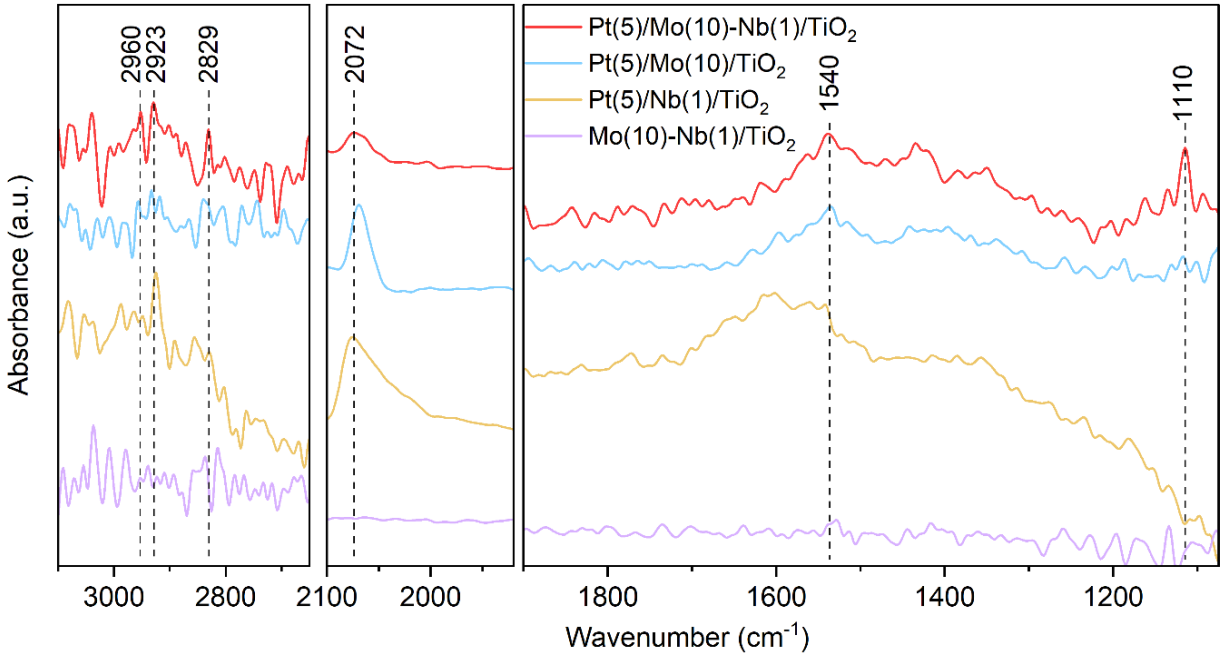

Figure 3.13. *In situ* DRIFTS measurements for the Pt(5)/Mo(10)-Nb(1)/TiO_2 (P25), Pt(5)/Mo(10)/TiO_2 (P25), Pt(5)/Nb(1)/TiO_2 (P25), and Mo(10)-Nb(1)/TiO_2 catalysts conducted under a gas flow containing CO_2 (5 mL min^{-1}) H_2 (15 mL min^{-1}) at 150 °C, 0.5 MPa.

To further understand the role of Nb, we hypothesized that its acidic nature could facilitate the desorption of methanol from the catalyst surface. Facile desorption of methanol is particularly important because previous studies have shown that methanol can undergo decomposition over Pt/MoO_X/TiO_2 catalysts.[60] Thus, promoting methanol desorption would reduce decomposition and enhance overall methanol productivity. To evaluate this hypothesis, methanol decomposition experiments were conducted under N_2 atmosphere (0.5 MPa) over both the Pt(5)/Mo(10)-Nb(1)/TiO_2 catalyst and its Nb-free counterpart. As shown in **Scheme 4.1**, the Nb-containing catalyst exhibited a lower methanol decomposition rate than its Nb-free counterpart, suggesting that the Nb species contribute to the facile desorption of methanol and suppression of its decomposition. This finding underscores the beneficial role of Nb as an acidic species in the facile desorption of methanol from the catalyst

surface to promote methanol synthesis. It is worth mentioning here that even though Nb brings acidity to the system, unlike oxide-zeolite catalyst systems, it does not further convert methanol to secondary products such as hydrocarbons or DME mainly because of low reaction temperature.

Based on these observations, a possible mechanistic pathway is proposed. CO_2 is initially adsorbed at oxygen-deficient sites of the undercoordinated MoO_x species. Pt nanoparticles, serving as the primary H_2 activation sites, dissociate molecular hydrogen, enabling the formation of formate intermediates over MoO_x. Subsequent H_2 dissociation over Pt leads to the conversion of formate into methanol. Owing to their acidic character, the Nb species promote facile methanol desorption from the catalyst surface, thereby minimizing its decomposition and enhancing the yield. Furthermore, Nb promotes the formation of electron-deficient metallic Pt species, thereby mitigating CO poisoning. This synergistic interplay among Pt, Mo, and Nb, each fulfilling a distinct role, is crucial for obtaining a highly active and stable Pt(5)/Mo(10)-Nb(1)/TiO_2 catalyst for low-temperature CO_2 hydrogenation to methanol.

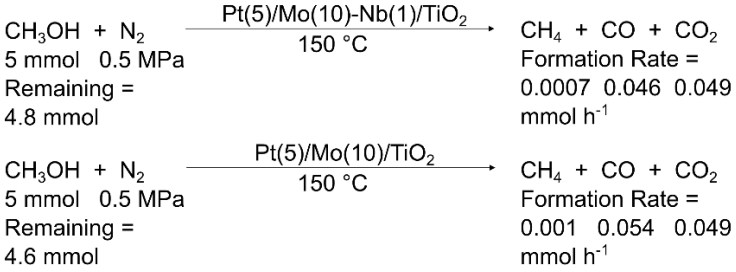

Scheme 4.1. Methanol decomposition over Pt(5)/Mo(10)-Nb(1)/TiO_2 and Pt(5)/Mo(10)/TiO_2. Pretreatment: H_2 (20 mL min^{-1}), 300 °C, 0.5 h. Catalytic reaction conditions: catalyst (100 mg), 150 °C, methanol (5 mmol), 0.5 MPa N_2, 1 h.

3.4 Conclusions

In this study, we developed and investigated a series of Nb-promoted Pt(5)/Mo(10)-Nb(X)/TiO_2 catalysts for the low-temperature CO_2 hydrogenation to methanol. The Pt(5)/Mo(10)-Nb(1)/TiO_2 catalyst showed the best performance, achieving one of the highest reported methanol formation rates at 150 °C. Systematic catalytic evaluation revealed that Nb promotion significantly enhanced methanol formation, achieving a higher activity than that of the unpromoted Pt(5)/Mo(10)/TiO_2 catalyst. Through comprehensive structural and mechanistic characterizations, including *in situ/operando* DRIFTS, *in situ* XAS, and AP-XPS, we elucidated the distinct roles of each catalyst component in the methanol synthesis pathway. Pt was identified as the primary site for H_2 dissociation, while the MoO_X species played a pivotal redox role, generating oxygenated intermediates including formate and methoxy. Nb demonstrated an essential promotional function by enhancing the acidic properties of the catalyst surface, thereby facilitating the desorption of methanol and suppressing its decomposition. In addition, the presence of Nb increased the electron-deficiency of metallic Pt, consequently mitigating CO poisoning. Overall, this study highlights the importance of designing multifunctional catalytic systems wherein each component contributes to a specific step of the reaction.

3.5 References

(1) Ra, E. C.; Kim, K. Y.; Kim, E. H.; Lee, H.; An, K.; Lee, J. S. Recycling Carbon Dioxide through Catalytic Hydrogenation: Recent Key Developments and Perspectives. *ACS Catal*. **2020**, *10* (19), 11318–11345.

(2) Bao, J.; Yang, G.; Yoneyama, Y.; Tsubaki, N. Significant Advances in C1 Catalysis: Highly Efficient Catalysts and Catalytic Reactions. *ACS Catal*. **2019**, *9* (4), 3026–3053.

(3) Ye, J.; Dimitratos, N.; Rossi, L. M.; Thonemann, N.; Beale, A. M.; Wojcieszak, R. Hydrogenation of CO_2 for Sustainable Fuel and Chemical Production. *Science* **2025**, *387* (6737), eadn9388.

(4) Gao, P.; Zhang, L.; Li, S.; Zhou, Z.; Sun, Y. Novel Heterogeneous Catalysts for CO_2 Hydrogenation to Liquid Fuels. *ACS Cent. Sci.* **2020**, *6* (10), 1657–1670.

(5) Ye, R. P.; Ding, J.; Gong, W.; Argyle, M. D.; Zhong, Q.; Wang, Y.; Russell, C. K.; Xu, Z.; Russell, A. G.; Li, Q.; Fan, M.; Yao, Y. G. CO_2 Hydrogenation to High-Value Products via Heterogeneous Catalysis. *Nat. Commun*. **2019**, *10* (1), 1–15.

(6) Sharma, P.; Sebastian, J.; Ghosh, S.; Creaser, D.; Olsson, L. Recent Advances in Hydrogenation of CO_2 into Hydrocarbons via Methanol Intermediate over Heterogeneous Catalysts. *Catal. Sci. Technol*. **2021**, *11* (5), 1665–1697.

(7) Palo, D. R.; Dagle, R. A.; Holladay, J. D. Methanol Steam Reforming for Hydrogen Production. *Chem. Rev.* **2007**, *107* (10), 3992–4021.

(8) Song, C. Global Challenges and Strategies for Control, Conversion and Utilization of CO_2 for Sustainable Development Involving Energy, Catalysis, Adsorption and Chemical Processing. *Catal. Today* **2006**, *115* (1–4), 2–32.

(9) Lappa, F.; Khalil, I.; Morales, A.; Leonard, G.; Dusselier, M. One Step Methanol-Mediated CO_2 Conversion to Gasoline: Comprehensive Review and Critical Outlook. *Energy and Fuels* **2024**, *38*, 18265–18291.

(10) Olah, G. A.; Goeppert, A.; Prakash, G. K. S. Beyond Oil and Gas: The Methanol Economy: Second Edition; *Wiley-VCH*, **2009**.

(11) Niu, J.; Liu, H.; Jin, Y.; Fan, B.; Qi, W.; Ran, J. Comprehensive Review of Cu-Based CO_2 Hydrogenation to CH_3OH: Insights from Experimental Work and Theoretical Analysis. *Int. J. Hydrogen Energy* **2022**, *47* (15), 9183–9200.

(12) Zhao, D.; Han, S.; Kondratenko, E. V. CO_2 Hydrogenation to CH_3OH over Cu-Based Catalysts: Primary and Side Reactions. *ChemCatChem* **2023**, *15* (20), e202300679.

(13) Ting, K. W.; Toyao, T.; Siddiki, S. M. A. H.; Shimizu, K. I. Low-Temperature Hydrogenation of CO_2 to Methanol over Heterogeneous TiO_2-Supported Re Catalysts. *ACS Catal*. **2019**, *9* (4), 3685–3693.

(14) Sugiyama, H.; Miyazaki, M.; Sasase, M.; Kitano, M.; Hosono, H. Room-Temperature CO_2 Hydrogenation to Methanol over Air-Stable Hcp-PdMo Intermetallic Catalyst. *J. Am. Chem. Soc*. **2023**, *145* (17), 9410–9416.

(15) Chen, Y.; Choi, S.; Thompson, L. T. Low Temperature CO_2 Hydrogenation to Alcohols and Hydrocarbons over Mo_2C Supported Metal Catalysts. *J. Catal.* **2016**, *343*, 147–156.

(16) Zhang, Z.; Zuo, J.; Luo, L.; Yang, X.; Ma, Z.; Jin, H.; Yuan, Y.; Qian, Q.; Chen, Q.; Luo, Y. Sodium-Assisted MoS_2 for Boosting CO_2 Hydrogenation to Methanol: The Crucial Role of Sodium in Defect Evolution and Modification. *J. Catal.* **2024**, *436*, 115621.

(17) Hong, S.; Reddy, K. P.; Song, Y.; Park, D.; Park, J. Y. Enhanced Methanol Formation in CO_2 Hydrogenation through Synergistic Copper and Gallium Interaction. *J. Catal.* **2024**, *437*, 115643.

(18) Hu, J.; Yu, L.; Deng, J.; Wang, Y.; Cheng, K.; Ma, C.; Zhang, Q.; Wen, W.; Yu, S.; Pan, Y.; Yang, J.; Ma, H.; Qi, F.; Wang, Y.; Zheng, Y.; Chen, M.; Huang, R.; Zhang, S.; Zhao, Z.; Mao, J.; Meng, X.; Ji, Q.; Hou, G.; Han, X.; Bao, X.; Wang, Y.; Deng, D. Sulfur Vacancy-Rich MoS_2 as a Catalyst for the Hydrogenation of CO_2 to Methanol. *Nat. Catal.* **2021**, *4* (3), 242–250.

(19) Huang, C.; Zhang, S.; Wang, W.; Zhou, H.; Shao, Z.; Xia, L.; Wang, H.; Sun, Y. Modulation of Electronic Metal-Support Interaction between Cu and ZnO by Er for Effective Low-Temperature CO_2 Hydrogenation to Methanol. *ACS Catal.* **2024**, *14* (3), 1324–1335.

(20) Gau, A.; Hack, J.; Maeda, N.; Meier, D. M. Operando Spectroscopic Monitoring of Active Species in CO_2 Hydrogenation at Elevated Pressure and Temperature: Steady-State versus Transient Analysis. *Energy and Fuels* **2021**, *35* (18), 15243–15246.

(21) Liu, G.; Liu, P.; Meng, D.; Zhao, T.; Qian, X.; He, Q.; Guo, X.; Qi, J.; Peng, L.; Xue, N.; Zhu, Y.; Ma, J.; Wang, Q.; Liu, X.; Chen, L.; Ding, W. CO_x Hydrogenation to Methanol and Other Hydrocarbons under Mild Conditions with Mo_3S_4@ZSM-5. *Nat. Commun*. **2023**, *14* (1), 513.

(22) Chen, F.; Liang, J.; Wang, F.; Guo, X.; Gao, W.; Kugue, Y.; He, Y.; Yang, G.; Reubroycharoen, P.; Vitidsant, T.; Tsubaki, N. Improved Catalytic Activity and Stability of Cu/ZnO Catalyst by Boron Oxide Modification for Low-Temperature Methanol Synthesis. *Chem. Eng. J.* **2023**, *458*, 141401.

(23) Zhou, S.; Ma, W.; Anjum, U.; Kosari, M.; Xi, S.; Kozlov, S. M.; Zeng, H. C. Strained Few-Layer MoS_2 with Atomic Copper and Selectively Exposed in-Plane Sulfur Vacancies for CO_2 Hydrogenation to Methanol. *Nat. Commun*. **2023**, *14* (1), 5872.

(24) Zhou, S.; Zeng, H. C. Boxlike Assemblages of Few-Layer MoS_2 Nanosheets with Edge Blockage for High-Efficiency Hydrogenation of CO_2 to Methanol. *ACS Catal.* **2022**, *12* (16), 9872–9886.

(25) Zhou, Y.; Liu, F.; Geng, S.; Yao, M.; Ma, J.; Cao, J. Tuning the Content of S Vacancies in MoS_2 by Cu Doping for Enhancing Catalytic Hydrogenation of CO_2 to Methanol. *Mol. Catal.* **2023**, *547*, 113288.

(26) Olsbye, U.; Nova, A.; Gutterød, E. S.; Pulumati, S. H.; Kaur, G.; Lazzarini, A.; Solemsli, B. G.; Gunnæs, A. E.; Ahoba-Sam, C.; Kalyva, M. E.; Sannes, J. A.; Svelle, S.; Skúlason, E. Influence of Defects and H_2O on the Hydrogenation of CO_2 to Methanol over Pt Nanoparticles in UiO-67 Metal-Organic Framework. *J. Am. Chem. Soc*. **2020**, *142* (40), 17105–17118.

(27) Liang, H.; Zhang, G.; Li, Z.; Zhang, Y.; Fu, P. Catalytic Hydrogenation of CO_2 to Methanol over Cu-Based Catalysts: Active Sites Profiling and Regulation Strategy as Well as Reaction Pathway Exploration. *Fuel Process. Technol.* **2023**, *252*, 107995.

(28) Chen, F.; Liang, J.; Wang, F.; Gao, W.; Kugue, Y.; He, Y.; Guo, X.; Yang, G.; Liu, G.; Wu, J.; Reubroycharoen, P.; Vitidsant, T.; Tsubaki, N. Alcohol Solvent Assisted Synthesis of Metallic and Metal Oxide Catalysts: As-Prepared $Cu/ZnO/Al_2O_3$ Catalysts for Low-Temperature Methanol Synthesis with an Ultrahigh Yield. *ACS Catal.* **2023**, *13* (9), 6169–6184.

(29) Ruland, H.; Song, H.; Laudenschleger, D.; Stürmer, S.; Schmidt, S.; He, J.; Kähler, K.; Muhler, M.; Schlögl, R. CO_2 Hydrogenation with $Cu/ZnO/Al_2O_3$: A Benchmark Study. *ChemCatChem* **2020**, *12* (12), 3216–3222.

(30) Mosrati, J.; Ishida, T.; Mac, H.; Al-Yusufi, M.; Honma, T.; Parliniska-Wojtan, M.; Kobayashi, Y.; Klyushin, A.; Murayama, T.; Abdel-Mageed, A. M. Low-Temperature Hydrogenation of CO_2 to Methanol in Water on ZnO-Supported CuAu Nanoalloys. *Angew. Chemie Int. Ed*. **2023**, *62* (51), e202311340.

(31) Zhong, J.; Yang, X.; Wu, Z.; Liang, B.; Huang, Y.; Zhang, T. State of the Art and Perspectives in Heterogeneous Catalysis of CO_2 Hydrogenation to Methanol. *Chem. Soc. Rev.* **2020**, *49* (5), 1385–1413.

(32) Beck, A.; Zabilskiy, M.; Newton, M. A.; Safonova, O.; Willinger, M. G.; van Bokhoven, J. A. Following the Structure of Copper-Zinc-Alumina across the Pressure Gap in Carbon Dioxide Hydrogenation. *Nat. Catal.* **2021**, *4* (6), 488.

(33) Jiang, X.; Nie, X.; Guo, X.; Song, C.; Chen, J. G. Recent Advances in Carbon Dioxide Hydrogenation to Methanol via Heterogeneous Catalysis. *Chem. Revi.* **2020**, *120*(15), 7984-8034..

(34) Divins, N. J.; Kordus, D.; Timoshenko, J.; Sinev, I.; Zegkinoglou, I.; Bergmann, A.; Chee, S. W.; Widrinna, S.; Karslioglu, O.; Mistry, H.; Luna, M. L.; Zhong, J. Q.; Hoffman, A. S.; Boubnov, A.; Boscoboinik, J. A.; Heggen, M.; Dunin-Borkowski, R. E.; Bare, S. R.; Cuenya, B. R. Operando High-Pressure Investigation of Size-Controlled CuZn Catalysts for the Methanol Synthesis Reaction. *Nat. Commun.* **2021**, *12* (1), 1435.

(35) Pacchioni, G. From CO_2 to Methanol on $Cu/ZnO/Al_2O_3$ Industrial Catalyst. What Do We Know about the Active Phase and the Reaction Mechanism? *ACS Catal*. **2024**, *14* (4), 2730–2745.

(36) Gothe, M. L.; Pérez-Sanz, F. J.; Braga, A. H.; Borges, L. R.; Abreu, T. F.; Bazito, R. C.; Gonçalves, R. V; Rossi, L. M.; Vidinha, P. Selective CO_2 Hydrogenation into Methanol in a Supercritical Flow Process. *J. CO2 Util*. **2020**, *40*, 101195.

(37) Zhang, H.; Liu, P. Fine-Tuning Catalytic Selectivity by Modulating Catalyst-Environment Interactions: CO_2 Hydrogenation over Pd-Based Catalysts. *Chem Catal*. **2024**, *5* (1), 101156.

(38) Ojelade, O. A.; Zaman, S. F. A Review on Pd Based Catalysts for CO_2 Hydrogenation to Methanol: In-Depth Activity and DRIFTS Mechanistic Study. *Catal. Surv. from Asia* **2020**, *24* (1), 11–37.

(39) Bahruji, H.; Bowker, M.; Hutchings, G.; Dimitratos, N.; Wells, P.; Gibson, E.; Jones, W.; Brookes, C.; Morgan, D.; Lalev, G. Pd/ZnO Catalysts for Direct CO_2 Hydrogenation to Methanol. *J. Catal.* **2016**, *343*, 133–146.

(40) Sha, F.; Han, Z.; Tang, S.; Wang, J.; Li, C. Hydrogenation of Carbon Dioxide to Methanol over Non−Cu-Based Heterogeneous Catalysts. *ChemSusChem* **2020**, *13* (23), 6160–6181.

(41) Docherty, S. R.; Phongprueksathat, N.; Lam, E.; Noh, G.; Safonova, O. V; Urakawa, A.; Copéret, C. Silica-Supported PdGa Nanoparticles: Metal Synergy for Highly Active and Selective CO_2-to-CH_3OH Hydrogenation. *JACS Au* **2021**, *1* (4), 450.

(42) Makhmutov, D.; Fedorova, E.; Zanina, A.; Kubis, C.; Zhao, D.; Doronkin, D.; Rockstroh, N.; Bartling, S.; Armbruster, U.; Wohlrab, S.; Kondratenko, E. V. Reaction Pathways of Methanol Formation in CO_2 Hydrogenation over Pd-Based Catalysts. *ACS Catal*. **2025**, *15*, 2328–2341.

(43) Liu, L.; Mezari, B.; Kosinov, N.; Hensen, E. J. M. Al Promotion of In_2O_3 for CO_2 Hydrogenation to Methanol. *ACS Catal.* **2023**, *13* (24), 15730–15745.

(44) Sun, K.; Fan, Z.; Ye, J.; Yan, J.; Ge, Q.; Li, Y.; He, W.; Yang, W.; Liu, C. J. Hydrogenation of CO_2 to Methanol over In_2O_3 Catalyst. *J. CO2 Util*. **2015**, *12*, 1–6.

(45) Lee, K.; Mendes, P. C. D.; Jeon, H.; Song, Y.; Dickieson, M. P.; Anjum, U.; Chen, L.; Yang, T. C.; Yang, C. M.; Choi, M.; Kozlov, S. M.; Yan, N. Engineering Nanoscale H Supply Chain to Accelerate Methanol Synthesis on $ZnZrO_X$. *Nat. Commun*. **2023**, *14* (1), 1–11.

(46) Dang, S.; Ding, X.; Li, J.; Chang, J.; Zhang, Z.; Gao, P.; Tu, W.; Han, Y. Structure Sensitivity of an Atomic Co-Promoted In_2O_3 Catalyst toward CO_2 Hydrogenation to Methanol. *ACS Catal*. **2025**, *15* (5), 3967–3979.

(47) Dang, S.; Qin, B.; Yang, Y.; Wang, H.; Cai, J.; Han, Y.; Li, S.; Gao, P.; Sun, Y. Rationally Designed Indium Oxide Catalysts for CO_2 Hydrogenation to Methanol with High Activity and Selectivity. *Sci. Adv.* **2020**, *6* (25), 2060–2077.

(48) Wang, J.; Zhang, G.; Zhu, J.; Zhang, X.; Ding, F.; Zhang, A.; Guo, X.; Song, C. CO_2 Hydrogenation to Methanol over In_2O_3-Based Catalysts: From Mechanism to Catalyst Development. *ACS Catal*. **2021**, *11* (3), 1406–1423.

(49) Meng, M.; Li, J.; Zou, H.; Zheng, J.; Wu, T. A.-S.; Chan, T. I.-S.; Soo, Y.-L.; Wu, X. I.-P.; Gong, X.-Q.; Ianyi Chen, T.; Roy, K.; Held, G.; Chi, S.; Tsang, E. Methanol Synthesis at a Wide Range of H_2/CO_2 Ratios over a Rh-In Bimetallic Catalyst. *Angew. Chemie* **2020**, *132* (37), 16173–16180.

(50) Feng, W. H.; Yu, M. M.; Wang, L. J.; Miao, Y. T.; Shakouri, M.; Ran, J.; Hu, Y.; Li, Z.; Huang, R.; Lu, Y. L.; Gao, D.; Wu, J. F. Insights into Bimetallic Oxide Synergy during Carbon Dioxide Hydrogenation to Methanol and Dimethyl Ether over $GaZrO_x$ Oxide Catalysts. *ACS Catal*. **2021**, *11* (8), 4704–4711.

(51) Dostagir, N. H. M.; Thompson, C.; Kobayashi, H.; Karim, A. M.; Fukuoka, A.; Shrotri, A. Rh Promoted In_2O_3 as a Highly Active Catalyst for CO_2 Hydrogenation to Methanol. *Catal. Sci. Technol*. **2020**, *10* (24), 8196–8202.

(52) Tada, S.; Ochiai, N.; Kinoshita, H.; Yoshida, M.; Shimada, N.; Joutsuka, T.; Nishijima, M.; Honma, T.; Yamauchi, N.; Kobayashi, Y.; Iyoki, K. Active Sites on Zn_xZr_1-xO_2-x Solid Solution Catalysts for CO_2-to-Methanol Hydrogenation. *ACS Catal.* **2022**, *12* (13), 7748–7759.

(53) Wang, J.; Tang, C.; Li, G.; Han, Z.; Li, Z.; Liu, H.; Cheng, F.; Li, C. High-Performance MaZrOx (Ma = Cd, Ga) Solid-Solution Catalysts for CO_2 Hydrogenation to Methanol. *ACS Catal*. **2019**, *9* (11), 10253–10259.

(54) Yang, C.; Pei, C.; Luo, R.; Liu, S.; Wang, Y.; Wang, Z.; Zhao, Z. J.; Gong, J. Strong Electronic Oxide-Support Interaction over In_2O_3/ZrO_2 for Highly Selective CO_2 Hydrogenation to Methanol. *J. Am. Chem. Soc.* **2020**, *142* (46), 19523–19531.

(55) Araújo, T. P.; Morales-Vidal, J.; Giannakakis, G.; Mondelli, C.; Eliasson, H.; Erni, R.; Stewart, J. A.; Mitchell, S.; López, N.; Pérez-Ramírez, J. Reaction-Induced Metal-Metal Oxide Interactions in Pd-In_2O_3/ZrO_2 Catalysts Drive Selective and Stable CO_2 Hydrogenation to Methanol. *Angew. Chemie Int. Ed.* **2023**, *62* (42), e202306563.

(56) Wang, J.; Li, G.; Li, Z.; Tang, C.; Feng, Z.; An, H.; Liu, H.; Liu, T.; Li, C. A Highly Selective and Stable ZnO-ZrO_2 Solid Solution Catalyst for CO_2 Hydrogenation to Methanol. *Sci. Adv.* **2017**, *3* (10), e1701290.

(57) Wang, L.; Guan, E.; Wang, Y.; Wang, L.; Gong, Z.; Cui, Y.; Meng, X.; Gates, B. C.; Xiao, F. S. Silica Accelerates the Selective Hydrogenation of CO_2 to Methanol on Cobalt Catalysts. *Nat. Commun.* **2020**, *11* (1), 1–9.

(58) Khan, M. U.; Wang, L.; Liu, Z.; Gao, Z.; Wang, S.; Li, H.; Zhang, W.; Wang, M.; Wang, Z.; Ma, C.; Zeng, J. Pt_3Co Octapods as Superior Catalysts of CO_2 Hydrogenation. *Angew. Chemie Int. Ed.* **2016**, *55* (33), 9548–9552.

(59) Zhang, W.; Wang, L.; Liu, H.; Hao, Y.; Li, H.; Khan, M. U.; Zeng, J. Integration of Quantum Confinement and Alloy Effect to Modulate Electronic Properties of RhW Nanocrystals for Improved Catalytic Performance toward CO_2 Hydrogenation. *Nano Lett.* **2017**, *17* (2), 788–793.

(60) Toyao, T.; Kayamori, S.; Maeno, Z.; Siddiki, S. M. A. H.; Shimizu, K. I. Heterogeneous Pt and MoO_x Co-Loaded TiO_2 Catalysts for Low-Temperature CO_2 Hydrogenation to Form CH_3OH. *ACS Catal.* 2019, *9* (9), 8187–8196.

(61) Zhao, S.; Mine, S.; Wang, G.; Zhang, W.; El Fakir, A. A.; Yang, B.; Qin, Z.; Dostagir, N. H. M. D.; Matsushita, K.; Takigawa, I.; Shimizu, K.; Toyao, T. Development of Highly Active Catalysts for Low-Temperature CO_2 Hydrogenation to Methanol Using a Machine Learning Approach. J*. Am. Chem. Soc.* **2025**, *147* (34), 31121–31135.

(62) Huff, C. A.; Sanford, M. S. Cascade Catalysis for the Homogeneous Hydrogenation of CO_2 to Methanol. *J. Am. Chem. Soc.* **2011**, *133* (45), 18122–18125.

(63) Wesselbaum, S.; vom Stein, T.; Klankermayer, J.; Leitner, W. Hydrogenation of Carbon Dioxide to Methanol by Using a Homogeneous Ruthenium–Phosphine Catalyst. *Angew. Chemie Int. Ed*. **2012**, *51* (30), 7499–7502.

(64) Wesselbaum, S.; Moha, V.; Meuresch, M.; Brosinski, S.; Thenert, K. M.; Kothe, J.; Stein, T. vom; Englert, U.; Hölscher, M.; Klankermayer, J.; Leitner, W. Hydrogenation of Carbon Dioxide to Methanol Using a Homogeneous Ruthenium–Triphos Catalyst: From Mechanistic Investigations to Multiphase Catalysis. *Chem. Sci.* **2015**, *6* (1), 693–704.

(65) Kothandaraman, J.; Goeppert, A.; Czaun, M.; Olah, G. A.; Prakash, G. K. S. Conversion of CO_2 from Air into Methanol Using a Polyamine and a Homogeneous Ruthenium Catalyst. *J. Am. Chem. Soc*. **2016**, *138* (3), 778–781.

(66) Schneidewind, J.; Adam, R.; Baumann, W.; Jackstell, R.; Beller, M. Low-Temperature Hydrogenation of Carbon Dioxide to Methanol with a Homogeneous Cobalt Catalyst. *Angew. Chemie Int. Ed*. **2017**, *56* (7), 1890–1893.

(67) Ribeiro, A. P. C.; Martins, L. M. D. R. S.; Pombeiro, A. J. L. Carbon Dioxide-to-Methanol Single-Pot Conversion Using a C-Scorpionate Iron(Ii) Catalyst. *Green Chem.* **2017**, *19* (20), 4811–4815.

(68) Kar, S.; Goeppert, A.; Kothandaraman, J.; Prakash, G. K. S. Manganese-Catalyzed Sequential Hydrogenation of CO2 to Methanol via Formamide. *ACS Catal*. **2017**, *7* (9), 6347–6351.

(69) Everett, M.; Wass, D. F. Highly Productive CO_2 Hydrogenation to Methanol – a Tandem Catalytic Approach via Amide Intermediates. *Chem. Commun.* **2017**, *53* (68), 9502–9504.

(70) Kar, S.; Sen, R.; Goeppert, A.; Prakash, G. K. S. Integrative CO_2 Capture and Hydrogenation to Methanol with Reusable Catalyst and Amine: Toward a Carbon Neutral Methanol Economy. *J. Am. Chem. Soc*. **2018**, *140* (5), 1580–1583.

(71) Scharnagl, F. K.; Hertrich, M. F.; Neitzel, G.; Jackstell, R.; Beller, M. Homogeneous Catalytic Hydrogenation of CO_2 to Methanol – Improvements with Tailored Ligands. *Adv. Synth. Catal.* **2019**, *361* (2), 374–379.

(72) Reller, C.; Pöge, M.; Lißner, A.; Mertens, F. O. R. L. Methanol from CO_2 by Organo-Cocatalysis: CO_2 Capture and Hydrogenation in One Process Step. *Environ. Sci. Technol.* **2014**, *48* (24), 14799–14804.

(73) Chen, Y.; Choi, S.; Thompson, L. T. Low-Temperature CO_2 Hydrogenation to Liquid Products via a Heterogeneous Cascade Catalytic System. *ACS Catal*. **2015**, *5* (3), 1717–1725.

(74) He, Z.; Qian, Q.; Ma, J.; Meng, Q.; Zhou, H.; Song, J.; Liu, Z.; Han, B. Water-Enhanced Synthesis of Higher Alcohols from CO_2 Hydrogenation over a Pt/Co_3O_4 Catalyst under Milder Conditions. *Angew. Chemie Int. Ed.* **2016**, *55* (2), 737–741.

(75) Bai, S.; Shao, Q.; Feng, Y.; Bu, L.; Huang, X. Highly Efficient Carbon Dioxide Hydrogenation to Methanol Catalyzed by Zigzag Platinum–Cobalt Nanowires. *Small* **2017**, *13* (22), 1604311.

(76) Li, H.; Wang, L.; Dai, Y.; Pu, Z.; Lao, Z.; Chen, Y.; Wang, M.; Zheng, X.; Zhu, J.; Zhang, W.; Si, R.; Ma, C.; Zeng, J. Synergetic Interaction between Neighbouring Platinum Monomers in CO_2 Hydrogenation. *Nat. Nanotechnol.* **2018**, *13* (5), 411–417.

(77) Zheng, X.; Lin, Y.; Pan, H.; Wu, L.; Zhang, W.; Cao, L.; Zhang, J.; Zheng, L.; Yao, T. Grain Boundaries Modulating Active Sites in RhCo Porous Nanospheres for Efficient CO_2 Hydrogenation. *Nano Res.* **2018**, *11* (5), 2357–2365.

(78) Kothandaraman, J.; Dagle, R. A.; Dagle, V. L.; Davidson, S. D.; Walter, E. D.; Burton, S. D.; Hoyt, D. W.; Heldebrant, D. J. Condensed-Phase Low Temperature Heterogeneous Hydrogenation of CO_2 to Methanol. *Catal. Sci. Technol.* **2018**, *8* (19), 5098–5103.

(79) Gau, A.; Hack, J.; Maeda, N.; Meier, D. M. Operando Spectroscopic Monitoring of Active Species in CO_2 Hydrogenation at Elevated Pressure and Temperature: Steady-State versus Transient Analysis. *Energy and Fuels* **2021**, *35* (18), 15243–15246.

(80) Jin, F.; Yang, X.; Yang, J.; Lei, Y.; Xu, W.; Jiang, W.; Ma, Z.; Liang, G.; Ben, H.; Li, X. Unraveling the Influence of Oxygen Vacancies in MoOx Catalysts on CO_2 Hydrogenation. *Chem. Eng. J.* **2024**, *495*, 153333.

(81) Kuwahara, Y.; Mihogi, T.; Hamahara, K.; Kusu, K.; Kobayashi, H.; Yamashita, H. A Quasi-Stable Molybdenum Sub-Oxide with Abundant Oxygen Vacancies That Promotes CO_2 Hydrogenation to Methanol. *Chem. Sci.* **2021**, *12* (29), 9902–9915.

(82) Ge, H.; Kuwahara, Y.; Yamashita, H. Development of Defective Molybdenum Oxides for Photocatalysis, Thermal Catalysis, and Photothermal Catalysis. *Chem. Commun.* **2022**, *58* (61), 8466–8479.

(83) Farges, F. Ab Initio and Experimental Pre-Edge Investigations of the Mn K-Edge XANES in Oxide-Type Materials. *Phys. Rev. B* **2005**, *71* (15), 155109.

(84) Tanaka, T.; Yoshida, T.; Yoshida, H.; Aritani, H.; Funabiki, T.; Yoshida, S.; Jehng, J. M.; Wachs, I. E. XAFS Study of Niobium Oxide on Alumina. *Catal. Today* **1996**, *28* (1–2), 71–78.

(85) Yoshida, S.; Tanaka, T.; Hanada, T.; Hiraiwa, T.; Kanai, H.; Funabiki, T. Analysis of XANES for Identification of Highly Dispersed Transition Metal Oxides on Supports. *Catal. Letters* **1992**, *12* (1–3), 277–285.

(86) Gaikwad, R.; Reymond, H.; Phongprueksathat, N.; Rudolf Von Rohr, P.; Urakawa, A. From CO or CO_2?: Space-Resolved Insights into High-Pressure CO_2 Hydrogenation to Methanol over Cu/ZnO/Al_2O_3. *Catal. Sci. Technol.* **2020**, *10* (9), 2763–2768.

(87) Kattel, S.; Yan, B.; Yang, Y.; Chen, J. G.; Liu, P. Optimizing Binding Energies of Key Intermediates for CO_2 Hydrogenation to Methanol over Oxide-Supported Copper. *J. Am. Chem. Soc.* **2016**, *138* (38), 12440–12450.

(88) Li, G.; Meeprasert, J.; Wang, J.; Li, C.; Pidko, E. A. CO_2 Hydrogenation to Methanol over Cd_4/TiO_2 Catalyst: Insight into Multifunctional Interface. *ChemCatChem* **2022**, *14* (5), e202101646.

(89) Bando, K. K.; Sayama, K.; Kusama, H.; Okabe, K.; Arakawa, H. In-Situ FT-IR Study on CO_2 Hydrogenation over Cu Catalysts Supported on SiO_2, Al_2O_3, and TiO_2. *Appl. Catal. A Gen*. **1997**, *165* (1–2), 391–409.

(90) Mattsson, A.; Hu, S.; Hermansson, K.; Österlund, L. Adsorption of Formic Acid on Rutile TiO_2 (110) Revisited: An Infrared Reflection-Absorption Spectroscopy and Density Functional Theory Study. *J. Chem. Phys*. **2014**, *140* (3), 34705.

(91) Tagawa, T.; Nomura, N.; Shimakage, M.; Goto, S. Effect of Supports on Copper Catalysts for Methanol Synthesis from CO_2 + H_2. *Res. Chem. Intermed*. **1995**, *21* (2), 193–202.

(92) Manzoli, M.; Chiorino, A.; Boccuzzi, F. Decomposition and Combined Reforming of Methanol to Hydrogen: A FTIR and QMS Study on Cu and Au Catalysts Supported on ZnO and TiO_2. *Appl. Catal. B Environ.* **2005**, *57* (3), 201–209.

(93) He, M. Y.; White, J. M.; Ekerdt, J. G. CO and CO_2 Hydrogenation over Metal Oxides: A Comparison of ZnO, TiO_2 and ZrO_2. *J. Mol. Catal.* **1985**, *30* (3), 415–430.

(94) Liu, H. X.; Wang, W. W.; Fu, X. P.; Liu, J. C.; Jia, C. J. Direct Cleavage of C=O Double Bond in CO_2 by the Subnano MoO_x Surface on Mo_2N. *Nat. Commun.* **2024**, *15* (1), 1–12.

(95) Murugappan, K.; Anderson, E. M.; Teschner, D.; Jones, T. E.; Skorupska, K.; Román-Leshkov, Y. Operando NAP-XPS Unveils Differences in MoO_3 and Mo_2C during Hydrodeoxygenation. *Nat. Catal.* **2018**, *1* (12), 960–967.

(96) Sun, S.; Gao, P.; Shen, Y.; Wu, T.; An, Q. Enhanced Water Dissociation Promotes Photocatalytic CO_2 Hydrogenation to Methane: A Case Study of Pt-Loaded MoO_3 Catalyst. *ACS Sustain. Chem. Eng.* **2024**, *12* (40), 14760–14770.

(97) Hada, K.; Nagai, M.; Omi, S. XPS and TPR Studies of Nitrided Molybdena - Alumina. *J. Phys. Chem. B* **2000**, *104* (9), 2090–2098.

(98) Shetty, M.; Murugappan, K.; Prasomsri, T.; Green, W. H.; Román-Leshkov, Y. Reactivity and Stability Investigation of Supported Molybdenum Oxide Catalysts for the Hydrodeoxygenation (HDO) of m-Cresol. *J. Catal.* **2015**, *331*, 86–97.

(99) Mine, S.; Yamaguchi, T.; Ting, K. W.; Maeno, Z.; Siddiki, S. M. A. H.; Oshima, K.; Satokawa, S.; Shimizu, K. I.; Toyao, T. Reverse Water-Gas Shift Reaction over $Pt/MoO_x/TiO_2$: Reverse Mars-van Krevelen Mechanismviaredox of Supported MoO_X. *Catal. Sci. Technol*. **2021**, *11* (12), 4172–4180.

(100) Islam, K.; Sultana, R.; Satpati, B.; Chakraborty, S. Studies on Structural and Dielectric Properties of NbO_2-Nb_2O_5 Thin-Film-Based Devices. *Vacuum* **2022**, *195*, 110675.

(101) Weibin, Z.; Weidong, W.; Xueming, W.; Xinlu, C.; Dawei, Y.; Changle, S.; Liping, P.; Yuying, W.; Li, B. The Investigation of NbO_2 and Nb_2O_5 Electronic Structure by XPS, UPS and First Principles Methods. *Surf. Interface Anal.* **2013**, *45* (8), 1206–1210.

(102) Wang, Z.; Yang, C.; Lin, T.; Yin, H.; Chen, P.; Wan, D.; Xu, F.; Huang, F.; Lin, J.; Xie, X.; Jiang, M. H-Doped Black Titania with Very High Solar Absorption and Excellent Photocatalysis Enhanced by Localized Surface Plasmon Resonance. *Adv. Funct. Mater.* **2013**, *23* (43), 5444–5450.

(103) Zhang, C.; Wang, L.; Etim, U. J.; Song, Y.; Gazit, O. M.; Zhong, Z. Oxygen Vacancies in Cu/TiO_2 Boost Strong Metal-Support Interaction and CO_2 Hydrogenation to Methanol. *J. Catal.* **2022**, *413*, 284–296.

(104) Dostagir, N. H. M.; Fukuoka, A.; Shrotri, A. Redox Behavior of In−O−Ti Interface for Selective Hydrogenation of CO_2 to CO in Doped In−TiO_2 Catalyst. *ChemCatChem* **2023**, *15* (3), e202201348.

(105) Huygh, S.; Bogaerts, A.; Neyts, E. C. How Oxygen Vacancies Activate CO_2 Dissociation on TiO_2 Anatase (001). *J. Phys. Chem. C* **2016**, *120* (38), 21659–21669.

(106) Wang, G.; Mine, S.; Chen, D.; Jing, Y.; Ting, K. W.; Yamaguchi, T.; Takao, M.; Maeno, Z.; Takigawa, I.; Matsushita, K.; Shimizu, K.; Toyao, T. Accelerated Discovery of Multi-Elemental Reverse Water-Gas Shift Catalysts Using Extrapolative Machine Learning Approach. *Nat. Commun*. **2023**, 14 (1), 5861.

Chapter 4

Machine learning assisted catalysts discovery for low-temperature methanol synthesis from CO_2 and H_2 in flow system

4.1 Introduction

Growing environmental pressures and the urgent need to move beyond fossil-based resources have intensified global interest in renewable carbon feedstocks for both energy applications and chemical manufacturing.[1,2] Although CO_2 is widely known as the dominant greenhouse gas, it can also be used as a carbon building block for the production of fuels and industrial chemicals. Among the various CO_2-derived products, methanol synthesized via catalytic CO_2 hydrogenation has attracted considerable attention owing to its versatility as a chemical intermediate, fuel, and liquid energy carrier.[3]

The relevance of CO_2 hydrogenation for methanol production is closely tied to concepts of carbon valorization and circular carbon utilization, with methanol serving as a practical medium for energy storage.[4] Industrial efforts have demonstrated direct CO_2-to-methanol conversion using Cu-based catalysts, but only when operated at elevated pressures (5–10 MPa) and temperatures above 220 °C.[5] Despite this achievement, the process suffers from low thermodynamic equilibrium conversion of CO_2 at such temperatures, requiring substantial recycle of unreacted gases after separation. Lower operational temperatures could, in theory, favor higher methanol yields and reduce energy input. However, developing highly active catalysts for methanol synthesis at lower temperatures poses a challenge.[6–10] While methanol synthesis is exothermic in nature, the chemical inertness of CO_2 hinders hydrogenation at temperatures below 200 °C,[11–14] leading to poor methanol productivity.[15–20] Developing catalysts capable of driving efficient CO_2 hydrogenation at low temperatures is therefore an essential challenge.

Rapid progress in molecular and materials informatics has reshaped the way functional materials are designed, opening new pathways for systematic catalyst discovery. Artificial intelligence has shown strong promise for accelerating this process by reducing cost and development time, though most existing studies remain confined to benchmark datasets and rarely yield truly novel materials or new reaction pathways.[21–30] A major limitation is that many machine-learning models tend to stay within the known data domain rather than extrapolate toward unexplored yet potentially exceptional candidates.[31] This issue is particularly prominent in catalysis, where reactions involve complex, dynamic, and time-dependent behavior that is costly to simulate with high precision. A key challenge of machine learning (ML) models is their tendency to optimize known datasets rather than extrapolating beyond existing materials to discover exceptional candidates. This issue is particularly evident in

catalysis informatics, where reactions involve dynamic and time-dependent phenomena.[24,32–36] In contrast to materials informatics, catalysis research is often empirical, lacking high-quality datasets due to the high computational costs of accurately modeling heterogeneous catalysts.[37–42] Furthermore, high-throughput experimental techniques, which have successfully advanced other scientific fields, are still underdeveloped in catalysis.[43–45] Compared with materials science, catalysis research still suffers from small, incomplete datasets due to the high computational expense of modeling heterogeneous catalysts and the slow development of high-throughput experimental systems. Additionally, the lack of negative experimental results further hinders data-driven exploration.[46] Hence, there is a strong demand for ML methods capable of navigating wide chemical spaces and extracting promising, previously unconsidered catalyst compositions directly from experimental data.[47–49]

Our group addressed these issues by proposing a machine-learning framework that encodes catalysts using chemically meaningful elemental descriptors (such as electronegativity and melting point) rather than directly using their compositions.[50,51] Each catalyst is represented by a weighted combination of these elemental properties, proportional to the elemental content. This representation facilitates genuine extrapolation, allowing exploration of catalysts with compositions and even elements not present in the original dataset.[50,52,53] Other studies employing advanced feature-engineering strategies have further confirmed the strength of such approaches.[54–56] Using this strategy, we previously developed multi-elemental catalysts for low-temperature CO_2 hydrogenation to methanol in batch reactions. The best catalyst was identified as Pt(5)/Mo(8)–Re(1)–W(0.7)/TiO_2.[50,52,55,57] Starting from a set of 90 catalysts, we performed 43 ML-experiment cycles, tested 580 candidates, and ultimately identified several catalysts outperforming previously reported high-performance materials in the 150 °C.

In the present work, we extended this ML-driven discovery framework to develop multi-element catalysts for methanol synthesis via low-temperature CO_2 hydrogenation in flow system. Beginning with a dataset of 314 catalysts, we conducted 25 closed-loop iterations combining ML predictions and experimental testing. Through this iterative workflow, and combined with the experience we got before, we developed an efficient catalyst Pt(5)/Mo(8)–Cr(0.7)-V(0.7)-La(0.7)-Re(1)/TiO_2.

4.2 Materials and methods

4.2.1 Catalyst preparation

The catalysts were prepared using the sequential impregnation method and named $PGM_1(X_{P1})$–$PGM_2(X_{P2})$–$PGM_3(X_{P3})$/$PR_1(X_{Pr1})$–$PR_2(X_{Pr2})$/$Add_1(X_{A1})$–$Add_2(X_{A2})$–$Add_3(X_{A3})$–$Add_4(X_{A4})$–$Add_5(X_{A5})$/Support_CalcT. In this study, PGM refers to Pt, Pd, Ru, Rh, Ir, and Au, and PR refers to Li, K, Sr, Cs, Na, Ca, Mg, Rb, Ba. For the additive (Add) elements, a total of 47 elements with atomic numbers 3 (Li) to 83 (Bi), excluding Be, B, C, N, O, F, Cl, As, Br, Tc, Pm, Hg, Tl, PR elements and platinum group metals, were used, along with 17 different supports (X represents the loading amount of PGM, PR and Add elements). Information regarding the purity and sources of the chemicals can be found in **Table 4.1**. CalcT denotes the corresponding calcination temperature in degrees Celsius. In the first step of catalyst preparation, single or multiple additive components (Add) were impregnated onto the support. An appropriate amount of support and the corresponding Add elements were combined in a 100 mL glass vessel with 20 mL of deionized water, stirred for 15 min at room temperature, evaporated to dryness at 50 °C, dried at 110 °C for 12 h, and calcinated in static air for 3 h to yield $PR_1(X_{Pr1})$–$PR_2(X_{Pr2})$/$Add_1(X_{A1})$–$Add_2(X_{A2})$–$Add_3(X_{A3})$–$Add_4(X_{A4})$–$Add_5(X_{A5})$/Support_CalcT. Subsequently, the formed $PR_1(X_{Pr1})$–$PR_2(X_{Pr2})$/$Add_1(X_{A1})$–$Add_2(X_{A2})$–$Add_3(X_{A3})$–$Add_4(X_{A4})$–$Add_5(X_{A5})$/Support_CalcT was further impregnated with an aqueous solution containing the precursors of the PGM elements (with a maximum loading of 5%). The mixture was evaporated to dryness at 50°C, followed by drying in static air at 110°C for 12 h to obtain the $PGM_1(X_{P1})$–$PGM_2(X_{P2})$–$PGM_3(X_{P3})$/$PR_1(X_{Pr1})$–$PR_2(X_{Pr2})$/$Add_1(X_{A1})$–$Add_2(X_{A2})$–$Add_3(X_{A3})$–$Add_4(X_{A4})$–$Add_5(X_{A5})$/Support_CalcT (Unreduced sample).

Table 4.1. Sources and additional information of the supports used.

Support name	Company name	Code name	Comment
γ-Al_2O_3	Sasol	Puralox	Gamma phase
Al_2O_3_AKP-G07	Sumitomo Chemical	AKP-G07	Theta phase
TiO_2_P25	Evonik (formerly Degussa)	P25	Anatase + rutile
SiO_2	Fuji Silysia Chemical	CARiACT Q-10	
ZrO_2_JRC3_RC-100	Daiichi Kigenso Kagaku Kogyo	RC-100 (JRC-ZRO-3)	Tetragonal + monocliric
ZrO_2_JRC4_EP	Daiichi Kigenso Kagaku Kogyo	EP (JRC-ZRO-4)	Tetragonal + monocliric
CeO_2_JRC2	Daiichi Kigenso Kagaku Kogyo	Type A (JRC-CEO-2)	
Nb_2O_5	Companhia Brasileira de Metalurgia e Mineração	HY-340	Prepared by calcining (500 °C for 3 h) niobic acid ($Nb_2O_5 \cdot nH_2O$, HY-340)
Co_3O_4	US Research Nanomaterials		>99.5%, 30–50 nm
MgO	Ube Material Industries	500A (JRC-MGO-4 500A)	
CeO_2(50%)-ZrO_2	Daiichi Kigenso Kagaku Kogyo	Z-1119	CeO_2 = 50 wt.%
SiO_2-Al_2O_3_JRC-SAL-6	Nikki-Shokubai Kasei	JRC-SAL-6	Al_2O_3 = 13 wt.%
SiO_2-Al_2O_3_JRC-SAH-7	Nikki-Shokubai Kasei	JRC-SAH-7	Al_2O_3 = 28 wt.%
H-ZSM-5_11	Tosoh	JRC-Z-HM20	Si/Al ratio = 11
H-Y_15	Tosoh	HSZ-372HUA	Si/Al ratio = 15
H-BEA_20	Tosoh	HSZ-940HOA	Si/Al ratio = 20
H-MOR_10	Tosoh	JRC-Z-HM20	Si/Al ratio = 10

4.2.2 Catalytic methanol synthesis reactions

CO_2 hydrogenation reactions were conducted in a fixed-bed continuous-flow reactor operating at a total pressure of 4 MPa (40 bar). We used 1% Ar/99% H_2 (purity; H_2: 99.99999%, Ar: 99.9999%) and CO_2 (purity; 99.995%) gas cylinders to supply the reaction gases. The reactor was supplied with a gas mixture of H_2/CO_2/Ar in a ratio of 74.4/24.8/0.8, with Ar serving as an internal standard gas. Prior to the catalytic measurements, 300 mg of the catalyst was placed between quartz wool inside a 1/4 inch fixed-bed reactor (inside diameter: 3.79 mm). The catalyst was pretreated under ambient pressure at a H_2/Ar (99%) flow rate of 20 mL/min and temperature of 300 °C for 0.5 h. Following the pretreatment, a H_2/CO_2/Ar (74.4/24.8/0.8) flow at a total flow rate of 40 mL/min passed through the catalyst bed at 4 MPa. The gas hourly space velocity (GHSV) was 8 L g_{cat}^{-1} h^{-1}. We conducted an aging treatment for 12 h at 210 °C under the reaction gas atmosphere as an accelerated

aging test before recording the results of the catalytic reaction. The products were analyzed using an online gas chromatograph (Shimadzu GC-2014) equipped with TCD (Shincarbon-ST column) and FID (Porapak Q column) detectors, within a reaction temperature range of 210–150 °C.

The CO_2 conversion (X_{CO2}) was calculated as follows.

$$X_{CO2} = \frac{\frac{c_{CO2}^{in}}{c_{Ar}^{in}} - \frac{c_{CO2}^{out}}{c_{Ar}^{out}}}{\frac{c_{CO2}^{in}}{c_{Ar}^{in}}} \times 100\%$$

The selectivity (Si) for individual products was calculated by the following equation:

$$S_i = \frac{c_i \times n_i}{\sum (c_i \times n_i)} \times 100\%$$

Here, c_i is the molar fraction of product i (CO_2, CO, hydrocarbons, or oxygenates), and n_i is the carbon number of product i in the reaction.

4.2.3 Catalyst representations for ML

As detailed in Section 2.1, each catalyst consisted of three components (PGM, PR, Add, and Support) in addition to CalcT. The initial step in optimizing this data with ML involves developing a suitable input format for the ML model. For PGM, PR, Add, and Support, each containing multiple elements with corresponding composition ratios, two types of representation schemes were used: The first method, which is a conventional method, is similar to one-hot encoding and constructs a feature vector by storing the composition ratios of each element in an n-dimensional vector, with unused elements represented by zeros. The second approach, referred to as "element descriptors" for PGM, PR and Add, and "support descriptors" for Support, simplifies the representation by emphasizing specific chemical properties over individual element types. Assuming a catalyst comprises m elements, $E_1, E_2, \cdots, E_m$, with their respective composition ratios denoted by $X_1, X_2, \cdots, X_m$. Considering n candidate elements under consideration, the first representation becomes an n-dimensional vector. The second representation, which is defined as the weighted sum of elemental descriptors for each E_i scaled by its composition fraction X_i and can be expressed as

$$X_1\ vec(E_1) + X_2 vec(E_2) + \cdots + X_m vec(E_m)$$

where the elemental descriptor vector for element E_i is represented by $vec(E_i)$. Technically, this representation aggregates unordered information using weighted sum pooling, a permutation-invariant operation in which each element's contribution is weighted by its composition fraction. This is also referred to as the composition-based feature vector (CBFV).[47]

Based on these two schemes, three types of input representations were explored for each component of PGM, PR Add, and Support: (0) a direct representation that uses only elemental compositions or the support type (first scheme only); (1) an exploitative representation that uses both elemental compositions (or support type) and elemental/support properties (first and second schemes); and (2) an explorative representation that uses only elemental or support properties (second scheme only). With these representation options (0), (1), and (2), the input representation for a catalyst is denoted as a code $ijkl$, where $i, j, k, l \in \{0,1,2\}$ with i, j, k and l correspond to the chosen representation type for PGM, PR Add, and Support, respectively. For example, a catalyst representation coded as 0012 indicates that the PGM and PR is represented using (0), Add using (1), and Support using (2). A representative list of element descriptors for PGM, Add, and Support, along with the distribution of descriptor values and correlations between descriptors, is shown in **Table 4.2** and **Figures 4.1-4.3**. The actual input to the ML model is a feature vector formed by appending a single numerical value—the calcination temperature in °C (CalcT), which is explored in 50 °C intervals from 300 °C to 700 °C—to the catalyst representation vector. The choice of catalyst representation can be switched at each iteration.

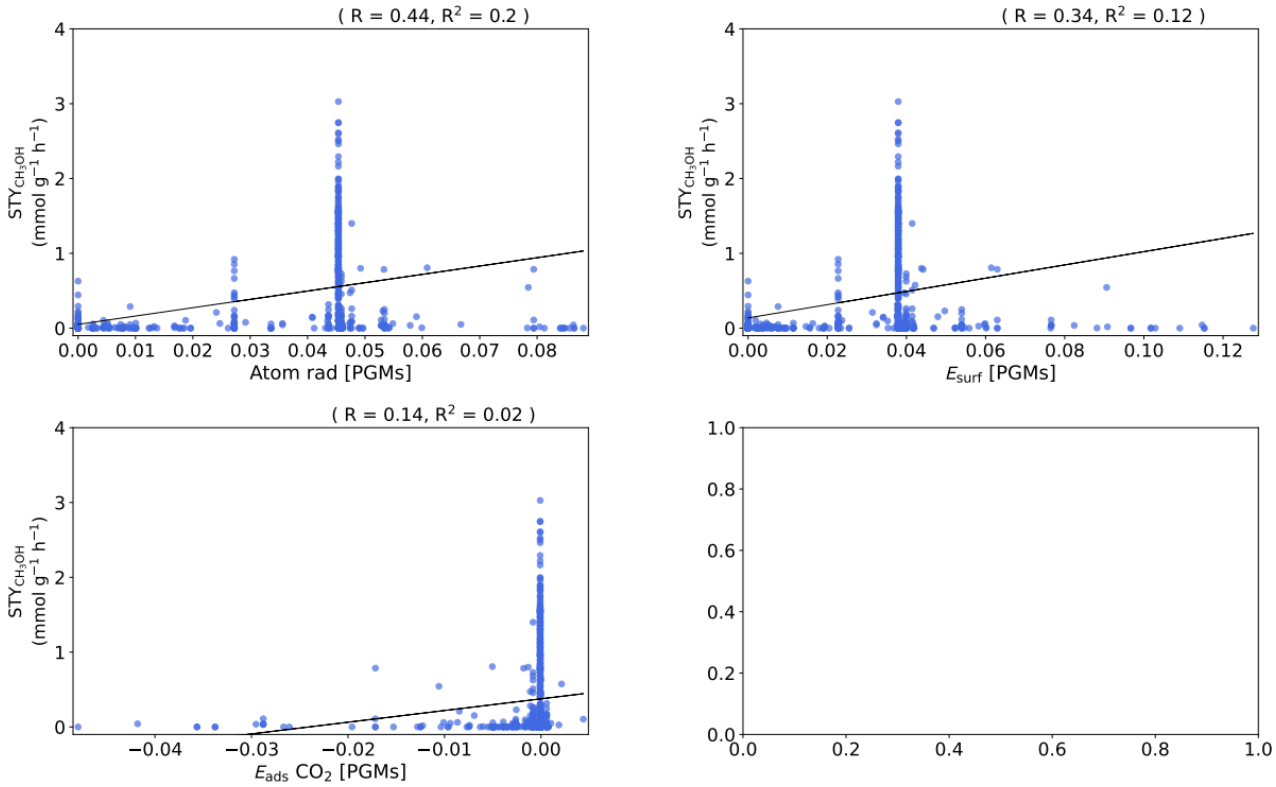

Figure 4.1. Correlation map for the seven selected descriptors for the PGM elements.

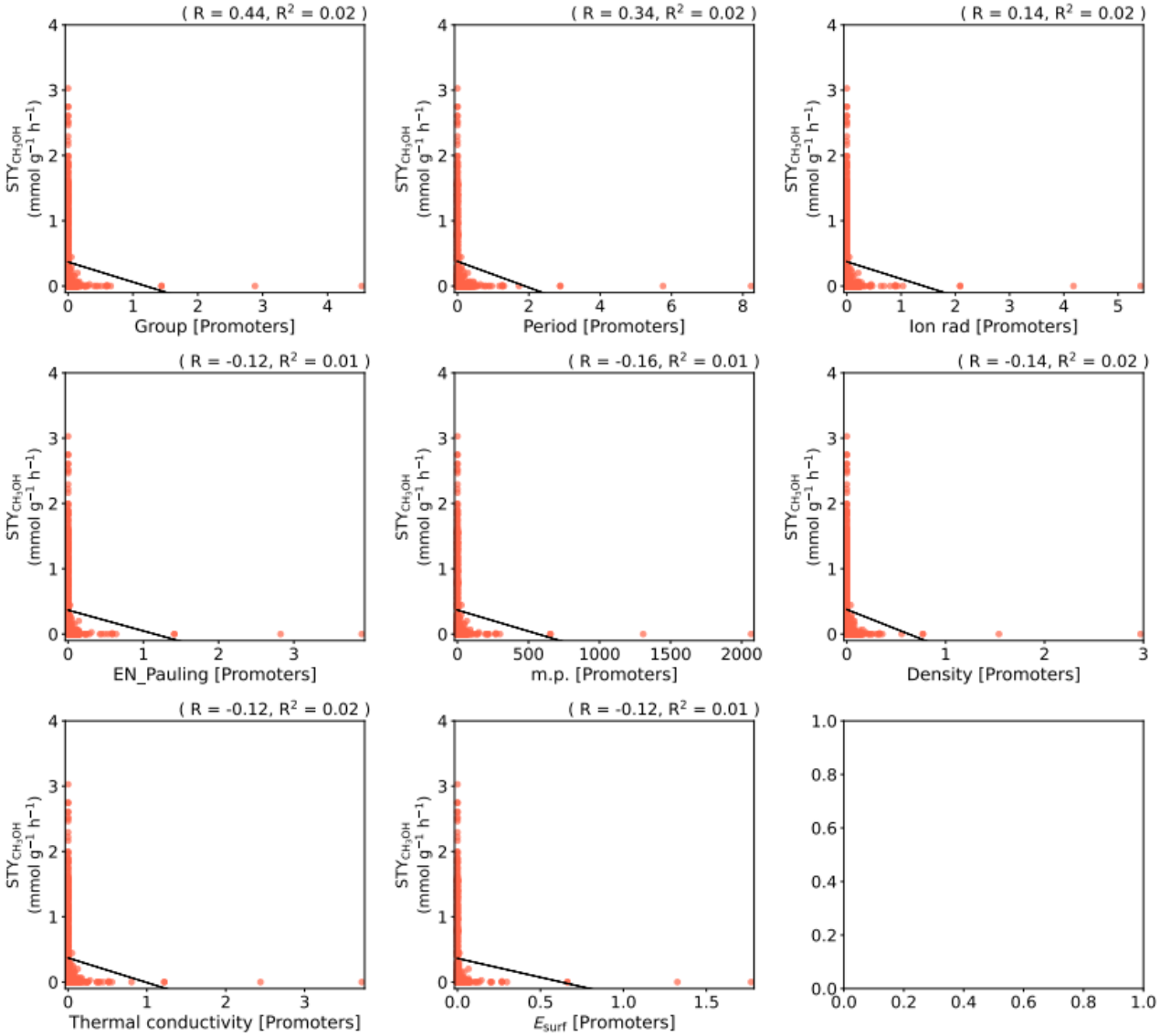

Figure 4.2. Correlation map for the five selected descriptors for the Promoter elements.

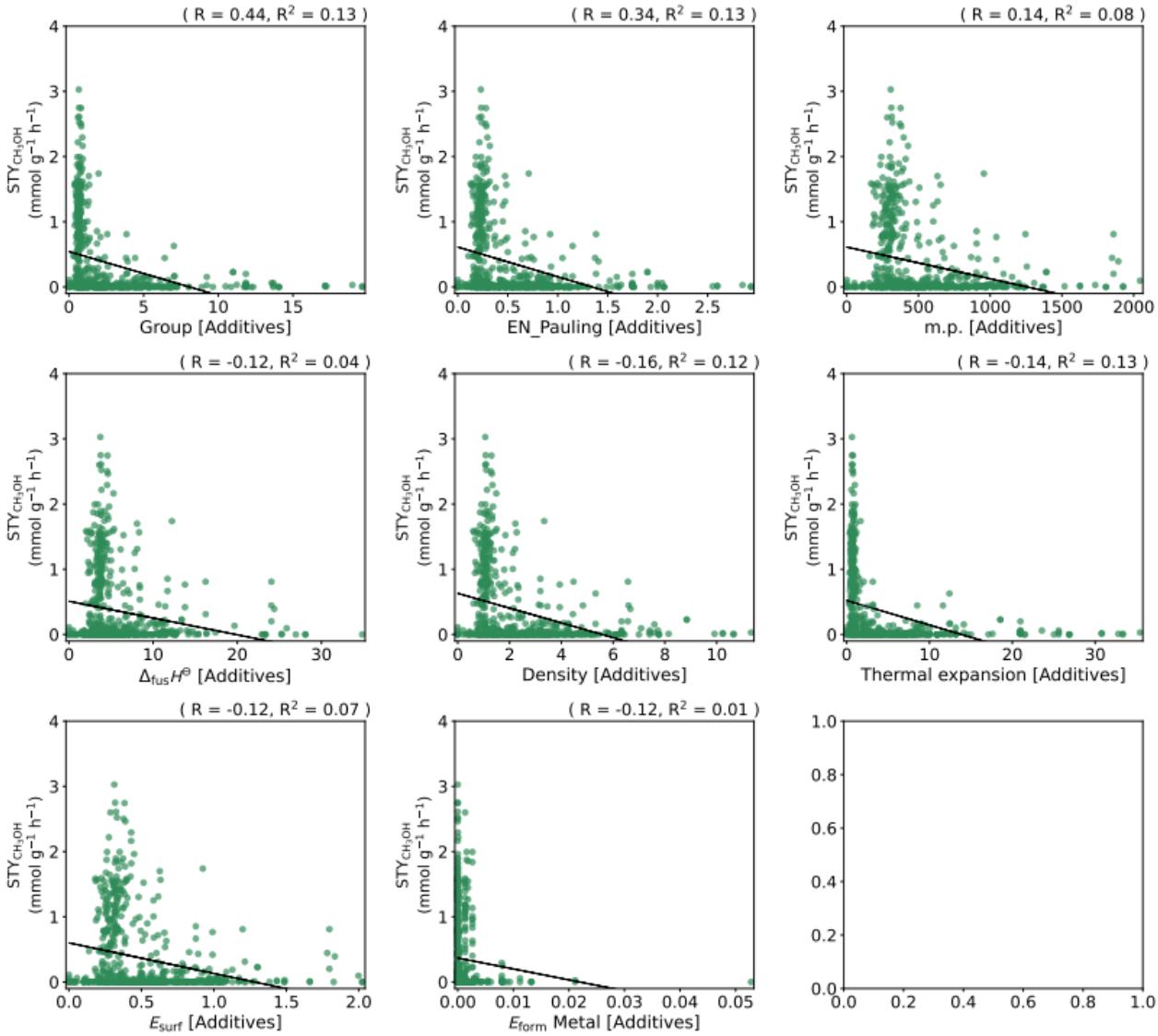

Figure 4.3. Correlation map for the four selected descriptors for the Additive.

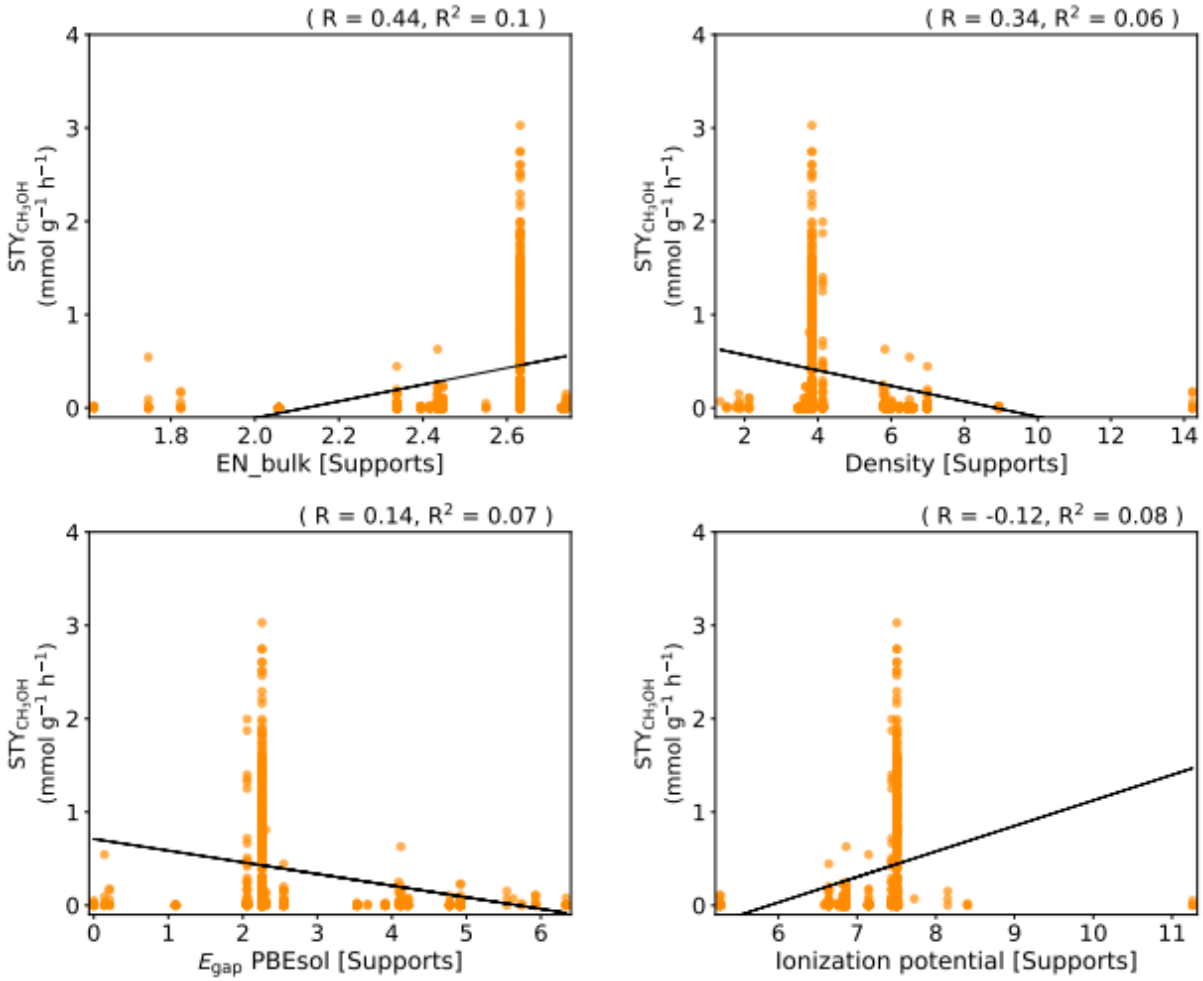

Figure 4.4. Correlation map for the four selected descriptors for the Supports.

As PGM elemental descriptors, we selected the following parameters for the initial exploration of catalysts (catalyst prediction at iteration = 1): Atomic radius (Atom rad), surface energy (E_surf), and adsorption energy of a CO_2 molecule on metallic surfaces (Eads_CO_2) calculated using the Vienna ab initio simulation package (VASP, version 5.4.4).[58,59] The Perdew-Burke-Ernzerhof functional revised for solids (PBEsol)[60] was employed in combination with the projector augmented wave (PAW)[61] method for calculations using VASP. An energy cut-off of 400 eV was used for the plane-wave basis set. Gaussian smearing with a width of 0.2 eV was applied for the occupation of electronic levels. The Brillouin zone was sampled using 2×2×1 Monkhorst-Pack grids. Van der Waals interactions were described using the dispersion-corrected DFT-D3 (BJ) function.[62] The convergence of the force on each atom was set to 0.03 eV Å^{-1}. The most stable and common metallic bulk structures and facets for each element were used.[63]

For PR elemental descriptors, we used the following eight parameters: group, period, ionic radius (Ion rad), pauling of electronegativity (EN_Pauling), melting point (m.p.), density, thermal conductivity, and surface energy (E_surf).[64] Note that these descriptors were presented as representatives and were not used in the post-analysis of the final dataset comprising 730 points.

For Add elemental descriptors, we used the following eight parameters for post-analysis of the final dataset: group, pauling of electronegativity (EN_Pauling), melting point (m.p.), delta fusion enthalpy (d_fus_H), density, thermal expansion, Energy of surface (E_{surf}), E_{form} Metal.[64]

As support descriptors for the support materials, we used the following four parameters for the post-analysis of the final dataset: band gap energy calculated using VASP with the GGA/PBEsol functional (BG_PBEsol), ionization potential, density, and electronegativity of compounds according to Sanderson's definition (EN_bulk).[65,66]

Although other chemical properties were also used as descriptors for elements and supports during the catalyst exploration process, only a representative list of descriptors for each catalyst component is provided in the main text due to space constraints.

Table 4.2. List of descriptors used in the ML-based catalyst exploration and statistical analysis in the present study[a].

Type	Descriptors
PGM	Adsorption energy of a CO_2 molecule on metallic surfaces (Eads_CO_2)
	Surface energy (E_surf)
	Atomic radius (Atom rad)
PR	Group
	Period
	Ionic radius (Ion rad)
	Pauling of electronegativity (EN_Pauling)
	Melting point (m.p.)
	Density
	Thermal conductivity
	Energy of surface (E_{surf})
Add	Group
	Pauling of electronegativity (EN_Pauling)
	Melting point (m.p.)
	Delta fusion enthalpy (d_fus_H)
	Density
	Thermal expansion
	Energy of surface (E_{surf})
	E_{form} Metal
Support	BG_PBEsol
	Ionization potential
	Density
	Bulk of electronegativity (EN_bulk)

[a] Descriptors for PGM shown in this table were used for the initial exploration of the catalysts (prediction of catalysts tested at the iteration = 1), whereas those for Add and Support were used in the post-analysis of the final dataset consisting of 580 points.

The direct input representation (Code number = 0) generated feature vectors with dimensions of 6, 9, 47, and 17 for PGM, Add, and Support, respectively, corresponding to the elements considered in this study (6 for PGM, 9 for PR, 47 for Add, and 17 for Support). Specifically, the representation for Add frequently exhibits high sparsity and lacks statistical significance when the training dataset is small but encompasses a large variety of elements

and supports. Moreover, it struggles to adequately address elements that are missing or statistically underrepresented in the training data.

In contrast, the explorative representation (Code number = 2) maintains a dimensionality equivalent to that of the user-specified elemental descriptor, typically resulting in more statistically stable outcomes for small-data problems. The feature vector dimensions for this representation were three, eight, eight and four for PGM, PR, Add, and Support, respectively, when the element descriptors listed in **Table 4.2** were used. Unlike a direct representation, it is not explicitly restricted to the elements present in the training dataset.

Notably, the explorative representation (Code number = 2) characterizes catalysts based solely on their physicochemical properties using specific descriptors without directly attributing contributions to individual elements. This abstraction enables broader and more exploratory analyses, allowing extrapolations beyond the elements in the training data while focusing solely on the defined physicochemical property space.[56] However, due to its irreversible nature, even if an optimal value is identified within this physicochemical property space, the exact catalyst composition cannot be directly inferred. In a previous study,[50] a method was developed to estimate the potential catalyst composition from elemental property representations. In the current study, we employed a more direct "grid search" approach, systematically testing all possible combinations of elemental loading values and calcination temperature values within a predefined discrete grid, ensuring explicit determination of the original catalyst composition and the calcination temperature.

4.2.4 ML-assisted CO_2 hydrogenation to methanol catalysts discovery

The overall pipeline of our ML-based catalyst exploration is dependent on the sequential model-based optimization we developed.[56,67,68] In this study, we used Extra-Trees regression (ETR)[50] in scikit-learn (version = 1.0.2)[69] as a base ML model and used the expected improvement (EI)[69] score as the guiding acquisition function.

We prepared and tested 90 different catalysts manually, without the assistance of ML, and constructed an initial dataset of 314 points, which was set as "Iteration" = 0. The ML method was trained using the ETR model with the initial dataset (314 points). The EI was calculated for all test points in the catalyst composition grid. Several notable catalyst candidates were chosen based on EI values and catalyst variety. The catalysts were synthesized using the sequential impregnation method. The CO_2 hydrogenation reaction was conducted to determine the "CH_3OH formation rate," which served as the ML prediction target.

The dataset was updated by incorporating the obtained data to close the loop. Subsequently, the ML model was retrained with the updated dataset, and a new set of catalyst candidates was selected for the next experiment. This iterative cycle was repeated 25 times, testing a total of 730 catalysts. During the initial 12 iterations, we used ETR model (with n_estimators=100, keeping the other hyperparameters at scikit-learn's default values) using only the explorative representation (Code number = 2) for PGM, PR, Add, and Support to allocate resources for exploring new candidates (2222 representation). Starting from the 13th iteration, the results up to the *t*th iteration ($t \geq 21$) were considered for representation selection. The best representation up to that point was chosen from all 81 combinations of ijkl, ranging from 0000 to 2222, based on prediction performance evaluated through 10-fold cross-validation. The optimal combination was then used to tune the ETR hyperparameter settings (n_estimators [100, 500, 1000, 1500] and [True, False]) through grid-search cross-validation in scikit-learn, employing 10-fold cross-validation. The ETR model with the highest accuracy was utilized for the (*t*+1)-th exploration, along with 2222 and 1111 representations, and this cycle was repeated. It is important to note that the 2222 representation was consistently used throughout the study, while the 1012 representation was introduced from the 13th iteration onwards as an additional base model for actual catalyst exploration.

In our ML approach, we incorporated human-in-the-loop exploration by utilizing expert judgment to select multiple catalyst candidates in each iteration.[70] It is generally important to consider various objectives and ambiguous criteria, such as novelty, cost, diversity, and the availability of catalyst compositions, when choosing catalysts for experiments. Hence, reducing these considerations to a single formulaic statistic is challenging. To address this issue, our ML system generates a list of the top 100 promising catalyst candidates for each representation, from which the experts select those to advance for catalytic experiments, primarily considering the diversity of constituent elements. Given that it is nearly impossible to test every suggested candidate in real tests, reducing the number of alternatives to this degree makes human selection feasible, because no candidates outside the ML-provided catalysts are considered. Therefore, even if some degree of bias is introduced during the selection process, the method would remain robust because candidates are primarily chosen based on high EI scores, each selected catalyst is still among the top recommendations from the ML model (catalyst candidates with high EI scores are essentially given preference). Following clustering with K = 100 for candidates with the highest EI values, a list of the top 100 candidates for each representation examined at each iteration was produced.

4.3 Results and Discussion

4.3.1 ML-based discovery of catalysts for methanol synthesis

To develop catalysts for low-temperature CO_2 hydrogenation to methanol, we explored PGM elements up to three types additive elements (Add) up to four types and one type of support for the $PGM_1(X_{P1})$–$PGM_2(X_{P2})$–$PGM_3(X_{P3})$/$PR_1(X_{Pr1})$–$PR_2(X_{Pr2})$/$Add_1(X_{A1})$–$Add_2(X_{A2})$–$Add_3(X_{A3})$–$Add_4(X_{A4})$–$Add_5(X_{A5})$/Support_CalcT catalysts (X represents the unique loading amount of PGM and Add elements). We used six PGM elements, 9 PR elements, 47 Add elements, and 17 different supports for this study. Therefore, the total number of catalyst candidates easily exceeded 10^{13} even if only three and four distinct values were considered as the loading amount of PGM and Add elements, respectively, along with nine distinct values for CalcT. An ML model trained on all collected data up to the previous iteration calculated EI values at each grid point in every iteration. The most promising points were recommended to experts for selecting candidates for actual tests in the subsequent iteration.

After experimentally testing 715 predicted new catalysts in total across 25 cycles of a closed-loop discovery system (ML prediction + experiment), we identified several catalysts with performance superior to the previously reported high-performance catalyst Pt(5)/Mo(20)/TiO2.[71] The composition of the best catalyst discovered through this approach was Pt(5)/Mo(8)-Cr(0.7)-V(0.7)-La(0.7)/TiO_2 (P25)_550, demonstrating the highest methanol production rate of 3.0 mmol g_{cat}^{-1} h^{-1} in a flow reactor system (**Table 4.3** Compared to the previous best catalyst,[71] the performance of the best catalyst was much superior under the same reaction conditions using a flow reactor (150 °C, 40 bar, H_2 : CO_2 = 3 : 1).

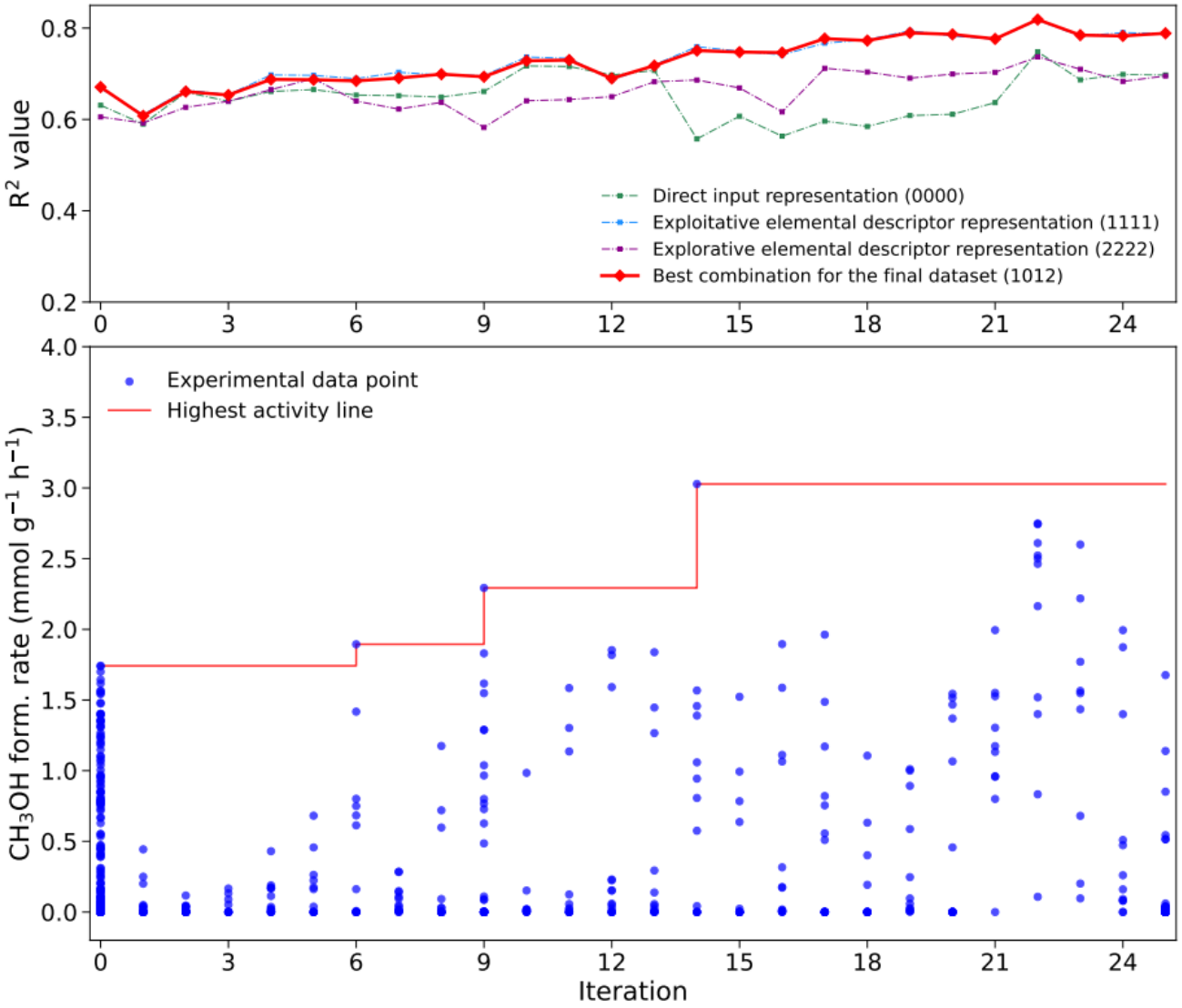

Figure 4.4. ML-assisted catalyst exploration for low-temperature CO_2 hydrogenation to methanol. Catalysts containing elements not included in the original dataset are indicated by diamond-shaped symbols, while those with elements from the original dataset are shown as circle-shaped symbols. The solid orange line represents the highest methanol synthesis activity (methanol formation rate at 150 °C) observed in each iteration. R^2 values were calculated using the 10-fold cross-validation as described in the ML methods section, based on the dataset at each iteration before experimental validation. From left to right, each representation name includes three numbers corresponding to descriptor types for the PGM, PR, Additive, and Support, respectively. A value of 0 represents a direct input representation, which uses only elemental compositions or support name; 1 represents an exploitative representation, which uses both elemental compositions/support name and elemental/support properties; and 2 represents an explorative representation, which uses only elemental/support properties.

In other words, our ML model can not only develop catalysts using known high-performance components but also discover new elements that have not been used before. Our extrapolative ML predictions using explorative representations led to this discovery. The emergence of new elements and supports predominantly occurred during the initial iterations, particularly within the first 12 iterations utilizing only 2222 representations. The appearance

of new elements and supports throughout the iterations was displayed in **Figure 4.5**. To facilitate interpolation across this abstracted representation, our approach incorporates continuous quantities for elemental descriptors defined by user-selected properties (e.g., density and electronegativity). Each element is represented as a distributed representation by several continuous elemental feature values, rather than as discrete, separate symbols.[50,52,72] This makes it possible to take into account similarities between elements based on chemical features, enabling the inclusion of components not present in the training data during the exploration process.

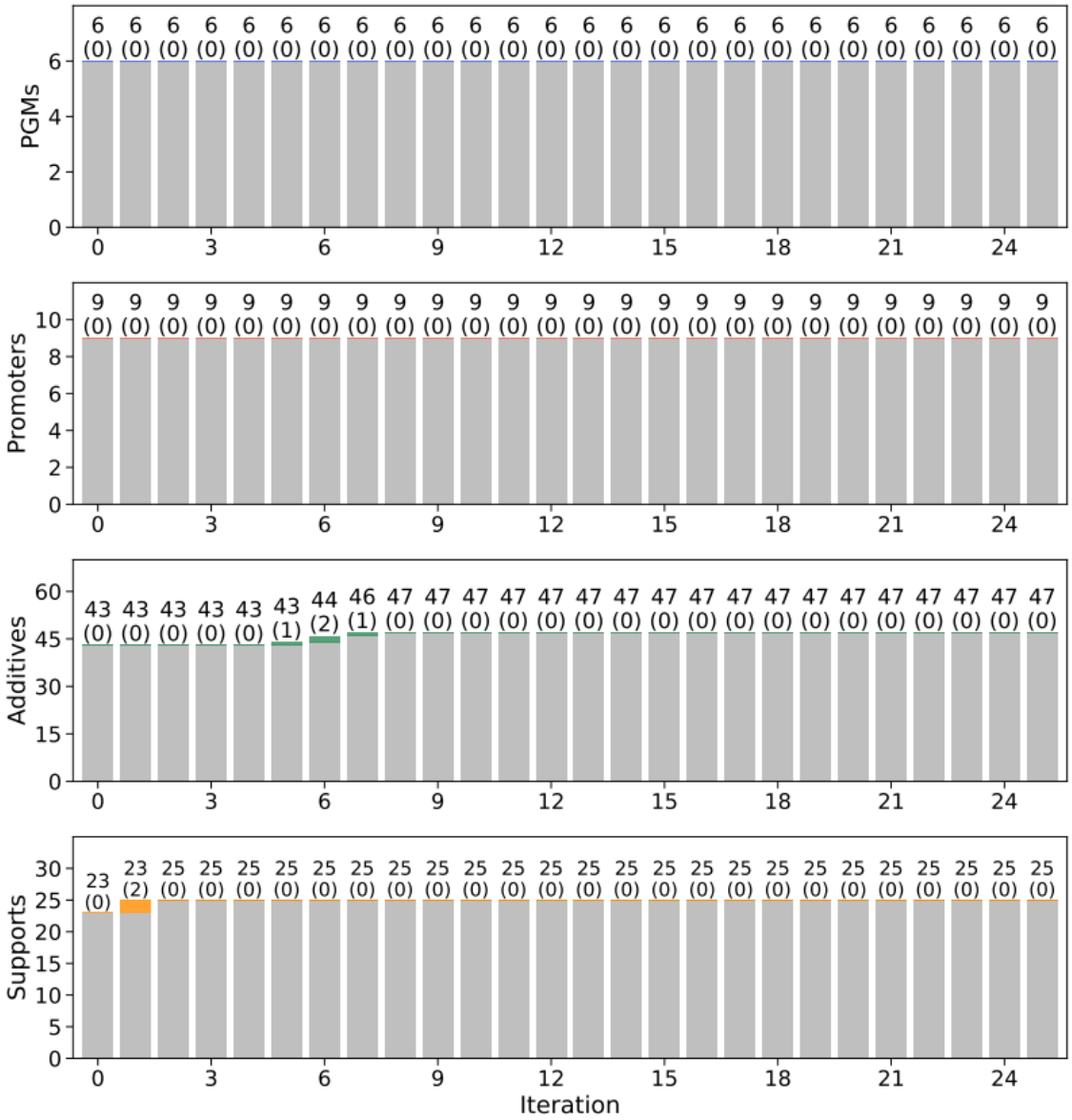

Figure 4.5. Visualization of the number PGMs, additives, and supports appeared for the first time in each iteration. Elements/supports appearing for the first time are shown in color, while those already present are shown in gray. The numbers above indicate the total count of elements/supports present at each iteration, while the numbers in parentheses below represent the count of elements/supports appeared for the first time in that iteration.

Table 4.3. Reports on low temperature (T ≤ 180 °C) CO_2 hydrogenation to methanol.

Catalyst	Additive	T (°C)	P (MPa)	H_2 :CO_2	Space velocity (mL h^{-1} g_{cat}^{-1})	MeOH formation rate (mmol h^{-1} g_{cat}^{-1})	Reaction System	Selectivity (%)			Reference
								MeOH	CO	CH_4	
Homogeneous catalytic system:											
Ru complex & $Sc(OTf_3)$	MeOH	135	4.0	3:1	-	2.5	Batch	Not shown			S[73]
Ru/Triphos	$HNTf_2$	140	8.0	3:1	-	9.2	Batch	Not shown			S[74]
Ru/Triphos	$HNTf_2$	140	8.0	3:1	-	18.4	Batch	Not shown			S[75]
Ru-Macho-BH	PEHA	145	7.5	9:1	-	6.0	Batch	Not shown			S[76]
Co/Triphos	$HNTf_2$	100	9.0	4.5:1	-	2.1	Batch	Not shown			S[77]
Fe(II)/C-scorpionate	PEHA	80	7.5	3:1	-	95	Batch	Not shown			S[78]
Mn(I)-PNP pincer	K_3PO_4	150	8.0	1:1	-	1.0	Batch	Not shown			S[79]
Ru complex	$^{i}Pr_2NH$, NaOEt	100	4.0	3:1	-	4.5	Batch	Not shown			S[80]
Ru-MACHO-BH	PEHA	145	7.0[c]	-	-	2.9	Batch	Not shown			S[81]
Co/modified triphos	$HNTf_2$	100	9.0	3.5:1	-	5.2	Batch	Not shown			S[82]
Heterogeneous catalytic system:											
Cu/ZnO-Al_2O_3	DEEA	100	7.0	6:1	–	0.54	Batch	Not shown			S[83]
Cu-Cr_2CuO_4 & Cu/Mo_2C	EtOH	135	4.0	3:1	–	0.023	Batch	77	Not shown		S[84]
Cu/Mo_2C	–	135	4.0	3:1	–	0.0034	Batch	93	4.1	2.6	S[16]
Pd/Mo_2C	–	135	4.0	3:1	–	0.0046	Batch	95	3.6	1.6	S[16]
Co/Mo_2C	–	135	4.0	3:1	–	0.003	Batch	84	5.7	9.4	S[16]
Pt/Co_3O_4	–	140	8.0	3:1	–	0.05	Batch	Not shown			S[18]
Pt_3Co octapods	–	150	3.2	3:1	–	0.18	Batch	Not shown			S[17]
$Rh_{75}W_{25}$ nanosheets	–	150	3.2	3:1	–	0.004	Batch	Not shown			S[85]
Pt_4Co nanowires/Carbon	–	150	3.2	3:1	–	0.19	Batch	Not shown			S[86]
Pt/MoS_2	–	150	3.2	3:1	–	0.05	Batch	81	Not shown		S[87]
RhCo porous nanosphere	–	150	3.2	3:1	–	0.1	Batch	Not shown			S[88]
Cu/ZnO/Al_2O_3	NEt_3, EtOH	120	6.0	2:1	–	0.874	Batch	Not shown			S[89]
MoS_2 nanosheets	–	120	5.0	3:1	1500	0.28	Flow	>96	-	-	S[8]
MoS_2 nanosheets	–	180	5.0	3:1	15000	4.06	Flow	96	-	-	S[8]
PdCuZnZrBa/Al_2O_3	–	150	3.0	4:1	12000	1.17	Flow	100	0	0	S[9]
B/Cu/ZnO	–	170	7.0	-	1800	1.56	Flow	100	0	0	S[90]
h-PdMo/Mo_2N	–	160	0.1	3:1	30000	0.05	Flow	5.16	93.9	0.94	S[20]
$Cu_{10}Ga_{10}$/SBA-15	–	180	0.5	3:1	15000	0.07	Flow	100	0	0	S[19]
MoS_2-NS	–	140	5.0	3:1	36000	7.81	Flow	＞98	＜1	＜1	S[3]
Cu/MoS_2@SiO_2	–	180	5.0	4:1	8000	2.0	Flow	95	-	5	S[91]
5% Cu-MoS_2	–	180	5.0	4:1	12000	1.82	Flow	87	5	8	S[92]
Mo_3S_4@NaZSM-5	–	150	4.0	3:1	1200	0.26	Flow	>99	-	-	S[15]
h-MoS_2/ZnS	–	160	5.0	4:1	6000	0.53	Flow	>99	-	-	S[93]
$Er_{0.2}$CuZnO	–	170	5.0	3:1	1800	1.53	Flow	90	10	-	S[94]
Pt(5)/Mo(8)-Re(1)-W(0.7)/ TiO_2 (P25)_550	–	150	6.0	5:1	-	1.46	Batch	71	18	11	Chapter 2
Pt(5)/Mo(8)-Re(1)-W(0.7)/ TiO_2 (P25)_550 [c]	–	150	4.0	3:1	8000	1.8	Flow	44	56	<1	Chapter 2
Pt(5)/Mo(8)-Re(1)-W(0.7)/ TiO_2 (P25)_550 [c]	–	150	4.0	3:1	20000	2.8	Flow	32	67	1	Chapter 2
Pt(5)/Mo(10)-Nb(1)/TiO_2	–	150	4.0	3:1	8000	2.2	Flow	40	57	3	Chapter 3
Pt(5)/Mo(8)-V(0.7)-Cr(0.7)-La(0.7)/TiO2 (P25)_550	–	150	4.0	3:1	8000	3.0	Flow	50	49	1	This study

Based on previous experience from Chapter 2 that Re sublimes at high temperatures during calcination, we prepared Pt(5)/Mo(8)-Cr(0.7)-V(0.7)-La(0.7)-Re(1)/TiO_2 (P25)_550 catalyst by loading Re with PGM (after calcining Mo(8)-Cr(0.7)-V(0.7)-La(0.7)/TiO_2 (P25) at 550 °C) after loading the other elements and calcining the support. The catalyst's activity was significantly improved. We also investigated the effect of each additive element and confirmed that the best activity was achieved when all additive elements (Mo, Re, Cr, V and La) coexisted (**Figure 4.6**).

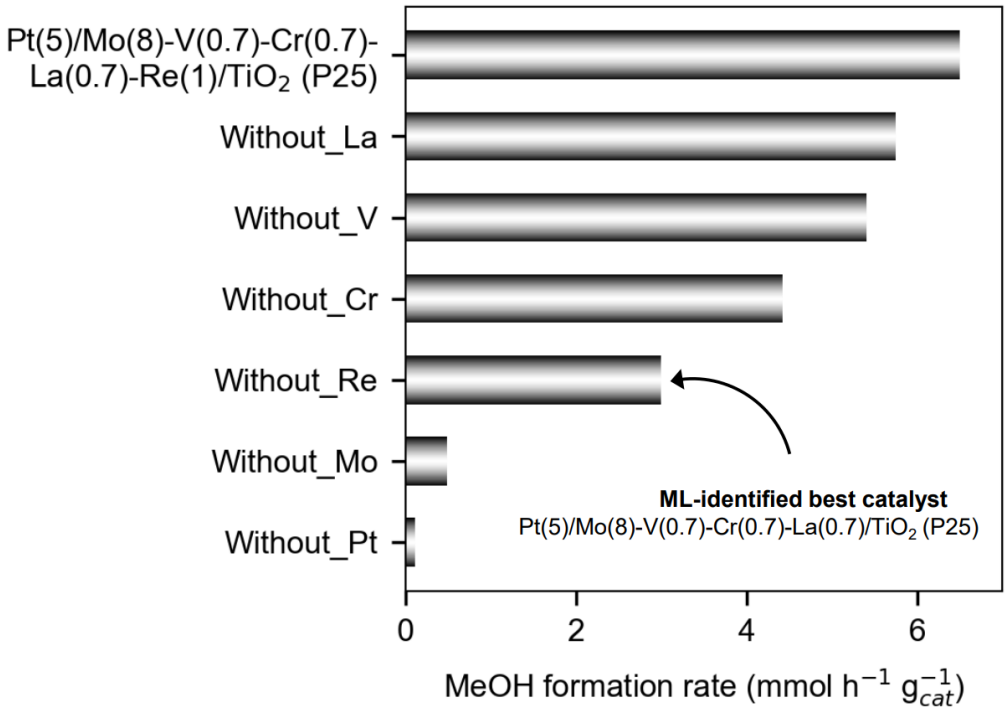

Figure 4.6. Effect of additive elements on the MeOH formation rate. Reaction conditions: 150 °C, 4 MPa, H_2 : CO_2 =3 : 1, 8000 mL $h^{-1}g_{cat}^{-1}$.

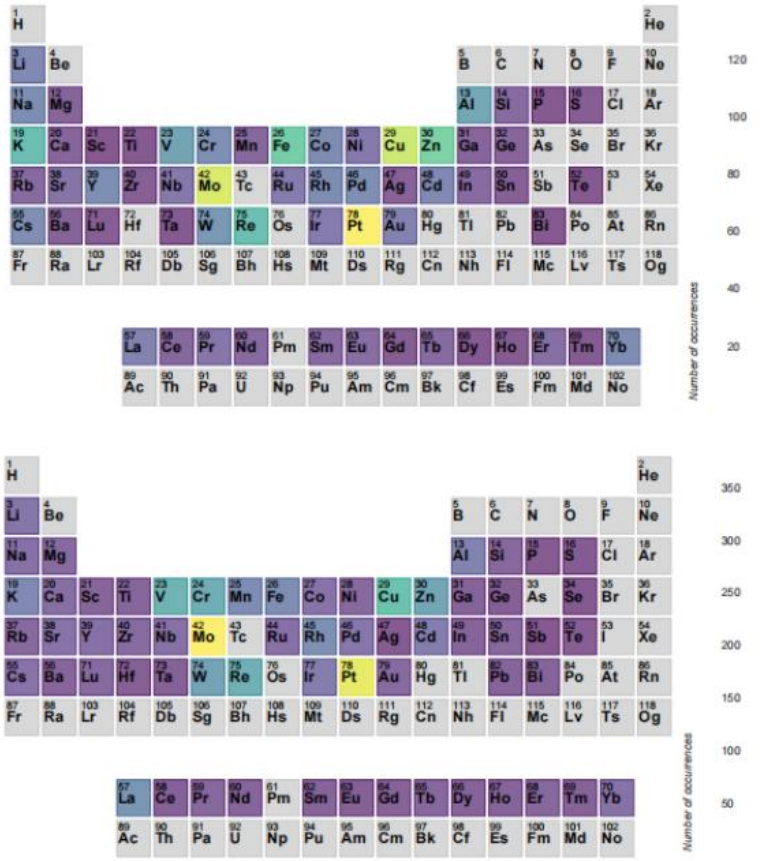

Figure 4.7. The elements in the (A) original and (B) final datasets are shown in the periodic tables.

Figure 4.4 display the variations in prediction accuracies of the ML models with different choices of representation (0000, 1111, 2222, and 1022) for each iteration. A 10-fold cross-validation, based on the data collected up to that iteration, was used to calculate the prediction accuracy (R^2, MAE, RMSE, and MSE) of each iteration. We used only the 2222 representation method for the first 20 iterations of the exploration process. Subsequently, we incorporated 1111, 2222, and the best model at each iteration according to the evaluated prediction accuracy. Identifying effective catalysts posed an initial challenge due to the low prediction accuracy of the ML model in the early stages, stemming from the difficulty in predicting catalytic results from a small and diverse set of examples. However, we were able to identify good catalysts as the volume of data grew and the prediction accuracy increased. In the realm of ML, this phenomenon is commonly referred to as the exploration-exploitation trade-off, emphasizing the requirement of balance between "exploration" to gather additional data on unknown parts and "exploitation" to utilize the existing data. Our strategy of using

2222 during the initial phase and subsequently transitioning to the best model based on prediction accuracy after the initial 20 iterations exemplified this trade-off.

The goal of this study was to employ an iterative and sequential experimental design, even if our dataset is small (715 data points) and the best prediction accuracy achieved after 25 cycles (R^2 = 0.79) is not significantly high. As a result, more attention is paid to optimizing the utilization of the available data (even though they are relatively small in size from a statistical perspective) to plan future experiments for identifying superior catalysts.[95] Thus, we believe that the prediction accuracy achieved through a standard approach (up to R^2 = 0.79) would suffice for statistically guiding the direction of forthcoming research.

Figure 4.8 displays histograms for each (A) Additive, (B) PGM, (C) PR and (D) Support component, along with the catalyst calcination temperature, categorized by their methanol synthesis activity (CH_3OH formation rate (mmol g^{-1} h^{-1}) at 150 °C). Pt appeared most frequently among the PGM, while Mo, V, Cr, La and Re appeared frequently among the additive elements. For support, TiO_2 (P25) (a mixture of anatase and rutile)[96] was the most frequent. These elements and supports are frequently associated with a higher proportion of highly active catalysts. These trends are also depicted in the boxplots for visualization of CO_2 hydrogenation to methanol catalyst (**Figure 4.8**). To gain further insights into the catalytic system, the impacts of the loading amounts of PGM and Add elements, as well as the descriptor values of the Add elements, on the CH_3OH formation rate are summarized in **Figure 4.9-4.11**. Catalysts with relatively low loading of additive oxides (below 2%, except for Mo; optimal loading of Mo is over 5 wt%) tend to exhibit a high CH_3OH formation rate. **Figure 4.12D** indicates that catalysts calcined at 500–600 °C constituted a significant portion of highly active catalysts. It should be noted that by incorporating CalcT as an input variable in our ML model, a broader design space of both catalyst composition and preparation parameters was taken into account as compared to the design space when only catalyst composition was considered.

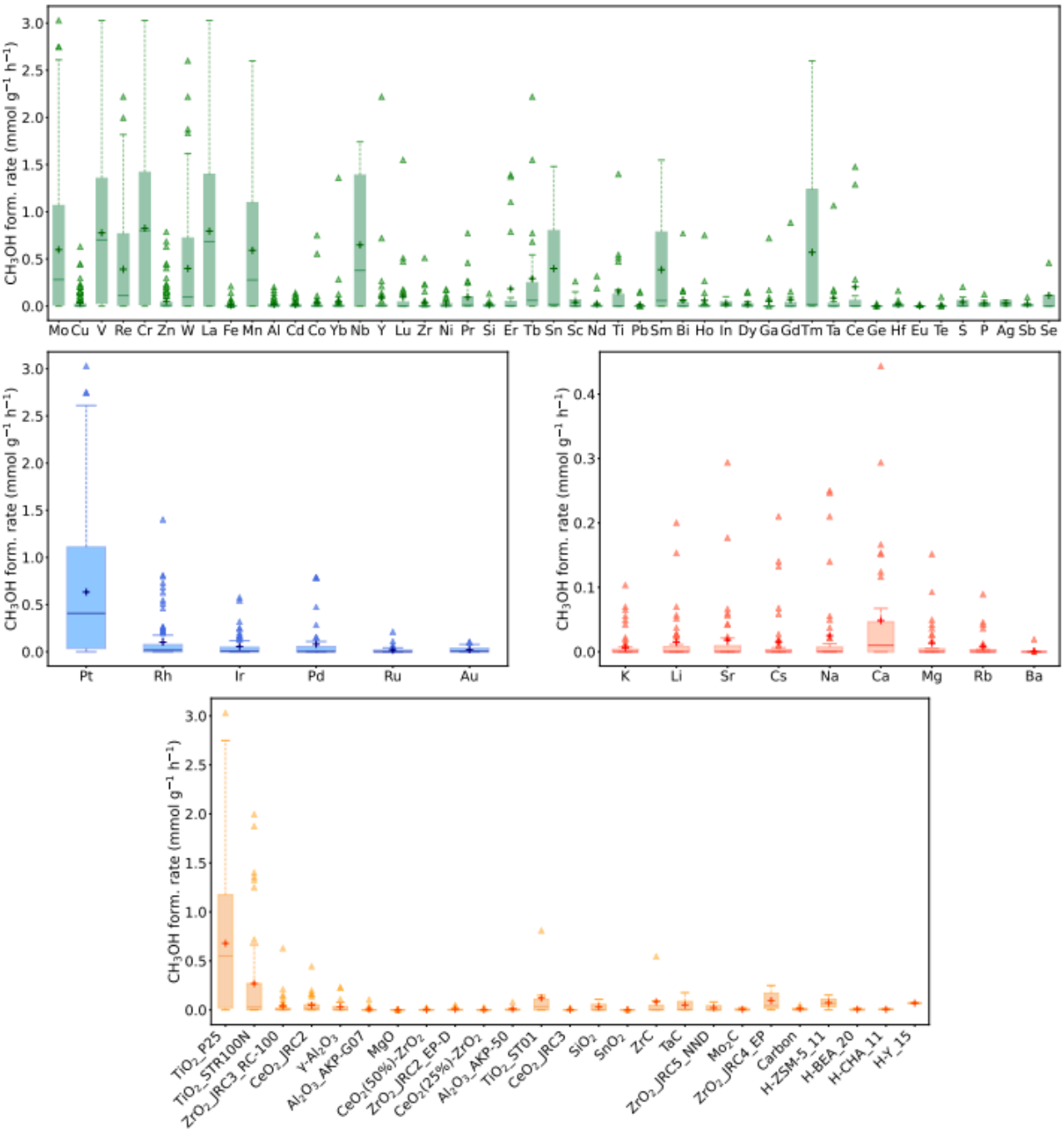

Figure 4.8. Visualization of methanol formation catalyst datasets. Boxplot for each additive oxide component. The boxes represent the interquartile range, spanning from the first quartile to the third quartile, with a horizontal line indicating the median. Whiskers extend up to 1.5 times the interquartile range, encompassing the largest and smallest observed data points falling within this range. Individual data points are displayed as dots.

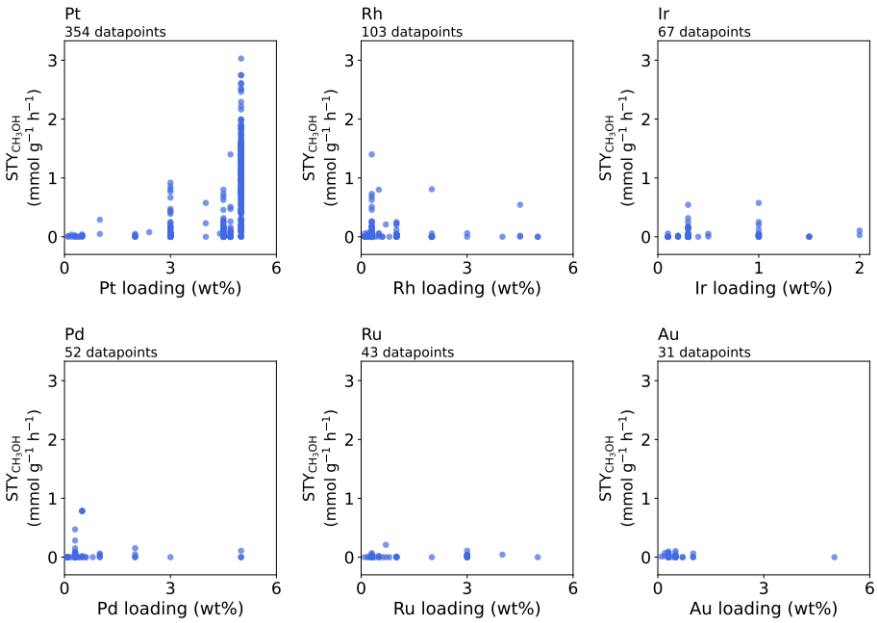

Figure 4.9. Effects of the loading amount of PGM elements on the CH_3OH formation rate.

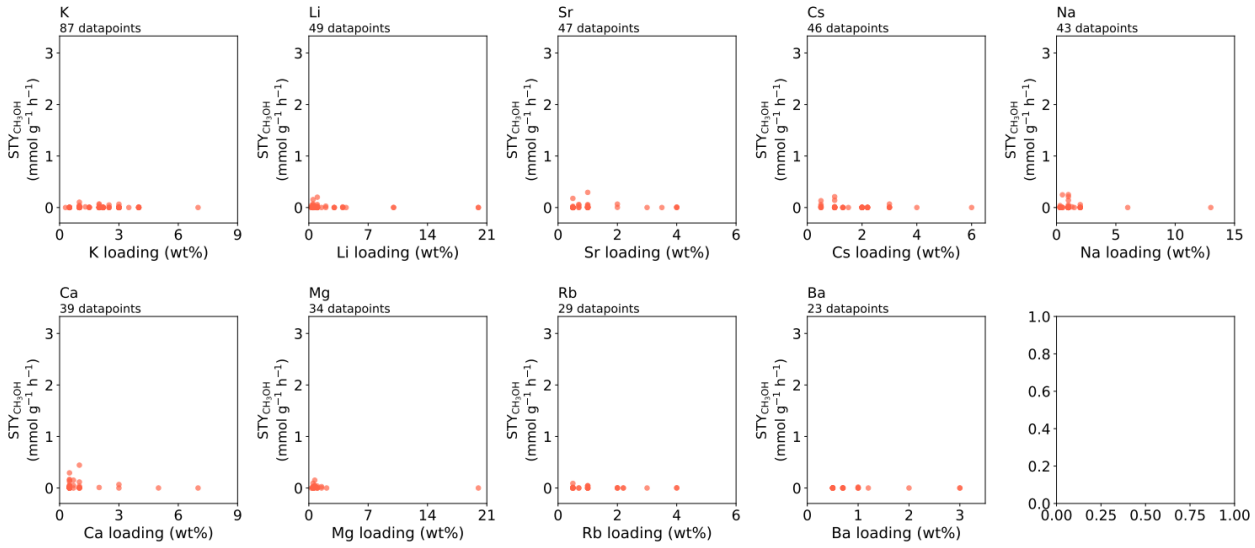

Figure 4.10. Effects of the loading amount of Promoter elements on the CH_3OH formation rate.

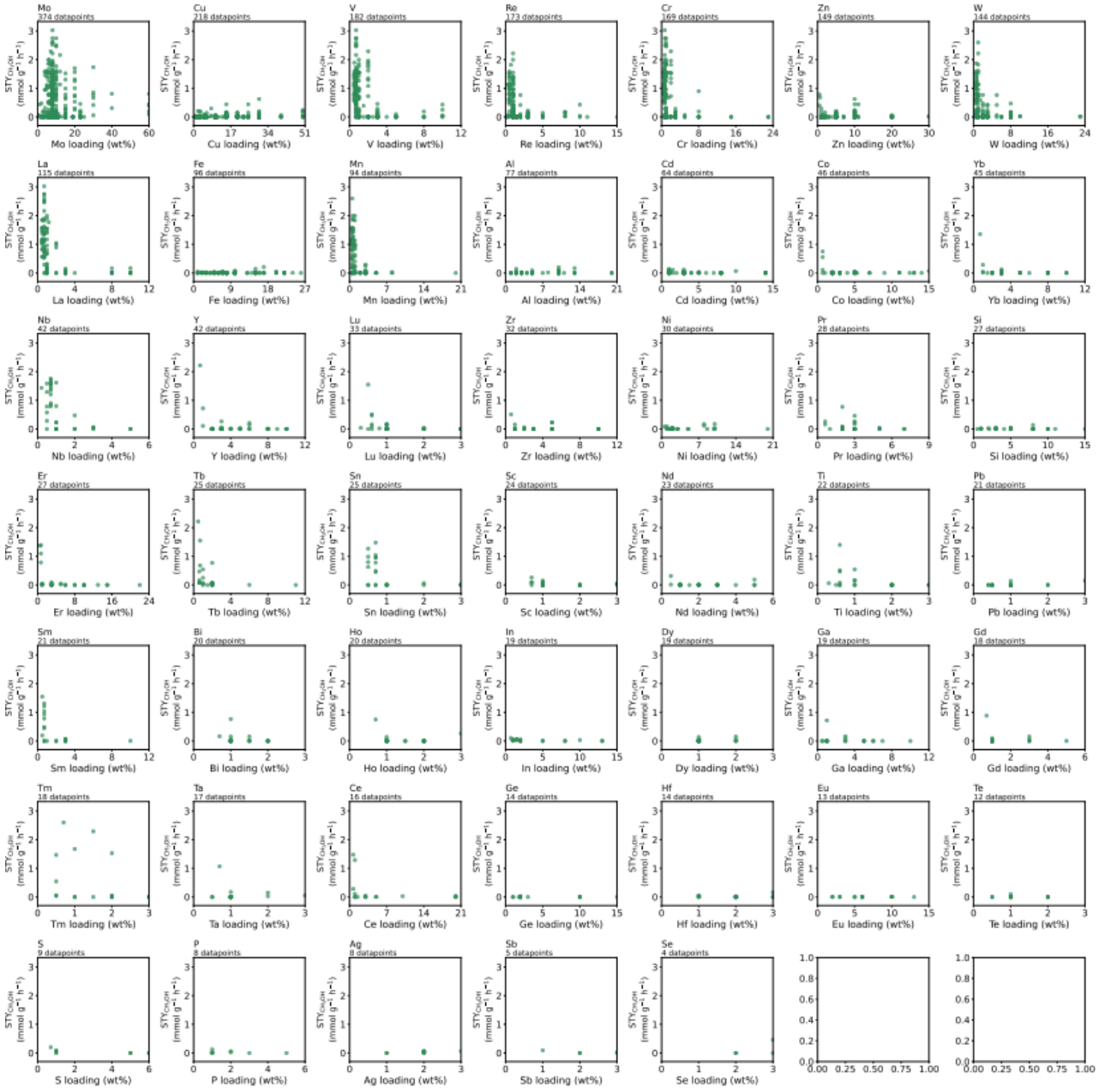

Figure 4.11. Effects of the loading amount of Additive elements on the CH_3OH formation rate.

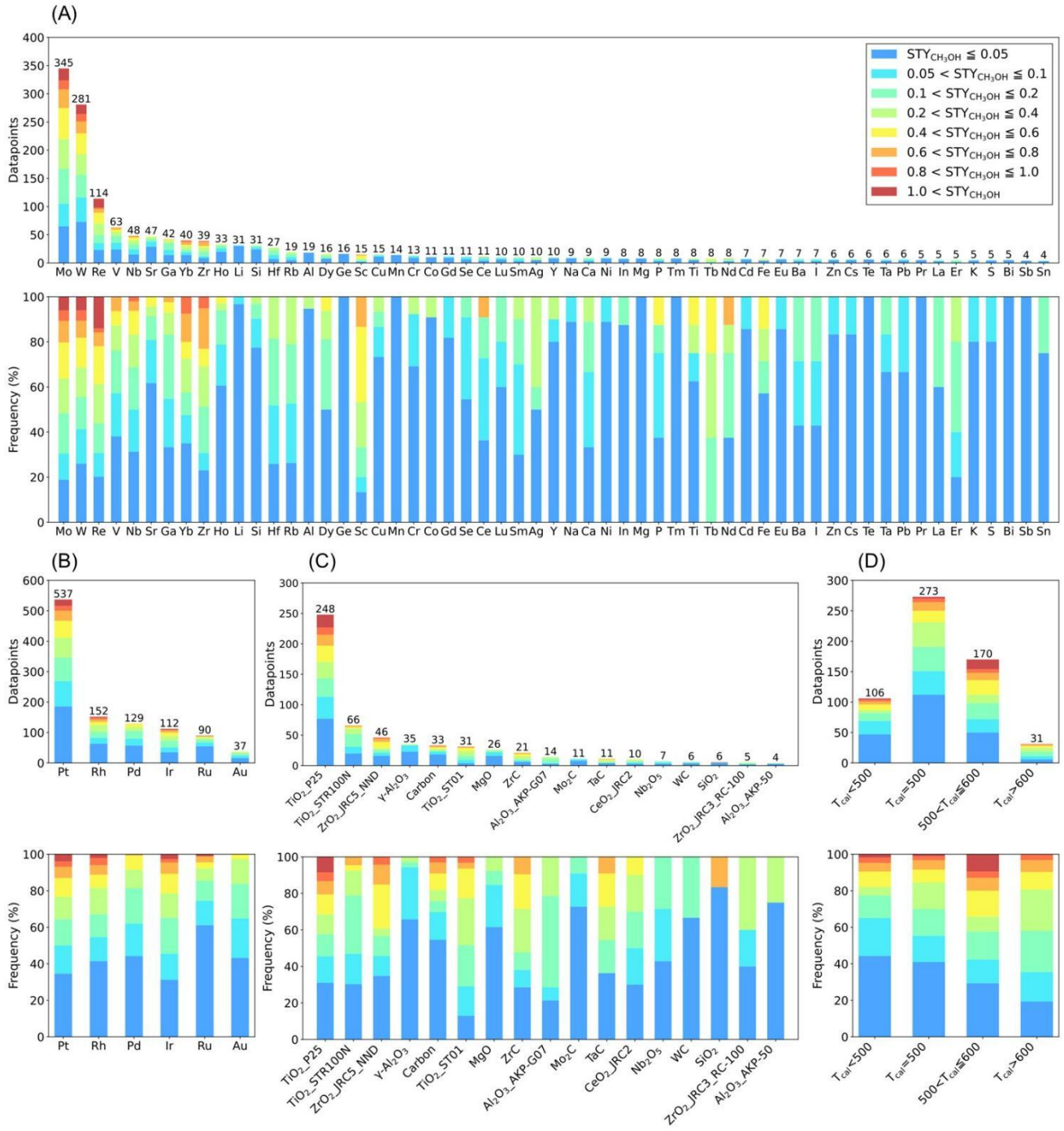

Figure 4.12. Histograms for each (A) Add, (B) PGM, and (C) Support components, along with (D) calcination temperature, categorized by methanol synthesis activity (methanol formation rate at 150 °C). The upper panels show the absolute number of data points for each category, while the lower panels indicate the percentage distribution across methanol synthesis activity levels. The maximum Y-axis values in the top figures reflect the sum of the number of data points, while those in the bottom figures represent percentage of catalysts within each methanol formation rate category.

4.3.2 ML-based statistical analysis (post hoc analysis)

Although ML is often utilized as a black box, supervised ML models can reveal significant chemical insights that impact predictions, even without detailed knowledge of the underlying mechanisms.[97–99] Besides identifying effective catalyst compositions, our extrapolative ML approach can offer essential elemental features and electronic properties crucial for designing optimal catalysts accurately. To assess the importance of each descriptor in ML predictions, we conducted a post hoc analysis using SHapley Additive exPlanations (SHAP) on all 715 data points, as shown in **Figure 4.13**.[100–103] The thermal expansion of additive elements (thermal expansion [Additives]) and the calcined temperature were identified as important features for predicting the CH_3OH formation rate (**Figure 4.13**). SHAP analysis was used to understand the dependence of model output (e.g., CH_3OH formation rate) on the value of each descriptor.[50] For example, relatively high feature values (highlighted in red in **Figure 4.13**) for “Pt” and “TiO_2_P25” correlated with a high methanol formation rate (SHAP value), indicating a positive impact of these elements on achieving high activity.

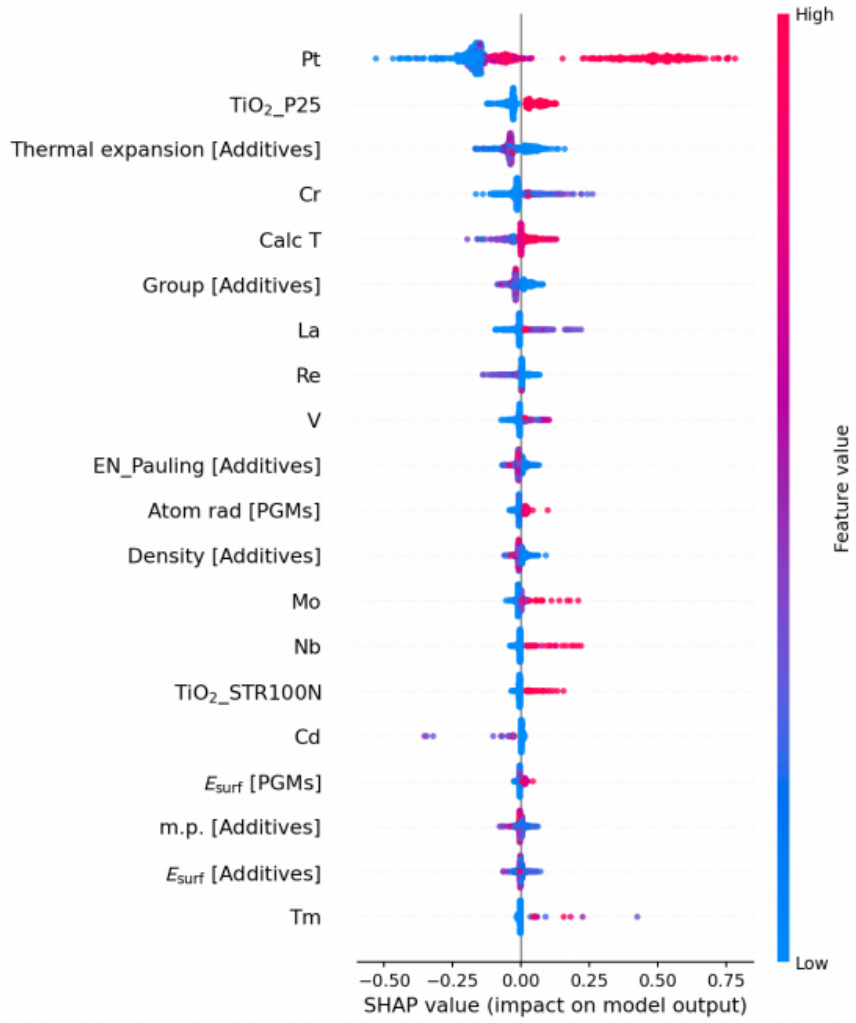

Figure 4.13. SHAP values of the descriptors (summary plot) used to predict CH_3OH formation rates of all the 730 catalysts in our final dataset as a post hoc analysis (red and blue for SHAP analysis correspond to high and low features, respectively). Features are in descending order based on the sum of their absolute SHAP values. The vertical dispersion of dots indicates the density of data points at a given SHAP value. each feature are shown in red and blue, respectively. The explorative elemental descriptor representation was used in the analysis.

4.3.3 Catalyst characterization

After confirming the high activity of the Pt(5)/Mo(8)-Cr(0.7)-V(0.7)-La(0.7)-Re(1)/TiO_2 (P25)_550 catalyst, various characterization techniques were utilized to investigate the structural details of the catalyst in operation. In the X-ray diffraction (XRD) pattern (**Figure 4.14**), both anatase and rutile phases were observed for the pristine TiO_2 (P25). Upon loading the Mo, Cr, V, La and Re species onto TiO_2 (P25), Mo(8)-Cr(0.7)-V(0.7)-La(0.7)-Re(1)/TiO_2 (P25)_550 showed the presence of MoO_3. Peaks corresponding to the Re and W species were not observed. Similar observations were made for the unreduced Pt(5)/Mo(8)-Cr(0.7)-V(0.7)-La(0.7)-Re(1)/TiO_2 (P25)_550, suggesting that in the unreduced state, the Mo species

exists as crystalline MoO_3. Simultaneously, the absence of structural features for Pt, Re and W indicates that these species were highly dispersed on the TiO_2 (P25) surface. Following reduction at 300 °C, the MoO_3 peaks disappeared, and only the peaks for TiO_2 (P25) were observed, indicating the loss of crystallinity of the Mo oxides under the reduction conditions. It is important to note that even in the reduced sample, Pt, Re, and W species remained highly dispersed.

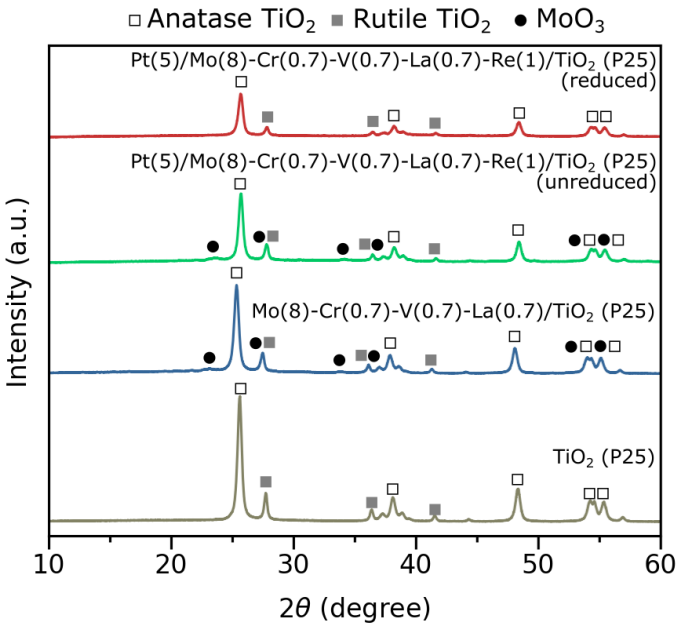

Figure 4.14. XRD patterns of pristine Pt(5)/Mo(8)-Cr(0.7)-V(0.7)-La(0.7)-Re(1)/TiO_2 (P25)_550 (after H_2 reduction), Pt(5)/Mo(8)-Cr(0.7)-V(0.7)-La(0.7)-Re(1)/TiO_2 (P25)_550 (before H_2 reduction), Mo(8)-Cr(0.7)-V(0.7)-La(0.7)-Re(1)/TiO_2 (P25)_550, and TiO_2 (P25)_ 550. 550 is the calcination temperature (°C).

High-angle annular dark-field scanning transmission electron microscopy (HAADF-STEM) was employed to further clarify the structure of the reduced Pt(5)/Mo(8)-Cr(0.7)-V(0.7)-La(0.7)-Re(1)/TiO_2 (P25)_550 catalyst (**Figure 4.15**). Highly dispersed Pt nanoparticles were observed with an average size of 2.3 nm. Notably, large individual oxide particles of Mo, Re, V, Cr and La were not observed (**Figure 4.15** and **4.16**). According to the energy-dispersive X-ray spectroscopy (EDX) mapping analysis of Pt, bright nanoparticles in the HAADF-STEM image were Pt nanoparticles highly dispersed over the TiO_2 surface. It is worth mentioning that TiO_x overlayer formation over the Pt nanoparticle indicative of strong metal-support interaction (SMSI)[104] was not observed. Furthermore, CO adsorption band clearly observed over Pt nanoparticles (vide infra) during *in situ/operando* DRIFTS analyses also suggests that Pt surface was not covered by TiO_x species and remained accessible to

reactant molecules. In addition, EDX mapping of Mo, Re, V, Cr and La species suggested their high dispersion on the TiO_2 surface, consistent with XRD analysis of the reduced catalyst.

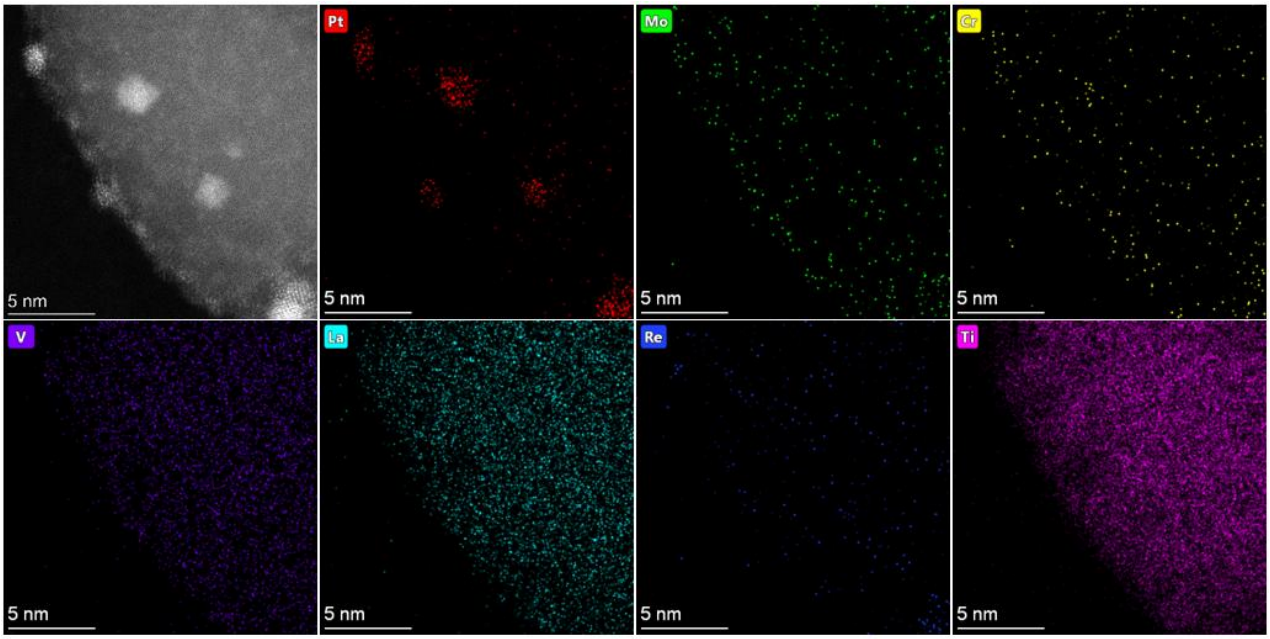

Figure 4.15. HAADF-STEM image and EDX mapping images of Pt(5)/Mo(8)-Cr(0.7)-V(0.7)-La(0.7)-Re(1)/TiO_2 (P25)_550 after reduction at 300 °C. The Pt, Mo, Re, W, and Ti signals are related to the catalyst composition.

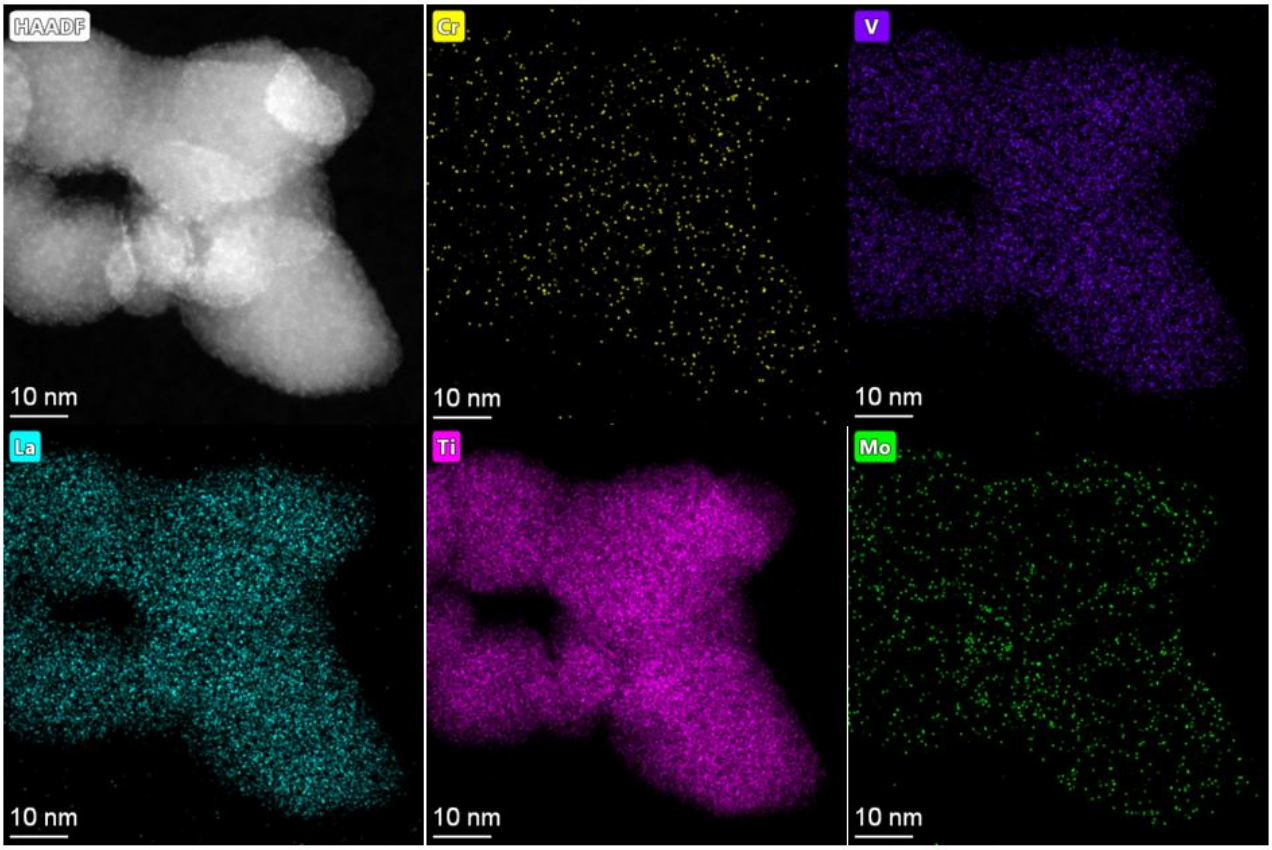

Figure 4.16. HAADF-STEM image and EDX mapping images of Mo(8)-Cr(0.7)-V(0.7)-La(0.7)-Re(1)/TiO_2 (P25)_550 after reduction at 300 °C. The Pt, Mo, Re, W, and Ti signals are related to the catalyst composition.

To understand the chemical environments of Pt, Mo and Re in the Pt(5)/Mo(8)-Cr(0.7)-V(0.7)-La(0.7)-Re(1)/TiO_2 (P25)_550 catalyst, *in situ*-X-ray absorption spectroscopy (XAS) analysis was carried out. It should be noted that because the best catalyst developed in this study contains multiple elements, we selected and measured absorption edges that could be analyzed without overlapping other absorption edges for each element (V and Cr could not be analyzed due to the same reason). The result of Pt L_3-edge and Mo K-edge were as same as the Pt(5)/Mo(8)–Re(1)–W(0.7)/TiO_2 and the Pt(5)/Mo(10)-Nb(1)/TiO_2 catalysts as discussed in Chapter 2 and 3 respectively indicating that Pt was present as metallic Pt species while Mo was present as partially reduced MoO_x species and showed redox behavior.[57,105] Re L_3-edge as shown in **Figure 4.17** indicates a slight redox behavior of ReO_x under reaction condition.

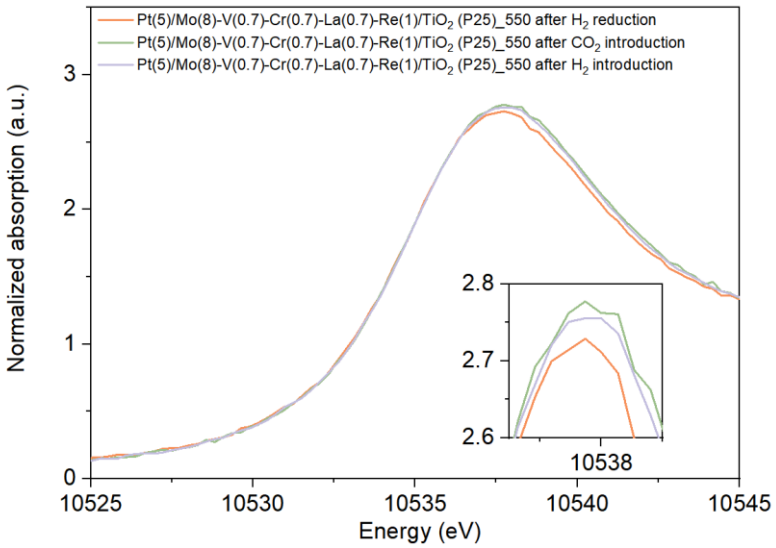

Figure 4.17. *In situ* XANES measurements of Re L_3-dege for the Pt(5)/Mo(8)-Cr(0.7)-V(0.7)-La(0.7)-Re(1)/TiO_2 (P25)_550 catalyst conducted at 150 °C.

In summary, in the unreduced catalyst, all elements were in oxide forms, while under reaction conditions, Mo and Re existed as highly dispersed partially reduced oxides, Pt was present as metallic Pt nanoparticles on the TiO_2 surface, and Mo still exhibits a redox mechanism.

Furthermore, we compared the H_2-temperature programmed reduction (H_2-TPR) profile of the best catalyst with that of the control catalyst (**Figure 4.18**). Without Pt, the Mo(8)-Cr(0.7)-V(0.7)-La(0.7)-Re(1)/TiO_2 (P25)_550 catalyst exhibited reduction peaks at higher temperatures compared to the Pt containing best catalyst. Pt underwent reduction at a significantly lower temperature and facilitated the reduction of other species during pretreatment at 300 °C, and Mo, Cr, V, and Re should be present as partially reduced oxide. This observation aligns with the XANES results.

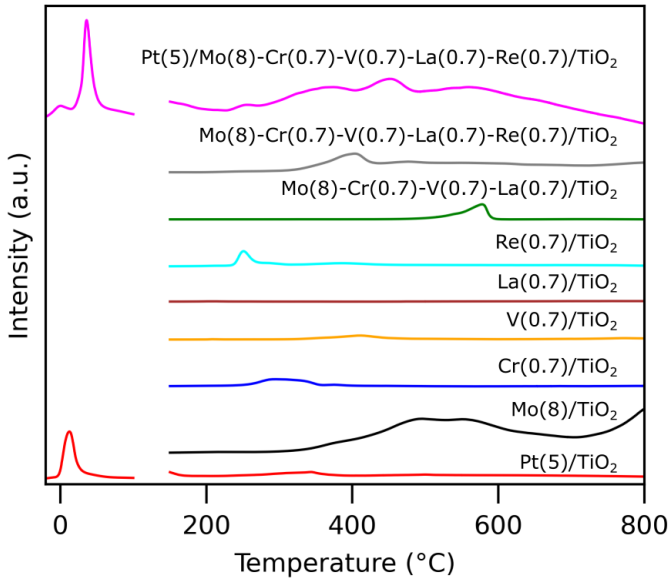

Figure 4.18. H_2-TPR profiles of Pt(5)/Mo(8)-Cr(0.7)-V(0.7)-La(0.7)-Re(1)/TiO_2 (P25)_550, Mo(8)-Cr(0.7)-V(0.7)-La(0.7)-Re(1)/TiO_2 (P25)_550, Mo(8)-Cr(0.7)-V(0.7)-La(0.7)- /TiO_2 (P25)_550, Mo(8)/TiO_2 (P25), Pt(5)/TiO_2 (P25), Re(1)/TiO_2 (P25), La(0.7)/TiO_2 (P25), V(0.7)/TiO_2 (P25) and Cr(0.7)/TiO_2 (P25).

4.3.4 Mechanistic study

CO_2 hydrogenation to methanol can occur through two distinct mechanisms: (i) through the formate intermediate, and (ii) through the RWGS reaction combined with the CO hydrogenation pathway.[106–108] Our previous research demonstrated that a Pt/MoO_x/TiO_2 catalyst primarily generated methanol mainly using the formate intermediate.[71] The rate of methanol production via CO hydrogenation was lower compared to direct CO_2 hydrogenation. In this study, *operando* diffuse reflectance infrared Fourier-transform spectroscopy (DRIFTS) was employed to investigate the surface adsorbates involved in the catalytic processes of methanol synthesis over Pt(5)/Mo(8)-Cr(0.7)-V(0.7)-La(0.7)-Re(1)/TiO_2 (P25)_550 (**Figure 4.19A**). Upon the introduction of CO_2, spectral bands corresponding to surface adsorbates such as carbonate and formate immediately appeared in the 1800–1200 cm^{-1} range, concomitant with the appearance of adsorbed CO, as suggested by bands observed at 2100–1950 cm^{-1}. Bands around 1550, 1388, and 1369 cm^{-1}, along with bands in the 2800–2980 cm^{-1} region, were assigned to ν(CH), indicating the formate formation.[109] Notably, formate formation in the absence of H_2 should be attributed to the presence of dissociated hydrogen species on the surface during H_2 pretreatment. Formate was found to be a prevalent species on the surface. Following H_2 introduction, the intensity of the 1550 cm^{-1} formate band initially increased and then decreased. The emergence of the 1110 cm^{-1} peak indicated methoxy species formation. The evolution of methanol yield (determined by GC at the outlet)

corresponded to the intensity of the formate peak in the DRIFTS spectrum, illustrating a direct correlation between surface formate species and methanol production (**Figure 4.19B**). Moreover, the adsorbed CO species decreased as the CO yield gradually increased, as detected by GC at the outlet. These findings suggest that methanol was predominantly produced via the formate pathway over the best catalyst, and CO did not serve as an intermediate in methanol production.

We have also conducted *in situ*-DRIFTS under reaction conditions from 1 bar to 20 bar (**Fugrue 4.19C**). With increasing pressure, the absorption of methoxy becomes clearly visible. For the other picks, the spectrum at 20 bar shows similar features as observed at 5 bar. This indicates that the mechanism did not change under high pressure.

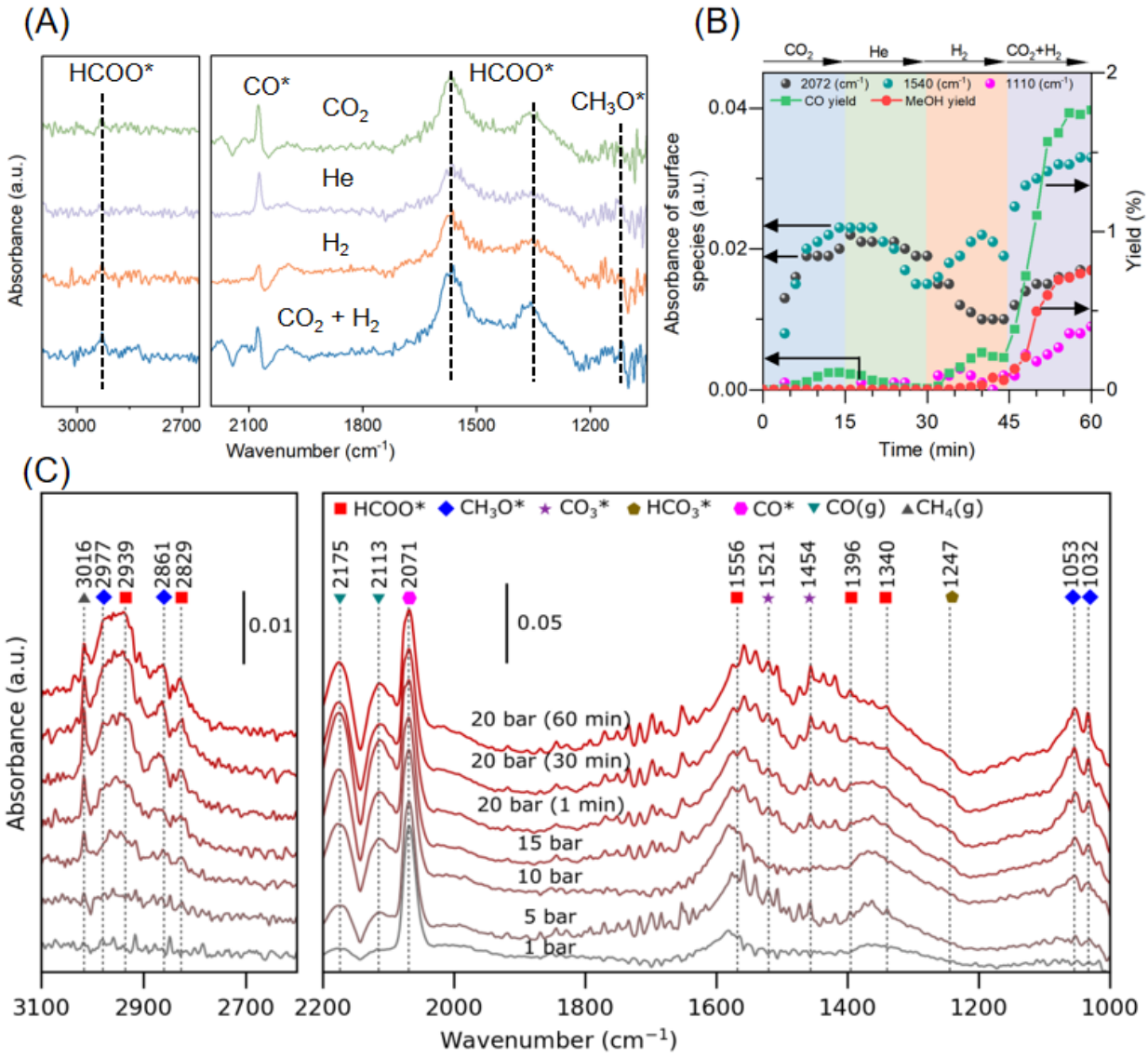

Figure 4.19. (A) *Operando* DRIFTS analyses of the Pt(5)/Mo(8)-Cr(0.7)-V(0.7)-La(0.7)-Re(1)/TiO_2 (P25)_550 catalyst conducted under a sequential flow of CO_2/He, He, H_2/He, and 25% CO_2 + 75% H_2 at 150 °C. (B) Temporal changes in the intensities of the DRIFTS peaks associated with surface-adsorbed species and the CO concentration in the effluent following CO_2 introduction. (C) *in situ*-DRIFTS for the Pt(5)/Mo(8)-Cr(0.7)-V(0.7)-La(0.7)-Re(1)/TiO_2 (P25)_550 under reaction conditions from 1bar to 20 bar.

To gain further insights into role of different elements in the methanol formation reaction, *in situ* DRIFTS analysis was conducted under the reaction conditions using various control catalysts and compared with the outcomes obtained with the best catalyst (**Figure 4.20**). The Mo(8)-Cr(0.7)-V(0.7)-La(0.7)-Re(1)/TiO_2 (P25)_550 catalyst, without Pt, displayed minimal formate (1550 cm^{-1}), methoxy (1110 cm^{-1}), or adsorbed CO intermediates (2065 cm^{-1}) (**Figure 4.20** and **4.21**), highlighting Pt as the primary hydrogen-dissociating component. In the absence of Mo, the Pt(5)/ Cr(0.7)-V(0.7)-La(0.7)-Re(1)/TiO_2 (P25)_550 catalyst showed

weak formate and methoxy formation but a substantial presence of adsorbed CO. This suggests that the partially reduced MoO_x species predominantly facilitated oxygenate formation for methanol production, supporting the *operando* DRIFTS and *in situ* XAS findings. Conversely, in the absence of Re, the Pt(5)/Mo(8)-Cr(0.7)-V(0.7)-La(0.7) /TiO_2 (P25)_550 (P25) catalyst exhibited high formate intensity and reduced methoxy intensity. Moreover, higher formate intensity and lower methanol yield was observed during *operando* DRIFTS analysis over Pt(5)/Mo(8)-Cr(0.7)-V(0.7)-La(0.7) /TiO_2 (P25)_550 catalyst than that over the best catalyst (**Figure 4.21**). These results indicate that the introduction of Re promoted the formate hydrogenation step to produce methoxy species. When La is absent, band intensity of carbonate, formate and methoxy were lower indicating that LaO_x promoted CO_2 activation. For the role of V and Cr, we performed the DRIFTS under the same conditions, however, the mechanisms involving Cr and V were still unclear.

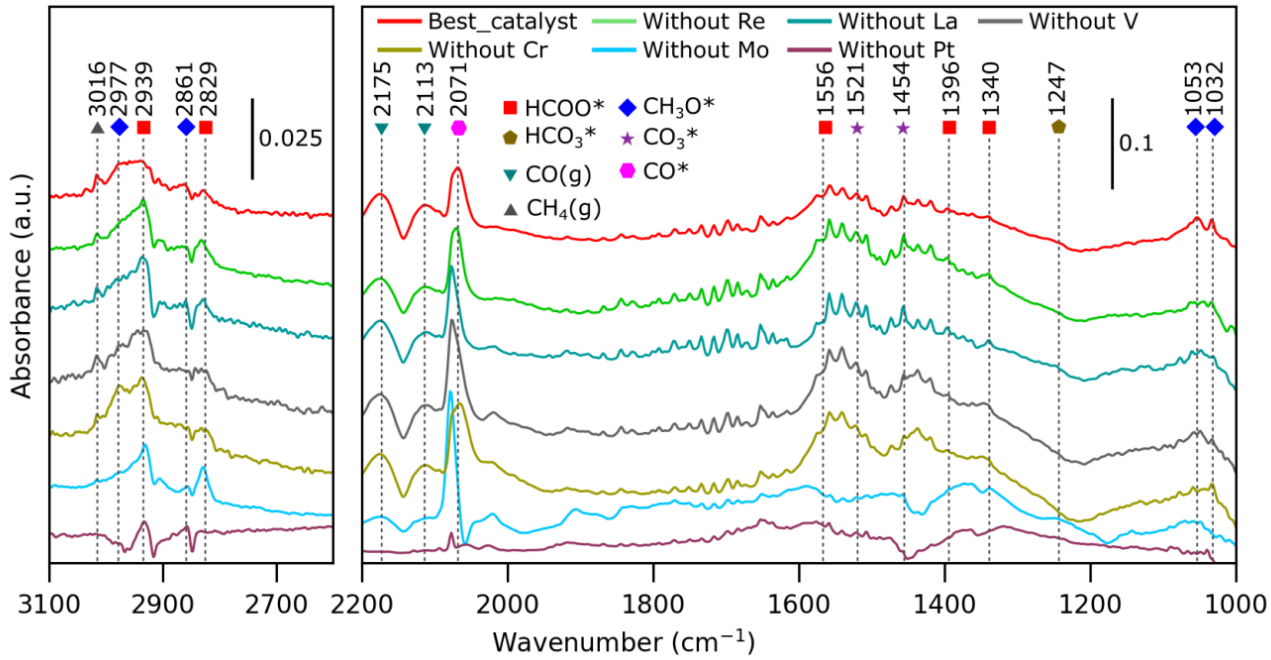

Figure 4.20. *In situ* DRIFTS analyses of Pt(5)/Mo(8)-Cr(0.7)-V(0.7)-La(0.7)-Re(1)/TiO_2 (P25)_550, Pt(5)/Mo(8)-Cr(0.7)-V(0.7)-La(0.7)/TiO_2 (P25)_550, Pt(5)/Mo(8)-Cr(0.7)-V(0.7)-Re(1)/TiO_2 (P25)_550, Pt(5)/Mo(8)-Cr(0.7)-La(0.7)-Re(1)/TiO_2 (P25)_550, Pt(5)/Mo(8)-V(0.7)-La(0.7)-Re(1)/TiO_2 (P25)_550, Pt(5)/-Cr(0.7)-V(0.7)-La(0.7)-Re(1)/TiO_2 (P25)_550 and Mo(8)-Cr(0.7)-V(0.7)-La(0.7)-Re(1)/TiO_2 (P25)_550 conducted under a gas flow containing CO_2 (5 mL min^{-1}) and H_2 (15 mL min^{-1}) at 150 °C and under a pressure of 20 bar.

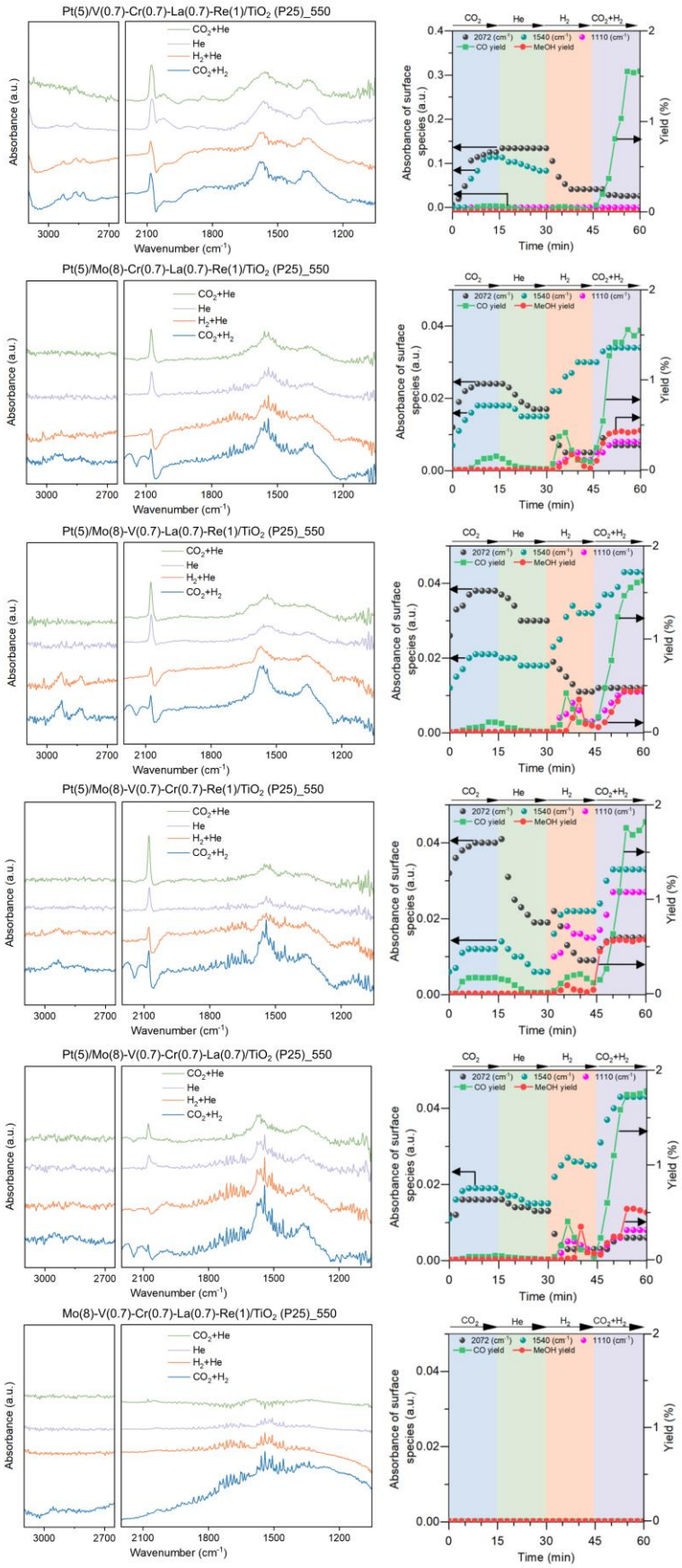

Figure 4.21. *In situ* DRIFTS for the each catalyst conducted under a sequential flow of CO_2/He, He, H_2, and 25% CO_2 + 75% H_2 at 150 °C.

We speculated that Cr and V might bring acidity to the system and hence might affect the methanol desorption from the surface. Previous studies have indicated that methanol decomposition reactions can take place on $Pt/MoO_x/TiO_2$ catalysts.[71] Consequently, the easy removal of methanol from the catalyst surface would inhibit methanol decomposition and enhance methanol production. To investigate this, we studied methanol decomposition over the best catalyst, Pt(5)/Mo(8)-Cr(0.7)-La(0.7)-Re(1)/TiO_2 (P25)_550 (without V) and Pt(5)/Mo(8)-V(0.7)-La(0.7)-Re(1)/TiO_2 (P25)_550 catalyst (without Cr) under N_2 atmosphere (0.5 MPa). As illustrated in **Figure 4.22**, the methanol decomposition rate over the best catalyst was lower than that observed for the Pt(5)/Mo(8)-Cr(0.7)-La(0.7)-Re(1)/TiO_2 (P25)_550 (without V) and Pt(5)/Mo(8)-V(0.7)-La(0.7)-Re(1)/TiO_2 (P25)_550 catalyst (without Cr). This finding underscores the advantageous role of Cr and V species in the facile desorption of methanol from the catalyst surface to facilitate methanol synthesis. Based on these findings, it can be inferred that CO_2 initially adsorbs on the oxygen-deficient sites of the undercoordinated MoO_x species. The primary H_2 dissociation agent, Pt nanoparticles, dissociate H_2, leading to the formation of formate over the MoO_x species. In addition to Pt, the Re species would help in converting formate to methanol, La promotes CO_2 activation, while Cr and V assist in the desorption of methanol molecules from the surface suppressing methanol decomposition and enhancing methanol production. Consequently, the co-existence of different elements with specific roles in different stages of methanol formation results in a highly active, selective, and stable catalyst for the direct CO_2 hydrogenation to methanol at low temperatures. It should be noted that although there is some ambiguity present in spectroscopic and microscopic analyses, our interpretation of the structure of Pt, Mo, Re, V, Cr and La species is supported by the evidences gathered from multiple characterization techniques. While mechanistic interpretations are based on observed correlations and trends, we treat them as hypotheses supported by multiple evidences rather than definitive conclusions.

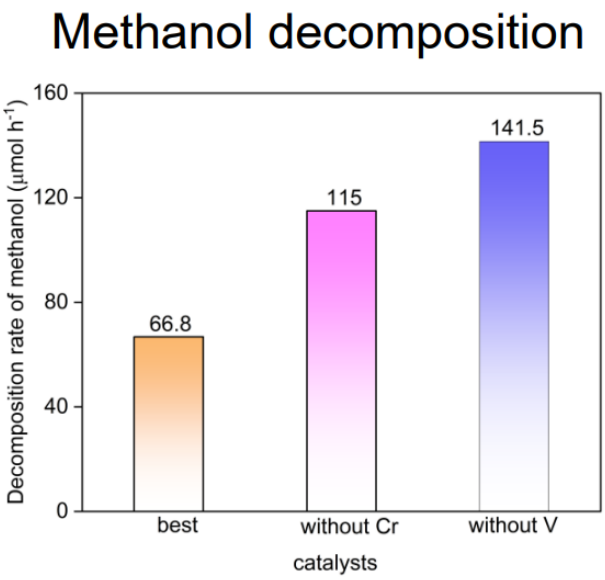

Figure 4.22. Methanol decomposition over Pt(5)/Mo(8)-Cr(0.7)-V(0.7)-La(0.7)-Re(1)/TiO_2 (P25)_550, Pt(5)/Mo(8)-V(0.7)-La(0.7)-Re(1)/TiO_2 (P25)_550 and Pt(5)/Mo(8)-Cr(0.7)- -La(0.7)-Re(1)/TiO_2 (P25)_550. Pretreatment: H_2(20 mL min^{-1}), 300 ℃, 0.5 h. Catalytic reaction conditions: catalyst (100 mg), 150 °C. The formation rate was calculated in mmol h^{-1} unit.

4.4 Conclusion

In summary, we developed highly active catalysts for low-temperature CO_2 hydrogenation to methanol in flow system using an extrapolative ML method. Using a closed loop discovery system of ML prediction and experimental validation for 25 iterations, Pt(5)/Mo(8)-V(0.7)-Cr(0.7)-La(0.7)/TiO_2 (P25)_550 was found to the best catalyst. Furthermore, a more efficient catalyst (Pt(5)/Mo(8)-V(0.7)-Cr(0.7)-La(0.7)-Re(1.0)/TiO_2 (P25)_550) was prepared by adding Re to the ML identified catalyst. In addition to the optimal catalyst compositions, our ML model unveiled the elemental features and electronic properties crucial for high catalytic activity. The Pt(5)/Mo(8)-V(0.7)-Cr(0.7)-La(0.7)-Re(1.0)/TiO_2 (P25)_550 catalyst exhibited one of the highest methanol formation rate ever reported at low temperatures. Moreover, experimental *in situ*/*operando* techniques were used to elucidate the reaction mechanism and role of each component of the best catalyst. Our findings revealed that Pt played a primary role in H_2 dissociation, partially reduced Mo oxides facilitated the activation of CO_2 and stabilized oxygenate species. Re promoted formate conversion to methoxy species, while Cr and V promoted facile desorption of methanol suppressing methanol decomposition, and La promoted CO_2 activation. We anticipate that our study will expedite the development of novel catalysts through machine learning approaches.

4.5 References

(1) Roosmalen, R. van; Rothenberg, G. Carbon Capture, Storage And Utilization: A Critical Overview. In *Handbook of Energy, Environment, and the Circular Economy*; Gitis, V., Rothenberg, G., Eds.;World Scientific Publishing Co, **2024**; pp 297–353.

(2) Fu, J.; Lym, J.; Zheng, W.; Alexopoulos, K.; Mironenko, A. V; Li, N.; Boscoboinik, J. A.; Su, D.; Weber, R. T.; Vlachos, D. G. C–O Bond Activation Using Ultralow Loading of Noble Metal Catalysts on Moderately Reducible Oxides. *Nat. Catal.* **2020**, *3* (5), 446–453.

(3) Zhang, Z.; Zuo, J.; Luo, L.; Yang, X.; Ma, Z.; Jin, H.; Yuan, Y.; Qian, Q.; Chen, Q.; Luo, Y. Sodium-Assisted MoS2 for Boosting CO_2 Hydrogenation to Methanol: The Crucial Role of Sodium in Defect Evolution and Modification. *J. Catal.* **2024**, *436*, 115621.

(4) Olah, G. A. Towards Oil Independence Through Renewable Methanol Chemistry. *Angew. Chemie Int. Ed.* **2013**, *52* (1), 104–107.

(5) Segler, M. H. S.; Preuss, M.; Waller, M. P. Planning Chemical Syntheses with Deep Neural Networks and Symbolic AI. *Nature* **2018**, *555* (7698), 604–610.

(6) Gutterød, E. S.; Lazzarini, A.; Fjermestad, T.; Kaur, G.; Manzoli, M.; Bordiga, S.; Svelle, S.; Lillerud, K. P.; Skúlason, E.; Øien-ØDegaard, S.; Nova, A.; Olsbye, U. Hydrogenation of CO_2 to Methanol by Pt Nanoparticles Encapsulated in UiO-67: Deciphering the Role of the Metal-Organic Framework. *J. Am. Chem. Soc.* **2020**, *142* (2), 999–1009.

(7) Butler, K. T.; Davies, D. W.; Cartwright, H.; Isayev, O.; Walsh, A. Machine Learning for Molecular and Materials Science. *Nature*. **2018**, *559*(7715), 547-555.

(8) Hu, J.; Yu, L.; Deng, J.; Wang, Y.; Cheng, K.; Ma, C.; Zhang, Q.; Wen, W.; Yu, S.; Pan, Y.; Yang, J.; Ma, H.; Qi, F.; Wang, Y.; Zheng, Y.; Chen, M.; Huang, R.; Zhang, S.; Zhao, Z.; Mao, J.; Meng, X.; Ji, Q.; Hou, G.; Han, X.; Bao, X.; Wang, Y.; Deng, D. Sulfur Vacancy-Rich MoS_2 as a Catalyst for the Hydrogenation of CO_2 to Methanol. *Nat. Catal.* **2021**, *4* (3), 242–250.

(9) Gau, A.; Hack, J.; Maeda, N.; Meier, D. M. Operando Spectroscopic Monitoring of Active Species in CO2 Hydrogenation at Elevated Pressure and Temperature: Steady-State versus Transient Analysis. *Energy and Fuels* **2021**, *35* (18), 15243–15246.

(10) Ting, K. W.; Toyao, T.; Siddiki, S. M. A. H.; Shimizu, K. I. Low-Temperature Hydrogenation of CO_2 to Methanol over Heterogeneous TiO_2-Supported Re Catalysts. *ACS Catal.* **2019**, *9* (4), 3685–3693.

(11) Gaikwad, R.; Bansode, A.; Urakawa, A. High-Pressure Advantages in Stoichiometric Hydrogenation of Carbon Dioxide to Methanol. *J. Catal.* **2016**, *343*, 127–132.

(12) Porosoff, M. D.; Yan, B.; Chen, J. G. Catalytic Reduction of CO_2 by H_2 for Synthesis of CO, Methanol and Hydrocarbons: Challenges and Opportunities. *Energy Environ. Sci*. **2016**, *9*(1), 62–73.

(13) Álvarez, A.; Bansode, A.; Urakawa, A.; Bavykina, A. V; Wezendonk, T. A.; Makkee, M.; Gascon, J.; Kapteijn, F. Challenges in the Greener Production of Formates/Formic Acid, Methanol, and DME by Heterogeneously Catalyzed CO_2 Hydrogenation Processes. *Chem. Rev.* **2017**, *117*(14), 9804–9838.

(14) Olah, G. A.; Goeppert, A.; Prakash, G. K. S. Chemical Recycling of Carbon Dioxide to Methanol and Dimethyl Ether: From Greenhouse Gas to Renewable, Environmentally Carbon Neutral Fuels and Synthetic Hydrocarbons. *J. Org. Chem.* **2009**, *74*(2), 487–498.

(15) Liu, G.; Liu, P.; Meng, D.; Zhao, T.; Qian, X.; He, Q.; Guo, X.; Qi, J.; Peng, L.; Xue, N.; Zhu, Y.; Ma, J.; Wang, Q.; Liu, X.; Chen, L.; Ding, W. CO_x Hydrogenation to Methanol and Other Hydrocarbons under Mild Conditions with Mo_3S_4@ZSM-5. *Nat. Commun.* **2023**, *14* (1), 513.

(16) Chen, Y.; Choi, S.; Thompson, L. T. Low Temperature CO_2 Hydrogenation to Alcohols and Hydrocarbons over Mo2C Supported Metal Catalysts. *J. Catal.* **2016**, *343*, 147–156.

(17) Khan, M. U.; Wang, L.; Liu, Z.; Gao, Z.; Wang, S.; Li, H.; Zhang, W.; Wang, M.; Wang, Z.; Ma, C.; Zeng, J. Pt_3Co Octapods as Superior Catalysts of CO_2 Hydrogenation. *Angew. Chemie Int. Ed.* **2016**, *55* (33), 9548–9552.

(18) He, Z.; Qian, Q.; Ma, J.; Meng, Q.; Zhou, H.; Song, J.; Liu, Z.; Han, B. Water-Enhanced Synthesis of Higher Alcohols from CO_2 Hydrogenation over a Pt/Co_3O_4 Catalyst under Milder Conditions. *Angew. Chemie Int. Ed.* **2016**, *55* (2), 737–741.

(19) Hong, S.; Reddy, K. P.; Song, Y.; Park, D.; Park, J. Y. Enhanced Methanol Formation in CO_2 Hydrogenation through Synergistic Copper and Gallium Interaction. *J. Catal.* **2024**, *437*, 115643.

(20) Sugiyama, H.; Miyazaki, M.; Sasase, M.; Kitano, M.; Hosono, H. Room-Temperature CO_2 Hydrogenation to Methanol over Air-Stable Hcp-PdMo Intermetallic Catalyst. *J. Am. Chem. Soc.* **2023**, *145* (17), 9410–9416.

(21) Sanchez-Lengeling, B.; Aspuru-Guzik, A. Inverse Molecular Design Using Machine Learning: Generative Models for Matter Engineering. *Science.* **2018**, *361* (6400), 360–365.

(22) Aykol, M.; Hegde, V. I.; Hung, L.; Suram, S.; Herring, P.; Wolverton, C.; Hummelshøj, J. S. Network Analysis of Synthesizable Materials Discovery. *Nat. Commun.* **2019**, *10* (1), 2018.

(23) Coley, C. W.; Thomas, D. A.; Lummiss, J. A. M.; Jaworski, J. N.; Breen, C. P.; Schultz, V.; Hart, T.; Fishman, J. S.; Rogers, L.; Gao, H.; Hicklin, R. W.; Plehiers, P. P.; Byington, J.; Piotti, J. S.; Green, W. H.; John Hart, A.; Jamison, T. F.; Jensen, K. F. A Robotic Platform for Flow Synthesis of Organic Compounds Informed by AI Planning. *Science.* **2019**, *365* (6453), eaax1566.

(24) Ras, E. J.; Rothenberg, G. Heterogeneous Catalyst Discovery Using 21st Century Tools: A Tutorial. *RSC Adv.* **2014**, *4* (12), 5963–5974.

(25) Erdem Günay, M.; Yıldırım, R. Recent Advances in Knowledge Discovery for Heterogeneous Catalysis Using Machine Learning. *Catal. Rev.* **2021**, *63* (1), 120–164.

(26) Ooka, H.; Wintzer, M. E.; Nakamura, R. Non-Zero Binding Enhances Kinetics of Catalysis: Machine Learning Analysis on the Experimental Hydrogen Binding Energy of Platinum. *ACS Catal.* **2021**, *11* (10), 6298–6303.

(27) Miyazaki, R.; Belthle, K. S.; Tüysüz, H.; Foppa, L.; Scheffler, M. Materials Genes of CO_2 Hydrogenation on Supported Cobalt Catalysts: An Artificial Intelligence Approach Integrating Theoretical and Experimental Data. *J. Am. Chem. Soc.* **2024**, *146* (8), 5433–5444.

(28) Peng, J.; Schwalbe-Koda, D.; Akkiraju, K.; Xie, T.; Giordano, L.; Yu, Y.; Eom, C. J.; Lunger, J. R.; Zheng, D. J.; Rao, R. R.; Muy, S.; Grossman, J. C.; Reuter, K.; Gómez-Bombarelli, R.; Shao-Horn, Y. Human- and Machine-Centred Designs of Molecules and Materials for Sustainability and Decarbonization. *Nat. Rev. Mater.* **2022**, *7* (12), 991–1009.

(29) Jayarathna, R.; Onsree, T.; Drummond, S.; Naglic, J.; Lauterbach, J. Experimental Discovery of Novel Ammonia Synthesis Catalysts via Active Learning. *J. Mater. Chem. A* **2024**, *12* (5), 3046–3060.

(30) Mazheika, A.; Wang, Y.-G.; Valero, R.; Viñes, F.; Illas, F.; Ghiringhelli, L. M.; Levchenko, S. V; Scheffler, M. Artificial-Intelligence-Driven Discovery of Catalyst Genes with Application to CO_2 Activation on Semiconductor Oxides. *Nat. Commun.* **2022**, *13* (1), 419.

(31) Raccuglia, P.; Elbert, K. C.; Adler, P. D. F.; Falk, C.; Wenny, M. B.; Mollo, A.; Zeller, M.; Friedler, S. A.; Schrier, J.; Norquist, A. J. Machine-Learning-Assisted Materials Discovery Using Failed Experiments. *Nature* **2016**, *533* (7601), 73–76.

(32) Medford, A. J.; Kunz, M. R.; Ewing, S. M.; Borders, T.; Fushimi, R. Extracting Knowledge from Data through Catalysis Informatics. *ACS Catal.* **2018**, *8* (8), 7403–7429.

(33) Takahashi, K.; Takahashi, L.; Miyazato, I.; Fujima, J.; Tanaka, Y.; Uno, T.; Satoh, H.; Ohno, K.; Nishida, M.; Hirai, K.; Ohyama, J.; Nguyen, T. N.; Nishimura, S.; Taniike, T. The Rise of Catalyst Informatics: Towards Catalyst Genomics. *ChemCatChem*. **2019**, *11*(4), 1146–1152.

(34) Masood, H.; Toe, C. Y.; Teoh, W. Y.; Sethu, V.; Amal, R. Machine Learning for Accelerated Discovery of Solar Photocatalysts. *ACS Catal*. **2019**, *9*(12), 11774–11787.

(35) Toyao, T.; Maeno, Z.; Takakusagi, S.; Kamachi, T.; Takigawa, I.; Shimizu, K. I. Machine Learning for Catalysis Informatics: Recent Applications and Prospects. *ACS Catal*. **2020**, *10*(3), 2260–2297.

(36) Maldonado, A. G.; Rothenberg, G. Predictive Modeling in Homogeneous Catalysis: A Tutorial. *Chem. Soc. Rev.* **2010**, *39* (6), 1891–1902.

(37) Calle-Vallejo, F.; Loffreda, D.; Koper, M. T. M.; Sautet, P. Introducing Structural Sensitivity into Adsorption-Energy Scaling Relations by Means of Coordination Numbers. *Nat. Chem.* **2015**, *7* (5), 403–410.

(38) Ulissi, Z. W.; Medford, A. J.; Bligaard, T.; Nørskov, J. K. To Address Surface Reaction Network Complexity Using Scaling Relations Machine Learning and DFT Calculations. *Nat. Commun.* **2017**, *8* (1), 14621.

(39) Li, Z.; Wang, S.; Xin, H. Toward Artificial Intelligence in Catalysis. *Nat. Catal.* **2018**, *1* (9), 641–642.

(40) Bruix, A.; Margraf, J. T.; Andersen, M.; Reuter, K. First-Principles-Based Multiscale Modelling of Heterogeneous Catalysis. *Nature Catal*. **2019**, *2*(8), 659-670.

(41) Shi, Y.-F.; Kang, P.-L.; Shang, C.; Liu, Z.-P. Methanol Synthesis from CO_2/CO Mixture on Cu–Zn Catalysts from Microkinetics-Guided Machine Learning Pathway Search. *J. Am. Chem. Soc.* **2022**, *144* (29), 13401–13414.

(42) Iwama, R.; Takizawa, K.; Shinmei, K.; Baba, E.; Yagihashi, N.; Kaneko, H. Design and Analysis of Metal Oxides for CO_2 Reduction Using Machine Learning, Transfer Learning, and Bayesian Optimization. *ACS Omega* **2022**, *7* (12), 10709–10717.

(43) Mosquera-Lois, I.; Kavanagh, S. R.; Ganose, A. M.; Walsh, A. Machine-Learning Structural Reconstructions for Accelerated Point Defect Calculations. *npj Comput. Mater.* **2024**, *10* (1), 121.

(44) Kalikadien, A. V; Valsecchi, C.; van Putten, R.; Maes, T.; Muuronen, M.; Dyubankova, N.; Lefort, L.; Pidko, E. A. Probing Machine Learning Models Based on High Throughput Experimentation Data for the Discovery of Asymmetric Hydrogenation Catalysts. *Chem. Sci.* **2024**, *15* (34), 13618–13630.

(45) Mou, T.; Pillai, H. S.; Wang, S.; Wan, M.; Han, X.; Schweitzer, N. M.; Che, F.; Xin, H. Bridging the Complexity Gap in Computational Heterogeneous Catalysis with Machine Learning. *Nat. Catal.* **2023**, *6* (2), 122–136.

(46) Taniike, T.; Takahashi, K. The Value of Negative Results in Data-Driven Catalysis Research. *Nat. Catal.* **2023**, *6* (2), 108–111.

(47) Schmack, R.; Friedrich, A.; Kondratenko, E. V; Polte, J.; Werwatz, A.; Kraehnert, R. A Meta-Analysis of Catalytic Literature Data Reveals Property-Performance Correlations for the OCM Reaction. *Nat. Commun.* **2019**, *10* (1), 441.

(48) Ting, K. W.; Kamakura, H.; Poly, S. S.; Takao, M.; Siddiki, S. M. A. H.; Maeno, Z.; Matsushita, K.; Shimizu, K. I.; Toyao, T. Catalytic Methylation of M-xylene, Toluene, and Benzene Using CO_2 and H_2 over TiO_2-supported Re and Zeolite Catalysts: Machine-Learning-Assisted Catalyst Optimization. *ACS Catal.* **2021**, *11* (9), 5829–5838.

(49) Mok, D. H.; Li, H.; Zhang, G.; Lee, C.; Jiang, K.; Back, S. Data-Driven Discovery of Electrocatalysts for CO_2 Reduction Using Active Motifs-Based Machine Learning. *Nat. Commun.* **2023**, *14* (1), 7303.

(50) Mine, S.; Takao, M.; Yamaguchi, T.; Toyao, T.; Maeno, Z.; Hakim Siddiki, S. M. A.; Takakusagi, S.; Shimizu, K. ichi; Takigawa, I. Analysis of Updated Literature Data up to 2019 on the Oxidative Coupling of Methane Using an Extrapolative Machine-Learning Method to Identify Novel Catalysts. *ChemCatChem* **2021**, *13* (16), 3636–3655.

(51) Suzuki, K.; Toyao, T.; Maeno, Z.; Takakusagi, S.; Shimizu, K. ichi; Takigawa, I. Statistical Analysis and Discovery of Heterogeneous Catalysts Based on Machine Learning from Diverse Published Data. *ChemCatChem* **2019**, *11* (18), 4537–4547.

(52) Mine, S.; Jing, Y.; Mukaiyama, T.; Takao, M.; Maeno, Z.; Shimizu, K. I.; Takigawa, I.; Toyao, T. Machine Learning Analysis of Literature Data on the Water Gas Shift Reaction toward Extrapolative Prediction of Novel Catalysts. *Chem. Lett.* **2022**, *51* (3), 269–273.

(53) Suvarna, M.; Preikschas, P.; Pérez-Ramírez, J. Identifying Descriptors for Promoted Rhodium-Based Catalysts for Higher Alcohol Synthesis via Machine Learning. *ACS Catal.* **2022**, *12* (24), 15373–15385.

(54) Wang, A. Y.-T.; Kauwe, S. K.; Murdock, R. J.; Sparks, T. D. Compositionally Restricted Attention-Based Network for Materials Property Predictions. *npj Comput. Mater.* **2021**, *7* (1), 77.

(55) Falkowski, A. R.; Kauwe, S. K.; Sparks, T. D. Optimizing Fractional Compositions to Achieve Extraordinary Properties. *Integr. Mater. Manuf. Innov.* **2021**, *10* (4), 689–695.

(56) Kresse, G.; Furthmüller, J. Efficient Iterative Schemes for Ab Initio Total-Energy Calculations Using a Plane-Wave Basis Set. *Phys. Rev. B* **1996**, *54* (16), 11169–11186.

(57) Kresse, G.; Furthmüller, J. Efficiency of Ab-Initio Total Energy Calculations for Metals and Semiconductors Using a Plane-Wave Basis Set. *Comput. Mater. Sci.* **1996**, *6* (1), 15–50.

(58) Perdew, J. P.; Ruzsinszky, A.; Csonka, G. I.; Vydrov, O. A.; Scuseria, G. E.; Constantin, L. A.; Zhou, X.; Burke, K. Restoring the Density-Gradient Expansion for Exchange in Solids and Surfaces. *Phys. Rev. Lett.* **2008**, *100* (13), 136406.

(59) Blöchl, P. E. Projector Augmented-Wave Method. *Phys. Rev. B* **1994**, *50* (24), 17953–17979.

(60) Grimme, S.; Ehrlich, S.; Goerigk, L. Effect of the Damping Function in Dispersion Corrected Density Functional Theory. *J. Comput. Chem.* **2011**, *32* (7), 1456–1465.

(61) Zheng, H.; Li, X.-G.; Tran, R.; Chen, C.; Horton, M.; Winston, D.; Persson, K. A.; Ong, S. P. Grain Boundary Properties of Elemental Metals. *Acta Mater.* **2020**, *186*, 40–49.

(62) Tran, R.; Xu, Z.; Radhakrishnan, B.; Winston, D.; Sun, W.; Persson, K. A.; Ong, S. P. Surface Energies of Elemental Crystals. *Sci. Data* **2016**, *3* (1), 160080.

(63) Hinuma, Y.; Toyao, T.; Kamachi, T.; Maeno, Z.; Takakusagi, S.; Furukawa, S.; Takigawa, I.; Shimizu, K. Density Functional Theory Calculations of Oxygen Vacancy Formation and Subsequent Molecular Adsorption on Oxide Surfaces. *J. Phys. Chem. C* **2018**, *122* (51), 29435–29444.

(64) Sanderson, R. T. Principles of Electronegativity Part II. Applications. *J. Chem. Educ.* **1988**, *65* (3), 227.

(65) Wang, G.; Mine, S.; Chen, D.; Jing, Y.; Ting, K. W.; Yamaguchi, T.; Takao, M.; Maeno, Z.; Takigawa, I.; Matsushita, K.; Shimizu, K.; Toyao, T. Accelerated Discovery of Multi-Elemental Reverse Water-Gas Shift Catalysts Using Extrapolative Machine Learning Approach. *Nat. Commun.* **2023**, *14* (1), 5861.

(66) Oviedo, F.; Ferres, J. L.; Buonassisi, T.; Butler, K. T. Interpretable and Explainable Machine Learning for Materials Science and Chemistry. *Accounts Mater. Res.* **2022**, *3* (6), 597–607.

(67) Choudhary, K.; DeCost, B.; Chen, C.; Jain, A.; Tavazza, F.; Cohn, R.; Park, C. W.; Choudhary, A.; Agrawal, A.; Billinge, S. J. L.; Holm, E.; Ong, S. P.; Wolverton, C. Recent Advances and Applications of Deep Learning Methods in Materials Science. *npj Comput. Mater.* **2022**, *8* (1), 59.

(68) Pedregosa, F.; Varoquaux, G.; Gramfort, A.; Michel, V.; Thirion, B.; Grisel, O.; Blondel, M.; Prettenhofer, P.; Weiss, R.; Dubourg, V.; Vanderplas, J.; Passos, A.; Cournapeau, D.; Brucher, M.; Perrot, M.; Duchesnay, É. Scikit-Learn: Machine Learning in Python. *J. Mach. Learn. Res.* **2011**, 12, 2825–2830.

(69) Scheurer, C.; Reuter, K. Role of the Human-in-the-Loop in Emerging Self-Driving Laboratories for Heterogeneous Catalysis. *Nat. Catal.* **2025**, *8* (1), 13–19.

(70) Toyao, T.; Kayamori, S.; Maeno, Z.; Siddiki, S. M. A. H.; Shimizu, K. I. Heterogeneous Pt and MoO_x Co-Loaded TiO_2 Catalysts for Lowerature CO_2 Hydrogenation to Form CH_3OH. *ACS Catal.* **2019**, *9* (9), 8187–8196.

(71) Belkin, M.; Hsu, D.; Mitra, P. P. Overfitting or Perfect Fitting? Risk Bounds for Classification and Regression Rules That Interpolate. *Adv. Neural Inform. Process. Syst*. **2018**, *31*.

(72) Huff, C. A.; Sanford, M. S. Cascade Catalysis for the Homogeneous Hydrogenation of CO_2 to Methanol. *J. Am. Chem. Soc.* **2011**, *133* (45), 18122–18125.

(73) Wesselbaum, S.; vom Stein, T.; Klankermayer, J.; Leitner, W. Hydrogenation of Carbon Dioxide to Methanol by Using a Homogeneous Ruthenium–Phosphine Catalyst. *Angew. Chemie Int. Ed.* **2012**, *51* (30), 7499–7502.

(74) Wesselbaum, S.; Moha, V.; Meuresch, M.; Brosinski, S.; Thenert, K. M.; Kothe, J.; Stein, T. vom; Englert, U.; Hölscher, M.; Klankermayer, J.; Leitner, W. Hydrogenation of Carbon Dioxide to Methanol Using a Homogeneous Ruthenium–Triphos Catalyst: From Mechanistic Investigations to Multiphase Catalysis. *Chem. Sci.* **2015**, *6* (1), 693–704.

(75) Kothandaraman, J.; Goeppert, A.; Czaun, M.; Olah, G. A.; Prakash, G. K. S. Conversion of CO_2 from Air into Methanol Using a Polyamine and a Homogeneous Ruthenium Catalyst. *J. Am. Chem. Soc.* **2016**, *138* (3), 778–781.

(76) Schneidewind, J.; Adam, R.; Baumann, W.; Jackstell, R.; Beller, M. Low-Temperature Hydrogenation of Carbon Dioxide to Methanol with a Homogeneous Cobalt Catalyst. *Angew. Chemie Int. Ed.* **2017**, *56* (7), 1890–1893.

(77) Ribeiro, A. P. C.; Martins, L. M. D. R. S.; Pombeiro, A. J. L. Carbon Dioxide-to-Methanol Single-Pot Conversion Using a C-Scorpionate Iron(Ii) Catalyst. *Green Chem.* **2017**, *19* (20), 4811–4815.

(78) Kar, S.; Goeppert, A.; Kothandaraman, J.; Prakash, G. K. S. Manganese-Catalyzed Sequential Hydrogenation of CO_2 to Methanol via Formamide. *ACS Catal.* **2017**, *7* (9), 6347–6351.

(79) Everett, M.; Wass, D. F. Highly Productive CO_2 Hydrogenation to Methanol – a Tandem Catalytic Approach via Amide Intermediates. *Chem. Commun.* **2017**, *53* (68), 9502–9504.

(80) Kar, S.; Sen, R.; Goeppert, A.; Prakash, G. K. S. Integrative CO_2 Capture and Hydrogenation to Methanol with Reusable Catalyst and Amine: Toward a Carbon Neutral Methanol Economy. *J. Am. Chem. Soc.* **2018**, *140* (5), 1580–1583.

(81) Scharnagl, F. K.; Hertrich, M. F.; Neitzel, G.; Jackstell, R.; Beller, M. Homogeneous Catalytic Hydrogenation of CO_2 to Methanol – Improvements with Tailored Ligands. *Adv. Synth. Catal.* **2019**, *361* (2), 374–379.

(82) Reller, C.; Pöge, M.; Lißner, A.; Mertens, F. O. R. L. Methanol from CO_2 by Organo-Cocatalysis: CO_2 Capture and Hydrogenation in One Process Step. *Environ. Sci. Technol.* **2014**, *48* (24), 14799–14804.

(83) Chen, Y.; Choi, S.; Thompson, L. T. Low-Temperature CO_2 Hydrogenation to Liquid Products via a Heterogeneous Cascade Catalytic System. *ACS Catal.* **2015**, *5* (3), 1717–1725.

(84) Zhang, W.; Wang, L.; Liu, H.; Hao, Y.; Li, H.; Khan, M. U.; Zeng, J. Integration of Quantum Confinement and Alloy Effect to Modulate Electronic Properties of RhW Nanocrystals for Improved Catalytic Performance toward CO_2 Hydrogenation. *Nano Lett.* **2017**, *17* (2), 788–793.

(85) Bai, S.; Shao, Q.; Feng, Y.; Bu, L.; Huang, X. Highly Efficient Carbon Dioxide Hydrogenation to Methanol Catalyzed by Zigzag Platinum–Cobalt Nanowires. *Small* **2017**, *13* (22), 1604311.

(86) Li, H.; Wang, L.; Dai, Y.; Pu, Z.; Lao, Z.; Chen, Y.; Wang, M.; Zheng, X.; Zhu, J.; Zhang, W.; Si, R.; Ma, C.; Zeng, J. Synergetic Interaction between Neighbouring Platinum Monomers in CO_2 Hydrogenation. *Nat. Nanotechnol.* **2018**, *13* (5), 411–417.

(87) Zheng, X.; Lin, Y.; Pan, H.; Wu, L.; Zhang, W.; Cao, L.; Zhang, J.; Zheng, L.; Yao, T. Grain Boundaries Modulating Active Sites in RhCo Porous Nanospheres for Efficient CO_2 Hydrogenation. *Nano Res.* **2018**, *11* (5), 2357–2365.

(88) Kothandaraman, J.; Dagle, R. A.; Dagle, V. L.; Davidson, S. D.; Walter, E. D.; Burton, S. D.; Hoyt, D. W.; Heldebrant, D. J. Condensed-Phase Low Temperature Heterogeneous Hydrogenation of CO_2 to Methanol. *Catal. Sci. Technol.* **2018**, *8* (19), 5098–5103.

(89) Chen, F.; Liang, J.; Wang, F.; Guo, X.; Gao, W.; Kugue, Y.; He, Y.; Yang, G.; Reubroycharoen, P.; Vitidsant, T.; Tsubaki, N. Improved Catalytic Activity and Stability of Cu/ZnO Catalyst by Boron Oxide Modification for Low-Temperature Methanol Synthesis. *Chem. Eng. J.* **2023**, *458*, 141401.

(90) Zhou, S.; Ma, W.; Anjum, U.; Kosari, M.; Xi, S.; Kozlov, S. M.; Zeng, H. C. Strained Few-Layer MoS_2 with Atomic Copper and Selectively Exposed in-Plane Sulfur Vacancies for CO_2 Hydrogenation to Methanol. *Nat. Commun.* **2023**, *14* (1), 5872.

(91) Zhou, Y.; Liu, F.; Geng, S.; Yao, M.; Ma, J.; Cao, J. Tuning the Content of S Vacancies in MoS_2 by Cu Doping for Enhancing Catalytic Hydrogenation of CO_2 to Methanol. *Mol. Catal.* **2023**, *547*, 113288.

(92) Zhou, S.; Zeng, H. C. Boxlike Assemblages of Few-Layer MoS2 Nanosheets with Edge Blockage for High-Efficiency Hydrogenation of CO_2 to Methanol. *ACS Catal.* **2022**, *12* (16), 9872–9886.

(93) Huang, C.; Zhang, S.; Wang, W.; Zhou, H.; Shao, Z.; Xia, L.; Wang, H.; Sun, Y. Modulation of Electronic Metal-Support Interaction between Cu and ZnO by Er for Effective Low-Temperature CO_2 Hydrogenation to Methanol. *ACS Catal.* **2024**, *14* (3), 1324–1335.

(94) Kunkel, C.; Rüther, F.; Felsen, F.; Pare, C. W. P.; Terzi, A.; Baumgarten, R.; Gioria, E.; Naumann d'Alnoncourt, R.; Scheurer, C.; Rosowski, F.; Reuter, K. Systematic Exploration of a Multi-Promoter Catalyst Composition Space with Limited Experiments: Non-Oxidative Propane Dehydrogenation to Propylene. *ACS Catal.* **2024**, *14* (11), 9008–9017.

(95) Amano, F.; Nakata, M.; Yamamoto, A.; Tanaka, T. Rutile Titanium Dioxide Prepared by Hydrogen Reduction of Degussa P25 for Highly Efficient Photocatalytic Hydrogen Evolution. *Catal. Sci. Technol.* **2016**, *6* (14), 5693–5699.

(96) Esterhuizen, J. A.; Goldsmith, B. R.; Linic, S. Interpretable Machine Learning for Knowledge Generation in Heterogeneous Catalysis. *Nat. Catal*. **2022**, 175–184.

(97) Yang, Q.; Skrypnik, A.; Matvienko, A.; Lund, H.; Holena, M.; Kondratenko, E. V. Revealing Property-Performance Relationships for Efficient CO_2 Hydrogenation to Higher Hydrocarbons over Fe-Based Catalysts: Statistical Analysis of Literature Data and Its Experimental Validation. *Appl. Catal. B Environ.* **2021**, *282*, 119554.

(98) Yang, W.; Abdelfatah, K. E.; Kundu, S. K.; Rajbanshi, B.; Terejanu, G. A.; Heyden, A. Machine Learning Accelerated First-Principles Study of the Hydrodeoxygenation of Propanoic Acid. *ACS Catal.* **2024**, *14* (13), 10148–10163.

(99) Lundberg, S. M.; Lee, S. I. A Unified Approach to Interpreting Model Predictions. In Advances in Neural Information Processing Systems. *Adv. Neural Inform. Process. Syst.* **2019**, 32.

(100) Lundberg, S. M.; Nair, B.; Vavilala, M. S.; Horibe, M.; Eisses, M. J.; Adams, T.; Liston, D. E.; Low, D. K.-W.; Newman, S.-F.; Kim, J.; Lee, S.-I. Explainable Machine-Learning Predictions for the Prevention of Hypoxaemia during Surgery. *Nat. Biomed. Eng.* **2018**, *2* (10), 749–760.

(101) Lundberg, S. M.; Erion, G.; Chen, H.; DeGrave, A.; Prutkin, J. M.; Nair, B.; Katz, R.; Himmelfarb, J.; Bansal, N.; Lee, S. I. From Local Explanations to Global Understanding with Explainable AI for Trees. *Nat. Mach. Intell.* **2020**, *2* (1), 56–67.

(102) Praveen, C. S.; Comas-Vives, A. Design of an Accurate Machine Learning Algorithm to Predict the Binding Energies of Several Adsorbates on Multiple Sites of Metal Surfaces. *ChemCatChem* **2020**, *12* (18), 4611–4617.

(103) van Deelen, T. W.; Hernández Mejía, C.; de Jong, K. P. Control of Metal-Support Interactions in Heterogeneous Catalysts to Enhance Activity and Selectivity. *Nat. Catal.* **2019**, *2* (11), 955–970.

(104) Li, G.; Meeprasert, J.; Wang, J.; Li, C.; Pidko, E. A. CO_2 Hydrogenation to Methanol over Cd_4/TiO_2 Catalyst: Insight into Multifunctional Interface. *ChemCatChem* **2022**, *14* (5), e202101646.

(105) Zhong, J.; Yang, X.; Wu, Z.; Liang, B.; Huang, Y.; Zhang, T. State of the Art and Perspectives in Heterogeneous Catalysis of CO_2 Hydrogenation to Methanol. *Chem. Soc. Rev.* **2020**, *49* (5), 1385–1413.

(106) Ra, E. C.; Kim, K. Y.; Kim, E. H.; Lee, H.; An, K.; Lee, J. S. Recycling Carbon Dioxide through Catalytic Hydrogenation: Recent Key Developments and Perspectives. *ACS Catal.* **2020**, *10* (19), 11318–11345.

(107) Zhang, W.; Zhao, S.; Ando, Y.; He, C.; Yang, B.; Dostagir, N.; Anzai, A.; Toyoshima, R.; Kondo, H.; Shimizu, K.; Toyao, T. Nb-Promoted Pt/MoOx/TiO_2 Catalysts for Low-Temperature CO_2 Hydrogenation to Methanol. *Chem. Eur. J.* **2025**, e02546.

(108) Kattel, S.; Yan, B.; Yang, Y.; Chen, J. G.; Liu, P. Optimizing Binding Energies of Key Intermediates for CO_2 Hydrogenation to Methanol over Oxide-Supported Copper. *J. Am. Chem. Soc.* **2016**, *138* (38), 12440–12450.

Chapter 5

General Conclusion

In this work, I focused on developing supported catalysts to enhance the efficiency of methanol synthesis via the direct hydrogenation of CO_2. The conversion of CO_2 into methanol represents a promising strategy for carbon utilization and sustainable chemical production. However, current industrial processes rely on Cu-based catalysts, which suffer from low CO_2 conversion, limited methanol yield, and require high reaction temperatures and pressures. Operating at low temperatures offers advantages such as reduced operating cost and higher conversion of CO_2 to methanol due to the exothermic nature of the reaction. Therefore, the aim of this dissertation is to develop highly active catalysts that can operate efficiently under such conditions. By integrating advanced data science approaches with comprehensive catalyst characterization, we not only discovered high-performance catalysts for CO_2 hydrogenation to methanol but also clarified the specific role of each element in enhancing catalytic activity. *In situ/operando* spectroscopic techniques addressed the structure-activity relationships in promoting methanol synthesis efficiency. The main conclusions are summarized as follows:

Chapter 2 displays the development of highly active heterogeneous catalysts for CO_2 hydrogenation to methanol using machine learning approach. In this study, we utilized a machine learning approach to develop low-temperature CO_2 hydrogenation catalysts. By employing iterative ML model predictions and experimental validation in batch reactors, we screened 580 distinct catalysts and identified 33 catalysts that outperformed the previously reported highly active catalyst (Pt(3)/Mo(20)/TiO_2). The best catalyst, Pt(5)/Mo(8)–Re(1)–W(0.7)/TiO_2, exhibited a methanol production rate of 1.46 mmol g^{-1} h^{-1} in a batch reactor and a high production rate of 1.8 mmol g^{-1} h^{-1} in a flow reactor at 150 °C under 4 MPa (H_2/CO_2 = 3). In situ/operando spectroscopic analysis was conducted to elucidate the function of each catalyst component in methanol synthesis. Detailed analysis revealed that in the best catalyst, Pt primarily facilitated H_2 dissociation, partially reduced Mo oxides were crucial in generating oxygenated species, and the presence of acidic W promoted methanol desorption from the catalyst surface. Re promoted the formate conversion to methanol thus accelerating the overall methanol formation.

Chapter 3 introduces the development of highly efficient catalyst for methanol production in flow systems based on the insights obtained in Chapter 2. In this study, we developed a series of Nb-promoted Pt/MoO_x/TiO_2 catalysts for efficient CO_2 hydrogenation at temperatures below 200 °C. Pt(5)/Mo(10)-Nb(1)/TiO_2 was found to be best catalyst exhibiting superior performance, achieving a high methanol productivity of 3.8 mmol g_{cat}^{-1} h^{-1} at 150 °C,

outperforming the commercial Cu-ZnO/Al_2O_3 catalyst under comparable conditions. The catalyst showed stable performance during a 400 h long-term reaction. Detailed *in situ* and *operando* spectroscopic studies revealed that Pt sites are primarily responsible for H_2 activation, while partially reduced MoO_x species facilitate the formation of oxygenated intermediates. The incorporation of highly dispersed Nb species promoted methanol de sorption and inhibited its decomposition, thereby contributing to the overall catalytic efficiency. This study outlines a rational design approach for constructing robust low-temperature catalysts and provides mechanistic insights into the synergistic roles of the metal and oxide components in CO_2-to-methanol conversion.

In Chapter 4, I optimized the existing machine learning model for the discovery of highly active catalysts for methanol formation in flow system. After performing 25 iterations of ML prediction and experimental validation, the Pt(5)/Mo(8)-Cr(0.7)-V(0.7)-La(0.7)/TiO_2 catalyst was discovered as the most effective catalyst in methanol synthesis (STY_{MEOH}: 3.0 mmol g_{cat}^{-1} h^{-1}). Using the knowledge gained from Chapter 2, we loaded Re on the catalyst and developed a new catalyst having much higher methanol productivity (Pt(5)/Mo(8)-Cr(0.7)-V(0.7)-La(0.7)-Re(1)/TiO_2; STY_{MEOH}: 6.2 mmol g_{cat}^{-1} h^{-1}). Detailed characterization studies clarified the role of each element in the catalytic reaction. Highly dispersed Pt nanoparticles were responsible for H_2 dissociation, partially reduced Mo species promoted CO_2 activation and oxygenate generation, Re promotes formate hydrogenation to methoxy, La promotes CO_2 activation, Cr provides stabilization of intermediates and easy desorption of methanol and V contributed to facile desorption of methanol. Overall, this work demonstrates that the integration of machine learning with experimental catalyst design is an effective strategy for discovering efficient and stable CO_2 hydrogenation catalysts, and it provides useful insights into the development of next-generation methanol synthesis systems.

Acknowledgement

I would like to express my deepest gratitude to my supervisors, Prof. Ken-ichi Shimizu and Prof. Takashi Toyao, for giving me the opportunity to join their laboratory and for their generous guidance, insightful advice, and continuous support throughout my doctoral studies. I am also sincerely thankful to Asst. Prof. Akihiko Anzai and Asst. Prof. Shaikh Nazmul Hasan MD Dostagir for their helpful discussions and encouragement.

I am deeply grateful to Prof. Ichigaku Takigawa from the University of Tokyo, Prof. Gang Wang from the University of Chinese Academy of Sciences, Dr. Pengfei Du from the Shimizu Lab, Asst. Prof. Ryo Toyoshima from Keio University, as well as Dr. Shinya Mine and Dr. Abdellah Ait El Fakir, postdoctoral researchers in the Shimizu Lab, for their valuable technical expertise and collaborative support, which greatly contributed to the completion of this work.

I would also like to acknowledge the Advanced Graduate School Program and the EXEX Doctoral Fellowship at Hokkaido University for providing me with the opportunity and financial support to pursue my PhD studies.

My sincere appreciation extends to all members of Prof. Shimizu's laboratory for their assistance, cooperation, and the friendly research environment they created.

Finally, I would like to express my heartfelt gratitude to my family and friends—especially my wife Liang Han, my mother Jing Wang, and my son Long Zhao—for their unwavering support, understanding, and encouragement throughout this journey. I am also profoundly grateful to my late father, whose values, love, and blessings have continued to guide and strengthen me. This achievement is as much his as it is mine.

Shirun ZHAO